DEVELOPMENT OF GRAPHENE BASED BIOSENSORS FOR EARLY DETECTION OF ALZHEIMER'S DISEASE

HINA Y. ABBASI

Swansea University
Prifysgol Abertawe

*Submitted to Swansea University in fulfilment of the requirements for the Degree of **Doctor of Philosophy** in **Nanotechnology***

Swansea University

July 2022

ABSTRACT

There has been extensive research on the electronic and physical properties of graphene since it was first discovered in 2004. This research has shown graphene to be a wonder material and makes it an ideal candidate for use in next-generation sensor technologies. Graphene consists of a single atomic layer of sp^2 hybridized carbon atoms and has exceptionally ballistic electronic transport, alongside high specific surface area, strong mechanical strength, and flexibility, which is essential for constructing biosensor devices.

This thesis describes the development of graphene-based biosensors for the early diagnosis of Alzheimer's disease (AD). For that purpose, this work was focused on developing novel functionalization chemistries for the attachment of bioreceptors to graphene and subsequent detection of AD biomarkers. Three different functionalization mechanisms i.e., diazonium grafting, pDAN electropolymerization, and neutravidin protein attachment were studied and explored in detail. Amongst them, the pDAN electropolymerization, and neutravidin protein attachment methods were utilized for graphene surface functionalization and successful development of biosensors for the detection of three biomarkers i.e., Aβ(1-40), Aβ(1-42), and Tau-352 that have been reported as potential candidate biomarkers for AD. The lowest limit of detection for all three biomarkers was observed when using the neutravidin protein attachment method on rGO-modified screen printed electrodes. The proposed approach showed a wide logarithmically linear range of detection from 10 fg/mL to 10 ng/mL in both diluted human plasma as well as phosphate-buffered saline (PBS) solutions. The fabricated sensors also showed stability of up to 6 weeks.

The reported immunosensors can be utilized for the rapid screening of patients. In addition to that, the electrochemical sensing techniques used in this thesis are easily adaptable and hence can be miniaturized to develop portable and nonexpensive devices. These devices have the

capability of performing rapid measurements on solutions with biomolecules even at very low concentrations. Hence, point-of-care monitoring and diagnostics can be performed using these devices.

DECLARATIONS

This work has not previously been accepted in substance for any degree and is not being concurrently submitted in candidature for any degree.

[redacted]..

31-07-2022
Date...

This thesis is the result of my own investigations, except where otherwise stated. Other sources are acknowledged by footnotes giving explicit references. A bibliography is appended.

[redacted]..

31-07-2022
Date...

I hereby give consent for my thesis, if accepted, to be available for photocopying and for inter-library loan, and for the title and summary to be made available to outside organisations.

[redacted]..

31-07-2022
Date...

The University's ethical procedures have been followed and, where appropriate, that ethical approval has been granted.

[redacted]..

31-07-2022
Date..

MARIE SKłODOWSKA-CURIE ACTIONS

Blood Biomarker-based Diagnostic Tools for Early Stage Alzheimer's Disease (BBDIAG)

EU-H2020-MSCA-ITN-ETN-2016

The Marie Skłodowska-Curie Actions are the EU flagship programme for doctoral and postdoctoral training, equipping researchers with new knowledge and skills through mobility across borders and exposure to different sectors and disciplines.

This research is financially supported by H2020 MSCA-ITN-ETN BBDiag project under grant No. 721281

ACKNOWLEDGMENTS

Firstly, I cannot thank enough my Lord, ALLAH (SWT), Whose constant blessings in my life are immeasurable, unperceivable, unforgettable, and never cease to exist and there is no end to it. With every passing day, my belief and trust in ALLAH increases which keeps me inspired and humble.

Working on the PhD has been a journey full of challenging experiences for me at the academic level together with my personal life. It has allowed me to discover my true potential as a researcher. Success in this academic journey would not have been possible without the untiring support of my supervisor Prof. Owen Guy, for which I am extremely grateful. I feel deeply indebted to you for your irreplaceable guidance and continuous feedback which paved the way for my research work. Thank you for being so generous in sharing your knowledge which allowed me to develop my expertise in the field of biosensors. Your unwavering support is the reason I have been able to complete my thesis work.

I would like to express my sincere gratitude to the Marie Skłodowska-Curie fellowship program for funding my PhD thesis work and turning it into reality. I am grateful to all the BBDiag consortium who provided me the opportunity to be a part of this incredible researchers’ network and the opportunity to present at consortium events and to gain a wealth of knowledge and experience in the field of biosensors.

To my research colleagues Zari, Anitha, Ehsaneh, Ffion & Mo, thank you for being so welcoming in sharing your valuable knowledge, and expertise and for discussing ideas that greatly helped me in achieving the desired research outputs. I feel very lucky to have worked with you and to learn from you guys. Especially I am full of thanks to Zari and Anitha for being trustworthy fellows from the beginning to the end of my research work. I truly enjoyed working with you and found you guys always ready to provide me with a helping hand whenever I reached out. Whether the work was related to planning to develop an experimental setup in the lab, understanding complex chemical equations, paper write-ups, or preparation for meetings and conference presentations your ingenious suggestions & insights always proved to be fruitful and saved me a lot of time & energy. Thanks for being some awesome colleagues. I also very much appreciate the assistance extended to me by Mo in paper write-ups and in completing this dissertation. I highly admire your support for always helping me with my XPS results.

Finally, I would also like to give special thanks to my husband, Ahsin for his continuous encouragement, unfailing love, and moral support during my pursuit of a PhD degree. Thanks for being patient and understanding all the way through my research work and thesis writing. Your love is what has gotten me through the gloomy times. To my beloved son, Hadi, you have made me stronger, better, more compassionate, and more fulfilled than I could have ever imagined. You are pure proof that everything will work out just perfectly. I also express my deepest gratitude to my parents, my siblings Athar, Umar, and Noor, and my sister-in-law Kanza for all the love, support, encouragement, and prayers they have sent my way along this journey. To my parents your unconditional love and support have meant the world to me, I hope that I have made you proud. To Kanza thank you so much for always taking care of Hadi during the lockdown times when it was difficult to send him to the nursery and when I was working from home.

“And whoever relies upon Allah – then He is sufficient for him. Indeed, Allah will accomplish His purpose. Allah has already set for everything a [decreed] extent”

[Quran 65:3]

TABLE OF CONTENTS

ABSTRACT ---------- **2**

DECLARATIONS ---------- **4**

ACKNOWLEDGMENTS ---------- **7**

TABLE OF CONTENTS ---------- **10**

LIST OF FIGURES: ---------- **19**

LIST OF TABLES ---------- **27**

LIST OF ABBREVIATIONS ---------- **28**

CHAPTER 1 ---------- **30**

INTRODUCTION AND THESIS STRUCTURE ---------- **30**

1.1 INTRODUCTION ---------- **30**

1.2 THESIS STRUCTURE ---------- **32**

BIBLIOGRAPHY ---------- **35**

CHAPTER 2 ---------- **38**

LITERATURE REVIEW ---------- **38**

2.1 INTRODUCTION ---------- **38**

2.2 ALZHEIMER'S DISEASE (AD) ---------- **39**

  2.2.1 ALZHEIMER'S PATHOPHYSIOLOGY: ---------- 40

  2.2.2 ALZHEIMER'S TOPOGRAPHY: ---------- 43

  2.2.3 STAGES OF ALZHEIMER'S DISEASE: ---------- 45

    2.2.3.1 Pre-clinical Phase: ---------- *45*

2.2.3.2 Prodromal Stage:--*46*

2.2.3.2.1 Mild Cognitive Impairment (MCI):---46

2.2.3.3 Dementia Phase: ---*47*

2.2.4 OTHER DEMENTIA TYPES AND THEIR CONNECTION TO ALZHEIMER'S:------------------**47**

2.2.4.1 Vascular Dementia (VD): --*47*

2.2.4.2 Dementia with Lewy Bodies (DLB):---*48*

2.2.4.3 Parkinson's disease: --*48*

2.2.5 THE CURRENT DIAGNOSTIC TECHNIQUES FOR ALZHEIMER'S DISEASE: ------------------**48**

2.2.5.1 Brain Imaging Technique:---*49*

2.2.5.2 Amyloid Positron Emission Topography (PET) Imaging: -------------------------*50*

2.2.5.3 Fluorodeoxyglucose (FDG) PET: --*50*

2.2.5.4 Tau PET imaging:---*51*

2.2.6 CURRENT TREATMENT OPTIONS FOR AD: ---**51**

2.2.6.1 Acetylcholinesterase Inhibitors: ---*51*

2.2.6.2 (N-Methyl-D-aspartate) NMDA Receptor Antagonists: ---------------------------*51*

2.2.6.3 Non-Steroidal Anti-inflammatory Drugs (NSAIDs): -------------------------------*52*

2.2.7 BIOMARKERS FOR ALZHEIMER'S DISEASE:---**52**

2.2.7.1 Characteristics of an Ideal Biomarker:---*53*

2.2.7.2 Sensitivity/Limits of Detection: --*53*

2.2.7.3 Cerebrospinal Fluid (CSF) Biomarkers: --*54*

2.2.7.4 Plasma Biomarkers: --*55*

2.3 INTRODUCTION TO BIOSENSING: ---56

2.3.1 BIOSENSORS:---57

2.3.2 ELECTROCHEMICAL BIOSENSORS:---58

2.3.3 GRAPHENE: ---**63**

2.3.3.1 Properties of Graphene: ---*64*

2.3.3.2 Graphene Functionalization Chemistry: --*67*

2.3.3.2.1 Covalent Functionalization: --67

2.3.3.2.2 Non-Covalent Functionalization:--68

2.3.3.3 Biofunctionalization:--*69*

2.3.3.4 Selective Antibody Orientation: --*70*

2.3.3.5 EDC/ NHS Activation of Antibodies:--*70*

2.3.3.6 Blocking Non-Specific Binding: ---*71*

2.3.3.7 Graphene substrate: --*73*

2.3.3.7.1 Screen-Printed Electrodes (SPEs): ---73

2.3.4 STATE-OF-THE-ART GRAPHENE-BASED BIOSENSORS FOR DETECTION OF AD BIOMARKERS:--**75**

2.3.4.1 Graphene Biosensors: ---*75*

2.3.4.2 Graphene-Based DNA and mRNA Electrochemical Sensors:----------------------*76*

2.3.4.3 Graphene-Based Electrochemical Immunosensors:--------------------------------*77*

2.3.4.4 Graphene-Based Field-Effect Transistor (FET) Biosensors: ----------------------*79*

2.3.4.5 Graphene-Based Optical Biosensors:---*80*

2.3.5 LIMITATIONS OF GRAPHENE-BASED DEVICES:---**81**

BIBLIOGRAPHY---**83**

CHAPTER 3 --- **101**

MATERIALS AND METHODS -- **101**

3.1 MATERIALS--- **102**

3.1.1 GRAPHENE: -- **102**

3.1.2 GLASSY CARBON (GC): --- **102**

3.2 EXPERIMENTAL METHODS--- 103

3.2.1 SURFACE FUNCTIONALIZATION TECHNIQUES: --- **103**

3.2.1.1 Electrochemical Functionalization:-- 103

3.2.1.1.1 Diazotisation: --- 104

3.2.1.1.2 Electropolymerization of 1,5-Diaminonapthalene (DAN): ------------------ 105

3.2.1.1.3 Functionalization via Neutravidin Attachment:-------------------------------- 107

3.2.2 BIOFUNCTIONALIZATION TECHNIQUE: --- **109**

3.2.3 CHARACTERIZATION TECHNIQUES: --- **110**

3.2.3.1 Scanning Electron Microscopy (SEM):--- 110

3.2.3.2 Atomic Force Microscopy (AFM): --- 112

3.2.3.3 Raman Spectroscopy: --- 114

3.2.3.4 X-ray Photoelectron Spectroscopy (XPS): --------------------------------------- 118

3.2.3.5 Electrochemical Characterization:-- 121

3.2.3.5.1 Potentiometry: --- 123

3.2.3.5.2 Cyclic Voltammetry (CV): -- 124

3.2.3.5.3 Square Wave Voltammetry (SWV): --- 129

3.2.3.5.4 Differential Pulse Voltammetry (DPV): -------------------------------------- 132

3.2.3.5.5 Electrochemical Impedance Spectroscopy (EIS): ---------------------------- 134

BIBLIOGRAPHY--- 138

CHAPTER 4 --- 146

ASSESSING SURFACE COVERAGE OF AMINOPHENYL BONDING SITES ON DIAZOTISED GLASSY CARBON ELECTRODES FOR OPTIMIZED ELECTROCHEMICAL BIOSENSOR PERFORMANCE --------------------------------- 146

4.1 INTRODUCTION --- 147

4.2 MATERIALS AND METHODS ---------- 151

4.2.1 ELECTROCHEMICAL MEASUREMENTS: ---------- **152**

4.2.2 CHARACTERIZATION TECHNIQUES: ---------- **153**

4.3 RESULTS AND DISCUSSION ---------- 154

4.3.1 SURFACE FUNCTIONALIZATION OF GLASSY CARBON VIA DIAZOTIZATION: ---------- **154**

4.3.1.1 Attachment of 4-nitrophenyl to the glassy carbon electrode (GCE) surface: -- 154

4.3.1.2 Electrochemical reduction of 4-nitrophenyl layers on glassy carbon: ---------- 156

4.3.1.3 Calculation of the number of molecules on the surface: ---------- 158

4.3.1.4 Calculating the surface coverage: ---------- 160

4.3.1.4.1 Surface Coverage of aminophenyl after reduction in 0.1M KCL: ---------- 161

4.3.2 QUANTIFICATION OF SURFACE AMINE GROUPS: ---------- **161**

4.3.2.1 Surface Coverage estimation after FCA attachment: ---------- 163

4.3.3 ELECTROCHEMICAL SENSING VIA ANALYSIS OF THE ELECTRODES: ---------- **165**

4.3.4 CHARACTERIZATION OF SURFACE MORPHOLOGY ELECTRODE: ---------- **167**

4.4 CONCLUSIONS ---------- 169

BIBLIOGRAPHY ---------- 171

CHAPTER 5 ---------- 178

GRAPHENE BASED ELECTROCHEMICAL IMMUNOSENSOR FOR THE ULTRA-SENSITIVE LABEL FREE DETECTION OF ALZHEIMER'S BETA AMYLOID PEPTIDES AB(1-42) ---------- 178

5.1 INTRODUCTION ---------- 178

5.2 MATERIALS AND METHODS ---------- 183

5.2.1 MATERIALS: ---------- **183**

5.2.2 ELECTROPOLYMERIZATION: -- **184**

5.2.3 BIO-FUNCTIONALIZATION: -- **185**

5.2.3.1 Debye Length: -- 186

5.2.4 AMYLOID BETA (1-42) PRE-TREATMENT METHOD: -- **187**

5.2.5 HUMAN BLOOD COLLECTION AND PLASMA PREPARATION:-------------------------------- **187**

5.2.6 CHARACTERIZATION: -- **187**

5.3 RESULTS AND DISCUSSIONS--- 188

5.3.1 GRAFTING PDAN LAYERS ON SPGES:-- **188**

5.3.2 MECHANISM OF ACTION OF PDAN/GRAPHENE INTERFACES: ---------------------------- **189**

5.3.2.1 Electrochemical Analysis:-- 189

5.3.2.2 Quantification of Amine surface groups: -- 192

5.3.2.3 Structural and Chemical Analysis: -- 194

5.3.3 MECHANISM OF ANTIBODY/PDAN/GRAPHENE INTERFACES:----------------------------- **198**

5.3.3.1 Electrochemical Analysis:-- 198

5.3.3.2 Optimizing the Antibody Concentrations: -- 199

5.3.3.3 Optimising the Sensor for False-Positive:-- 200

5.3.4 EVALUATING THE ELECTROCHEMICAL IMMUNOSENSOR PERFORMANCE: --------------- **202**

5.3.4.1 Sensitivity Analysis: --- 202

5.3.4.2 Specificity and Stability Analysis: --- 205

5.3.4.3 Spiked Plasma Analysis: -- 206

5.4 CONCLUSIONS -- 207

BIBLIOGRAPHY-- 208

CHAPTER 6 -- 216

AN ELECTROCHEMICAL IMPEDIMETRIC BIOSENSOR BASED ON NEUTRAVIDIN- BIOTIN INTERACTION FOR FEMTOMOLAR RANGE DETECTION OF AD BIOMARKERS IN HUMAN PLASMA USING FLEXIBLE SCREEN-PRINTED GRAPHENE ELECTRODES-- 216

6.1 INTRODUCTION -- 217

6.2 MATERIALS AND METHODS -- 220

6.2.1 MATERIALS: -- **220**

6.2.2 CHARACTERIZATION: --- **220**

6.2.3 ELECTROCHEMICAL MEASUREMENTS: -- **221**

6.2.4 BIOSENSOR FABRICATION: --- **221**

6.2.5 INTERACTION OF BIOMARKERS WITH THE SENSOR: --------------------------------------- **223**

6.2.6 PLASMA SAMPLE ANALYSIS: --- **223**

6.3 RESULTS AND DISCUSSION -- 224

6.3.1 SURFACE MORPHOLOGY:-- **224**

6.3.2 STRUCTURAL AND CHEMICAL ANALYSIS:-- **225**

6.3.3 REACTION MECHANISM OF RGO/NVD/BIOTIN-ANTIBODY INTERFACES: `-------------- **226**

6.3.3.1 Electrochemical Analysis: -- 226

6.3.4 OPTIMIZING SENSOR PARAMETERS: -- **228**

6.3.4.1 Neutravidin immobilization time: -- 229

6.3.4.2 Antibody concentration: -- 230

6.3.4.3 Antibody immobilization time: -- 230

6.3.5 ANALYTICAL PERFORMANCE OF IMPEDIMETRIC IMMUNOSENSOR: ---------------------- **231**

6.3.5.1 Specific detection of target proteins in PBS: -------------------------------------- 231

6.3.5.2 Specific detection of target proteins in human plasma: -------------------------- 233

6.3.5.3 Optimizing the sensor for false-positive: -- *235*

6.3.5.4 Mouse plasma sample analysis: -- *236*

6.3.5.5 Specificity analysis: -- *237*

6.3.5.6 Stability studies: -- *239*

6.4 CONCLUSION--- 239

BIBLIOGRAPHY-- 241

CHAPTER 7 --- 246

CONCLUSION AND FUTURE WORK-- 246

7.1 CONCLUSION -- 246

7.1.1 LITERATURE REVIEW:---**247**

7.1.2 MATERIALS AND METHODS:---**247**

7.1.3 ASSESSING SURFACE COVERAGE OF AMINOPHENYL BONDING SITES ON DIAZOTISED GLASSY CARBON ELECTRODES FOR OPTIMIZED ELECTROCHEMICAL BIOSENSOR PERFORMANCE:-- **248**

7.1.4 GRAPHENE-BASED ELECTROCHEMICAL IMMUNOSENSOR FOR THE ULTRA-SENSITIVE LABEL-FREE DETECTION OF ALZHEIMER'S BETA-AMYLOID PEPTIDES AB(1-42):-------------- **251**

7.1.5 AN ELECTROCHEMICAL IMPEDIMETRIC BIOSENSOR BASED ON NEUTRAVIDIN- BIOTIN INTERACTION FOR FEMTOMOLAR RANGE DETECTION OF AD BIOMARKERS IN HUMAN PLASMA USING FLEXIBLE SCREEN-PRINTED GRAPHENE ELECTRODES:---------------------------------- **253**

7.2 FUTURE WORK --- 255

APPENDICES -- 258

SUBMITTED/ PUBLISHED ARTICLES: -- **258**

PLANNED PUBLICATIONS: --- **259**

CONFERENCES AND NETWORK EVENTS: -- **259**

LIST OF FIGURES:

Figure 2. 1 Scheme of the amyloid-β (Aβ) cascade hypothesis in Alzheimer's disease [42]. ... 43

Figure 2. 2: An illustration of the atrophy of the brain tissue resulted in AD displayed by the cross section of brain. 44

Figure 2. 3: An illustration of the hippocampus and amygdala (parts of limbic system separated by the uncus) [46]. 45

Figure 2. 4: The model of Clinical Glide path of AD representing the phase of preclinical AD before MCI [50]........ 46

Figure 2. 5: Components of a biosensor, commonly used analytes and types of signal transducers [86]........ 58

Figure 2. 6: Schematic representation of a three-electrode electrochemical cell set-up; illustrating the working electrode (WE), counter electrode (CE), and reference electrode (RE) in an electrolyte solution i.e, potassium ferro/ferricyanide. The inset shows the reaction at the WE, where the target proteins are attached to the bioreceptors which are immobilized on the surface of electrode. As the concentration of the target analyte changes, the redox reaction also changes which in turn changes the voltage or current thus resulting in a measurable reading........ 60

Figure 2. 7: A schematic representation of a target analyte detection applying the direct current-voltage measurement technique using a direct assay. In this case, a source is used for applying the voltage while the drain reads out the current. 62

Figure 2. 8: Illustration of 2D graphene i.e., wrapped into 0D fullerene, rolled into 1D carbon nanotube, and stacked into 3D graphite........ 64

Figure 2. 9: Electronic structure of graphene (a) Graphene's hexagonal lattice. Each carbon atom with an angle of 120° is bounded to three other carbon atoms.(b) The sp^2 orbitals and the p

orbital of single carbon atom within the hexagonal lattice structure. (c) A schematic illustration showing the sp^2 orbitals forming the σ-bonds and p orbitals forming the π-bonds. 65

Figure 2. 10: An illustration of the Metrohm dropsens Screen printed Electrode (SPE). 73

Figure 3. 1: Electro-grafting of 4-nitrobenzenediazonium tetrafluoroborate salt. 104

Figure 3. 2: A schematic representation of the polymerization of 1,5-DAN monomers into polymer DAN. 106

Figure 3. 3: Ribbon diagram of (a) avidin structure with bound biotin (spheres) (b) monomeric streptavidin with bound biotin (c) tetrameric structure of neutravidin. 107

Figure 3. 4: Schematic interpretation of carbodiimide crosslinking of bioreceptor to the surface of sensor utilizing EDC/NHS activation method to attach to the amines. (a) A bioreceptor (carboxyl terminated) is reacted to EDC and form an intermediate product (b) that is an unstable reactive o-acylisourea. (c) The substitution between EDC and the NHS to create a stable NHS ester takes place. (d) which reacts with amine group on the surface of sensor to create a stable link in form of an amide bond. 109

Figure 3. 5: A schematic representation of Scanning Electron Microscopy (SEM). 111

Figure 3. 6: A schematic representation of an Atomic Force Microscopy (AFM) apparatus.. 113

Figure 3. 7: A schematic representation of a Raman Spectrometer [50]. 114

Figure 3. 8: Raman spectrum for graphene showing the G, G'(2D) and D bands. 115

Figure 3. 9: An illustration of Raman process inside graphene chemical structure. First order process forms the G band and second order process also called as double resonance proce forms D and 2D or G’ band. D band is created via elastic scattering from a defect and inelastic scattering from a phonon. 2D or G’ band is created via inelastic scattering of two phonons. 116

Figure 3. 10: A typical Raman spectra of graphene samples showing change in peaks with increasing the number of graphene layers and also includes Raman spectra of graphite. 117

Figure 3. 11: A schematic representation of X-ray photoelectron spectroscopy (XPS) instrumentation. 120

Figure 3. 12: A schematic illustration of the reactions occurring at the electrode surface. The redox couple used here is ferricyanide and ferrocyanide ($[Fe(CN)_6]^{3-}$/$[Fe(CN)_6]^{4-}$) as the oxidant and reductant species. 122

Figure 3. 13: A schematic illustration of the setup of three-electrode electrochemical cell, in the case of this thesis the WE is the graphene based SPE, silver/ silver chloride (Ag/ AgCl) is used as RE, and Platinum wire is used as the CE. A potentiostat controls the electrochemical cell, and the visual display unit the PC presents the resulting graphs. 123

Figure 3. 14: A cyclic voltammogram showing the peak anodic potential (E_{pa}), anodic current (i_{pa}), peak cathodic potential (E_{pc}) and the cathodic current (i_{pc}). 124

Figure 3. 15: Mechanism of immobilization of electrochemically active ferrocene carboxylic acid (FCA) to the amine functionalized surfaces via the carbodiimide cross-linking process. 128

Figure 3. 16: An illustration of voltage pulses for square wave voltammetry (SWV). 129

Figure 3. 17: An illustration of voltage pulses of square wave voltammetry (SWV) (forward and a reverse pulse). 130

Figure 3. 18: An illustration of voltage pulses for the differential pulse voltammetry (DPV). 132

Figure 3. 19: A schematic of an interface showing the electrons at negatively charged surface and solvent is adsorbed at the surface. The corresponding Randle's equivalent circuit for EIS analysis is also shown (Rs is the solution resistance, Rp is polarization resistance, Zω is the mass-transport (Warburg's) impedance and Cd is the double-layer capacitance). 134

Figure 3. 20: The Nyquist plot arising from an idealized Randle's equivalent circuit........... 136

Scheme 4.1: (a) Important antibody chemical species for targeting, (b) EDC/NHS coupling of the antibody carboxyl group to surface amine group. 149

Figure 4. 1: Cyclic voltammograms (50 mV/s) of glassy carbon electrode (GCE) in Bu_4NBF_4 in acetonitrile 0.1 M before (black curve) and after the addition of diazonium (DIZ) (orange curve); after repeated voltammetry cycles (five scans, fifth scan olive green curve), there was no further reduction. The experiment was repeated four times............................... 155

Figure 4. 2: (a) Electron transfer from a glassy carbon electrode to the diazonium cation and subsequent loss of N_2 to form an aryl radical. (b) Nitrophenyl radical and an electron from the surface glassy carbon electrode generate covalent bond with the release of an electron. 156

Scheme 4. 2 Electrochemical reduction pathway of nitro group (NO_2) to an amino group (NH_2) in an aqueous electrolyte [19]. 157

Figure 4. 3: Cyclic voltammograms (50 mV/s) of the reduction of surface-grafted 4-nitro-phenyl on GCE in 0.1 M KCl in water: ethanol (9:1) electrolyte: (a) black curve - one scan; (b) green curve- five scans. The inset figure shows the change of peak current with the number of cycles at -0.2 V. The experiment was repeated four times. 158

Figure 4. 4: Area under the reduction curve of surface-grafted 4-nitrophenyl on GCE in 0.1 M KCl in water: ethanol (9:1) electrolyte, with scan rate of 50 mV/s the shaded area corresponds to a charge of 1.44176 x10^{-5} C (see Table 4.2)... 159

Figure 4. 5: (a) Cyclic voltammograms (5 mV/s) of FCA-functionalization of amine functionalized GCEs prepared using a different number of reduction scans (scans 1-5), in PBS electrolyte. (b) The bar chart shows the degree of FCA functionalization which is a maximum for the amine functionalized GCE prepared using three scans. 162

Scheme 4. 3: Immobilisation mechanism of electrochemically active FCA on to an amine modified GCE through carbodiimide linking. 162

Figure 4. 6: Area under the reduction curve of FCA functionalized GCE after 3 scans of nitrophenyl to aminophenyl in 0.1 M KCl in water: ethanol (9:1) electrolyte, reference electrode (Ag/AgCl), with scan rate of 5 mV s^{-1} the shaded area corresponds to a charge of 1.478 $x10^{-7}$ C (see Table 4.3). 163

Figure 4. 7: Differential pulse voltammetry (DPV) results for Aβ (1-42) peptide sensors made from amino functionalized substrates using different numbers of reduction scans. (a-b) 3 and 5scans; (c-d) corresponding calibration curves of $\%I_R$ $[\Delta I(I_a-I_o)/I_o)\%]$ (percentage current reduction) against log Aβ(1-42) concentrations. 166

Figure 4. 8: Control Differential pulse voltammetry (DPV) results for Aβ (1-42) peptide sensors made from amino functionalized substrates using different numbers of reduction scans. (a-b) 0 and 2 scans respectively. 167

Figure 4. 9: Morphology of HOPG electrode with AFM (a) blank -before diazotisation (b) after diazotisation one scan (c) after three scans (d) after five scans. 168

Figure 4. 10: Morphology of HOPG electrode with SEM (a) blank -before diazotisation (b) after diazotisation one scan (c) after three scan (d) after five scans 169

Figure 5. 1: Bar chart representing the antibody incubation time vs the percentage reduction in the peak current obtained from DPV analysis (n=3). 185

Figure 5. 2: Electropolymerization of pDAN for after 5 repeated voltammetry cycles. Cyclic voltammetry (CV) was carried out between 0 V to 0.9 V with 50 mVs^{-1} scan rate. 189

Figure 5. 3: Cyclic Voltammograms of Blank and pDAN modified SPGEs in 5mM $[Fe(CN)_6]^{3-/4-}$ redox couple at scan rates 10 mVs^{-1}, 20 mVs^{-1}, 30 mVs^{-1}, 40 mVs^{-1}, 50 mVs^{-1}, 60 mVs^{-1}, 70 mVs^{-1}, 80 mVs^{-1}, 90 mVs^{-1}, and 100mVs^{-1} and step size of -0.00244 V (a) Blank SPGE (b) 1 Cycle pDAN SPGE (c) 2 Cycles pDAN SPGE (d) 3 Cycles pDAN SPGE (e) 5 Cycles pDAN SPGE and (f) 10 Cycles pDAN SPGE. 190

Figure 5. 4: Anodic and Cathodic Peak Current (Ip) values from CV curves of Blank and pDAN modified SPGEs (a) Blank SPGE (b)1 Cycle pDAN SPGE (c) 2 Cycles pDAN SPGE (d) 3 Cycles pDAN SPGE (e) 5 Cycles pDAN SPGE (f) 10 Cycles pDAN SPGE. 191

Figure 5. 5: Bar chart illustrating the change in charge transfer diffusion coefficient (D_{CT}) vs. number of pDAN scan cycles... 192

Figure 5. 6: (a) Cyclic voltammogram of ferrocene carboxylic acid functionalized SPGE and pDAN modified SPGEs at different scan cycles. PBS was used as the electrolyte and the CVs were recorded at a 5 mVs^{-1} scan rate. (b) Bar chart showing amine surface coverage vs the number of pDAN scan cycles…………………………………………………………………193

Figure 5. 7: Comparison of Blank and pDAN functionalized graphene SPE at 3 scan cycles (a) Raman Spectrum (b) XPS spectrum showing wide scan, pDAN functionalized SPGE showing (c) N 1s spectrum (d) C 1s spectrum. 195

Figure 5. 8: AFM images of pDAN layers deposited on SPGE surface at different scan cycles (a) 0 cycles (Blank) (b) 3 cycles (c) 5 cycles (d) 10 cycles. 197

Figure 5. 9: (a) Schematic representation of electrochemical immunosensor showing change on surface after each functionalization stage (b) Differential pulse voltammetry (DPV) response (c) Square wave voltammetry (SWV) response... 198

Figure 5. 10: (a) Peak current reduction in DPV and SWV measurements (%i_r) at each concentration of Aβ antibody. (b) Percentage reduction in peak current to the exposure to DI water and PBS (0.1 mM) (n=3). 200

Figure 5. 11: Bar chart illustrating the peak current reduction (%i_r) with exposure to the 0.1 mM PBS only (negative runs with respect to each peptide concentration) and log of different concentrations of beta amyloid peptide. 201

Figure 5. 12: Differential pulse voltammetry (DPV) results at 20 μgmL^{-1}, 40 μgmL^{-1} and 60μgmL^{-1} concentration of Aβ antibodies: (a-c) DPV plots of 20 μgmL^{-1}, 40 μgmL^{-1} and

60µgmL^{-1} antibodies at each stage of sensing (d-f) Corresponding calibration curves of Ip as against Log Aβ(1-42) concentrations. All data points are mean value of three independent electrodes. The error bars (calculated as standard deviation) provide a measure of repeatability of the system (n=3). 203

Figure 5. 13: Peak current reduction %i$_r$ obtained from DPV and SWV plots for non-specific testing using APO-E4, Aβ(1-40), Tau-352 and Aβ(1-42) (n=3). 205

Figure 5. 14: (a) DPV response from spiked concentrations of Aβ(1–42) (at 1, 10, 100 and 1000 pgmL^{-1}) in human plasma. (b) Bar chart illustrating comparison of peak current reduction (%i$_r$) with exposure to the different concentrations of Aβ(1-42) spiked in human plasma and 0.1 mM PBS (negative runs with respect to each peptide concentration) (n=3). 206

Figure 6. 1: Schematic representation of electrochemical immunosensor showing changes on the surface of flexible printed graphene electrode after each functionalization stage. 222

Figure 6. 2: SEM images of (a) graphene and (b) rGO-graphene dual layer 224

Figure 6. 3: Comparison of Blank and rGO modified SPE (a) Raman Spectrum (b) Wide XPS Spectrum (c) C 1s spectrum. 225

Figure 6. 4: Nyquist plots (−Z″ vs Z′) of graphene electrodes (a) blank (black) and after each modification step. Inset: Equivalent circuit for unmodified and GO modified electrode (b) rGO/NVD/ antibody/BSA electrode. Inset: Equivalent circuit for rGO/NVD/ antibody/BSA/Antigen electrode. 227

Figure 6. 5: Optimization parameters (a) Neutravidin immobilization time (b) Biotin antibody concentration (c) Biotin antibody incubation time. 229

Figure 6. 6: Electrochemical impedimetric performances of the biosensor with different target concentrations in PBS; (a,b,c) Nyquist plots obtained as a function of different concentrations of Aβ(1-40), Aβ(1-42) and Tau-352; (d,e,f) Corresponding calibration plots

Aβ(1-40), Aβ(1-42) and Tau-352 (n=3). The error bar provides the measure of reproducibility of the system. 232

Figure 6. 7: Electrochemical impedimetric performances of the biosensor with different target concentrations in diluted human plasma; (a,b,c) Nyquist plots obtained as a function of different concentrations of Aβ(1-40), Aβ(1-42) and Tau-352; (d,e,f) Corresponding calibration plots Aβ(1-40), Aβ(1-42) and Tau-352 (n=5). The error bar provides the measure of reproducibility of the system. 234

Figure 6. 8: Bar chart illustrating the change in charge transfer resistance (ΔR_{CT}) with exposure to (a) PBS only (b) diluted human plasma (negative runs with respect to each peptide concentration) and log of different concentrations of Tau-352 (n=3). 235

Figure 6. 9: Bar chart illustrating the responses obtained from EIS measurements from mouse plasma samples of non-transgenic (NTG), 9 months and 15 months old AD transgenic (3TG) mice respectively (n=3). 236

Figure 6. 10: (a, b and c) Changes in R_{CT} obtained from EIS analysis for specificity study of (a) Aβ(1-40), (b) Aβ(1-42), (c) Tau-352 using 1ng/mL concentration of interfering agents (n=3). (d) Changes in peak current reduction obtained from CV measurements for stability study of biotin anti tau 210-230 antibody modified devices (n=3). 238

LIST OF TABLES

Table 2. 1: A comparison of the ideal characteristics of biomarkers in the plasma. 56

Table 2. 2: List of graphene-based sensing technologies reviewed in this section. 81

Table 4. 1: 4-p-nitrophenyl surface coverage on carbon-based substrates……………………148

Table 4. 2: Surface coverage of aminophenyl groups, estimated using an electrochemical method. 161

Table 4. 3: Surface coverage of aminophenyl groups, estimated using an electrochemical method. 164

Table 5. 1: Surface coverage values are calculated by integrating the reduction part of CV curves obtained after FeCOOH attachment on the SPGEs at different scan cycles…………………..194

Table 5. 2: List of Elemental Concentrations of Blank SPGE and pDAN-Modified SPGEs.. 196

Table 5. 3: List of Carbon Component Concentrations of Blank SPGE and pDAN-Modified SPGEs. 196

Table 5. 4: List of Nitrogen Component Concentrations of Blank SPGE and pDAN-Modified SPGEs. 197

Table 5. 5: List of LOD and LOQ obtained for the electrodes functionalized with different concentrations of antibody. 204

Table 5. 6: An overview of recently reported label-free biosensors for Aβ(1–42) detection. . 204

LIST OF ABBREVIATIONS

2D	Two Dimensional
3D	Three Dimensional
Aβ	Amyloid beta
ACN	Acetonitrile
AD	Alzheimer's Disease
AFM	Atomic Force Microscopy
APTES	3-aminopropyltrimethoxysilane
BSA	Bovine Serum Albumin
CE	Counter Electrode
CV	Cyclic Voltammetry
DAN	1,5-diaminonapthaline
DI	De-ionized
DPV	Differential Pulse Voltammetry
EDC/EDAC	N-(3-dimethylaminopropyl)-N'-ethylcarbodiimide
EIS	Electrochemical Impedance Spectroscopy
ELISA	Enzyme-linked Immunosorbent Assays
FCA	Ferrocene Carboxylic Acid
GC	Glassy Carbon
G-FET	Graphene Field Effect Transistor
GO	Graphene Oxide
HOPG	Highly Ordered Pyrolytic Graphite
NVD	Neutravidin
PBS	Phosphate Buffer Saline

pDAN	Poly(1,5-diaminonapthalene)
POC	Point-of-Care
RE	Reference Electrode
rGO	Reduced Graphene Oxide
RMS	Root Mean Square/ Surface Roughness
SEM	Scanning Electron Microscope
SPE	Screen Printed Electrode
SPGE	Graphene modified Screen Printed Electrode
SWV	Square Wave Voltammetry
WE	Working Electrode
XPS	X-ray Photoelectron Spectroscopy

CHAPTER 1

INTRODUCTION AND THESIS STRUCTURE

1.1 INTRODUCTION

Alzheimer's Disease (AD) is the most common cause of dementia that influence millions of people across the world and becomes more prevalent with aging. AD is a neurodegenerative disease triggered by the extracellular accumulation of amyloid β peptide (Aβ), the intracellular appearance of neurofibrillary tangles, and neuronal loss [1-3]. This degeneration leads to changes in behaviour, personality, and functional capacity, which deters the daily life of the patient. In 2020, an estimated 35 million people suffer from AD globally and it is predicted to affect 115 million individuals by 2050 [4]. The existing investigation methods of AD are complicated and are usually made when the disease is already in an advanced stage. In addition, there are no treatments available to avoid this condition [5] and current therapies only slow the advancement of the disease [5]. Thus, there is an intense need for the development of easy analytical tools for the rapid detection of AD biomarkers for early-stage point-of-care diagnosis [6-8].

Most recent AD biomarker-based diagnostic criteria include A, T, and N classification systems, which refer to concentrations of Aβ, tau protein, and neurodegeneration biomarkers, respectively [9]. Amongst these biomarkers, Aβ and tau protein play a vital role in the early diagnosis of AD and are considered core candidate biomarkers for AD [9, 10]. Aβ and tau proteins are also related to the initial progression of AD [11]. Aβ(1–42) peptide, is the key element of the senile plaques present in AD [12]. Other pathological characteristics of AD consist of intraneuronal inclusions of hyperphosphorylated tau protein in neurofibrillary tangles, together with downstream processes such as inflammation and oxidative stress. Additionally, a certain isoform of apolipoprotein ApoE4, is a foremost genetic risk factor for AD, because it also leads to an excess of amyloid formation in the brain [13]. All these components cause the loss of synaptic integrity, progressive neurodegeneration, and effective neural network connectivity [7, 14, 15].

There are several limitations associated with the conventional methods to quantify the AD biomarker concentration in biofluids which are discussed in detail in this thesis. To overcome those, numerous studies have been conducted for the analysis of AD biomarkers such as optical [16], electrical [17, 18], electrochemical [19-21], and impedimetric [22-24] methods. Amongst these methods, electrochemical biosensors are the most attractive and, hence, widely preferred. The potential applications of electrochemical biosensors in clinical diagnosis for sensing and quantification of proteins is one of the most ubiquitous research areas [25, 26]. This is ascribed to various advantages such as portability [24], high sensitivity [27], the possibility of label-free sensing [20, 21], simplicity of apparatus, and easy handling [20].

The main objective of this thesis was to develop a proof-of-concept biosensor technology for dementia applications, more specifically for the early diagnosis and monitoring of Alzheimer's disease. The platform chosen for the development of the biosensor devices used in this thesis were graphene and reduced graphene oxide modified screen printed electrodes and glassy carbon electrodes.

Graphene-based electrodes were chosen for biomarker detection due to their high conductivity, large surface-to-volume ratio, low cost, and low environmental impact, in the fabrication of sensors and biosensor-based devices [28, 29]. Graphene biosensors enable the advantages of high sensitivity, lower detection limits, and high throughput detection when compared to other methods. All these advantages allowed for graphene devices to be manufactured and used for the fabrication and development of point-of-care biosensors for the diagnosis and monitoring of AD with the help of the biosensing methods explained in this thesis.

1.2 THESIS STRUCTURE

This thesis is divided into 7 chapters.

Chapter 1: Introduction and Thesis Structure

In this chapter, a brief introduction to this thesis is provided. The outline and the structure of this thesis are also summarized.

Chapter 2: Literature Review

In this chapter, a general overview of the current literature surrounding Alzheimer's disease, its pathophysiology, different disease stages, and available treatment options is discussed in detail. This chapter also provides the potential of graphene-based biosensor technology that may be used for the detection of biomarkers related to Alzheimer's disease.

Chapter 3: Materials and Methods

In this chapter, the materials, main characterization equipment used to evaluate the surface chemistry and morphology of biosensor devices, and electrochemical characterization techniques utilized for the characterization of biosensors before and after functionalization are described in detail.

Chapter 4: Assessing surface coverage of aminophenyl bonding sites on diazotised glassy carbon electrodes for optimized electrochemical biosensor performance

In this chapter, the amine group coverage on glassy carbon and highly ordered pyrolytic graphite (HOPG) electrodes were optimized via measurement of electron transfer during the electrochemical addition of ferrocene carboxylic acid (FCA) to aminophenyl groups. Also, the effect of nitro to amino CV reduction scans was investigated by controlling the number of CV scans. Moreover, The efficiency of our experimental parameter optimization was studied by developing biosensors prepared by coupling between the electrode-bound phenylamino and a carboxyl-terminated anti-beta amyloid antibody specific to Aβ (1-42) peptide, which is a potential marker for Alzheimer's disease. Aβ (1-42) was used as a model biomarker to illustrate the successful diazotisation and validate the claim of achieving diazotisation via optimization of the experimental parameters.

Chapter 5: Graphene based electrochemical immunosensor for the ultra-sensitive label-free detection of Alzheimer's beta-amyloid peptides Aβ(1-42)

In this chapter, the development of a label-free, electrochemical immunosensor, using graphene-modified screen-printed electrodes (SPGEs) for high sensitivity detection of beta-amyloid peptides Aβ (1-42) was reported. The graphene electrode surface was modified with amine functional groups using a 1,5-diaminonaphthalene (DAN) electropolymerization process with optimized amine surface coverage, whilst maintaining minimal thickness for better charge transfer from the electrolyte solution to the electrode surface. It was observed that polymer DAN (pDAN) modification provided a controlled amount of amines without even compromising the actual properties of graphene. Subsequent attachment of the anti-beta amyloid antibody onto the sensor was performed and the influence of antibody concentrations with respect to Aβ(1-42) peptide sensing efficiency has been analyzed in detail. BSA was used as a blocking agent. Moreover, the implications of this work towards developing a commercially viable, robust, and sensitive immunosensor for Alzheimer's disease by using Aβ(1-42) biomarkers were discussed.

Chapter 6: An electrochemical impedimetric biosensor based on neutravidin- biotin interaction for femtomolar range detection of AD biomarkers in human plasma using flexible screen-printed graphene electrodes

In this chapter, the development of a novel impedimetric immunosensor using flexible printed graphene screen printed electrodes (SPEs) was discussed that was made for ultra-sensitive detection of multiple biomarkers of AD (Aβ(1-40), Aβ(1-42), and Tau-352) pathogenesis in two different physiological solutions (i.e., PBS and diluted human plasma). The reported immunosensor comprises of covalent attachment of neutravidin protein to the rGO surface via amide bonds using the carbodiimide crosslinking chemistry. Antibody immobilization with accurate orientation fosters a great step forward in attaining ideal immunosensor performance via high signal amplification and lowering the limit of detection. Therefore, in this work biotinylated antibodies were used for the specific attachment of antibodies over the neutravidin-modified sensor surface. The proposed biosensor showed highly sensitive and selective detection of Aβ(1-40), Aβ(1-42), and Tau-352 biomarkers with one of the lowest reported LODs in the femtomolar range. The reported biosensor platform is expected to present a universal electrochemical biosensing strategy for multiplexed detection of protein biomarkers and their associated clinical diagnosis.

Chapter 7: Conclusion and future work

In this chapter, the summary and the main findings of this thesis are presented. Also, the suggestions for future experiments for multiplexing and to enhance the sensitivity and limits of detection of the electrochemical biosensing devices are discussed.

BIBLIOGRAPHY

1. Blennow, K., *Leon MJ de, Zetterberg H (2006) Alzheimer's disease.* Lancet. **368**: p. 387-403.
2. Cummings, J.L. and G. Cole, *Alzheimer disease.* Jama, 2002. **287**(18): p. 2335-2338.
3. Blennow, K., M.J. de Leon, and H. Zetterberg, *Alzheimer's disease.* The Lancet, 2006. **368**(9533): p. 387-403.
4. Cummings, J.L., *Biomarkers in Alzheimer's disease drug development.* Alzheimer's & Dementia, 2011. **7**(3): p. e13-e44.
5. Association, A.s., *2019 Alzheimer's disease facts and figures.* Alzheimer's & Dementia, 2019. **15**(3): p. 321-387.
6. Kang, D.-Y., et al., *Ultra-sensitive immunosensor for β-amyloid (1–42) using scanning tunneling microscopy-based electrical detection.* Biosensors and Bioelectronics, 2009. **24**(5): p. 1431-1436.
7. Hampel, H., et al., *Biological markers of amyloid β-related mechanisms in Alzheimer's disease.* Experimental neurology, 2010. **223**(2): p. 334-346.
8. Craig-Schapiro, R., A.M. Fagan, and D.M. Holtzman, *Biomarkers of Alzheimer's disease.* Neurobiology of disease, 2009. **35**(2): p. 128-140.
9. Lee, J.C., et al., *Diagnosis of Alzheimer's disease utilizing amyloid and tau as fluid biomarkers.* Experimental & Molecular Medicine, 2019. **51**(5): p. 1-10.
10. Parnetti, L., et al., *CSF and blood biomarkers for Parkinson's disease.* The Lancet Neurology, 2019. **18**(6): p. 573-586.
11. Nisbet, R.M., et al., *Tau aggregation and its interplay with amyloid-β.* Acta Neuropathologica, 2015. **129**(2): p. 207-220.

12. Hardy, J. and D.J. Selkoe, *The amyloid hypothesis of Alzheimer's disease: progress and problems on the road to therapeutics.* science, 2002. **297**(5580): p. 353-356.

13. Polvikoski, T., et al., *Apolipoprotein E, dementia, and cortical deposition of β-amyloid protein.* New England Journal of Medicine, 1995. **333**(19): p. 1242-1248.

14. Cummings, J.L., *Biomarkers in Alzheimer's disease drug development*. 2011, Elsevier.

15. Zetterberg, H., K. Blennow, and E. Hanse, *Amyloid β and APP as biomarkers for Alzheimer's disease.* Experimental gerontology, 2010. **45**(1): p. 23-29.

16. Carrico, Z.M., G. Le, and R. Malinow, *A fluorescence assay for detecting amyloid-β using the cytomegalovirus enhancer/promoter.* J. Biol. Methods, 2017. **4**.

17. Oh, J., et al., *A carbon nanotube metal semiconductor field effect transistor-based biosensor for detection of amyloid-beta in human serum.* Biosensors and Bioelectronics, 2013. **50**: p. 345-350.

18. Park, D., et al., *Multiplexed femtomolar detection of Alzheimer's disease biomarkers in biofluids using a reduced graphene oxide field-effect transistor.* Biosensors and Bioelectronics, 2020. **167**: p. 112505.

19. Hassan, Q. and K. Kerman, *Electrochemical approaches for the detection of amyloid-β tau, and α-synuclein.* Current Opinion in Electrochemistry, 2019. **14**: p. 89-95.

20. Dai, Y., A. Molazemhosseini, and C.C. Liu, *In Vitro Quantified Determination of β-Amyloid 42 Peptides, a Biomarker of Neuro-Degenerative Disorders, in PBS and Human Serum Using a Simple, Cost-Effective Thin Gold Film Biosensor.* Biosensors, 2017. **7**(3): p. 29.

21. Abbasi, H.Y., et al., *Graphene based electrochemical immunosensor for the ultra-sensitive label free detection of Alzheimer's beta amyloid peptides Aβ (1–42).* Nanoscale Advances, 2021. **3**(8): p. 2295-2304.

22. Ngoc Le, H.T., et al., *Sensitive electrochemical detection of amyloid beta peptide in human serum using an interdigitated chain-shaped electrode.* Biosensors and Bioelectronics, 2019. **144**.

23. Ngoc Le, H.T., et al., *Sensitive electrochemical detection of amyloid beta peptide in human serum using an interdigitated chain-shaped electrode.* Biosensors and Bioelectronics, 2019. **144**: p. 111694.

24. Lien, T.T., et al., *Modified screen printed electrode for development of a highly sensitive label-free impedimetric immunosensor to detect amyloid beta peptides.* Analytica Chimica Acta, 2015. **892**: p. 69-76.

25. Mascini, M., I. Palchetti, and S. Tombelli, *Aptamers smart molecules for biosensing clinical samples.* CHIMICA OGGI-CHEMISTRY TODAY, 2011. **29**(2): p. 16-18.

26. Zhou, J., M.R. Battig, and Y. Wang, *Aptamer-based molecular recognition for biosensor development.* Analytical and Bioanalytical Chemistry, 2010. **398**(6): p. 2471-2480.

27. Yoo, Y.K., et al., *A highly sensitive plasma-based amyloid-β detection system through medium-changing and noise cancellation system for early diagnosis of the Alzheimer's disease.* Scientific reports, 2017. **7**(1): p. 1-10.

28. Geim, A.K. and K.S. Novoselov, *The rise of graphene*, in *Nanoscience and Technology: A Collection of Reviews from Nature Journals*. 2010, World Scientific. p. 11-19.

29. Tehrani, Z., et al., *Generic epitaxial graphene biosensors for ultrasensitive detection of cancer risk biomarker.* 2D Materials, 2014. **1**(2): p. 025004.

CHAPTER 2

LITERATURE REVIEW

2.1 INTRODUCTION

This chapter presents an overview of Alzheimer's Disease (AD). It provides a review of the pathogenesis and different stages of AD. The Alzheimer’s incidence rate, its risks, and symptoms will also be highlighted in this chapter alongside the current diagnostic and therapeutic techniques for various types of dementia and their link with AD.

The potential of biosensor technology, which could ultimately be used for detecting the biomarkers related to AD, is also discussed in this chapter. Biosensors are a promising field of diagnostic tests. They can provide prompt and quantitative point-of-care measurements, with exceptionally high sensitivity and specificity. Biosensors are usually based on electrical, electrochemical, and optical techniques for instance current-voltage measurements, potentiometry, and UV-Vis spectroscopy respectively.

This chapter also the potential of graphene for biosensors as well as its material properties which make it an appropriate substrate for sensor development. Additionally, this chapter presents the elemental properties of a biosensor, by briefly discussing the developmental process from device surface modification to biofunctionalization and the biomarker detection.

2.2 ALZHEIMER'S DISEASE (AD)

Alzheimer's disease (AD) was first defined by the German Bavarian neurologist and psychiatrist Alois Alzheimer in 1907 [1]. AD is the most common cause of dementia that affects millions of people across the world and becomes more prevalent with aging. The formation of senile plaques (SP) by amyloid beta (Aβ) and neurofibrillary tangles (NFTs) composed of phosphorylated tau protein, in the hippocampus part of the brain is considered to be the pathological cause of AD [2]. It is a progressive neurological disorder which causes the brain to shrink (atrophy) and brain cells to die. Furthermore, AD is a widespread degenerative central nervous system disease in the elderly. As per the Alzheimer's Association's statistics, AD is the reason for between 60–80% of dementia cases [3].

The progression of AD increases with the age but a few cases have been identified in young people as well. Constituting about two-thirds of the cases of dementia, AD is reported to affect about 10% of individuals between the ages 65 and 75 and 32% of persons above 80 years [4-6]. In 2020, an estimated 35 million people suffer from AD globally and it is predicted to affect 115 million individuals by 2050 [4]. Neurodegeneration leads to changes in behaviour, personality, and functional capacity, which detrimentally affects the daily life of the patient [7].

Although AD is prominent in the older generation, nearly 250,000 people endure early-onset AD (EOAD) with symptoms initiating before they are in the mid-60s [8]. After the first diagnosis, the average life span of AD patients is estimated between 7 to 15 years. This broad span is because of poor clinical analysis and existing medications that only lessen the disease-associated symptoms [9, 10].

Presently, the diagnostic procedures for AD are complicated and are usually made when the disease is already in its advanced stage. Besides, currently, there has been no cure identified to stop the progression of AD, attributed to the intricacy of its pathophysiology [11]. Also, existing therapies can only slow down the disease progression [11].

Therefore, there has been increasing demand for the development of simple analytical tools for providing rapid, sensitive, and reliable early-stage point-of-care diagnostic platforms for the detection of AD biomarkers [12-14], in the hope that earlier intervention may allow more effective treatments. Past study shows that “Amyloid cascade hypothesis”, which promotes an imbalance between the production and degradation of Aβ in the brain, is the originating event in AD, which further leads to the formation of extracellular deposits of Aβ (senile plaques) [15]. However, it has been consistently shown that the amyloid cascade hypothesis is not a major event in the development of AD. For example, a lot of research has reported that neuronal loss and cognitive decline are not correlated with the accumulation and deposition of Aβ. Also, many individuals do not indicate any signs of memory impairment, but their PET scan shows a significant amount of amyloid plaques [16-18].

2.2.1 ALZHEIMER’S PATHOPHYSIOLOGY:

The primary neuropathological features in the brain are called beta-amyloid (Aβ) and tau. With the accretion inside the brain, beta-amyloid (Aβ) and tau proteins lose their ability to function and communicate with each other which causes healthy neurons to die. During the early developmental stages of AD, an increase in these features and their degenerative changes are acknowledged with more precedence in the entorhinal cortex and hippocampus [19]. Berti & co-workers found in their studies in 2011 that the neuropathological variations in AD are found to be present many years before its clinical representation [20].

Familial AD, also referred to as early-onset Alzheimer’s appears owing to the mutation of amyloid precursor protein (APP), presenilin 1, and presenilin 2 (PS 1 and PS 2). Familial AD is often very rare, usually diagnosed in midlife, and accounts for only 5% of all the AD cases. The mutations in these proteins lead to the improper cleavage of protein, which results in the build-up of Aβ that eventually forms plaques. The studies indicate that APP could be associated with synapse development, cell adhesion, and durability. However, its actual physiological role is still not clear [21]. It may be sundered by α, β, and γ secretase. The first two enzymes produce the amyloid-beta peptide upon cleavage. However, the γ secretase generates sticky non-amyloidogenic fragments [22, 23]. The theory behind the assumption is that the accumulation of these fragments in the brain triggers the interference of nerve cells. This in turn activates the inflammatory responses because the brain trying to repair itself, hence causing an increase in AD. The neurofibrillary tangles are also generated because of these little fragments. These tangles contain the tau protein that also promotes brain cell destruction, subsequently leading to dementia symptoms [24, 25].

On the other hand, the presenilin (1 and 2) are particularly shielded. PS 1 and PS 2 are biologically cleaved which forms two polypeptides, which take part in managing apoptosis [26]. It has been reported that the tau pathology usually occurs initially in transentorhinal cortex which is mostly in the absence of the plaques. This thus suggest the uniform and invariant pattern in comparison to the amyloid beta pathology (i.e., neuron to neuron mechanism [27]).

On the other hand, the late-onset and sporadic form of AD is the reason for most AD cases and occurs normally after the age of 65. Enhanced BACE (β-site amyloid precursor protein (APP) cleaving enzyme) activity along with defective clearance have been attributed to the accumulation of Aβ in the brain, in case of late-onset sporadic AD [28, 29].

Age is the foremost risk factor for sporadic AD, however, increased risk for this form can also be related to the diverse genetic abnormalities [30, 31]. The apolipoprotein E ε4 (APOE*ε4) allele is linked to the major genetic risk factor for late-onset sporadic AD, and also promotes both an early onset of Aβ accumulation and defective Aβ clearance out of the brain [32-34]. APO-E is the fat-binding protein, which is usually formed by astrocytes and carries cholesterol to the neurons through APOE receptors. The polymorphic APOE gene has three major alleles: APOE*ε2, APOE*ε3, and APOE*ε4. While the APOE*ε2 allele might confer protection against AD, the risk of AD in people with two APOE*ε4 alleles is about 15-fold more than in APOE*ε3 carriers. The APOE*ε3 allele appears to be neutral concerning AD risk. With APOE-2 being the most effective and APOE-4 being the least effective, different APO-E proteins exhibit different potentials to facilitate Aβ clearance [35]. The APOE*ε4 allele predicts longitudinal Aβ aggregation in plaque-free elderly people with no dementia and is always associated with the abnormal Aβ accumulation [36].

Aβ aggregation in the brain is considered the initial event of the AD process. The build-up of Aβ begins in the hippocampus and entorhinal cortex. Moreover, progressive cytoskeletal changes and disrupted axonal transport are also caused by the intracellular deposition of hyperphosphorylated tau protein in neurofibrillary tangles (NFTs). In 1991, three independent research groups proposed the theory that Aβ accumulation is the central event in AD pathology [37-39]. Following that, Hardy and Higgins formally proposed the theory of the ‘amyloid cascade hypothesis’, 1 year later [40].

At first, the hypothesis suggested that cognitive impairment, tau phosphorylation, neurofibrillary tangles (NFTs) formation, synapse loss, and neuron death are driven by the accumulation of Aβ in the brain. Later on, it was also discovered that autosomal dominant mutations in the APP gene and PS 1 and PS 2 enhanced Aβ production, which promotes Aβ accumulation and thereby results in AD [41]. **Figure 2.1** shows the schematic of the amyloid-β (Aβ) cascade hypothesis in Alzheimer's disease [42].

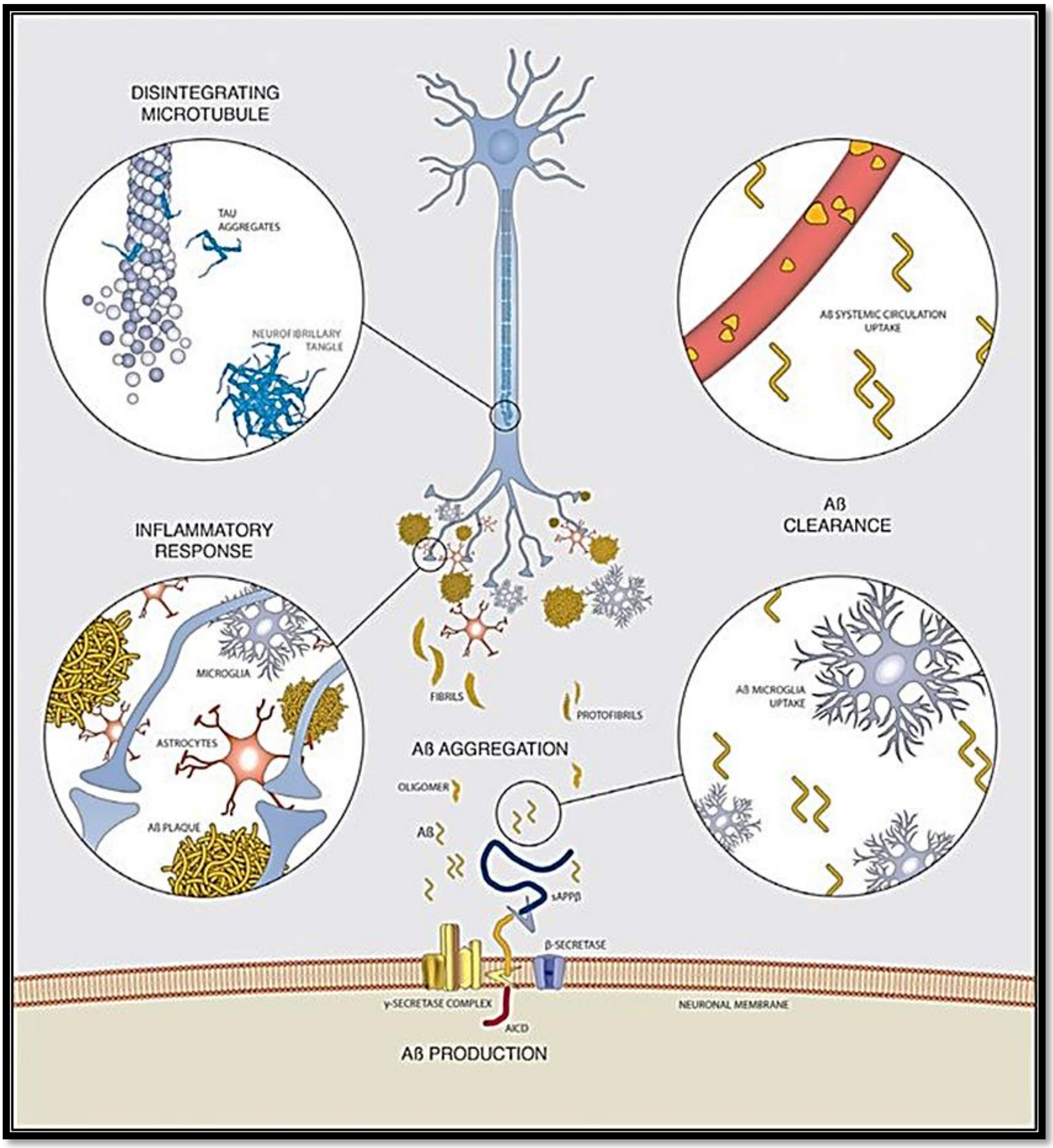

Figure 2. 1 Scheme of the amyloid-β (Aβ) cascade hypothesis in Alzheimer's disease [42].

2.2.2 ALZHEIMER’S TOPOGRAPHY:

The aggregation of the amyloid plaques and degeneration of neurofibrillary are two main reasons for the determination of atrophy of cortex detected in Alzheimer’s [19]. The major parts of brain associated with memory, where the atrophy is first shown in AD are the entorhinal cortex and transentorhinal cortex [43]. Another major region of brain that is crucial for learning abilities is

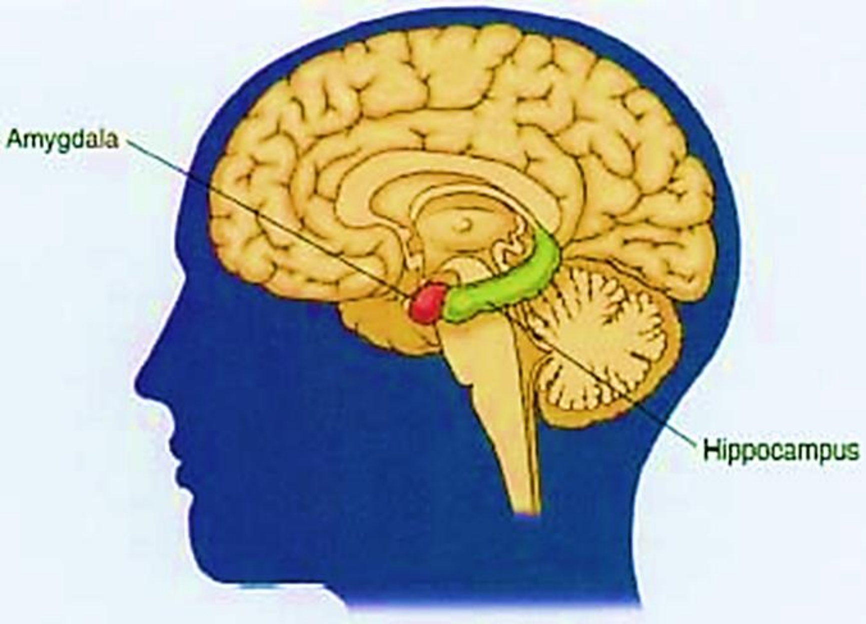

Figure 2. 2: An illustration of the atrophy of the brain tissue resulted in AD displayed by the cross section of brain.

the hippocampus is also affected at early onset of Alzheimer's and is at high risk of shrinkage [44]. Besides, the amygdala is another essential subcortical part of the brain which is affected at the early stage of AD (**Figure 2.2**). The amygdala in the brain is responsible for memorizing and processing the emotional reactions as well as influencing the behaviours and other activities [45].

All the areas of the brain are affected with the progression of AD with time and atrophy spreads to the temporal cortex resulting in progressive thinning of cortex and overall shrinkage of the brain (**Figure 2.3**). The damaged left cerebral hemisphere of the brain, which is responsible for languages and the semantic memory, even makes it challenging to choose a right word in a conversation for Alzheimer's patient [46]. According to a research still there are regions of cortex in the occipital lobe that are possibly not affected in late stages of the Alzheimer's are primary visual cortex and primary motor cortex [47].

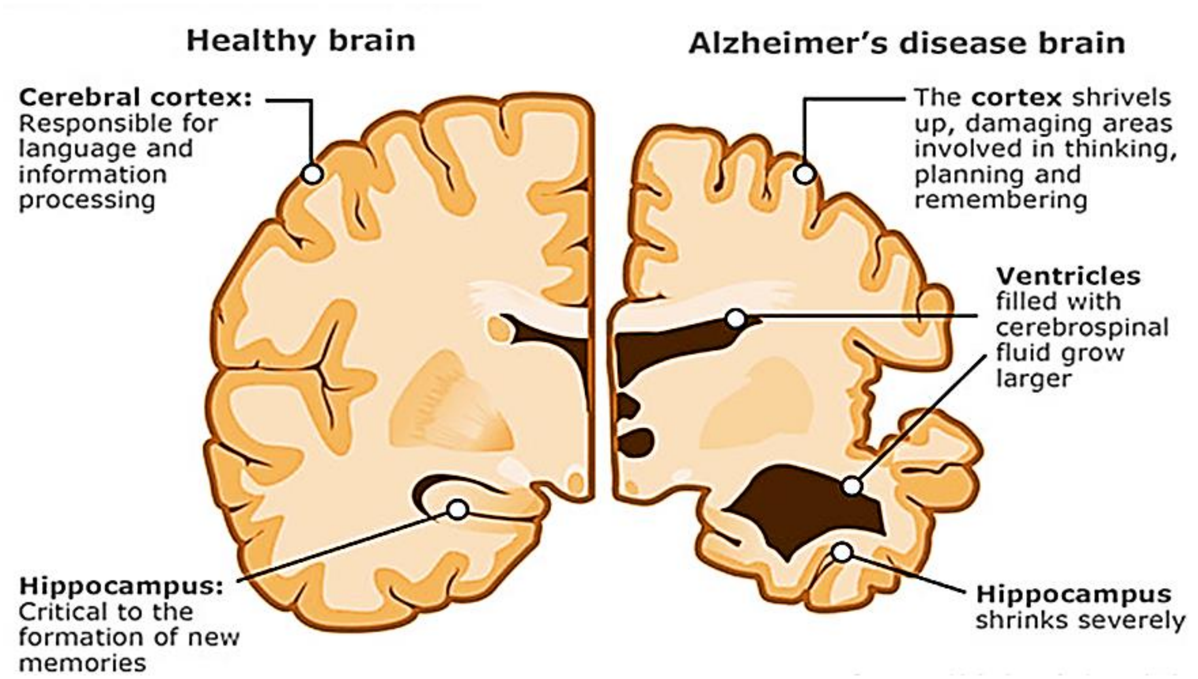

Figure 2. 3: An illustration of the hippocampus and amygdala (parts of limbic system separated by the uncus) [46].

2.2.3 STAGES OF ALZHEIMER'S DISEASE:

The symptoms of AD development depend on the particular person. Therefore, it is difficult to accurately predict the rate at which the condition can become critical. The symptoms are typically divided into the following three phases [48].

2.2.3.1 Pre-clinical Phase:

This is a period of cognitive decline that can go on for years as shown in figure 4 below until the amyloid cascade is triggered by the overproduction and accumulation of Aβ in the brain [49]. **Figure 2.4** shows the clinical glide model of AD that shows the phase of preclinical AD that started before the MCI [50].

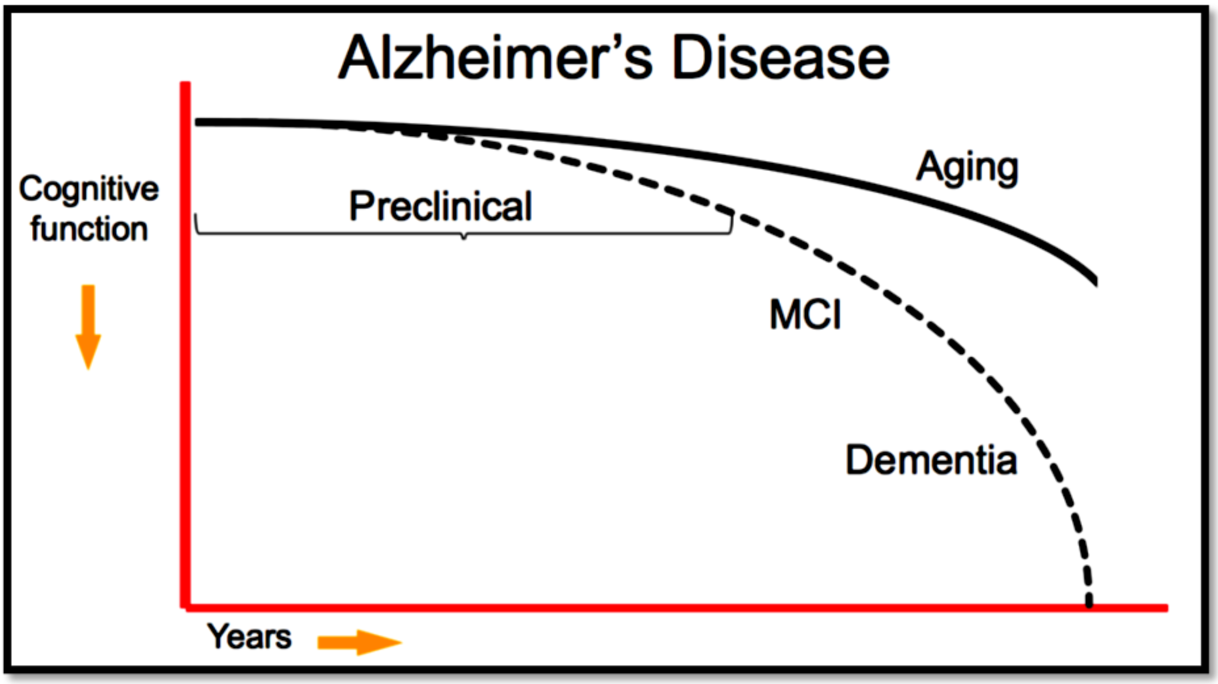

Figure 2. 4: The model of Clinical Glide path of AD representing the phase of preclinical AD before MCI [50].

2.2.3.2 Prodromal Stage:

This is a pre-dementia phase of AD that is widely encompassed in the mild cognitive impairment category and is distinguished by symptoms that are not as grave as those that would normally meet the currently recognized criteria for diagnosing AD [51].

2.2.3.2.1 Mild Cognitive Impairment (MCI):

MCI is a varied condition between the onset of dementia and usual aging that affects 19% of people aged 65 and over. Studies have shown that in 46% of people with MCI develops into dementia within 3 years [52]. For most people, this is characterized by a subtle but progressive decline that does not particularly hinder functioning capacity but ends with a noticeable cognitive decline in the semantic (facts and general knowledge) and the implicit memory (the unintentional impact of previous experience on upcoming performance) [53]. High levels of CSF tau have been found in 90% of MCI cases that further developed into AD but not in the cases that remained as MCI [54].

MCI is sub-divided into amnestic and non-amnestic types. Where amnestic impairment is common in about 90% of patients with AD symptoms and is denoted by a growing forgetfulness. Nonetheless, the use of language, executive function, verbal ability, perceptual speed, visual conceptualization, and comprehension, is conserved to a certain extent [55]. Non-amnestic impairment is not as common as amnestic and is indicated by a gradual and vague decrease in functions that have no association with memory but affects other cognitive abilities such as executive function and the use of language. Studies have shown that this type of impairment may be a precursor for dementia with Lewy bodies and frontotemporal lobar degeneration [55].

2.2.3.3 Dementia Phase:

At this phase, symptoms satisfy the currently recognized dementia and AD diagnostic criteria [51].

2.2.4 OTHER DEMENTIA TYPES AND THEIR CONNECTION TO ALZHEIMER'S:

2.2.4.1 Vascular Dementia (VD):

It is the distinct and most common type of dementia after Alzheimer's. VD shares the similarities with AD in some of the early symptoms for instance the loss of memory. However, in the case of VD, cerebrovascular disease or strokes can instantly initiate the dementia symptoms [56]. It is observed that as compared to people with AD, individuals with VD are able to maintain their overall personality and response to the emotional events at normal levels even at the late stages of the dementia [57].

2.2.4.2 Dementia with Lewy Bodies (DLB):

The German doctor FH Lewy first identified the Lewy bodies which are the small clumps of proteins, that appear in the nerve cells of the brain and are the cause of DLB. Dementia with Lewy bodies is also one of the common types of degenerative dementia. About 60% of AD cases show the presence of Lewy bodies in the brain [58]. Lewy bodies cause a variety of symptoms that are shared with AD. However, symptoms like movement, visual hallucinations, and difficulties judging distances are the important cause of disability early in DLB [56]. DLB is also closely related to the Parkinson’s disease and mostly shares some of the similar disease symptoms, which include difficulty with the movement, thinking, and how well the body works.

2.2.4.3 Parkinson’s disease:

Accumulation of Lewy bodies in the brain cells is also the main cause of Parkinson’s disease. As DLB and Parkinson’s disease both share some of the same symptoms however individuals with Parkinson’s disease show dementia symptoms after several years of the development of movement problems as compared to the DLB where the person develops symptoms of dementia before or alongside the problems with movement [59]. The main symptoms of the Parkinson’s include tremors in different parts of the body including hands, arms, and jaws, stiffness in muscles, difficulty in movement, and a decrease in balance and coordination [60]. It is believed that the Parkinson’s disease results from a combination of genetic and environmental factors, such as exposure to some toxic chemicals.

2.2.5 THE CURRENT DIAGNOSTIC TECHNIQUES FOR ALZHEIMER'S DISEASE:

The AD diagnostic current techniques can be achieved through clinical procedures that require examination of brains, MRI, CT-Scans, using different biomarkers, and many other new techniques. These techniques help identify any cognitive dysfunction resulting from dementia or any other neurological disorder that can lead to AD. The clinical diagnosis includes medical records, laboratory tests, neuroimaging, and other neurological examinations that can help identify the diagnosis at moderate to severe stages [61].

2.2.5.1 Brain Imaging Technique:

The brain imaging technique helps to monitor and scan the whole image of the brain using computer tomography (CT) as well as magnetic resonance imaging (MRI) which helps to show the anatomy of the brain which helps the physicians to differentiate between dementia and other brain disorders by observing the decrease in brain size [62]. Other neurological problems like neural loss, atrophy, and problems in neuro-fibrils can also be detected using these techniques. MRI is the standard method used for scientific prognosis. Information supplied by MRI is consistent with those provided by the various biomarkers. High-resolution structural MRIs are able to show the tissue atrophy which is resulting from gradual neuronal and synaptic loss [63]. Regardless of its ease of accessibility, a lot of research has shown that MRI is more sensitive than CT.

To study its importance and new techniques implemented in the detection of AD, in 2019 Acharya et al., presented a new technique called computer aided brain diagnosis (CABD) which intended to show if a brain scan can be beneficial to identify AD. The researchers used the MRI technique due to its wide adoption in hospitals to examine cognitive disabilities. The comparative analysis was done to analyze the use of extraction techniques of tissues in examining AD. The findings showed that shearlet transform, a new extraction technique helps in diagnosing AD more accurately than alternative methods [64]. Moreover, Ledig et al., in their research utilized the validated methods for cross-sectional and longitudinal segmentation of MR brain images from the AD neuroimaging initiative (ADNI) cohort. They also used the MRI technique for extraction and segmentation purposes using different markers [65].

Another technique that is used widely for imaging diseases named as positron emission tomography (PET). PET is a technique that uses a low-level radioactive tracer that is less harmful and reactive as compared to high-level rays. These tracers are injected into the blood and then monitored to have a clear function of the brain and its parts that can help to diagnose the disease. The PET scanning includes the following:

2.2.5.2 Amyloid Positron Emission Topography (PET) Imaging:

As indicated by the name, the amyloid PET imaging scans the amyloid fibers in the brain that are accumulated and deposited in the brain. The amyloid deposits hinder the normal functioning of the brain, and this scanning can help to identify these deposits. The radioactive dye that is used for this scanning is Amyvid (florbetapir), a dye with the properties that can bind to the plaques present in different parts of the brain. There are several plaques in the bloodstream that can detect the percentage of plaques present in the brain and this dye measures the amyloid plaque in the blood. This scanning is used for people with dementia or with early-onset of cognitive impairment symptoms [66].

2.2.5.3 Fluorodeoxyglucose (FDG) PET:

Sometimes cognitive impairment and neurological disorders occur due to insufficient nutrients supplied to the brain. The scan using FDG PET can help to identify the number of nutrients in the brain that is the leading cause of AD and other types of dementia. The areas that have low metabolism show degenerative patterns and can be traced using FDG PET. This can be used for research purposes and also for the diagnosis of disorders [67].

2.2.5.4 Tau PET imaging:

Tau proteins are the microtubules associated with proteins present in the brain. The neurofibrillary tangles in the brain cause AD and related disorders. The tau proteins help in regulating the maintenance and assembly of microtubules structure in the brain. The tangles formed in the microtubules of tau protein can be measured using Tau PET imaging [68].

2.2.6 CURRENT TREATMENT OPTIONS FOR AD:

Alzheimer's disease was thought to be an untreated ailment and could not recover once get diagnosed. Some of the assumptions and findings of the scientists are true as they cannot be recovered back. Pharmacological therapy helps to regulate the illness and treat the symptoms of Alzheimer's, but it is not the final solution for this disorder. But, still, there is a need for further medications and treatment programs for AD that can help to stop or slow down the neural damage to the brain that results in dementia and cognitive disability [69]. The drug treatments that can be used are as follows:

2.2.6.1 Acetylcholinesterase Inhibitors:

AD pathogenesis has also been linked to a deficiency in a brain neurotransmitter, acetylcholine. Acetylcholinesterase inhibitors are the category of medicinal drugs that maintain acetylcholine levels in the brain by decreasing its malfunction. In the drug market, they are known as Galantamine or donepezil. They help neurons to transmit acetylcholine to enact muscles, which in turn helps in learning by enhancing memory, and motivation [70]. These drugs are used for AD treatment from the very beginning [71].

2.2.6.2 (N-Methyl-D-aspartate) NMDA Receptor Antagonists:

NMDA receptor antagonist drugs can treat cognitive loss and mental illness caused by AD. The excitatory synapse glutamate can bind to the NMDA receptor's region. When glutamate binds to

NMDA receptors, calcium is released into nerve cells. This is crucial for memory and learning. Increased glutamate levels in the brain lead to excessive calcium release, which can injure neurons and nerve cells [72]. NMDA antagonists bind to NMDA receptors and prevent glutamate restriction, and do not allow calcium from entering nerve cells. Memantine is the major antagonist of the glutamate receptor subtype NMDA. It's used to prevent neurotoxicity, which has been linked to Alzheimer's disease and other neurological diseases [73].

2.2.6.3 Non-Steroidal Anti-inflammatory Drugs (NSAIDs):

NSAIDs lower the probability of AD onset and stabilize the neurotransmitters in the brain. Mainly the deposition of beta-amyloid (A beta) peptide and neurofibrillary tangles cause Alzheimer’s that are surrounded by inflammatory cells. By interfering with several mechanisms, such as the suppression of cyclooxygenases (COX) and the activation of the peroxisome proliferator-initiated receptor gamma, the NSAIDs are able to suppress their activation and control the onset of disease. There are many medicines that are present in the class of NSAIDs such are flurbiprofen, ibuprofen, and sulindac acting as beta-lowering medications, as evidenced and supported by the research done on mice [74].

2.2.7 BIOMARKERS FOR ALZHEIMER'S DISEASE:

Biomarkers are essential in clinical examinations for the diagnosis of multiple disorders. Their role as critical endpoints in clinical preliminaries is now almost universally recognized. Explicit biomarkers have been extensively documented and repeatedly demonstrated to properly predict relevant clinical results across a wide range of drugs and populations. In general, biomarker "legitimacy" is expected to be examined and re-evaluated regularly. The clinical data presents that the cerebrospinal fluids (CSF) biomarkers i.e., amyloid- (Aβ-42), phosphorylated tau (P-tau), and total tau (T-tau) indicate major components of AD pathology [75]. Significantly, different studies have consistently demonstrated that these biomarkers have symptomatically valuable data, even in the early stages of illness. Continuous technological advancements have made it possible to quantify these biomarkers using computerized tests with excellent accuracy and consistency [76].

2.2.7.1 Characteristics of an Ideal Biomarker:

The biomarkers should have distinct characteristics that help them to identify AD more easily and accurately. Biomarkers of AD should at least have the following features:

- It should differentiate other neurological disorders and dementia from AD. As dementia is a symptom of AD so it should not be confused with dementia-related disorders. AD has its symptoms and neuropathology so; the biomarkers should make it specific and distinguishable.
- An ideal biomarker should have the ability to trace brain pathology and reflect all aging processes.
- The biomarkers should have a higher sensitivity to detect minor pathology in the brain areas.
- The biomarkers should be quantifiable and also reproducible and can be used over time.
- The biomarkers tests should be cheap and affordable for the patients to diagnose at an early stage i.e., at least 10 years before the disease onset.

2.2.7.2 Sensitivity/Limits of Detection:

The tests expected in deciphering biomarkers have high sensitivity but low specificity and at a lower cost. In an ideal scenario, a biomarker used for the clinical diagnostics of AD would have sensitivity and specificity of ≥ 0.9. Depending on whether there are any symptoms of AD and the kind of indication, patients can enter the AD symptomatic stream at various phases [77].

2.2.7.3 Cerebrospinal Fluid (CSF) Biomarkers:

The CSF is a semi-transparent fluid present in the brain that cushions the brain and provides mechanical support to the brain from any harm or injury. It is present in the subarachnoid space of the brain covering the ventricular system on each side of the brain. The patients showing AD symptoms have neural accumulation in the CSF. Hence, it is the common and feasible source for the diagnosis of many neurological disorders including AD [78]. Aβ-42, P-tau, and T-tau are a few particular CSF biomarkers that can assist in diagnosing AD relatively early on in the disease's onset. As decreased levels have been found in healthy old people who first show no harmful effects but subsequently develop AD after a year or two of follow-up. The levels of Aβ can fluctuate according to the person's age and gender, even though it is believed to be the most significant biomarker for diagnosing Alzheimer's disease. Tau levels can also predict the progression of MCI to AD, making them a useful prognostic indicator [79].

Although the CSF biomarkers show promising diagnostic potential, there are still some important limitations associated with their clinical utility. For Example, an important limitation is CSF procedural route through Lumbar puncture, which is regarded as an invasive technique, and may be harmful to the individuals. It leads to headaches, meningitis, hematoma, and in the worst cases death. Also, the repeated follow-up measurements are utterly challenging [78, 80, 81]. Another disadvantage is the global cut-off values for the concentrations of different biomarkers and also the biomarker assays are not standardized. The significant difference in the concentration of biomarkers between different studies is due to the CSF handling methods and using the numerous antibodies and technical platforms [82]. Another main drawback is the overlapping between the profiles of different proteins of various types of dementia [83].

2.2.7.4 Plasma Biomarkers:

Blood is the biological fluid that is most often utilized in healthcare testing because it is simple to collect, and it represents the majority of compounds that are created in the body. Plasma is the portion of blood that is transparent and contains blood cells floating in the solution. Fluids in the environment, such as plasma, provide a rich source of biomarkers in Alzheimer's disease. A study indicates that plasma complement C3 was significantly up in Alzheimer's disease (AD) patients, but plasma δ-fibrinogen was significantly elevated in mild cognitive impairment (MCI) patients [84]. Estimating the concentration of analytes in the blood samples would have without a doubt a significant effect on a variety of aspects of Alzheimer's disease (AD) diagnosis and treatment. Moreover, in connection to the risk of AD, amyloid beta in plasma has also been examined extensively. The researchers concluded that even though plasma amyloid-beta is difficult to detect because it binds to certain other proteins and cells in the blood, it still has the potential to serve as a prognosis when following up on patients with AD [85]. Due to the presence of the blood-brain barrier, the low concentration of proteins that originated in the brain that are detected in the blood is much lower than that which is found in the cerebrospinal fluid (CSF).

This thesis mainly focuses on blood-based biomarkers, hence the table below gives a list of presently deployed and relevant blood plasma marker proteins and their efficacy in the diagnosis of AD. The chart helps identify the biomarkers that are most suitable for use in biosensors.

BIOMARKERS	MOLECULAR MASS	CONCENTRATIONS	
		Alzheimer’s	**Normal Controls**
Apolipoprotein A1	28.3 kDa	176±18 µg/mL [86]	103±17 µg/mL [86]
Apolipoprotein E (APOE)	38000 Da	-	-
Beta-defensin-2	4328.22 Da	603±113 pg/mL [86]	369±70 pg/mL [86]
Plasma (Clusterin alpha and beta)	85000 Da	-	-
Plasma Complement C3	176000 Da	-	8–37 ng/mL [87]
Plasma Complement Factor H(CFH)	139096 Da	-	-
Plasma Cystatin C	13343 – 13359 Da	-	-
Plasma Gelsolin	85698 Da	-	-
Plasma Aβ40	30-440 k Da	164 pg/mL [88]	-
Plasma Aβ42	4516.31 Da	39.3 pg/mL [88]	-
Serum Amyloid Protein (SAP)	11.4–12.5 kDa	48±16 µg/mL [86]	7.7±1.7 µg/mL [86]

Table 2. 1: A comparison of the ideal characteristics of biomarkers in the plasma.

2.3 INTRODUCTION TO BIOSENSING:

In the past few years, detecting biomarkers at low concentrations has gained tremendous attention. This growing interest resulted in the development of various rapid and efficient analytical techniques including nanoparticle immunoassays [89, 90], microfluidic point-of-care (POC) devices [90, 91] and various optical methods [92-94]. As discussed before, diagnosing AD as soon as possible is of utmost importance, however, at the preliminary stages, the disease-related biomarkers are usually present in very low concentrations. Hence, detecting these low concentrations of chemicals is vital for the early detection or prevention of several illnesses and diseases including AD. Therefore, the high-level sensitivity and specificity of modern biosensor technologies offer a medical advantage. Likewise, several types of biological fluids can be analyzed utilizing biosensor technology. This includes blood, saliva, and urine which vary according to the molecule to be detected. Advance biosensors with submicron-sized dimensions are also capable of performing intracellular measurements. Hence, there have been huge potential benefits presented by nanotechnology in the area of biosensing [95].

2.3.1 BIOSENSORS:

A biosensor is an analytical device that measures biological or chemical reactions by producing signals that are proportional to the concentration of an analyte involved within the reaction. The components of a typical biosensor are shown in **Figure 2.5** [96]. It comprises of an analyte which is the substance that is going to be detected by the biosensor. A bioreceptor, such as Enzymes, cells, aptamers, DNA, and antibodies, is the molecule acting as the recognition element and interacts with the analyte. This bioreceptor analyte interaction generates a signal known as bio-recognition. The transducer converts the bio-recognition event into a quantifiable signal called as signalization. The signals produced are proportional to the number of bioreceptor and analyte interactions. Mostly optical or electrical signals are produced. Signals generated by the

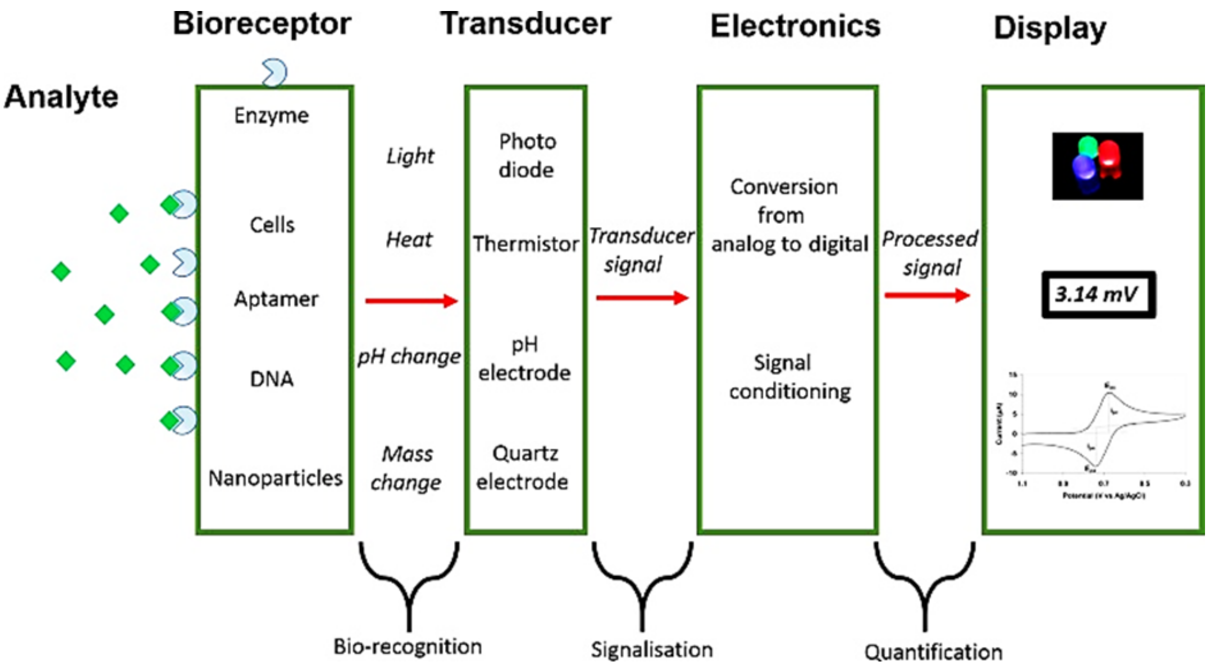

Figure 2. 5: Components of a biosensor, commonly used analytes and types of signal transducers [86].

transducer are processed and displayed at the complex electronic circuitry part. These processed signals are then quantified by the display unit. It consists of both software and hardware that produces results from the biosensor in a user-friendly interface [97].

Biosensors are usually said to be comprised of the following important features, high sensitivity, reproducibility, lower manufacturing cost, mass-scale production, and ease to use. Numerous biosensors have been reported to date. For instance, glucose sensors are one of the successful point-of-care biosensors presented in the clinical setting. Biosensors are usually categorized into electrochemical, piezoelectric, optical, electronic, and gravimetric biosensors.

2.3.2 ELECTROCHEMICAL BIOSENSORS:

Over the past half-century, utilizing electrochemistry for identifying target analytes within biological samples has gained immense attention. This interest began when Clark and Lyons first reported the enzyme-based electrochemical biosensor for blood glucose detection in 1962 [98]. Ever since that time electrochemical biosensing has been developing constantly with different types of biosensors used in industrial applications, for instance, clinical diagnostics and health monitoring systems, explosive detection, pesticides and heavy metal toxicants detection, biomarker detection and use within the food industry [98-101].

Electrochemical biosensor is an analytical device that transduces the biochemical interactions i.e., antibody-antigen interaction into the electrical signals [102]. These signals can be in the form of current (I), voltage (V), impedance or capacitance measurements [103]. The techniques which have been extensively utilized while using electrochemical biosensors include; current-voltage measurements, cyclic voltammetry (CV), square wave voltammetry (SWV), differential pulse voltammetry (DPV), and electrochemical impedance spectroscopy (EIS) [104].

A typical electrochemical biosensor consists of an electrode that is utilized as solid support for the attachment of the biomolecules (i.e., enzyme, antibody, and nucleic acid, etc) as well as for the ionic movement. Until now numerous methods for chemical functionalization of electrode surface have been reported depending upon the functional groups on the electrode surface. For example, aldehyde- (hydrazide), amine- and carboxyl (1-ethyl-3-(3-dimethylaminopropyl) carbodiimide: EDC), and thiol based chemical modifications [105-107]. It is an important step to maintain the orientation and the biological activity of biomolecules upon binding to the electrode surface. This is due to the reason that improper attachment to the electrode can result in non-specific measurements, less activity and biocompatibility. Therefore, electrode functionalization is considered the crucial step in fabricating a high-performance biosensor.

In the electrochemical biosensors, the oxidation-reduction reactions take place at the surface of the electrode. The charge transport from the electrolyte towards the electrode is controlled by the binding events and the biomolecules present at electrode surface [102].

A typical electrochemical biosensor comprises a three-electrode system and an electrolyte as a redox mediator (i.e., Ferro/Ferricyanide (Fe^{2+}/Fe^{3+})) as shown in **Figure 2.6**. Depending on the charge on the biomolecule that is attached to the surface of the working electrode the electrolyte solution is oxidized or reduced. The simultaneous movement of electrons to and from the working electrode (WE) surface is presented and defined by the following equation 2.1:

$$Fe^{2+} \leftrightarrow Fe^{3}+ + e- \tag{2.1}$$

Hence, the current or potential at the working electrode (WE) with respect to the counter or auxiliary electrode (CE) and a reference electrode (RE) is modulated by this charge transfer process. This change in the charge transfer process results in a significant change in the signal that tells the information about the concentration of the analyte [108].

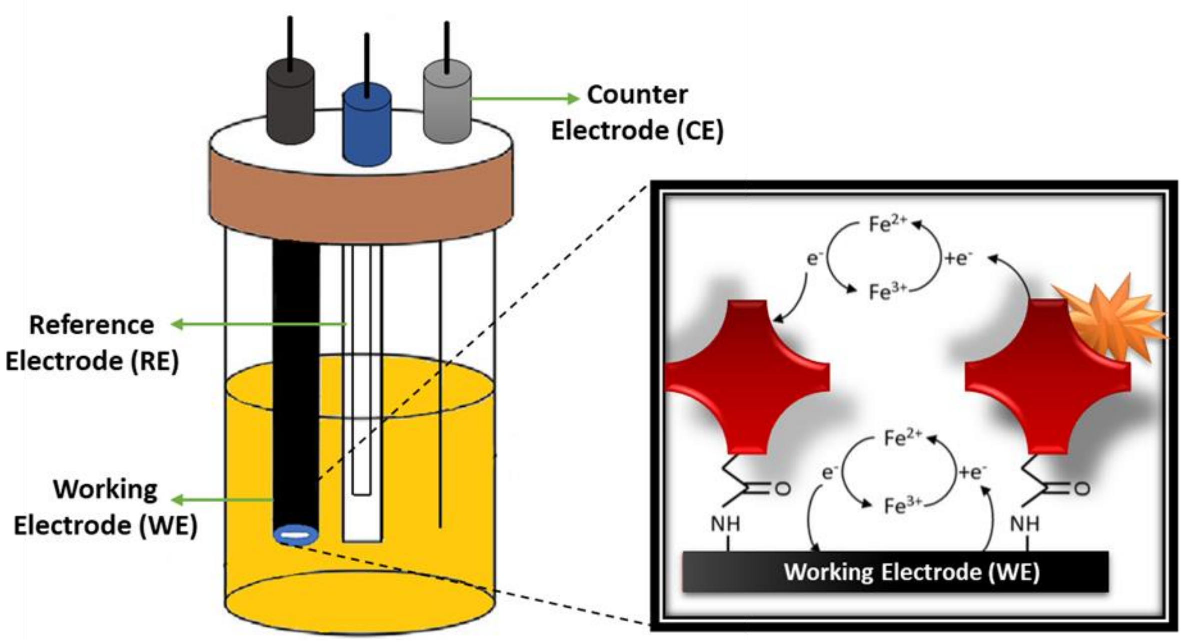

Figure 2. 6: Schematic representation of a three-electrode electrochemical cell set-up; illustrating the working electrode (WE), counter electrode (CE), and reference electrode (RE) in an electrolyte solution i.e, potassium ferro/ferricyanide. The inset shows the reaction at the WE, where the target proteins are attached to the bioreceptors which are immobilized on the surface of electrode. As the concentration of the target analyte changes, the redox reaction also changes which in turn changes the voltage or current thus resulting in a measurable reading.

There are two types of detection methods for electrochemical transducers or biosensors: Amperometric or Potentiometric.

In the case of amperometry, the concentration of the electroactive species is measured by measuring the current change between the WE and CE. Since the electrode potential is varied as a function of current and time, therefore this is the case of voltammetry which is defined as amperometry [109]. On the other hand, the potentiometric analysis involves the potential difference between the WE and RE when there is no current flowing across them. This potential difference is relative to the concentration of electroactive species. In this case, the potential of WE changes depending on the electrolyte solution and the biomolecule concentration, whereas the RE maintains the constant potential. Usually, potentiometric detection is utilized for the analysis of charged target biomolecules i.e., ions [109]. Ideally, label-free biosensors should be developed as they eliminate the need for radioactive and fluorescence labelling. This is due to the reason that they are comparatively expensive and sample preparation is complex and takes more time. Label-free assays quantify the protein concentration by measuring the change in the electrical behavior of the sensor device.

A huge number of successful electrochemical biosensors have been presented to date however, the direct assays are also reported as one of the ideal methods for analyte detection. This method typically involves the direct transfer or withdrawal of electrons between the conductive substrate and the binding event. The advantage of this method is that the analyte detection can be done in a simpler manner using direct assays [108]. Therefore, it is considered as the preferred choice in most of the point-of-care diagnostic applications. As demonstrated in **Figure 2.7**, in the case of direct assays oxidation or reduction reaction is not essential. Instead, a change in the electrical conductivity is obtained as a result of the binding of the target analyte to the highly-selective bioreceptor protein [110]. In the case of a direct current-voltage assay, a current is measured by

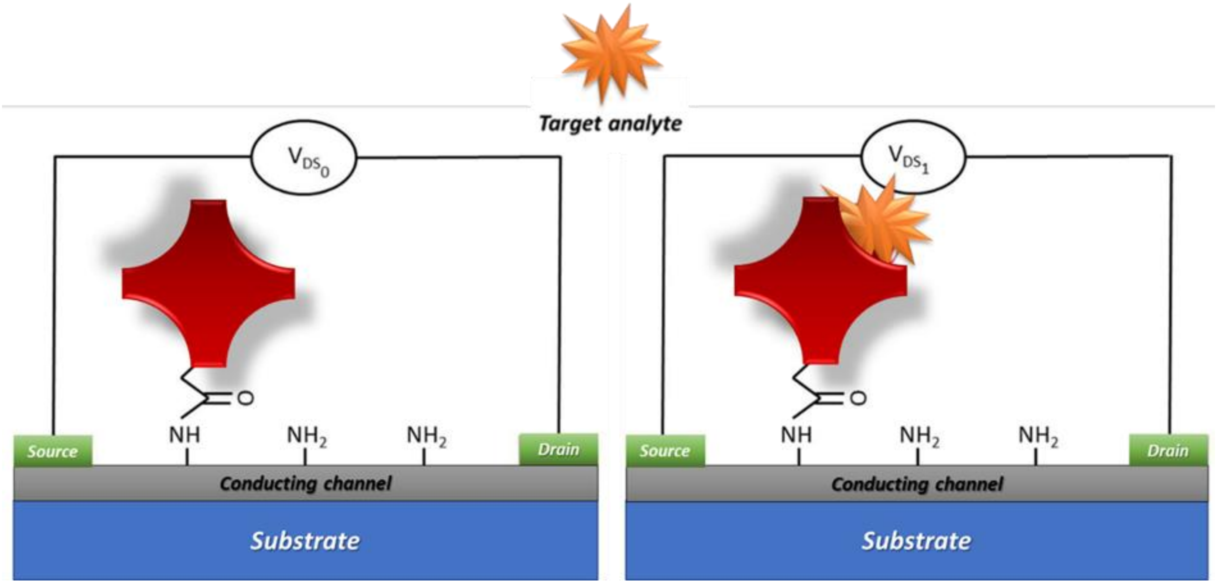

Figure 2. 7: A schematic representation of a target analyte detection applying the direct current-voltage measurement technique using a direct assay. In this case, a source is used for applying the voltage while the drain reads out the current.

applying the voltage to the conductive substrate, and the resulting current change relates to the binding event amongst the target analyte and the bioreceptor, which leads to the measurable signal change.

Zhou et al., reported the detection of carcinoembryonic antigen (CEA), a cancer biomarker, utilizing the real-time direct assay, in 2017. They utilized a graphene field-effect transistor (G-FET) and chemically modified it with pyrenebutanoic acid succinimidyl ester (PBASE) and anti-CEA. A limit of detection (LOD) of 0.5 pM was achieved using chronoamperometry as a detection technique [111]. Another electrical biosensor utilizing the direct assay was reported by Kim et al., in 2013. They also used G-FET as the working electrode and functionalize it with PBASE and DNA molecules for the detection of protective antigen (PA). A detection limit of 12 aM was achieved in this work while the detection was done using back-gated electrical measurements [112].

A large number of biosensors are reported till now which utilize conductive substrates for instance silicon or carbon-based substrates that include graphene, graphene oxide (GO), reduced graphene oxide (rGO), graphite, carbon nanotubes, glassy carbon, etc. The biosensors based on metals include nanomaterials for example metal nanoparticles, gold, and platinum [113]. However, this thesis mainly focuses on graphene-based electrochemical biosensors. Therefore, electrochemical biosensors will be discussed in more detail in the next chapters.

2.3.3 GRAPHENE:

Graphene is considered one of the most remarkable achievements in the field of science and technology since 2004 [114]. It is the base material for graphite, carbon nanotubes, and fullerenes as shown in figure [115]. Graphene is the single layer of graphite and is the most simple form. It is one of the important hexagonal crystalline allotropes of carbon atoms with a C–C bond at a distance of 0.142 nm. Graphene has gained extensive attention in the field of healthcare, sensors, composite materials as well as energy storage and microelectronics, etc [114, 116, 117]. Until the discovery of graphene, it was believed both experimentally and theoretically that 2D materials do not exist. It was because some researchers considered that 2D materials were thermodynamically not stable and therefore could not exist [118]. Nevertheless, in 2004 Novoselov and Geim invalidated these arguments with the discovery of graphene a 2D material [119]. Moreover, graphene is proven to be exceptional material for the next generation of ‘disruptive’ technologies due to its outstanding physical and electronic properties [120].

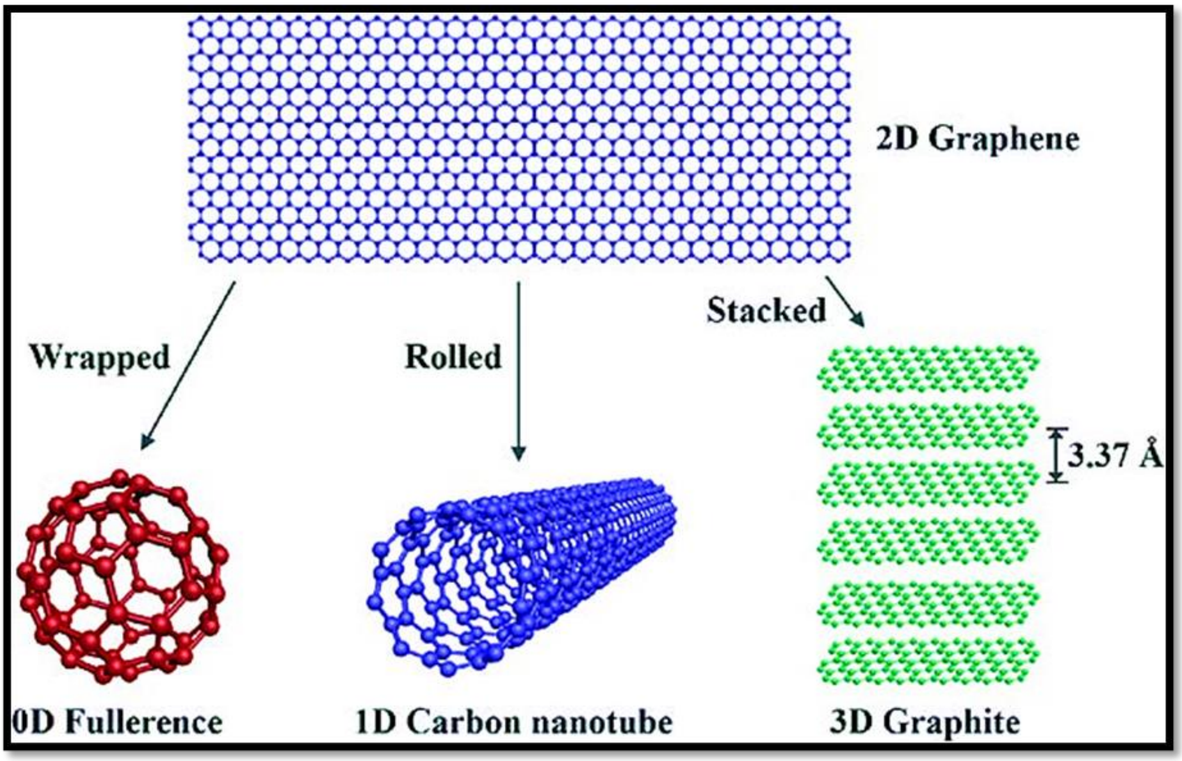

Figure 2. 8: Illustration of 2D graphene i.e., wrapped into 0D fullerene, rolled into 1D carbon nanotube, and stacked into 3D graphite.

Graphene is expected to play a potential role in contributing to the improvement of future technologies due to its unique set of properties including its large surface-to-volume ratio, excellent conductivity, fast electron transport, biocompatibility, etc [120].

2.3.3.1 Properties of Graphene:

Graphene possesses many interesting physical and chemical properties that made it a highly studied material with great possibilities. The extraordinary properties of graphene are due to its 2p orbitals that form the π-bonds. Typically, graphene is a single atomic layer of sp^2 hybridized carbon atoms. The carbon atoms are tightly packed in a honeycomb crystal lattice i.e., each atom is further attached to three other carbon atoms by forming the covalent σ-bonds with the bond angle of 120-degree as shown in **Figure 2.9(a)** [121, 122]. The carbon-to-carbon σ-bond length in the graphene is approximately 0.142 nm (1.42 Å). Within graphene lattice the σ-bonds (**Figure 2.9(c)**) form between 2ps, 2px, and 2py orbitals (**Figure 2.9(b)**) of the adjacent carbon atoms

[115]. The orbitals 2pz interact via forming the π-bonds which are weak in comparison and are oriented in the z-direction. The π-bonded 2pz electrons all together form a delocalized electronic cloud. It is distributed along the entire graphene plane [122]. These π-electrons are responsible for many unusual electronic properties of graphene for instance the carrier mobility. The exceptional charge transport properties of graphene make it a perfect candidate to be used in many electronic applications.

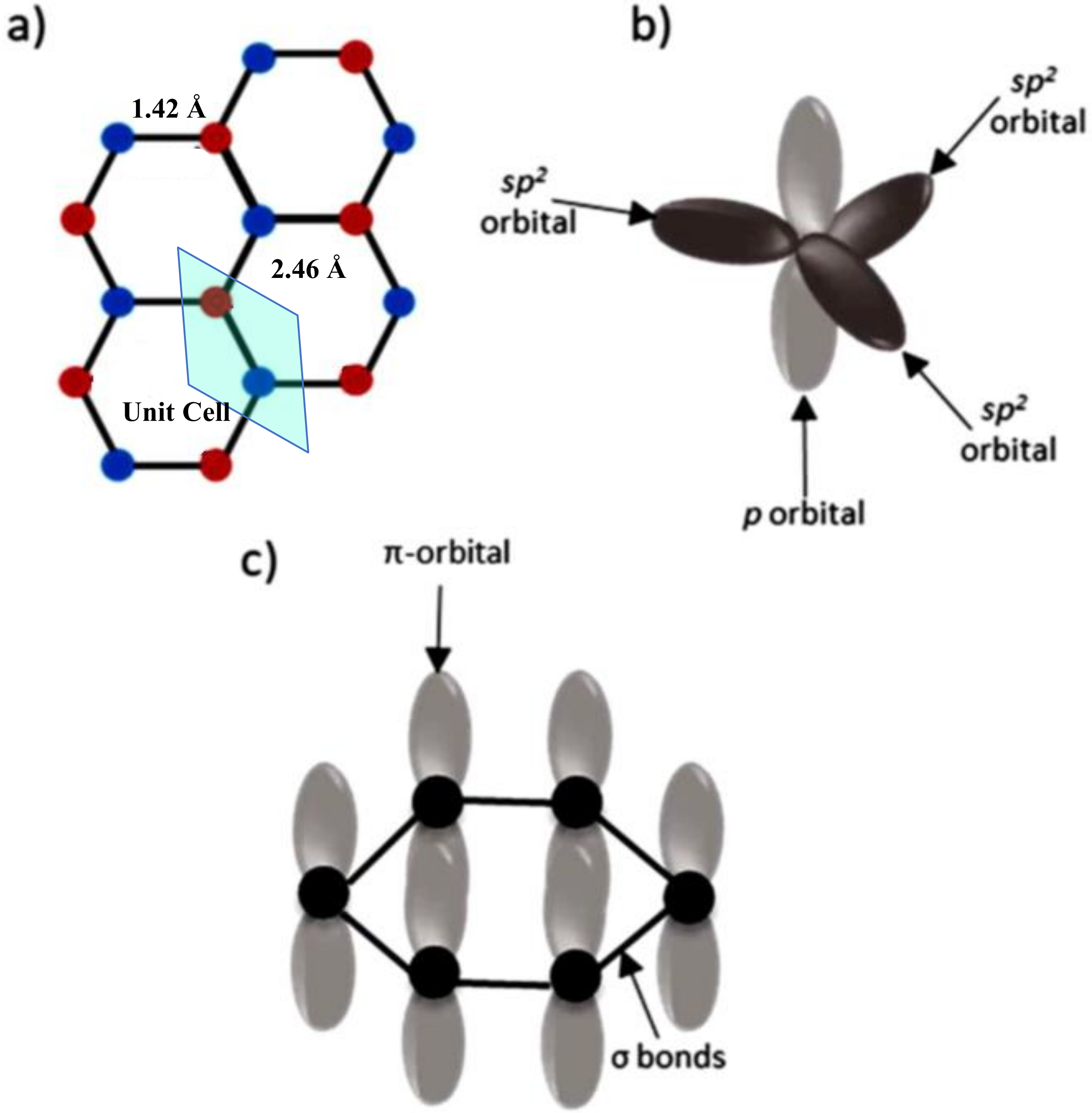

Figure 2. 9: Electronic structure of graphene (a) Graphene's hexagonal lattice. Each carbon atom with an angle of 120° is bounded to three other carbon atoms.(b) The sp^2 orbitals and the p orbital of single carbon atom within the hexagonal lattice structure. (c) A schematic illustration showing the sp^2 orbitals forming the σ-bonds and p orbitals forming the π-bonds.

Graphene's charge carrier mobilities are reported to be far higher than the silicon which is considered as the gold-standard semiconductor [121]. The intrinsic carrier mobilities of graphene are rarely realized experimentally however they are as high as 5×10^6 cm^2/Vs at 50 K temperature as per predicted via the simulations data [123]. Despite that the carrier mobilities of 10^5 cm^2/Vs have been reported for suspended graphene-based devices, which is two-fold higher than as seen in the silicon devices. Substrates like silicon dioxide (SiO_2) are usually required by graphene-based devices for better support and stability of the graphene layer. However, the substrate causes scattering mechanisms like the roughness of the surface and the charge impurities, and this drastically decreases graphene's carrier mobility [124]. For instance, carrier mobilities of 2.5×10^4 cm^2/Vs have been reported for mechanically exfoliated graphene onto the SiO_2 substrate which is 10 orders of magnitude less than for the suspended graphene. Besides, CVD graphene further reduces it to 4×10^3 cm^2/Vs. But still, these values are 3 to 4 times greater than that of silicon whose carrier mobility is approximately 1.5×10^3 cm^2/Vs [124].

As the physical properties of graphene are concerned, the remarkable property of graphene is its high thermal conductivity. The thermal conductivity of graphene is approximately 4000 W/mK and due to this high value, it is considered a powerful conductor of heat and electricity [125]. The graphene has a 2D structure of its atoms and due to this one atom thickness, graphene has high elasticity and flexibility that it can be molded into desired shapes and can withstand high mechanical stress and pressure. This allows graphene to occupy any space or area to carry out its functions admirably. Along with its flexibility and elasticity, graphene is stronger and harder than diamond due to the single plate of carbon atoms in the SD dimensional structure of graphene. The tight bonding between atoms makes it harder yet more flexible, that it can be molded into shapes but is unable to break easily. Another interesting property that keeps it a highly valuable material in the industry is its resistance to ionization. It cannot be ionized by radiation and can make electricity by extracting sunlight. Moreover, other physical properties of graphene are its high density and its antibacterial effect which means that it does not allow bacteria to grow on it and keeps it usable and functional all the time. It has a low joule effect and low power consumption as compared to other metals [126].

2.3.3.2 Graphene Functionalization Chemistry:

Van der Waal's forces in the graphene molecular structure are induced by the π-π interactions between individual graphene planes. These forces allow graphene to form agglomerates in a variety of solvents which in turn allow graphene to be modified with different chemical groups and biomolecules. Many potential graphene modification chemistries have been established including halogenation, animation, azidation, alkylation, epoxidation, and hydroxylation. Two methodologies are most commonly used for the chemical functionalization of graphene which are stated below.

2.3.3.2.1 Covalent Functionalization:

Graphene is capable of forming covalent bonds due to the presence of sp^2 carbon atoms. The oxidation process on graphene can be done using strong oxidants. The oxidation process of graphite with carboxylic groups on the edges as well as epoxy groups and hydroxyl groups at the basal planes make graphene oxide (GO). Which in turn offers its good dispersity in the hydrophilic and hydrophobic environment while maintaining stability for the long term [127]. There are mainly two covalent processes that help to make graphene functional by utilizing the plasma treatment i.e., fluorination [128] and hydrogenation [129]. In addition, another method used is the addition of free radicals in the hexagonal matrix to carbon atoms [130] for instance in the case of the diazotization process [131]. Besides, covalent attachment of graphene to polymers like PEG [130] and salinization by using APTES are also some of the methodologies used for graphene functionalization [132]. In one study researchers utilized the diazonium functionalization method and demonstrated the fabrication of GFET biosensors for cancer biomarkers with a detection limit of 0.1 ngmL^{-1} [133]. Moreover, in another study Teixeira et al demonstrated a GFET sensor that was functionalized using the APTES method. Their sensor showed the limit of detection of 0.62 ngmL^{-1} for the specific detection of human chorionic gonadotrophin (hCG) [132]. All these studies have proven that graphene modification using covalent chemistry is a successful approach, but it also has some drawbacks. The excellent electronic properties of graphene can be disturbed using covalent functionalization methods because it converts the sp^2 hybridization of graphene in to the sp^3 hybridization which in turn disrupts graphene's electronic structure [127]. Hence, other methods for chemical modification of graphene are also explored [134].

2.3.3.2.2 Non-Covalent Functionalization:

In the case of non-covalent functionalization, the chemical moieties are physiosorbed utilizing the weak Van der Waals forces over the graphene surface [134]. More precisely, the non-covalent functionalization occurs through the process known as π-π stacking. This process involves the interaction between the functional molecule and the graphene's π-electron cloud. A most common example of π-π stacking is graphite which exhibits multiple layers of graphene sheets. These sheets interact with each other via their respective π-electron clouds and hence are stacked on top of one another [130]. Hence the non-covalent formation of graphene does not affect its sp^2 nature and thus, the structural and electronic properties of the graphene are not disrupted at all [134]. Polymeric molecules such as pyrene show a strong chemical affinity with graphene through the π-πstacking [135]. Chen et al. utilized the tetrafulvalene (TTF) for graphene functionalization which is an electron donor and also the hexaazatriphenylene-hexacarbonitrile (HATCN) which is an electron acceptor molecule. This process resulted in the p-doping of graphene with an electron donor and n-doping with an electron acceptor molecule. Both processes did not harm or destroy the overall structure of graphene [134]. Other techniques that contribute to the noncovalent functionalization of graphene surfaces include the attachment of nanoparticles, for instance, gold, palladium, zinc oxide, platinum, etc [136-139]. The deposition of metal nanoparticles over the graphene surface can be done by dipping the graphene channels in a metal salt solution or via the chemical reduction process, or through the electrochemical deposition process.

2.3.3.3 Biofunctionalization:

Biosensors comprise numerous applications in clinical diagnostics i.e., by monitoring health conditions. The most essential part of biosensor development is biofunctionalization. For instance, in the case of graphene sensors, biofunctionalized graphene surfaces exhibit highly specific as well as highly selective biological recognition capabilities. The first step of this procedure is to chemically functionalize the surface of the graphene sensor with the help of linker groups. Following to that receptor molecules are attached to the sensor surface. The attachment of receptor molecules makes the sensor capable of efficiently measuring the biomarkers at very low concentrations with high selectivity.

Antibodies, enzymes, and nucleic acids are some of the examples of biomolecules that are used as bioreceptors. All these receptors work differently but they bind to the target molecules in the same manner. In the selective bioreceptor category, antibodies are considered the utmost and most well-known example. Antibodies are proteins made up of immunoglobins that are produced by a person's immune system to fight against foreign bodies. The advantage of using antibodies as bioreceptor is that these proteins exhibit a strong affinity for their target biomarkers via non-covalent interaction. They remain frequently utilized in immunoassays, such as enzyme-linked immunosorbent assays (ELISAs). Moreover, other bioreceptor molecules that are more frequently used for biosensor fabrication include but are not limited to aptamers also known as artificial oligonucleotides, cells and peptides, and proteins. These bio-receptors hold specific advantages which make them perfect for specific applications. For example, the aptamer binding affinity can be easily improved when compared with other bioreceptors [140]. Increasing a bioreceptor binding affinity leads to the target detection even at very small concentrations which further leads to the improvement of biosensors sensitivity for analyte detection.

2.3.3.4 Selective Antibody Orientation:

Antibodies when immobilized on the sensor surface are required to maintain their functioning capabilities and conformance. As a result, controlling the antibody's orientation after immobilization is very critical. This is because if the method is not controlled, the antibodies may attach in different directions. Therefore, it is highly desirable to perform the antibody immobilization in a manner that the Fc fragment of the antibody binds to the surface of the sensor. Hence the antigen binding sites of the antibodies i.e., the Fab fragments are facing away from the surface of the electrode which in turn allows more efficient and selective binding to the target biomarkers (antigens). Immobilizing the antibodies in a well-defined orientation also provides the immunosensor with excellent characteristics. For instance, it can avoid false-negative readings and provide higher sensitivity, specificity, and lower limit of detection (LOD) [141].

The most commonly used method for controlling the orientation of antibodies is utilizing the carbodiimide chemistry via using the EDC/ NHS. EDC/ NHS chemistry is used to activate the carboxylic group at the Fc terminal of the antibody [142].

2.3.3.5 EDC/ NHS Activation of Antibodies:

1-Ethyl-3-(3-dimethylaminopropyl) carbodiimide (EDC) is a water-soluble compound. This carbodiimide compound is used for crosslinking to the carboxylic acid and also for labelling.

Therefore, the carboxyl terminated antibodies react with EDC and form an unstable intermediate reactive o-acylisourea. The addition of N-Hydroxysuccinimide (NHS) leads the solution containing antibody/EDC to form a semi-stable NHS-ester (which is amine reactive). This process results in the peptide bond formation, which aids the antibodies to attach to the surface of the biosensor via covalent bonding [143].

Teixeira et al. developed a biosensor based on epitaxial graphene for selective detection of the hCG hormone which is used in pregnancy testing. For their sensor, they utilized the EDC/ NHS method for antibody immobilization [132]. Di-tert-butyl dicarbonate (t-BOC) was also used in their work which helps protect the amine groups of antibodies. This in turn prevented the aggregation and cross-linking between the antibodies while ensuring that the antibody's carboxylic groups were only bound to the amine-terminated functional groups on the surface of the biosensor. EDC/ NHS activated antibodies were attached to the surface of amine-terminated graphene devices. Subsequently, the protecting groups i.e., t-BOC were eliminated from the antibodies in order to restore their amine groups. For that purpose, trifluoroacetic acid (TFA) was used. In the last step, the remaining amine groups from the sensor surface were blocked using the 5% BSA solution in order to prevent any non-specific binding of the target molecules [132].

2.3.3.6 Blocking Non-Specific Binding:

One more essential step in developing high-performance immunoassays is to block the non-specific interactions which would lead to reducing the background noise. The background noise can disrupt the biosensor performance by providing false readings. If the target molecule binds to the free amine sites and not to the activated bioreceptor molecules can lead to the introduction of background noise in the biosensor system. Non-specific binding is one more reason for background noise that is facilitated through interaction between the sample and the surface of the biosensor. Hence it is essential to take measures to block any non-specific binding before undertaking the sample analysis.

Typically, the blocking agent binds to the specific sites on the antibody originally meant for antigen binding and also to the areas on the surface of the biosensor that is not biofunctionalized with antibodies. After the antigen introduction in the sensor, the blocker molecule is separated from the antibody epitope-binding region. This then leaves that specific region for the analyte to bind. The blocking agent dissociation occurs because of the reason that the corresponding antibody and antigen have a high affinity for one another as compared to the antibody's affinity towards the blocking agent [144].

It is therefore necessary to select an appropriate blocking agent for the biosensor system to enhance the specificity and sensitivity of the assay. Bovine serum albumin (BSA) is a well-known molecule used as a blocking agent. Many studies have reported that BSA is an effective blocker that blocks the non-specific analyte and surface binding. It can also block the pre-activated covalent-surfaces. Typically, a very low concentration of BSA is used in biosensors i.e., from 0.5% to 3%. BSA is a low-cost material that can either be stored in dry form or solution form at 4°C.

Despite all the advantages some limitations are also linked with BSA. These include firstly due to the fatty acid substance of BSA, there might be an inconsistency in the quality of one production lot to the next one, as for blocking purposes BSA should be free from fatty acids. Another drawback is the absence of molecular diversity (most of the blockers containing single molecules are unable to block some surfaces for instance ionic, hydrophobic, and surfaces with covalent characteristics). Regardless of all such drawbacks, to block the antibodies and other bioreceptor molecules, BSA is most commonly used for the development of biosensor immunoassays [144].

2.3.3.7 Graphene substrate:

2.3.3.7.1 Screen-Printed Electrodes (SPEs):

For biosensor development, the screen-printing technique has gained a lot of attention over the last two decades. This attention arises when initially the disposable glucose biosensor strips were commercialized [145]. Typically, a screen or an ink-blocking stencil is utilized to perform the screen printing. Printing inks for instance silver ink or carbon ink are deposited whereas the stencil defines where to deposit the respective ink [146]. Mostly a plastic or ceramic-based non-conductive substrate material is used for performing the printing application [145]. In the printing procedure, the screen and the substrate are aligned. The ink is then forced to pass through the open area of the screen by passing a roller over it which results in the formation of the electrodes (**Figure 2.10**). Usually, the screen-printed electrodes consist of three electrodes, the ink is also deposited in multiple layers; however, the first layer of ink must be solidified first before printing the second layer which is normally done by using a thermal treatment [146].

The SPEs are produced for developing electrochemical biosensors which are designed to work with a very low sample volume. A typical SPE consists of a counter electrode and a reference

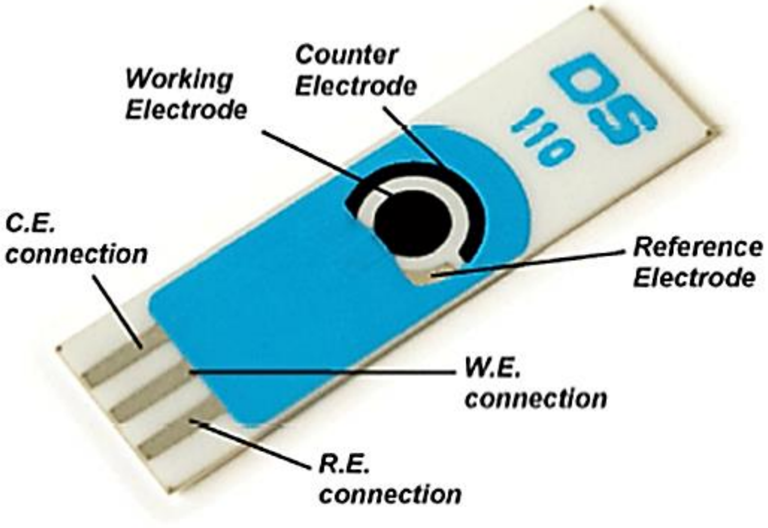

Figure 2. 10: An illustration of the Metrohm dropsens Screen printed Electrode (SPE).

electrode. The counter electrode is usually made of carbon ink and the reference electrode is made of silver or silver/silver chloride ink respectively. On the other hand, the working electrodes can be incorporated with a lot of different materials such as carbon nanostructured materials, nickel oxide, ferrocyanide, gold nanoparticles, streptavidin, quantum dots, or graphene. The incorporation is done in order to amplify the charge transfer properties of the electrochemical biosensors [147]. The amplification thus has improved the functionalization chemistries which in turn increase the selectivity and sensitivity of the electrodes [148]. This leads to the development of commercially available graphene-based screen-printed electrodes (SPEs), including Dropsens's, DRP-110Gph, graphene electrodes shown in **Figure 2.10** [147].

Due to the ease of manufacturing in bulk quantities, graphene based SPEs have been extensively explored for applications of electrochemical sensing applications. This mass manufacturing is reproducible, fast, and low-cost. And due to its ease of manufacturing, it has also challenged the conventional biosensing platforms used for electrochemical sensing for example glassy carbon [149]. Furthermore, SPEs are on-chip miniaturized portable devices which makes them an excellent candidate for the point of care diagnostics. Graphene SPEs are produced by electrochemically depositing the graphene onto the carbon surface of the working electrode [146]. Graphene-based SPEs have been reported for the detection of several biomarkers which includes melatonin and serotonin detection [150], hCG [132], β-lactoglobulin [151], and many more.

2.3.4 STATE-OF-THE-ART GRAPHENE-BASED BIOSENSORS FOR DETECTION OF AD BIOMARKERS:

2.3.4.1 Graphene Biosensors:

As previously discussed in detail in section 2.3.3, graphene is one-atom-thick material that consists of sp^2-bonded carbon atoms with a honeycomb structure [152]. Single-layer graphene sheets exhibit exceptional properties such as high mechanical strength [153], tunable bandgap and optical properties [118, 154, 155] thermal conductivity and high elasticity, demonstration of RT quantum Hall effect, and exceptional electronic mobility at room temperature (RT) [152]. These fascinating properties of graphene have inspired the scientific community in the fields of materials science, chemistry, and physics. Graphene is considered an exceptional material for biosensor-based devices as it is a low-cost transparent material with excellent conductivity and exhibits a large surface-to-volume ratio [118]. The large surface-to-volume ratio makes the graphene-based sensors extremely sensitive to any changes in their environment which in turn makes them ideal for sensing applications [156]. For instance, a drastic change in the electronic properties of graphene may occur with a very small change in the analyte concentration [157]. Graphene-modified biosensor devices have numerous advantages over other carbon-based materials such as lower limit of detection, higher sensitivity, and high throughput detection when compared to other methods like polymerase chain reaction (PCR), enzyme-linked immunosorbent assays (ELISA), and fluorescence.

A typical graphene sensor is composed of a conducting graphene channel across two metal contacts, the source and drain electrodes, through which the current is passed. The graphene is chemically functionalized with bioreceptors precise for the desired target molecule. These bioreceptors include antibodies, single-strand DNA probes, miRNAs, or enzymes, which afterward, selectively bind to the target biomolecules. Some of the graphene-based sensors include DNA-based sensors and immunosensors, graphene field effect transistors (GFETs), and optical biosensors. These sensors will be reviewed in the following part.

2.3.4.2 Graphene-Based DNA and mRNA Electrochemical Sensors:

The large 2D hexagonal honeycomb structure of graphene is an excellent substrate for the adsorption of biomolecules as well as ideal support to disperse and stabilize metal, metal oxide, and semiconductor nanomaterials [158]. A basic principle of DNA electrochemical biosensors depends on the specific hybridization among probe and target DNA. The ssDNA (probe DNA) is attached to the electrode surface by covalent interaction or physical adsorption to hybridize with the complementary target DNAs. The electrochemical signal is observed by an electrochemical workstation for the change in the conductivity and interfacial property of the electrode caused by the hybridization [159]. Li Wu et al. reported a novel ratiometric electrochemical DNA nanosensor platform based on graphene and mesoporous hybrid nanomaterials for the detection of the mutated apolipoprotein E gene associated with Alzheimer's disease. They achieved the detection limit of this assay down to 10 fM. Their work offered a new concept for improving traditional electrochemical sensing systems [160]. Moreover, Abdelmoneim et al. demonstrated a dual electrochemical as well as fluorescence-sensitive curcumin-graphene quantum dots sensing platform for sensing ApoE-4 DNA that is responsible for Alzheimer's disease. In their work, amperometric studies showed highly sensitive behavior towards the formation of DNA complex with a sensitivity of 4.74 nA.mL.pg^{-1} and a limit of detection of 0.48 pg mL^{-1}. They also recorded results in human blood plasma and demonstrated the high efficacy of curcumin system sensing [161]. A highly sensitive electrochemical nano biosensor was developed by Mostafa et al. to detect serum miR-137 as a validated biomarker of Alzheimer’s disease. They utilized electrochemically-reduced graphene oxide (ERGO) and gold nanowires (AuNWs) for the surface modification of screen-printed carbon electrode (SPCE) with the application of an intercalated label, doxorubicin (Dox). The limit of detection obtained was down to 1.7 fM [162]. More recently, Fan et al. propose a helicase-assisted Graphene oxide-based reaction platform for microRNA (miRNA) detection that was capable of shortening the detection duration from 4 h to 50 min, and its limit of detection for miRNA was calculated to be 4.2 fM as per 3σ rule. They combine helicase bioactivity in unwinding the hairpin structure of probes with the HCR/GO strategy for signal amplification. The sensitivity of the helicase-assisted HCR/GO sensing platform was found to be 2 orders of magnitude higher than the common HCR/GO sensing platform without enzymes [163].

2.3.4.3 Graphene-Based Electrochemical Immunosensors:

Graphene, being one of the most promising nanomaterials has been widely used in electrochemical immunosensors. Electrochemical immunosensors are based on specific interactions involving antibodies and antigens. The sensor works by employing enzyme-conjugated antibodies which bind to their associated antigen on an electrode surface, producing electrochemical activity in the enzyme that can be measured as a signal. For example, Panraksa et al. demonstrated a simple paper-based sensor with electrochemical detection for the determination of acetylcholinesterase (AChE) which plays an important role in the development of Alzheimer's and other neurological diseases. By using the screen-printed graphene electrodes as a sensing platform, they reported the limit of detection (LOD) to be 0.1 U/mL with AChE concentration in the range of 0.1–15 UmL^{-1}. They also successfully applied the sensor to detect AChE in blood samples [164]. Moreover, in another study, Eden et al. demonstrated the working of CdSe@ZnS quantum dots and the fluorescent dye Alexa as a reporter in a sandwich immunoassay microarray which is designed to detect apolipoprotein E a potential biomarker of Alzheimer's disease [165]. The two versions of the microarray were compared for performance and then compared to an ApoE assay based on a conventional ELISA. The QDs turn out to be efficient reporters in microarrays and their performance strongly varied as a function of excitation wavelength. The detection limit at 633 nm was about 247 pgmL^{-1}; however, it was 62 pgmL^{-1} at 532 nm, which is five folds more sensitive than the Alexa microarray (~307 pgmL^{-1}) and seven folds more than ELISA (~470 pgmL^{-1}). Serial dilutions from a human serum sample were assayed with high sensitivity and acceptable precision and accuracy [165]. Yoo et al. also reported the blood-based impedimetric detection of amyloid-β (Aβ) protein, which is a representative candidate biomarker for AD. Interdigitated microelectrode (IME) sensors were utilized as an impedimetric sensor platform. A combination of the signal processing system, as well as medium changes (plasma to buffer), were involved in the detection for AD diagnosis with around 100 times higher sensitivity. As constructed sensors showed the linear detection range of 100 fgmL^{-1} to 1 ngmL^{-1} with a detection limit of about 100 fgmL^{-1}. The detection of Aβ levels was also validated in transgenic and wild-type mouse plasma samples. The results confirmed that this system can be used to distinguish between the patients and healthy controls, which would allow the blood-based AD diagnosis [166]. In addition to that, Myung-Sic et al. used oxygen-plasma-treated rGO surfaces as reactive interfaces for the detection of amyloid-beta (Aβ) peptides, the pathological hallmarks of Alzheimer's disease (AD). Antibody immobilization and sensing performance were improved due to enhancement in surface functionality of oxygen-plasma-treated rGO sensors. This was confirmed by measuring the changes in electrical characteristics and topographic analysis, with a 3.33-fold steeper slope for electrical responses versus the analyte concentration curve compared to the untreated. They also evaluated clinical samples of neural-derived exosomal Aβ peptides extracted from apparent AD patients and normal controls. The oxygen-plasma-treated rGO sensors showed a significant p-value in the identification of clinical samples of AD and control subjects ($p<0.001$) as compared to the untreated sensors ($p=0.0460$) [167].

2.3.4.4 Graphene-Based Field-Effect Transistor (FET) Biosensors:

Field-effect transistors (FET) have received a great deal of interest in the biosensing area because they can provide full electronic detection that is completely unified into the electronic chips. Therefore, it is not only academia that is fascinated by these devices but there is a strong interest and investment from the industry as well [158]. FETs can be used to detect various analytes, including ions, proteins, and biomolecules, which obtained higher sensitivity and better stability compared with traditional electrochemical detection methods. For instance, Lebedev et al. reported a graphene-based sensor able to detect various protein molecules. The biosensor was checked using an immunochemical system consisting of fluorescein dye and monoclonal anti-fluorescein antibodies. The sensor detected fluorescein concentration at a level of 1-10 ngmL^{-1}and BSA-fluorescein conjugate at a level of 1-5 ngmL^{-1}. The proposed device has a good expectation for use for the early diagnostics of various diseases [168]. Lately, Chae et al demonstrated a reduced graphene oxide-based enzyme-modified FET (RGO-EnFET) to study the kinetics between acetylcholinesterase (AChE) and acetylcholine (ACh), which are linked to the advancement and treatment of Alzheimer's disease (AD). They measured the pH sensitivity of the RGO-EnFE to be 24.12 mV pH$^{−1}$ as well as ACh quantification in the concentration range of 1 µM–10 mM with a linear slope of 13.9 mV dec$^{−1}$ being acquired between ΔV_{Dirac} and ACh concentration. The effect of AChE inhibitors; donepezil and rivastigmine on the AChE enzymatic activity were also investigated. Inhibition rates acquired for both inhibitors were distinguishable at saturation levels of 90% and 75%, respectively. Results showed that these biosensors have the potential for future application in the study of enzymatic kinetics and drug screening for therapeutic purposes [169]. More recently Bungon et al reported a graphene field-effect transistor (GFET) biosensor for the ultrasensitive detection of Clusterin, which is the prominent AD diagnostic biomarker. Their proposed biosensor detected the Clusterin in the range from 1 to 100 pgmL^{-1} and showed the limit of detection of 300 fgmL^{-1}, using the direct current 4-probe electrical resistance measurements [170].

2.3.4.5 Graphene-Based Optical Biosensors:

Graphene oxide has localized electron-hole pairs within the sp^2 carbon clusters that are embedded within an sp^3 matrix which leads to the radiative recombination of small clusters and in turn shows light absorption from UV to near-infrared (NIR) regions [171]. The largely delocalized π-electrons of GO result in high fluorescence quenching ability which is very useful in optical-based biosensors [172]. Lin Liu et al. reported a GO-based fluorescence approach to detect Aβ oligomers selectively based on the specific interaction between Aβ oligomers and the PrP (95-110) peptide. More concretely, fluorescein iso-thiocyanate (FITC)-labelled PrP (95-110), called FITC-PrP (95-110), was adsorbed onto the GO surface by electrostatic and π-π interactions, leading to effective fluorescence quenching. However, in the presence of Aβ oligomers, the competitive binding of Aβ oligomers with GO for the peptide probe prevented the interaction between GO and FITC-PrP (95-110), which led to the fluorescence signal. As a result, the detection limit of Aβ oligomers was 1 nM [173]. Similarly, Vilela et al. successfully designed GO and up-conversion nanoparticle optical biosensors that are highly sensitive and specific and are capable of detecting analytes relevant to mRNAs present in Alzheimer’s disease as well as prostate cancer in human blood serum. The LOD achieved was in the range of 200- 500 fM [174].

Table 2.2 summarized the list of graphene-based biosensor technologies reviewed in the above sections.

Biomarker	Sensing Platform	Amplification strategies	Sample	LOD
Apolipoprotein E [160]	DNA Sensor	Unlabelled	---	10 fM
Apolipoprotein E- 4 [161]	Amperometric Sensor	Labelled	Human Blood Plasma	0.48 pgmL^{-1}
ApoE [175]	Immunosensor	Labelled	Human Blood	6.4–62.0 pM
Apolipoprotein E [165]	Immunosensor	Labelled	Human Serum	62 pgmL^{-1}
miR-137 [162]	Electrochemical Sensor	Labelled	Human Serum	1.7fM
miRNA [163]	Nucleic Acid Biosensor	Labelled	---	4.2 fM
miRNA [174]	Optical Biosensor	Labelled	Blood Serum	200-500 fM
amyloid-β (Aβ) protein [166]	Interdigitated microelectrode (IME) sensors	Unlabelled	Mouse plasma	100 fgmL^{-1}
amyloid-beta (Aβ) peptides [167]	Immunosensor	Unlabelled	Human Plasma	---
acetylcholinesterase (AChE) [164]	Amperometric Sensor	Unlabelled	Human Blood	0.1 UmL^{-1}
Acetylcholinesterase (AChE) and acetylcholine (ACh) [169]	FET/ PH Sensor	Unlabelled	---	---

Table 2. 2: List of graphene-based sensing technologies reviewed in this section.

2.3.5 LIMITATIONS OF GRAPHENE-BASED DEVICES:

One of the main challenges in graphene-based devices is that the biomolecules are not able to directly bind to the pristine graphene surface. This is due to the lack of hydrophilic functionalities. Moreover, a limited number of the electroactive site affect the sensitivity and response of the sensor [176]. On the other hand, graphene oxide (GO) has a large number of oxygen functionalities due to which it shows good electrochemical activity. However, these oxidized areas on the GO plane disturb the long-range conjugated network and the π electron cloud which in turn degrades the carrier mobility and conductivity [177]. Reduced graphene oxide (rGO) is therefore considered a fitter material for sensing as it has a reduced number of functionalities, structural similarities to graphene, and a large number of electroactive sites [178]. Similarly, the rGO -graphene double electrodes have also shown a huge potential when it comes to the sensitive detection systems. The rGO -graphene double layer sensor displayed higher sensitivity compared to rGO, graphene, and GO-graphene sensors [178]. It successfully detected the HIV-1 gene and can be modified for the detection of other protein biomarkers.

BIBLIOGRAPHY

1. Bondi, M.W., E.C. Edmonds, and D.P. Salmon, *Alzheimer’s disease: past, present, and future.* Journal of the International Neuropsychological Society, 2017. **23**(9-10): p. 818-831.
2. Fan, L., et al., *New Insights Into the Pathogenesis of Alzheimer's Disease.* Frontiers in Neurology, 2020. **10**.
3. Blennow, K., *Leon MJ de, Zetterberg H (2006) Alzheimer’s disease.* Lancet. **368**: p. 387-403.
4. Association, A.s., *2018 Alzheimer's disease facts and figures.* Alzheimer's & Dementia, 2018. **14**(3): p. 367-429.
5. Nussbaum, R.L. and C.E. Ellis, *Alzheimer's Disease and Parkinson's Disease.* The New England Journal of Medicine, 2003.
6. Goldman, J.S., et al., *Genetic counseling and testing for Alzheimer disease: Joint practice guidelines of the American College of Medical Genetics and the National Society of Genetic Counselors.* Genetics in Medicine, 2012: p. 597-605.
7. Cummings, J.L., *Biomarkers in Alzheimer's disease drug development*. 2011, Elsevier.
8. Goldman, J.S., *New approaches to genetic counseling and testing for Alzheimer’s disease and frontotemporal degeneration.* Current neurology and neuroscience reports, 2012. **12**(5): p. 502-510.
9. Nazem, A. and G.A. Mansoori, *Nanotechnology for Alzheimer's disease detection and treatment.* insciences journal, 2011: p. 169-193.

10. Wilcock, D.M. and C.A. Colton, *Anti-Aß immunotherapy in Alzheimer's disease; relevance of transgenic mouse studies to clinical trials.* Journal of Alzheimer's Disease, 2008: p. 555-569.

11. Association, A.s., *2019 Alzheimer's disease facts and figures.* Alzheimer's & Dementia, 2019. **15**(3): p. 321-387.

12. Kang, D.-Y., et al., *Ultra-sensitive immunosensor for β-amyloid (1–42) using scanning tunneling microscopy-based electrical detection.* Biosensors and Bioelectronics, 2009. **24**(5): p. 1431-1436.

13. Hampel, H., et al., *Biological markers of amyloid β-related mechanisms in Alzheimer's disease.* Experimental neurology, 2010. **223**(2): p. 334-346.

14. Craig-Schapiro, R., A.M. Fagan, and D.M. Holtzman, *Biomarkers of Alzheimer's disease.* Neurobiology of disease, 2009. **35**(2): p. 128-140.

15. Hardy, J. and D.J. Selkoe, *The amyloid hypothesis of Alzheimer's disease: progress and problems on the road to therapeutics.* science, 2002. **297**(5580): p. 353-356.

16. Aizenstein, H.J., et al., *Frequent amyloid deposition without significant cognitive impairment among the elderly.* Archives of neurology, 2008. **65**(11): p. 1509-1517.

17. Villemagne, V.L., et al., *Longitudinal assessment of Aβ and cognition in aging and Alzheimer disease.* Annals of neurology, 2011. **69**(1): p. 181-192.

18. Ricciarelli, R. and E. Fedele, *The amyloid cascade hypothesis in Alzheimer's disease: it's time to change our mind.* Current neuropharmacology, 2017. **15**(6): p. 926-935.

19. Reitz, C., et al., *Memory Performance is Related to Amyloid and Tau Pathology in the Hippocampus.* Journal of neurology, neurosurgery & psychiatry, 2009: p. 715-721.

20. Berti, V., et al., *Structural brain changes in normal individuals with a maternal history of Alzheimer's.* Neurobiology of aging, 2011. **32**(12): p. 2325. e17-2325. e26.

21. Turner, P.R., et al., *Roles of amyloid precursor protein and its fragments in regulating neural activity, plasticity and memory.* Progress in neurobiology, 2003. **70**(1): p. 1-32.

22. Forny-Germano, L., et al., *Alzheimer's disease-like pathology induced by amyloid-β oligomers in nonhuman primates.* Journal of Neuroscience, 2014. **34**(41): p. 13629-13643.

23. Nunan, J. and D.H. Small, *Regulation of APP cleavage by α-, β-and γ-secretases.* FEBS letters, 2000. **483**(1): p. 6-10.

24. Alzheimer's, A., *2019 Alzheimer's disease facts and figures.* Alzheimer's & Dementia, 2019. **15**(3): p. 321-387.

25. Khan, T.K. and D.L. Alkon, *Peripheral biomarkers of Alzheimer's disease.* Journal of Alzheimer's Disease, 2015. **44**(3): p. 729-744.

26. Wilcock, D.M. and C.A. Colton, *Anti-amyloid-β immunotherapy in Alzheimer's disease: relevance of transgenic mouse studies to clinical trials.* Journal of Alzheimer's Disease, 2008. **15**(4): p. 555-569.

27. Braak, H. and E. Braak, *Demonstration of amyloid deposits and neurofibrillary changes in whole brain sections.* Brain pathology, 1991. **1**(3): p. 213-216.

28. Mawuenyega, K.G., et al., *Decreased clearance of CNS β-amyloid in Alzheimer's disease.* Science, 2010. **330**(6012): p. 1774-1774.

29. Yang, L.-B., et al., *Elevated β-secretase expression and enzymatic activity detected in sporadic Alzheimer disease.* Nature medicine, 2003. **9**(1): p. 3-4.

30. Naj, A.C., et al., *Common variants at MS4A4/MS4A6E, CD2AP, CD33 and EPHA1 are associated with late-onset Alzheimer's disease.* Nature genetics, 2011. **43**(5): p. 436-441.

31. Dá Mesquita, S., et al., *Insights on the pathophysiology of Alzheimer's disease: The crosstalk between amyloid pathology, neuroinflammation and the peripheral immune system.* Neuroscience & Biobehavioral Reviews, 2016. **68**: p. 547-562.

32. Liu, C.-C., et al., *Apolipoprotein E and Alzheimer disease: risk, mechanisms and therapy.* Nature Reviews Neurology, 2013: p. 106-118.

33. Keene, C.D., et al., *Apolipoprotein E isoforms and regulation of the innate immune response in brain of patients with Alzheimer's disease.* Current opinion in neurobiology, 2011. **21**(6): p. 920-928.

34. Zlokovic, B.V., *Cerebrovascular effects of apolipoprotein E: implications for Alzheimer disease.* JAMA neurology, 2013. **70**(4): p. 440-444.

35. Liu, C.-C., et al., *Apolipoprotein E and Alzheimer disease: risk, mechanisms and therapy.* Nature Reviews Neurology, 2013. **9**(2): p. 106-118.

36. Lim, Y.Y., E.C. Mormino, and A.s.D.N. Initiative, *APOE genotype and early β-amyloid accumulation in older adults without dementia.* Neurology, 2017. **89**(10): p. 1028-1034.

37. Beyreuther, K. and C.L. Masters, *Amyloid Precursor Protein (APP) and BZA4 Amyloid in the Etiology of Alzheimer's Disease: Precursor-Product Relationships in the Derangement of Neuronal Function.* Brain Pathology, 1991. **1**(4): p. 241-251.

38. Hardy, J. and D. Allsop, *Amyloid deposition as the central event in the aetiology of Alzheimer's disease.* Trends in pharmacological sciences, 1991. **12**: p. 383-388.

39. Selkoe, D.J., *The molecular pathology of Alzheimer's disease.* Neuron, 1991. **6**(4): p. 487-498.

40. Hardy, J.A. and G.A. Higgins, *Alzheimer's disease: the amyloid cascade hypothesis.* Science, 1992. **256**(5054): p. 184-186.

41. Hardy, J. and D. Allsop, *Amyloid deposition as the central event in the aetiology of Alzheimer's disease.* Trends in pharmacological sciences, 1991: p. 383-388.

42. Panza, F., et al., *Amyloid-β immunotherapy for alzheimer disease: Is it now a long shot?* Annals of Neurology, 2019. **85**(3): p. 303-315.

43. Witter, M.P., *Entorhinal Area (Cortex).* 2009, Berlin: Springer Berlin Heidelber.

44. Cordero-Llana, O., et al., *Clusterin secreted by astrocytes enhances neuronal differentiation from human neural precursor cells.* Cell Death & Differentiation, 2011. **18**(5): p. 907-913.

45. Knafo, S., *Amygdala in Alzheimer's Disease*. 2012, Spain: Spanish National Research Council (CSIC)/Autonomous University of Madrid.

46. Binder, J.R., et al., *Where Is the Semantic System? A Critical Review and Meta-Analysis of 120 Functional Neuroimaging Studies.* Cerebral Cortex, 2009: p. 2767-2796.

47. Kenny, E.R., et al., *Functional connectivity in cortical regions in dementia with Lewy bodies and Alzheimer's disease.* Brain, 2012: p. 569-581.

48. Rafii, M.S. and P.S. Aisen, *Advances in Alzheimer's Disease Drug Development.* BioMed Central Medicine, 2015: p. 62.

49. Forlenza, O.V., B.S. Diniz , and W.F. Gattaz, *Diagnosis and biomarkers of predementia in Alzheimer's disease.* BMC Medicine, 2010: p. 89.

50. Sperling, R., et al. *Towards defining the preclinical stage of Alzheimer's disease*. www.alz.org, 2010.

51. Dubois, B., et al., *Research criteria for the diagnosis of Alzheimer's disease: revising the NINCDS–ADRDA criteria.* The LANCET Neurology, 2007: p. 734-746.

52. Cooper, C., et al., *Treatment for mild cognitive impairment: systematic review.* BJPsych, 2013: p. 255-264.

53. Burns, A., *Clinical Review* thebmj, 2009.

54. Humpel, C., *Identifying and validating biomarkers for Alzheimer's disease.* Trends in Biotechnology, 2011: p. 26-32.

55. Petersen, R.C., *Mild Cognitive Impairment.* The New England Journal of Medicine, 2011: p. 2227-2234.

56. Association, A.s., *2015 Alzheimer's disease facts and figures.* Alzheimer's & Dementia, 2015. **11**(3): p. 332-384.

57. Román, G.C., *Vascular dementia may be the most common form of dementia in the elderly*. Journal of the neurological sciences, 2002. **203**: p. 7-10.

58. Chintamaneni, M. and M. Bhaskar, *Biomarkers in Alzheimer's disease: a review.* International Scholarly Research Notices, 2012. **2012**.

59. Sveinbjornsdottir, S., *The clinical symptoms of Parkinson's disease.* Journal of neurochemistry, 2016. **139**: p. 318-324.

60. Samii, A., J.G. Nutt, and B.R. Ransom, *Parkinson's disease.* The Lancet, 2004. **363**(9423): p. 1783-1793.

61. Chintamaneni, M. and M. Bhaskar, *Biomarkers in Alzheimer's Disease: A Review*. ISRN Pharmacology, 2012.

62. *Brain Imaging: What Are the Different Types?* 2011.

63. Valeo, T., *New Brain-Imaging Techniques Help Diagnose Neurologic Conditions*. 2013.

64. Acharya, U.R., et al., *Automated detection of Alzheimer’s disease using brain MRI images–a study with various feature extraction techniques.* Journal of Medical Systems, 2019. **43**(9): p. 1-14.

65. Ledig, C., et al., *Structural brain imaging in Alzheimer’s disease and mild cognitive impairment: biomarker analysis and shared morphometry database.* Scientific reports 2018. **8**(1): p. 1-16.

66. Camacho, V., A, et al., *Amyloid PET in neurodegenerative diseases with dementia.* Revista Española de Medicina Nuclear e Imagen Molecular (English Edition), 2018. **37**(6): p. 397-406.

67. Carlson, M.L., et al., *Simultaneous FDG-PET/MRI detects hippocampal subfield metabolic differences in AD/MCI.* Scientific reports, 2020. **10**(01): p. 1-7.

68. Mueller, A., et al., *Tau PET imaging with 18F-PI-2620 in patients with Alzheimer disease and healthy controls: a first-in-humans study*. Journal of Nuclear Medicine, 2020. **61**(6): p. 911-919.

69. Yiannopoulou, K.G. and S.G. Papageorgiou, *Current and Future Treatments in Alzheimer Disease: An Update*. Journal of Central Nervous System Disease, 2020. **12**.

70. Santos, T.C.d., et al., *Naturally occurring acetylcholinesterase inhibitors and their potential use for Alzheimer's disease therapy*. Frontiers in Pharmacology, 2018. **9**: p. 1192.

71. Marucci, G., et al., *Efficacy of acetylcholinesterase inhibitors in Alzheimer's disease.* Neuropharmacology 2021. **190**: p. 108352.

72. Kabir, M.T., et al., *NMDA receptor antagonists: repositioning of memantine as a multitargeting agent for Alzheimer's therapy.* Current Pharmaceutical Design 2019. **25**(3): p. 3506-3518.

73. Franco, R., et al., *Adenosine A2A receptor antagonists affects NMDA glutamate receptor function. potential to address neurodegeneration in Alzheimer's disease.* Cells 2020. **9**(5): p. 1075.

74. Benito-León, J., et al., *Non-steroidal anti-inflammatory drugs use in older adults decreases risk of Alzheimer's disease mortality.* PLoS One 2019. **14**(9): p. e0222505.

75. Sharma, N. and A.N. Singh, *Exploring Biomarkers for Alzheimer's Disease.* Journal of Clinical and Diagnostic Research, 2016. **10**(7): p. 1-6.

76. Blennow, K. and H. Zetterberg, *Biomarkers for Alzheimer's disease: current status and prospects for the future.* Journal of internal medicine 2018. **284**(6): p. 643-663.

77. Arbaciauskaite, M., Y. Lei, and Y.K. Cho, *High-specificity antibodies and detection methods for quantifying phosphorylated tau from clinical samples.* Antibody therapeutics, 2021. **4**(1): p. 34-44.

78. Dhiman, K., et al., *Cerebrospinal fluid biomarkers for understanding multiple aspects of Alzheimer's disease pathogenesis.* Cellular and Molecular Life Sciences, 2019. **76**: p. 1833-1863.

79. Bjerke, M. and S. Engelborghs, *Cerebrospinal fluid biomarkers for early and differential Alzheimer's disease diagnosis.* Journal of Alzheimer's Disease 2018. **62**(3): p. 1199-1209.

80. Schneider, P., H. Hampel, and K. Buerger, *Biological marker candidates of Alzheimer's disease in blood, plasma, and serum.* CNS neuroscience & therapeutics, 2009. **15**(4): p. 358-374.

81. Henriksen, K., *O′ Bryant SE, Hampel H, et al.* The future of bloodbased biomarkers for Alzheimer′ s disease, 2014. **10**(1): p. 115-131.

82. Rosén, C., et al., *Fluid biomarkers in Alzheimer's disease–current concepts.* Molecular neurodegeneration, 2013. **8**(1): p. 1-11.

83. Schoonenboom, N.S., et al., *Cerebrospinal fluid markers for differential dementia diagnosis in a large memory clinic cohort.* Neurology, 2012. **78**(1): p. 47-54.

84. Simrén, J., et al., *The diagnostic and prognostic capabilities of plasma biomarkers in Alzheimer's disease.* Alzheimer's & Dementia, 2021. **17**(7): p. 1145-1156.

85. Smirnov, D.S., et al., *Plasma biomarkers for Alzheimer's Disease in relation to neuropathology and cognitive change.* Acta neuropathologica 2022. **143**(4): p. 487-503.

86. Marksteiner, J., et al., *Analysis of 27 vascular-related proteins reveals that NT-proBNP is a potential biomarker for Alzheimer's disease and mild cognitive impairment: A pilot-study.* Experimental Gerontology, 2014: p. 114-121.

87. Kim, P.Y., et al., *Identification of plasma Complement C3 as a potential biomarker for neuroblastoma using a quantitative proteomic approach.* Journal of Proteomics, 2014: p. 1-12.

88. Figurski, M.J., et al., *Improved protocol for measurement of plasma β-amyloid in longitudinal evaluation of Alzheimer's Disease Neuroimaging Initiative study patients.* Alzheimer's & Dementia; The journal of Alzheimer's Association, 2012: p. 250-260.

89. Tang, S. and I. Hewlett, *Nanoparticle-based immunoassays for sensitive and early detection of HIV-1 capsid (p24) antigen.* Journal of Infectious Diseases, 2010. **201**(Supplement_1): p. S59-S64.

90. Hung, L.-Y., et al., *Magnetic nanoparticle-based immunoassay for rapid detection of influenza infections by using an integrated microfluidic system.* Nanomedicine: Nanotechnology, Biology and Medicine, 2014. **10**(4): p. 819-829.

91. Cogan, D., et al., *Development of a low cost microfluidic sensor for the direct determination of nitrate using chromotropic acid in natural waters.* Analytical Methods, 2015. **7**(13): p. 5396-5405.

92. Wang, L.-J., et al., *A multichannel smartphone optical biosensor for high-throughput point-of-care diagnostics.* Biosensors and Bioelectronics, 2017. **87**: p. 686-692.

93. Liu, L., et al., *Facile screening of potential xenoestrogens by an estrogen receptor-based reusable optical biosensor.* Biosensors and Bioelectronics, 2017. **97**: p. 16-20.

94. Mariani, S., et al., *A reusable optical biosensor for the ultrasensitive and selective detection of unamplified human genomic DNA with gold nanostars.* Biosensors and Bioelectronics, 2015. **74**: p. 981-988.

95. Rai, M., et al., *Biomedical applications of nanobiosensors: the state-of-the-art.* Journal of the Brazilian Chemical Society, 2012.

96. in *subato.blogspot.co.uk.* 2011.

97. Bhalla, N., et al., *Introduction to biosensors.* Essays in biochemistry, 2016. **60**(1): p. 1-8.

98. Clark Jr, L.C. and C. Lyons, *Electrode systems for continuous monitoring in cardiovascular surgery.* Annals of the New York Academy of sciences, 1962. **102**(1): p. 29-45.

99. Piro, B., et al., *Comparison of electrochemical immunosensors and aptasensors for detection of small organic molecules in environment, food safety, clinical and public security.* Biosensors, 2016. **6**(1): p. 7.

100. Yang, A. and F. Yan, *Flexible Electrochemical Biosensors for Health Monitoring.* ACS Applied Electronic Materials, 2021. **3**(1): p. 53-67.

101. Hara, T.O. and B. Singh, *Electrochemical Biosensors for Detection of Pesticides and Heavy Metal Toxicants in Water: Recent Trends and Progress.* ACS ES&T Water, 2021. **1**(3): p. 462-478.

102. Cho, I.-H., D.H. Kim, and S. Park, *Electrochemical biosensors: perspective on functional nanomaterials for on-site analysis.* Biomaterials Research, 2020. **24**(1): p. 6.

103. Wang, Y., et al., *Electrochemical sensors for clinic analysis.* Sensors, 2008. **8**(4): p. 2043-2081.

104. Grieshaber, D., et al., *Electrochemical Biosensors - Sensor Principles and Architectures.* Sensors (Basel, Switzerland), 2008. **8**(3): p. 1400-1458.

105. Zheng, H., et al., *Label-free electrochemical impedance biosensor for sequence-specific recognition of double-stranded DNA.* Analytical Methods, 2013. **5**(19): p. 5005-5009.

106. Krishnan, S.K., et al., *A review on graphene-based nanocomposites for electrochemical and fluorescent biosensors.* RSC Advances, 2019. **9**(16): p. 8778-8881.

107. Kafi, A. and M.J. Crossley, *Synthesis of a conductive network of crosslinked carbon nanotube/hemoglobin on a thiol-modified Au Surface and its application to biosensing.* Biosensors and Bioelectronics, 2013. **42**: p. 273-279.

108. Kimmel, D.W., et al., *Electrochemical sensors and biosensors.* Analytical chemistry, 2012. **84**(2): p. 685-707.

109. Thévenot, D.R., et al., *Electrochemical biosensors: recommended definitions and classification1International Union of Pure and Applied Chemistry: Physical Chemistry Division, Commission I.7 (Biophysical Chemistry); Analytical Chemistry Division, Commission V.5 (Electroanalytical Chemistry).1.* Biosensors and Bioelectronics, 2001. **16**(1): p. 121-131.

110. Kurkina, T. and K. Balasubramanian, *Towards in vitro molecular diagnostics using nanostructures.* Cellular and molecular life sciences, 2012. **69**(3): p. 373-388.

111. Zhou, L., et al., *Label-free graphene biosensor targeting cancer molecules based on non-covalent modification.* Biosensors and Bioelectronics, 2017. **87**: p. 701-707.

112. Kim, D.J., et al., *Electrical Graphene Aptasensor for Ultra-Sensitive Detection of Anthrax Toxin with Amplified Signal Transduction.* Small, 2013. **9**(19): p. 3352-3360.

113. Pan, L.-H., et al., *An electrochemical biosensor to simultaneously detect VEGF and PSA for early prostate cancer diagnosis based on graphene oxide/ssDNA/PLLA nanoparticles.* Biosensors and Bioelectronics, 2017. **89**: p. 598-605.

114. Tiwari, S.K., et al., *Graphene research and their outputs: Status and prospect.* Journal of Science: Advanced Materials and Devices, 2020. **5**(1): p. 10-29.

115. Lee, C., et al., *Measurement of the elastic properties and intrinsic strength of monolayer graphene.* science, 2008. **321**(5887): p. 385-388.

116. Tiwari, S.K., et al., *Magical allotropes of carbon: prospects and applications.* Critical Reviews in Solid State and Materials Sciences, 2016. **41**(4): p. 257-317.

117. Yang, Y., et al., *Bottom-up fabrication of graphene on silicon/silica substrate via a facile soft-hard template approach.* Scientific reports, 2015. **5**(1): p. 1-7.

118. Geim, A.K. and K.S. Novoselov, *The rise of graphene*, in *Nanoscience and Technology: A Collection of Reviews from Nature Journals*. 2010, World Scientific. p. 11-19.

119. Novoselov, K.S., et al., *Electric field effect in atomically thin carbon films.* science, 2004. **306**(5696): p. 666-669.

120. Ferrari, A.C., et al., *Science and technology roadmap for graphene, related two-dimensional crystals, and hybrid systems.* Nanoscale, 2015. **7**(11): p. 4598-4810.

121. Forsyth, R., A. Devadoss, and O.J. Guy, *Graphene field effect transistors for biomedical applications: Current status and future prospects.* Diagnostics, 2017. **7**(3): p. 45.

122. Huang, P., et al., *Diazonium functionalized graphene: microstructure, electric, and magnetic properties.* Accounts of chemical research, 2013. **46**(1): p. 43-52.

123. Wang, J., et al., *Inverse relationship between carrier mobility and bandgap in graphene.* The Journal of chemical physics, 2013. **138**(8): p. 084701.

124. Hirai, H., et al., *Electron mobility calculation for graphene on substrates.* Journal of Applied Physics, 2014. **116**(8): p. 083703.

125. Sang, M., et al., *Electronic and Thermal Properties of Graphene and Recent Advances in Graphene Based Electronics Applications.* Nanomaterials, 2019. **9**(3): p. 374.

126. Rahman, M.R., et al., *Electrical and Chemical Properties of Graphene over Composite Materials: A Technical Review.* Material Science Research India, 2019. **16**(2): p. 142-163.

127. Mao, H.Y., et al., *Manipulating the electronic and chemical properties of graphene via molecular functionalization.* Progress in Surface Science, 2013. **88**(2): p. 132-159.

128. Chen, M., et al., *Layer-dependent fluorination and doping of graphene via plasma treatment.* Nanotechnology, 2012. **23**(11): p. 115706.

129. Jaiswal, M., et al., *Controlled hydrogenation of graphene sheets and nanoribbons.* ACS nano, 2011. **5**(2): p. 888-896.

130. Georgakilas, V., et al., *Functionalization of graphene: covalent and non-covalent approaches, derivatives and applications.* Chemical reviews, 2012. **112**(11): p. 6156-6214.

131. Tehrani, Z., et al. *Detection of monoclonal antibodies using chemically modified graphite substrates*. in *Sensors, 2010 IEEE*. 2010. IEEE.

132. Teixeira, S., et al., *Label-free human chorionic gonadotropin detection at picogram levels using oriented antibodies bound to graphene screen-printed electrodes.* Journal of Materials Chemistry B, 2014. **2**(13): p. 1852-1865.

133. Tehrani, Z., et al., *Generic epitaxial graphene biosensors for ultrasensitive detection of cancer risk biomarker.* 2D Materials, 2014. **1**(2): p. 025004.

134. Chen, L., et al., *Energy level alignment and charge carrier mobility in noncovalently functionalized graphene.* The Journal of Physical Chemistry Letters, 2013. **4**(13): p. 2158-2165.

135. Lonkar, S.P., Y.S. Deshmukh, and A.A. Abdala, *Recent advances in chemical modifications of graphene.* Nano Research, 2015. **8**(4): p. 1039-1074.

136. Cai, B., et al., *Gold nanoparticles-decorated graphene field-effect transistor biosensor for femtomolar MicroRNA detection.* Biosensors and Bioelectronics, 2015. **74**: p. 329-334.

137. Gutés, A., et al., *Graphene decoration with metal nanoparticles: towards easy integration for sensing applications.* Nanoscale, 2012. **4**(2): p. 438-440.

138. Singh, G., et al., *ZnO decorated luminescent graphene as a potential gas sensor at room temperature.* Carbon, 2012. **50**(2): p. 385-394.

139. Baby, T.T., et al., *Metal decorated graphene nanosheets as immobilization matrix for amperometric glucose biosensor.* Sensors and Actuators B: Chemical, 2010. **145**(1): p. 71-77.

140. Hasegawa, H., et al., *Methods for Improving Aptamer Binding Affinity*. Molecules, 2016. **21**(4): p. 421.

141. Hashemi, P., et al., *Well-orientation strategy for direct immobilization of antibodies: development of the immunosensor using the boronic acid-modified magnetic graphene nanoribbons for ultrasensitive detection of lymphoma cancer cells.* Analytical Chemistry, 2020. **92**(16): p. 11405-11412.

142. Ferreira, N.S. and M.G.F. Sales, *Disposable immunosensor using a simple method for oriented antibody immobilization for label-free real-time detection of an oxidative stress biomarker implicated in cancer diseases.* Biosensors and Bioelectronics, 2014. **53**: p. 193-199.

143. Sam, S., et al., *Semiquantitative study of the EDC/NHS activation of acid terminal groups at modified porous silicon surfaces.* Langmuir, 2009. **26**(2): p. 809-814.

144. Walker, J.M. and R. Rapley, *Molecular biomethods handbook*, in *Probe design, production, and applications*. 2005, Human Press. p. 14-7.

145. Grennan, K., A. J. Killard, and M. R. Smyth, *Physical characterizations of a screen-printed electrode for use in an amperometric biosensor system.* Electroanalysis: An International Journal Devoted to Fundamental and Practical Aspects of Electroanalysis, 2001. **13**(8-9): p. 745-750.

146. Li, M., et al., *Recent developments and applications of screen-printed electrodes in environmental assays—A review.* Analytica chimica acta, 2012. **734**: p. 31-44.

147. DropSens, in *www.dropsens.com*. 2015.

148. Lee, P.T., D. Lowinsohn, and R.G. Compton, *The Use of Screen-Printed Electrodes in a Proof of Concept Electrochemical Estimation of Homocysteine and Glutathione in the Presence of Cysteine Using Catechol.* Sensors, 2014: p. 10395-10411.

149. Ping, J., et al., *Direct electrochemical reduction of graphene oxide on ionic liquid doped screen-printed electrode and its electrochemical biosensing application.* Biosensors and Bioelectronics, 2011. **28**(1): p. 204-209.

150. Gomez, F.J.V., et al., *Screen-printed electrodes modified with carbon nanotubes or graphene for simultaneous determination of melatonin and serotonin.* Microchimica Acta, 2015. **182**(11): p. 1925-1931.

151. Eissa, S., et al., *Electrochemical immunosensor for the milk allergen β-lactoglobulin based on electrografting of organic film on graphene modified screen-printed carbon electrodes.* Biosensors and Bioelectronics, 2012. **38**(1): p. 308-313.

152. Novoselov, K.S., et al., *Electric Field Effect in Atomically Thin Carbon Films.* Science, 2004. **306**(5696): p. 666-669.

153. Bunch, J.S., et al., *Electromechanical Resonators from Graphene Sheets.* Science, 2007. **315**(5811): p. 490-493.

154. Nair, R.R., et al., *Fine Structure Constant Defines Visual Transparency of Graphene.* Science, 2008. **320**(5881): p. 1308.

155. Shi, Y., et al., *Photoelectrical Response in Single-Layer Graphene Transistors.* Small, 2009. **5**(17): p. 2005-2011.

156. Mali, K.S., et al., *Nanostructuring graphene for controlled and reproducible functionalization.* Nanoscale, 2015. **7**(5): p. 1566-1585.

157. Ni, J., M. Quintana, and S. Song, *Adsorption of small gas molecules on transition metal (Fe, Ni and Co, Cu) doped graphene: A systematic DFT study*. Physica E: Low-dimensional Systems and Nanostructures, 2020. **116**: p. 113768.

158. Wang, Y., et al., *Graphene and graphene oxide: biofunctionalization and applications in biotechnology*. Trends in Biotechnology, 2011. **29**(5): p. 205-212.

159. Song, Y., et al., *Recent advances in electrochemical biosensors based on graphene two-dimensional nanomaterials.* Biosensors and Bioelectronics, 2016. **76**: p. 195-212.

160. Wu, L., et al., *Label-free ratiometric electrochemical detection of the mutated apolipoprotein E gene associated with Alzheimer's disease.* Chemical Communications, 2016. **52**(81): p. 12080-12083.

161. Mars, A., et al., *Curcumin-graphene quantum dots for dual mode sensing platform: Electrochemical and fluorescence detection of APOe4, responsible of Alzheimer's disease.* Analytica Chimica Acta, 2018.

162. Azimzadeh, M., et al., *Early detection of Alzheimer's disease using a biosensor based on electrochemically-reduced graphene oxide and gold nanowires for the quantification of serum microRNA-137.* RSC Advances, 2017. **7**(88): p. 55709-55719.

163. Fan, X., et al., *A graphene-based biosensor for detecting microRNA with augmented sensitivity through helicase-assisted signal amplification of hybridization chain reaction.* Sensors and Actuators B: Chemical, 2018. **255**: p. 1582-1586.

164. Panraksa, Y., et al., *Paper-based amperometric sensor for determination of acetylcholinesterase using screen-printed graphene electrode.* Talanta, 2018. **178**: p. 1017-1023.

165. Morales-Narváez, E., et al., *Signal enhancement in antibody microarrays using quantum dots nanocrystals: Application to potential Alzheimer's disease biomarker screening.* Analytical chemistry, 2012. **84**(15): p. 6821-6827.

166. Yoo, Y.K., et al., *A highly sensitive plasma-based amyloid-β detection system through medium-changing and noise cancellation system for early diagnosis of the Alzheimer's disease.* Scientific Reports, 2017. **7**(1): p. 8882.

167. Chae, M.-S., et al., *Enhancing surface functionality of reduced graphene oxide biosensors by oxygen plasma treatment for Alzheimer's disease diagnosis.* Biosensors and Bioelectronics, 2017. **92**: p. 610-617.

168. Lebedev, A., et al., *Graphene-based biosensors.* Technical Physics Letters, 2016. **42**(7): p. 729-732.

169. Chae, M.-S., et al., *Graphene-based enzyme-modified field-effect transistor biosensor for monitoring drug effects in Alzheimer's disease treatment.* Sensors and Actuators B: Chemical, 2018.

170. Bungon, T., et al., *Graphene FET Sensors for Alzheimer's Disease Protein Biomarker Clusterin Detection.* Frontiers in Molecular Biosciences, 2021. **8**.

171. Eda, G., et al., *Blue Photoluminescence from Chemically Derived Graphene Oxide.* Advanced Materials, 2010. **22**(4): p. 505-509.

172. Morales-Narváez, E. and A. Merkoçi, *Graphene Oxide as an Optical Biosensing Platform.* Advanced Materials, 2012. **24**(25): p. 3298-3308.

173. Liu, L., et al., *A graphene oxide-based fluorescent platform for selective detection of amyloid-β oligomers.* Analytical Methods, 2015. **7**(20): p. 8727-8732.

174. Vilela, P., et al., *Graphene Oxide-Upconversion Nanoparticle Based Optical Sensors for Targeted Detection of mRNA Biomarkers Present in Alzheimer's Disease and Prostate Cancer.* ACS Sensors, 2017. **2**(1): p. 52-56.

175. Woo, N., et al., *Enhanced capillary electrophoretic screening of Alzheimer based on direct apolipoprotein E genotyping and one-step multiplex PCR.* Journal of Chromatography B, 2018. **1072**: p. 290-299.

176. Davies, T.J., M.E. Hyde, and R.G. Compton, *Nanotrench arrays reveal insight into graphite electrochemistry.* Angewandte Chemie - International Edition, 2005. **44**(32): p. 5121-5126.

177. Zhao, J., et al., *Efficient preparation of large-area graphene oxide sheets for transparent conductive films.* ACS Nano, 2010. **4**(9): p. 5245-5252.

178. Li, B., et al., *Graphene electrode modified with electrochemically reduced graphene oxide for label-free DNA detection.* Biosensors and Bioelectronics, 2015. **72**: p. 313-319.

CHAPTER 3

MATERIALS AND METHODS

The following chapter describes about the materials and experimental techniques used in this thesis. Surface functionalization and biofunctionalization methods are also discussed. This chapter also focuses on the techniques that were used to assess the surface chemistry of the electrodes, both before and after chemical functionalization. The principles of each methodology are discussed, and the specific methodology used in this thesis is detailed in this chapter.

3.1 MATERIALS

3.1.1 GRAPHENE:

The details of graphene's properties are described in Chapter 2, Section 2.2.7. A flood of reports has been published on graphene in recent years. It is a 2-D carbon material consisting of a one-atom-thick layer of graphite [1]. Graphene is highly considered as the ultimate electrode material as compared to carbon due to its exceptional properties such as large surface area, high electrical conductance, and excellent electrochemical properties such as fast electron rate, wide potential window, and low charge-transfer resistance [2]. Besides, it is a transparent zero-bandgap semiconductor material that can easily be modified with a variety of different functional groups making it a perfect absorbent material [3]. Moreover, the rGO surface can also be chemically functionalized to attach antibodies to its surface [4] which can be achieved by both, covalent and non-covalent modifications. The rGO layer over graphene provides much higher conductivity than on other materials such as carbon. Along with that rGO and graphene coupling also offer a large number of available active sites which is highly required for biosensing applications [5].

3.1.2 GLASSY CARBON (GC):

Glassy Carbon (GC) has been extensively studied since it was first produced in the early 1960s. GC is a glass-like carbon that has gathered a lot of attention for electroanalytical and electro-catalytic measurements owing to its manifest bulk characteristics for instance its numerous physical properties as well as the spatial ordering of chemical bonds and the versatility of carbon [6].

In order to obtain the reproducible electrode surface, GC is usually pre-treated either electrochemically or mechanically. Electrochemical pre-treatment is normally achieved by CV scanning over a wide potential range. And mechanical polishing is mostly performed by polishing the GC electrodes using a micro-fabric cloth with 1, 0.3 or 0.05 µm particle size or even finer alumina slurry or diamond paste, followed by sonication in an appropriate solvent to remove the alumina or the diamond paste. In this thesis, the mechanical pre-treatment method was used to prepare GC surfaces prior to functionalization.

3.2 EXPERIMENTAL METHODS

3.2.1 SURFACE FUNCTIONALIZATION TECHNIQUES:

In each chapter of this thesis, a different functionalization method was developed and used for biosensor fabrication. Therefore, the in-depth experimental methodology of each functionalization method is discussed in detail in the relevant chapters.

3.2.1.1 Electrochemical Functionalization:

In this work, three electrochemical functionalization processes have been developed for the surface modification of electrodes. These processes lead to the amino termination of GC and graphene electrode surfaces. The amino group can consequently be used to attach the biomolecules to the electrodes (as discussed in Chapters 4 and 5). The chemical functionalization mechanism of these processes is discussed below.

3.2.1.1.1 Diazotisation:

Diazonium salts are regarded as one of the most commonly used compounds to functionalize carbon nanotubes, glassy carbon electrodes, and graphene [7, 8]. This in turn leads to the formation of the covalent bond between the carbon/graphene and an aryl group of diazonium. Diazonium salts are found to be chemically unstable, so there is a great need of controlling the reagents and reaction conditions especially the temperature and the light exposure must be controlled. This chemical instability is considered the limitation of this method.

In order to generate the reactive intermediates with the help of the aryldiazonium salts, there are a variety of techniques that have been used including electrochemical reduction [9-11], thermolysis [12], photolysis [13] and chemical reduction [14, 15]. These processes lead to the formation of cationic species or aryl radicals. These reactive intermediates form the covalent bonds as a result of reacting with the carbon surface. For instance, various aryldiazonium salts yield an aryl radical intermediate and dinitrogen gas when electrochemically reduced in the non-aqueous electrolyte solution like acetonitrile which contains 0.1 M tetra alkyl ammonium salts. Subsequently, these electrogenerated aryl radicals result in bonding to the carbon electrode surface by forming the covalent bond [10] (**Figure 3.1**).

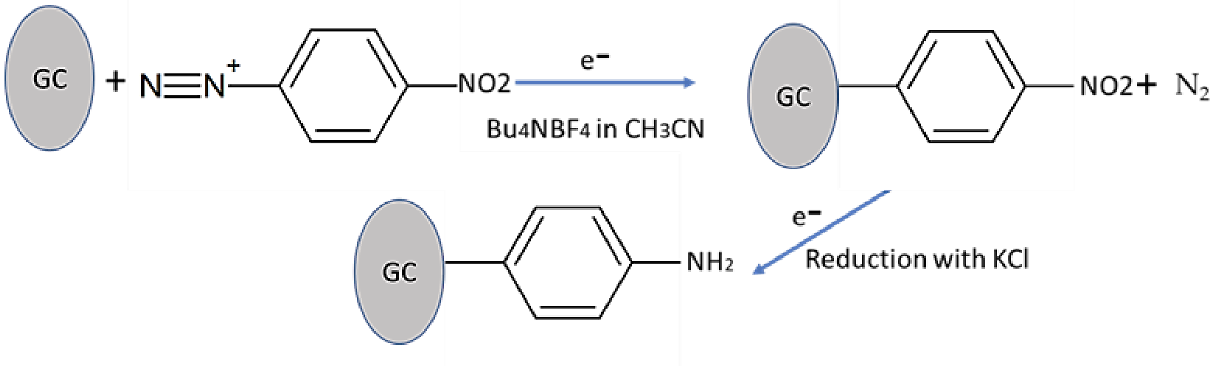

Figure 3. 1: Electro-grafting of 4-nitrobenzenediazonium tetrafluoroborate salt.

A lot of electrodes have been reported that undergo successful modifications using this method, this includes carbon fibre or powder [9], highly ordered pyrolytic graphite (HOPG) [9, 16], and screen-printed graphite electrodes [17] and glassy carbon [18-21].

Various factors can influence the modification process of carbon substrates via the process of electrochemical reduction of aryl diazonium salts. These factors include electrolysis time and applied potential [22, 23], electronic nature and concentration of the diazonium salt [24], the type of the solvent used, and the type of the carbon material [21, 25]. While on the other hand, in this method controlling the extent of the reaction becomes challenging because of the high reactivity of aryl diazonium salts during the functionalization process of the surfaces. Surface-grafted aryl groups are observed to be attacked by aryl radicals which in turn leads to the formation of multi-layers and also to multiple attachments [26, 27].

In our work, we reported for the first time the quantification of the electrochemical conversion of 4-nitrophenyl groups to the aminophenyl groups. Quantification of the amine group coverage over the GC electrode substrate was performed by measurement of electron transfer during electrochemical addition of ferrocene carboxylic acid (FCA) to aminophenyl groups. Full details of the diazotisation of GC electrodes and their characterization are presented in Chapter 4.

3.2.1.1.2 Electropolymerization of 1,5-Diaminonapthalene (DAN):

A significant amount of research has been done on the conductive π-stacking polymers for the electrochemical applications including electrochemical sensing. Much attention has been gained by the aromatic polymers like polypyrrole, polyaniline, and polythiophene [28].

Polymers that are made from aromatic amines are appealing for the biosensor’s applications due to the reason that they provide the amine functional groups thus allowing for the attachment of bio-receptors to the surface of the sensor. Previously reported aromatic amines utilized for the development of the electrodes coated with the polymeric film include o-aminophenol [29, 30] and o-phenylenediamine [31, 32].

However, for the first time in 1989 electrochemical polymerization of 2,3-diaminonapthalene (2,3-DAN) and 1,8-diaminonapthalene (1,8-DAN) was reported by Oyama et al., for the development of polymeric film coated electrodes [33]. After that in 1995, Jin et al. demonstrated the polymerization of 1,5-diaminonapthalene (1,5-DAN) onto the GC electrode [34]. This preliminary polymerization of pDAN was directed to various studies which utilized pDAN-coated electrodes [35]. The electropolymerization took place in an acidic solution of 0.1 M hydrochloric acid that led to the oxidation of monomers at positions 1- and 5-, which then resulted into the crosslinking of monomers in a ladder-like formation presented in Figure 3.2 [34].

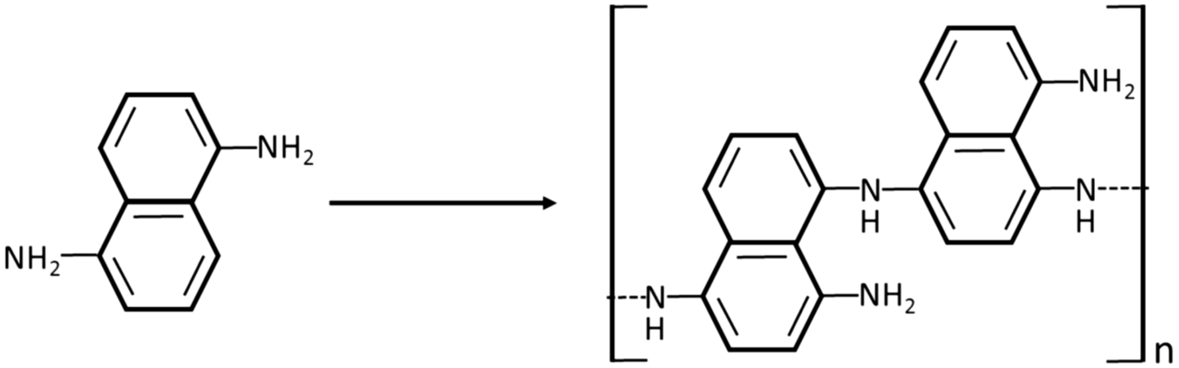

Figure 3. 2: A schematic representation of the polymerization of 1,5-DAN monomers into polymer DAN.

Electropolymerized DAN has the potential to be used for enhancing the performance of electrochemical biosensors [35]. Therefore, for the development of electrochemical biosensors for many disease applications, pDAN has been extensively used. For instance, a pyrolytic graphite biosensor modified by pDAN was developed by Goyal et al. The sensor device was able to detect paracetamol, aspirin, and caffeine in the nM range [36]. Moreover, a study reported in

2017 utilized pDAN for detecting the cancer antigen CA 15-3 via developing the nanowires which consist of a pDAN/polypyrrole bilayer [35].

In our work, Polymer DAN has been used for the development of an electrochemical immunosensor based on graphene-modified screen-printed electrodes (SPGEs) for highly sensitive and selective detection of Alzheimer's biomarker Aβ(1-42). The full biosensor fabrication, electropolymerization, and characterization details are described in Chapter 5.

3.2.1.1.3 Functionalization via Neutravidin Attachment:

Avidin, streptavidin, and neutravidin have similar structural and functional properties enabling them to bind with the biotin with very high binding affinity. Avidin is obtained from the eggs of the oviparous vertebrates [37], while streptomyces avidin is the source of obtaining the streptavidin. Neutravidin is the chemically modified form of avidin which is without glycosylation. The physical and chemical structures of all of them are different, despite having a similar tetramer molecular structure as well as biotin-binding affinity. Therefore, avidin analogs are frequently exploited in the areas of biotechnology and nanotechnology, relying on their special chemical and physical features [38]. Neutravidin protein with the mass of 60,000 Daltons is yielded by eliminating the glycosylation from avidin. Biotin-binding affinity is maintained while carbohydrate-based lectin binding is lowered to extremely low levels.

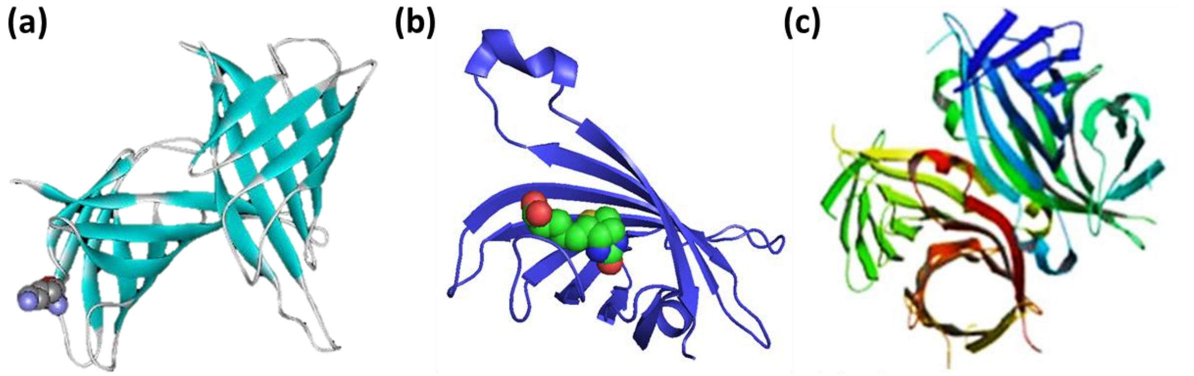

Figure 3. 3: Ribbon diagram of (a) avidin structure with bound biotin (spheres) (b) monomeric streptavidin with bound biotin (c) tetrameric structure of neutravidin.

Neutravidin has the advantage of balanced pI, which reduces inappropriate adsorption, as well as lysine residues that can be used for derivatization or the other tailored conjugation. Neutravidin is regarded as the most beneficial as it produces the lowest nonspecific binding as compared to all other well-renowned biotin-binding proteins. The specific activity of neutravidin for binding biotin is close to a theoretical maximum activity which is around 14 µg/mg of the protein. The pI slightly becomes acidic for the streptavidin and neutravidin in the case when carbohydrates are not present (pI ~10), and it helps to avert the nonspecific binding property of avidin. The positive charge at the physiological pH is due to the higher level of pI of avidin. Also, this higher pI is responsible for the non-specific binding with the negatively charged surfaces and molecules which may include the silica and cell membrane [39]. Avidin, neutravidin, and streptavidin represent the positive cooperativity which means that they have the positive affinity for the biotin explained by both Zhao et al and Nguyen et al, and also the affinity has the increasing order of avidin<streptavidin<neutravidin [39, 40].

Neutravidin’s nearly neutral charge prevents it from interacting with nonspecific proteins. In the techniques like ELISA, western blot, and IHC applications which require the biotin-binding probes, purified neutravidin performs exceptionally well with greater specificity, sensitivity, and signal-to-noise ratios as compared to streptavidin, which is much more costly.

In this thesis, neutravidin protein was used to attach on to the rGO modified screen printed electrodes. Neutravidin attachment provided the four biotin-binding sites per neutravidin protein attached to the surface. Furthermore, biotinylated antibodies were also used for the specific attachment of antibodies over the neutravidin-modified sensor surface. This was done in order to achieve high signal amplification and low limit of detection by achieving the accurate orientation antibody immobilization that promotes a great step forward in attaining ideal immunosensor performance. For that purpose, EDC/NHS was used to activate the carboxylic groups present on the rGO surface. Neutravidin protein utilizing its amine groups (e.g., lysine residues) [41] was then covalently attached to the rGO surface via amide bond formation also known as carbodiimide crosslinking chemistry. The detailed fabrication and functionalization mechanism of an impedimetric biosensor is discussed in chapter 6.

3.2.2 BIOFUNCTIONALIZATION TECHNIQUE:

In order to functionalize the electrode surface with a bioreceptor selective for the target analyte the carbodiimide cross-linking was performed. As already discussed in Section 2.3.3.3, the main purpose of carbodiimide cross-linking is to immobilize the bioreceptor to the surface of the sensor and this is usually achieved by the formation of a stable bond between the bioreceptor and the amine-functionalized graphene surface (**Figure 3.4**). In this thesis carbodiimide cross-linking

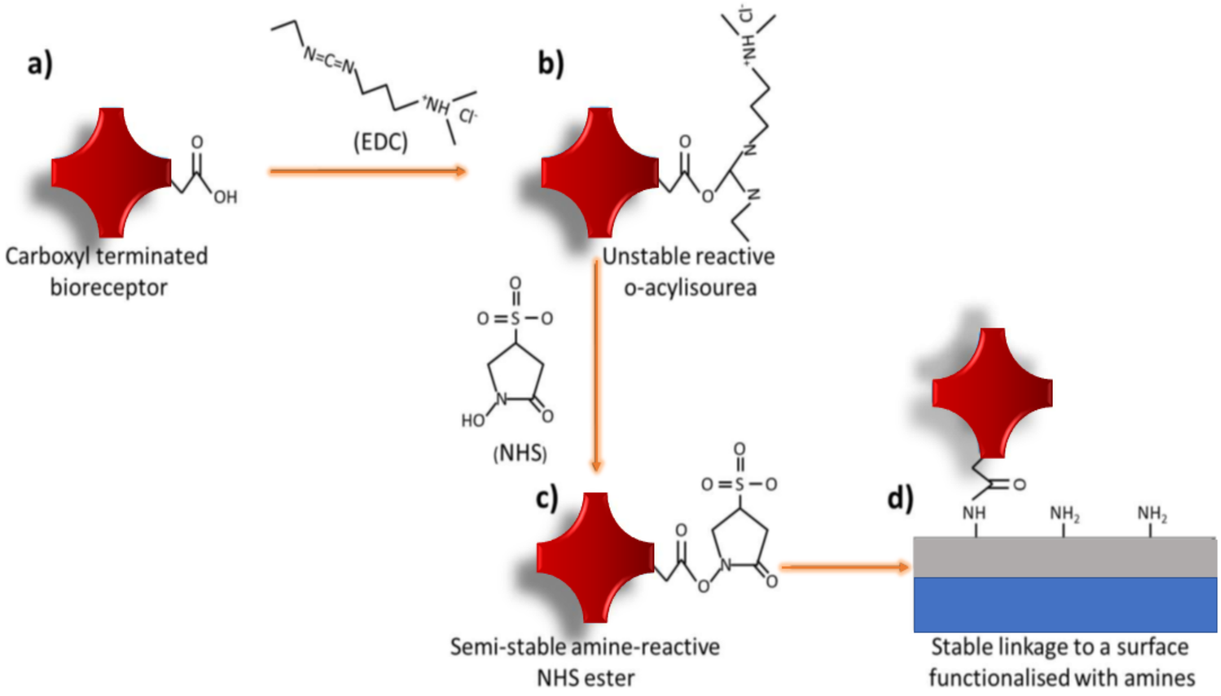

Figure 3. 4: Schematic interpretation of carbodiimide crosslinking of bioreceptor to the surface of sensor utilizing EDC/NHS activation method to attach to the amines. (a) A bioreceptor (carboxyl terminated) is reacted to EDC and form an intermediate product (b) that is an unstable reactive o-acylisourea. (c) The substitution between EDC and the NHS to create a stable NHS ester takes place. (d) which reacts with amine group on the surface of sensor to create a stable link in form of an amide bond.

was also used to attach the carboxylic groups on the rGO surface with amine groups (lysine residues) of neutravidin protein as discussed in section 3.2.1.1.3.

Although each chapter focuses on a different application, the biofunctionalization techniques are described in-depth within every chapter as needed.

3.2.3 CHARACTERIZATION TECHNIQUES:

3.2.3.1 Scanning Electron Microscopy (SEM):

In 1965, Scanning electron microscopy (SEM) emerged as a commercially available technique. SEM is a surface characterization methodology that provides a beam of electrons to examine the specimen's exterior. Condenser lenses are utilized to focus the electron beam which is emitted by the cathode gun with specified voltage and energy usually between 0.1 keV to 50 keV [42]. SEM has the magnification ability of up to 1,000,000x due to the short electron wavelength which is usually between 0.027 and 0.0009 nm depending on the applied voltage and energy. This magnification is significantly more than the 1,000x magnification capacity of a standard light microscope [43]. Additionally, SEM is capable of having a high-resolution range of up to 1 nm due to the short wavelength of electrons it has. Moreover, 3-D information of the sample can also be achieved by using SEM which is due to the large depth-of-field attained by using the electrons [44]. Therefore, useful information about the surface properties, including the topology of surface functionalization can be obtained by SEM [43]. The essential components of SEM include the electron gun, the lens system, the electron collector, and the visual and recording cathode ray tubes (**Figure 3.5**) [44].

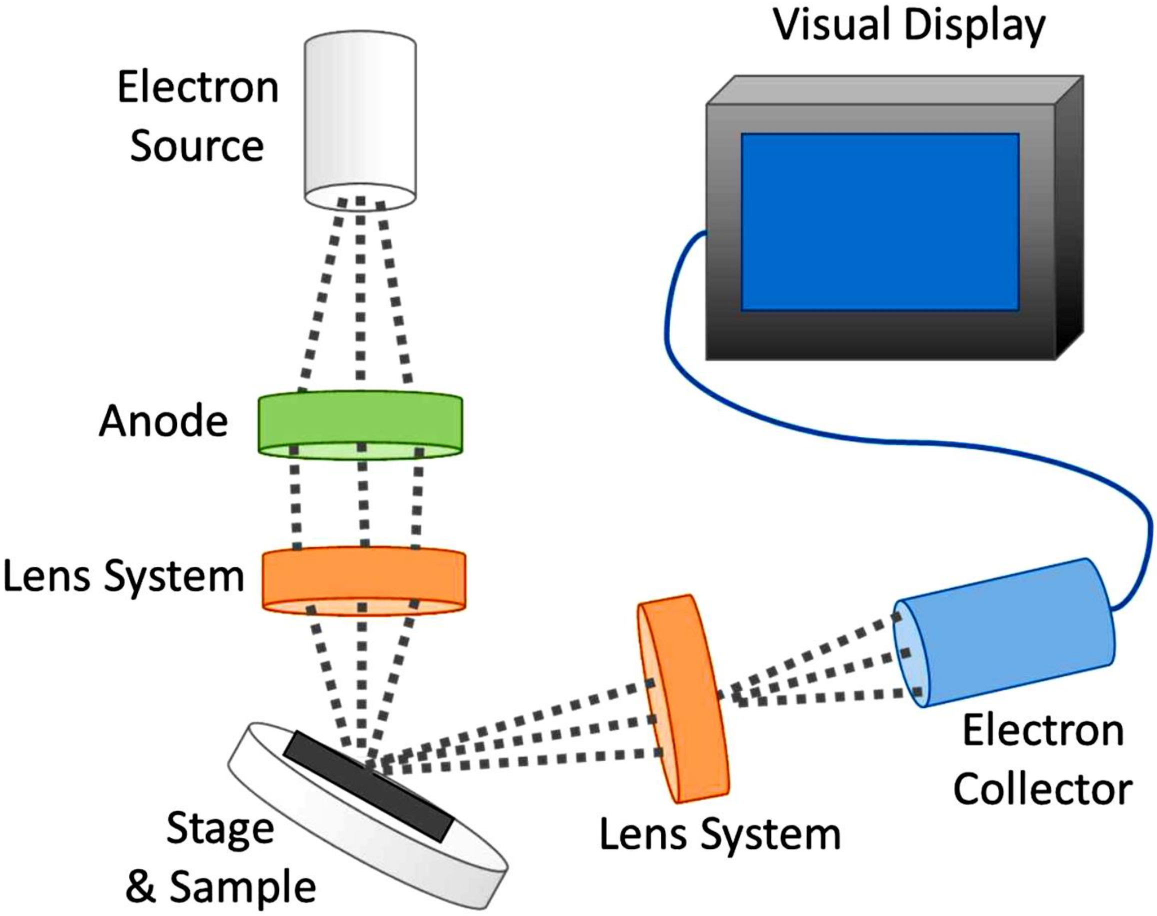

Figure 3. 5: A schematic representation of Scanning Electron Microscopy (SEM).

Electronic acceleration at the surface results in the detection of secondary electrons emitted from the substrate surface which in turn produce the scanning electron micrograph of the substrate surface. Scanning of the primary electron beam across the surface of the substrate is done in a raster pattern. Besides this scanning is done under the vacuum ranging from 10^{-4} - 10^{-8} Torr. Electrons interact with the atoms which are near or at the surface of the sample and this results in the emission of secondary or backscattered electrons. Specialized detectors are then utilized to detect the emission of these secondary electrons. Therefore, the highly morphological three-dimensional representation of the sample surface can be obtained as a result of using the detectors as they map the sample surface with the help of the secondary electrons.

In this thesis, SEM analysis was utilized to obtain the micrographs to see the topological changes before and after the functionalization of HOPG and graphene substrates in Chapters 4 and 6. SEM analysis was carried out using the Hitachi FE-SEM S-4800 scanning electron microscope. This SEM equipment has the highest resolution of 1.4 nm. A low acceleration voltage of around 10 kV and 20 mA emission current was applied in order to prevent the damage caused to the sample surface through the bombardment of the electrons.

3.2.3.2 Atomic Force Microscopy (AFM):

By integrating the principles of the stylus profilometer with the scanning tunnelling microscope, Binning et al. originally presented a new microscopic technique called the atomic force microscopy (AFM) in 1985. It was launched as an innovative microscopic technique that was proficient in atomic resolution [45]. Ever since its inception, atomic force microscopy was being used for a variety of purposes, one of the most common is the imaging of the topography of the sample surface at the nanometer scale [46]. The fundamental components of AFM consist of a cantilever, a probe tip, a controller, a scanner and a signal processing unit as shown in **Figure 3.6**.

AFM technique utilizes the probe which is a sharp tip present at the end of the cantilever to scan the surface of the sample. Scanning is done in a raster (line by line) pattern with the constant spacing which in turn delivers the information about the probe's height at every point. This procedure is done in two different directions, the tracing and retracing which results in the formation of a 3-D illustration of the surface of the sample via the tip interactions with the substrate surface. When the cantilever is held close to the sample's surface i.e., in the nanometre range, there are forces generated between the surface of the sample and the cantilever. Which in turn results in the formation of a three-dimensional image of the sample surface. As the scan progresses, the cantilever is deflected in response to the topological variations present at the

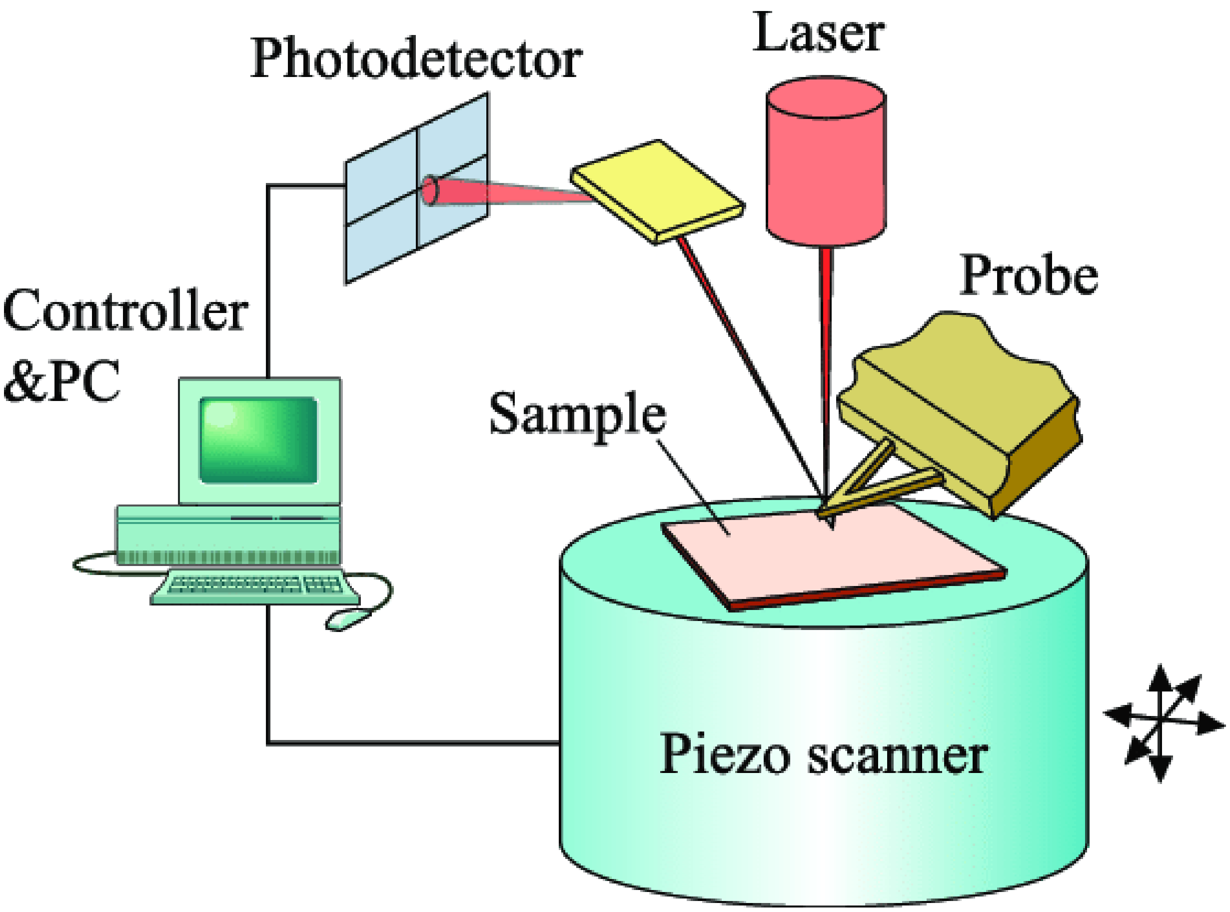

Figure 3. 6: A schematic representation of an Atomic Force Microscopy (AFM) apparatus.

surface of the specimen. A laser fixated on the cantilever detects individual deflections and converts them together into a three-dimensional representation.

There are two different operational modes according to which the AFM operates. The modes depend on the interaction among the surface of the substrate and the tip as well as depend on the way the cantilever is scanning across the surface. These modes are referred to as the dynamic or tapping (AC) mode and the static (DC) mode. As the name indicates during the AC imaging the oscillations occur at the cantilever either with a specific frequency or specific amplitude, while on the other hand the in the DC mode the cantilever is static and there are no vibrations [47].

In this thesis, AFM was performed using a JPK Nanowizard II AFM (Berlin, Germany) with JPK SPM 34 controller, in an intermittent contact mode with the tip resonant frequency, spring constant and the nominal radius of 320 kHz, 40 N/m, and 8 nm, respectively. N-doped silicon tips and Bruker NCHV probes were utilized to obtain the images. Additionally, the JPK data processing software was utilized for data representation and for determining the cross-sectional height profile and RMS value of the HOPG and graphene SPE samples before and after the surface functionalization.

3.2.3.3 Raman Spectroscopy:

Raman spectroscopy is extensively utilized in order to gain a better knowledge and understanding of the graphitic samples. Raman typically presents the structural information of the specimens. In the case of graphene-based samples, it is frequently utilized to offer an understanding of phonon and electron dynamics well within the sample as well as the structural knowledge [48]. Non-destructive analysis of structural and electrical characteristics of graphitic surfaces is possible with Raman spectroscopy.

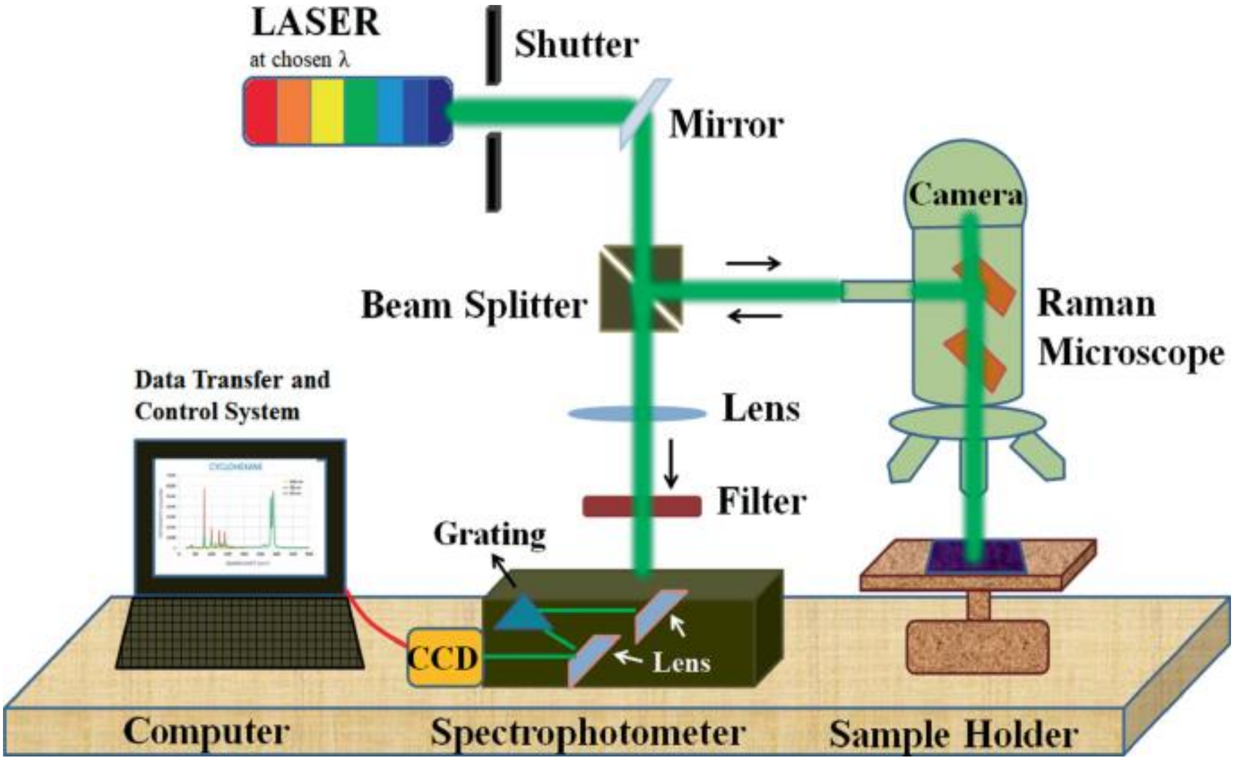

Figure 3. 7: A schematic representation of a Raman Spectrometer [50].

Furthermore, Raman's data presents an in-depth understanding of the chemical bonding of functional groups, graphene's electronic behaviour, and structural damage, and also delivers the information about the chemical modifications [49]. A typical Raman spectrometer comprises of the following parts: the laser, the mirrors for deflecting the laser, gratings, and a CCD detector as shown in **Figure 3.7** [50].

The laser provides the monochromatic light beam which is directed to the surface of the sample. The process called Raman scattering occurs when the beam of light reaches and spreads on the surface. Raman scattering is also called as an inelastic scattering process. A very few photons normally 1 in 100, as a result of dissipating through the vibrational modes of the molecules present at the surface of the substrate, generate the phonons. The majority of the remaining electrons are scattered back elastically by the process known as Rayleigh scattering. Therefore, Raman scattering generates the Raman spectrum which according to the characteristics of the sample is specific to the sample [48].

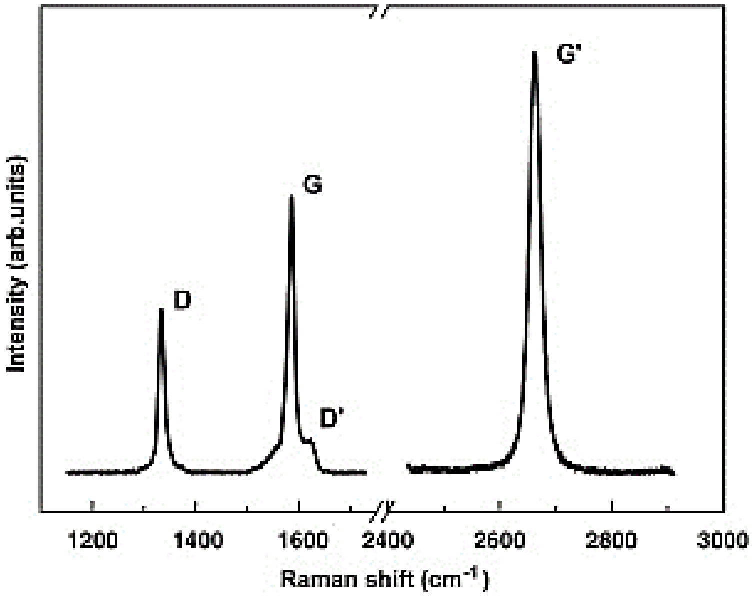

Figure 3. 8: Raman spectrum for graphene showing the G, G'(2D) and D bands.

The three distinctive characteristics of graphene's Raman spectrum are the G, D, and 2D or G' bands. In the Raman spectrum of the monolayer graphene, the two most prominent peaks of the G band and 2D or G' bands appear at about 1560 cm^{-1} and 2700 cm^{-1} respectively [48]. **Figure 3.8** shows the G band in the spectrum that arises from the bonds stretching amongst the paired sp^{2} atoms in graphene's carbon rings, where also the first order Raman scattering occurs [51].

Inelastic scattering of two photons occurs during the process as shown in **Figure 3.9**. In **Figure 3.8**, the G' band is linked to the second-order Raman scattering, which is induced by two phonon-related processes causing the inelastic scattering (**Figure 3.9**) [48]. While as a consequence of the double-resonance process, the D band is generated at 1360 cm^{-1} shown in **Figure 3.8**. At this point, a phonon within the substrate causes the inelastic scattering and the elastic scattering is caused by the defect in the substrate (**Figure 3.9**). The prerequisites that result in the existence of a D peak include the scattering of the electron/phonon, the electron-hole pair excitation, electron-hole recombination, and the defect scattering. Therefore, the D peak tells the information about the damage level or defective regions inside the graphene layer. As the G peak represents the sp^{2} bonding of the carbon atoms of graphene, the ratio of I(D) and I(G) provides the comparison of sp^{2} bonding to sp^{3} bonding and reveals the level of sp^{2} bonding. Hence for

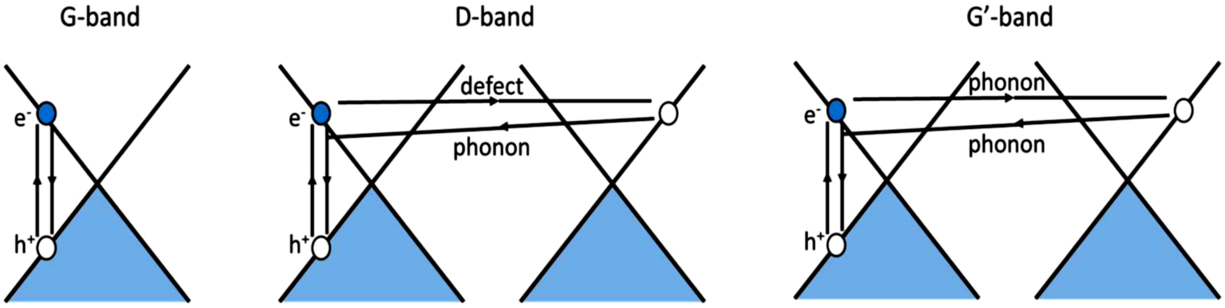

Figure 3. 9: An illustration of Raman process inside graphene chemical structure. First order process forms the G band and second order process also called as double resonance proce forms D and 2D or G' band. D band is created via elastic scattering from a defect and inelastic scattering from a phonon. 2D or G' band is created via inelastic scattering of two phonons.

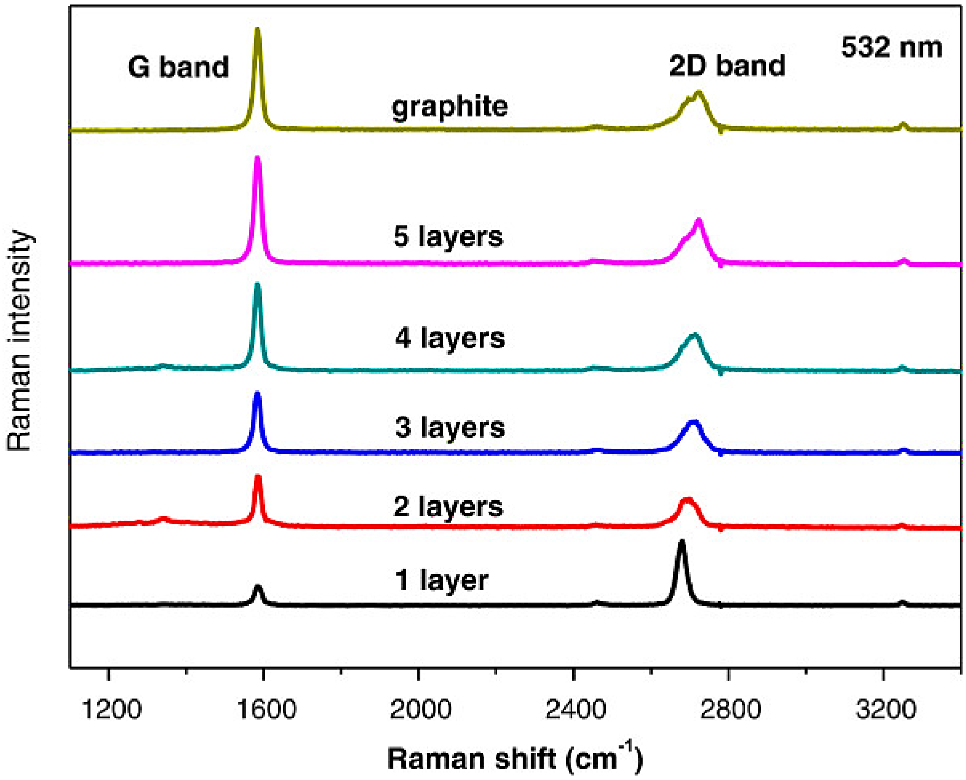

Figure 3. 10: A typical Raman spectra of graphene samples showing change in peaks with increasing the number of graphene layers and also includes Raman spectra of graphite.

comparing the samples at different states, this ratio offers a quantitative and qualitative value. The comparison of the pristine graphene with functionalized graphene can be taken as an instance of the situation [51].

Moreover, based upon the variations in the Raman spectra generated, Raman spectroscopy allows a faster and non-destructive approach for estimating the number of layers of graphene sheets available. The evident differences are observed between the 2D and G bands of the Raman spectra of graphite and single-layer graphene (SLG). A sharp and the symmetrical 2D band for single-layer graphene (SLG) is detected. On the other hand, for graphite typically a broader 2D band is seen. Mostly two peaks are observed for graphite as shown in **Figure 3.10** [52]. Whenever two or even more graphene sheets are layered, such difference is produced by the dispersion of π electrons across them [53].

Moreover, **Figure 3.10** shows that as the number of layers of graphene increases, the intensity of the G band also intensifies in a linear pattern [54]. This is because of the reason that the number of carbon atoms increases as the number of layers of graphene increases, hence the layer thickness of a graphene sample can be calculated by merging the analysis of the 2D band and the G band [52, 54].

In this thesis, the Renishaw inVia Reflux Raman spectrometer was used to perform the Raman spectroscopy. An excitation laser of 532 nm at the power of 2mW was used. The $I_{(D)}/I_{(G)}$ ratio was then used to measure the disorder inside the graphene.

3.2.3.4 X-ray Photoelectron Spectroscopy (XPS):

In the mid-1960s for the first time, the X-ray photoelectron spectroscopy (XPS) which is also known as electron spectroscopy for chemical analysis (ESCA) was established [50]. Ever since this spectroscopy becomes a well-known technique for chemical characterization of the sample substrates [55]. XPS provides a comprehensive elemental analysis of the material and hence as a powerful tool it aids in comprehending the chemical makeup of a variety of materials, and it also provides insights related to the chemical bonding inside the sample. Therefore, to explain and plot the chemical moieties present at the surface of the substrate the surface analysis via XPS can be performed. The surface of the sample is exposed to the monoenergetic soft X-rays under specific vacuum conditions, which results in the emission of electrons from the atomic orbitals of the reactive chemical species involved in the process. A hole is generated in the core level of the atom because of the ionization of the sample which is the cause of this whole process. The hole is generated due to the excitation of an electron to the surface. The Auger decay process where an emission or photoemission of the electrons occurs when an excited electron-ion relaxes back to its initial position is detected [56]. According to Einstein's law, the electrons that are emitted consist of a characteristic binding energy given by equation 3.1.

$$E_\mathrm{k} = h\nu - E_\mathrm{b} \qquad \textbf{(3.1)}$$

Where (E_k) represents the kinetic energy, hν denotes the incident radiation energy and E_b shows the binding energy. Kinetic energy is considered the measured characteristic of the discussed technique [55].

The binding energy can thus be determined in terms of the kinetic energy of the electron that is detected. Since each molecular orbital and biochemical condition have multiple binding energies, this binding energy is unique per each component and chemical context [56].

Chemical shifts that are observed on the spectra and which are away from the binding energy of the original element greatly aided in distinguishing the distinct chemical states. These chemical shifts are the result of a chemical bonding of the core atom. For instance, bond formation between the oxygen or fluorine the electronegative atoms, with the carbon atoms causes an increase in the binding energy of the carbon atom. The increase is due to the carbon atom's electrons which are drawn away from the electronegative atoms. Hence, the higher energy is required to release those electrons. Multiple peaks are formed for one element as a result of the chemical shift. This can be shown with an example that for diverse carbon environments, the carbon peaks can form various peaks such as C–O (286 eV), C=O (289 eV), C–C (284.8 eV), and many more. Consequently, both quantitative and qualitative evaluations of elements at the surface of the sample can be obtained through X-ray photoelectron [56]. The released electrons' intensity versus their respective kinetic energy collectively generates the resulting spectrum of XPS.

There are huge databases available that contain the information about the binding energies for chemical and elemental species. This then allows for the characterization of the surface chemistry of the samples.

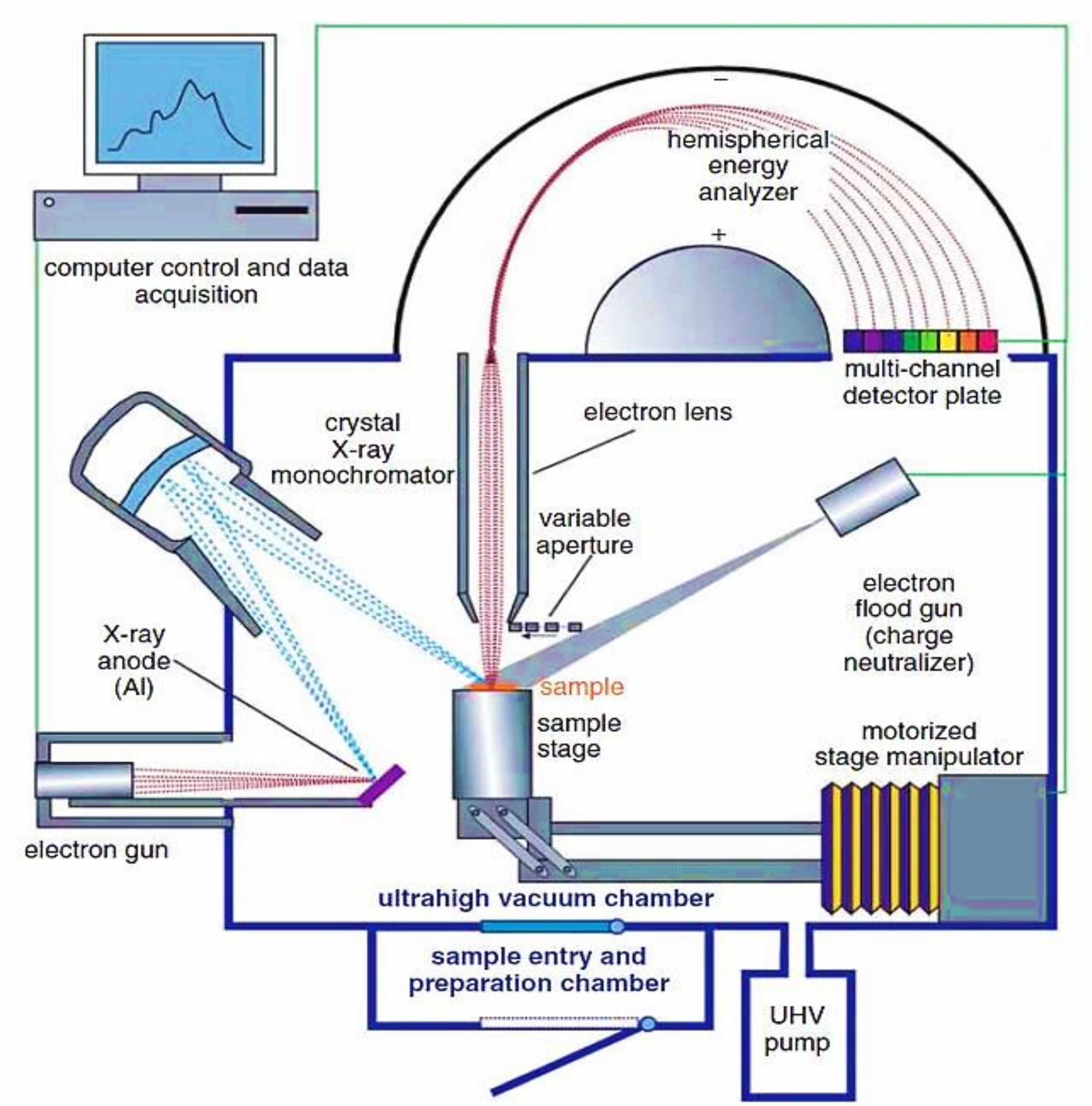

Figure 3. 11: A schematic representation of X-ray photoelectron spectroscopy (XPS) instrumentation.

Furthermore, combined with the method's surface sensitivity, which is attributable to the technology's modest penetration depth of 1–20 nm and low energy of the X-rays, makes XPS the first most useful, and easily understandable quantitative approach for surface chemistry analysis. [57]. The XPS comprises of the following key components; first, the X-ray sources are regarded as the main and vital components of the XPS (**Figure 3.11**). This technique mainly utilizes the

X-rays from various sources including the aluminium or the magnesium sources or might be excluded from the monochromatic aluminium source with an energy of the 1489.7 eV.

To generate the X-rays the magnesium or the aluminium sources are bombarded in the X-ray tube with the electrons. An adequate vacuum environment is required for the procedure, so the pumping system is also utilized during the process. The last most substantial components of the X-ray photoelectron spectrometer include the electron energy analyzer or spectrometer and the electron detector. Chemical insight about the surface of the sample can be obtained with the help of these key components as they aided in determining the kinetic energy of the electrons emitted from the sample's surface [55].

In this thesis presence of amine functional groups at the graphene/ rGO surface after chemical modification was confirmed via using the XPS technique. This spectrographic analysis was accomplished with the help of the AXIS Supra instrument from Kratos Analytical running the ESCApe software. All the experiments were performed under an ultra-high vacuum of the order of magnitude 10^{-9} Torr. The wide scan was obtained between the binding energies from 0 to 1200 eV. Finally, CasaXPS software was used to perform the data analysis and data fitting.

3.2.3.5 Electrochemical Characterization:

All the electrochemical techniques primarily consist of an electrode and the charge (electrons) transfer between the oxidants (O) and the reductants (R) within the electrode (equation 3.2). In addition, Nernst equation is used for better understanding and characterization of all electrochemical reactions (equation 3.3).

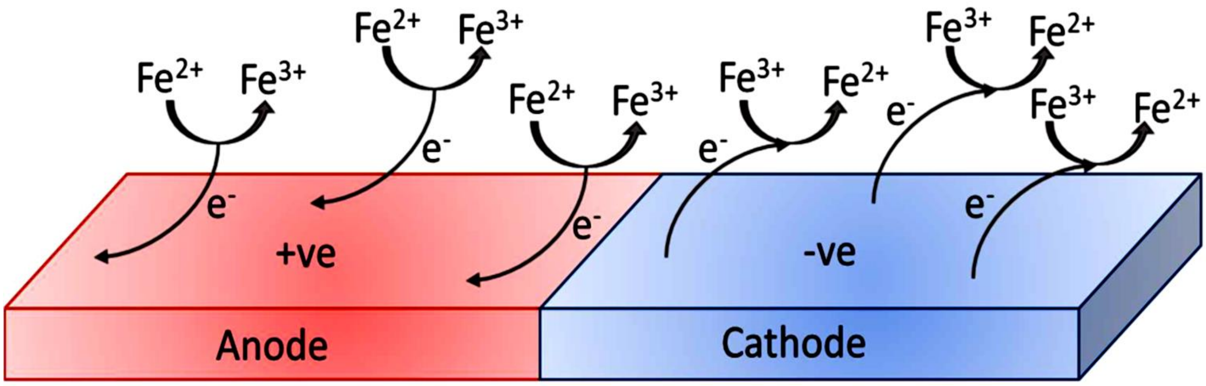

Figure 3. 12: A schematic illustration of the reactions occurring at the electrode surface. The redox couple used here is ferricyanide and ferrocyanide ($[Fe(CN)_6]^{3-}/[Fe(CN)_6]^{4-}$) as the oxidant and reductant species.

The relation between the electrode surface potential and the concentration of reduced and oxidized species can be addressed with the help of the Nernst equation.

$$O + n\bar{e} \leftrightarrow R \tag{3.2}$$

$$E = E^{\circ\prime} + \frac{RT}{nF}\ln\left(\frac{C_O}{C_R}\right) \tag{3.3}$$

Where, the redox potential of the redox species is symbolized by $E^{\circ\prime}$, it can be characterized as the redox couple used throughout the experiment whereas, at the electrode surface, the concentration of the oxidized and reduced species is represented by C_O and C_R [58].

For this thesis redox couple ferricyanide and ferrocyanide ($[Fe(CN)_6]^{3-}/[Fe(CN)_6]^{4-}$) was used which is referred to as Fe^{2+}/Fe^{3+}. In this redox couple when the more positive potential is applied to the electrode it oxidizes the ferrocyanide to ferricyanide and the electrode behaves as an anode. In the opposite case, when a more negative potential is applied to the electrode it reduces the ferricyanide to ferrocyanide and in this case, the electrode behaves as a cathode.

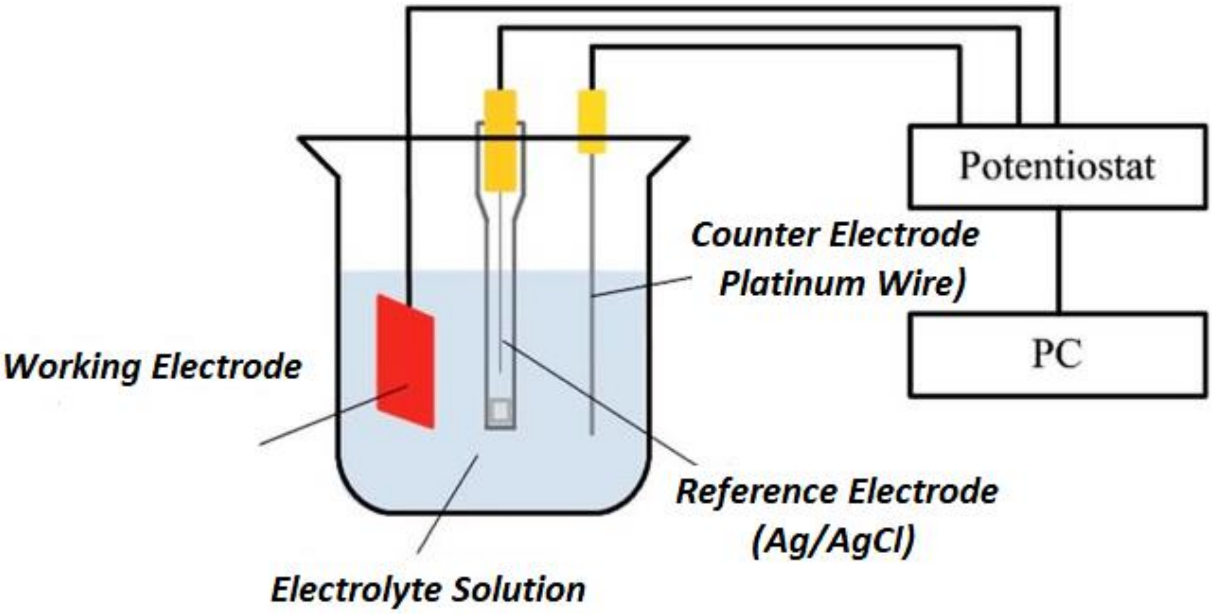

Figure 3. 13: A schematic illustration of the setup of three-electrode electrochemical cell, in the case of this thesis the WE is the graphene based SPE, silver/ silver chloride (Ag/ AgCl) is used as RE, and Platinum wire is used as the CE. A potentiostat controls the electrochemical cell, and the visual display unit the PC presents the resulting graphs.

Generally, an electrochemical analysis system consists of the three electrodes as shown in **Figure 3.13**, the working electrode (WE), the reference electrode (RE), and the counter electrode (CE). Potentiometry and Amperometry are the two main electrochemical measurement techniques that are normally utilized to characterize the sample. Potentiometry is the type of measurement where the potential that is developed between the electrodes is measured and amperometry is referred to as the measurement which mainly focuses on the flow of current amongst the electrodes.

3.2.3.5.1 Potentiometry:

A wide range of the analytical techniques comes under the term potentiometry. All the techniques measure the working electrode's potential which is controlled with respect to the reference electrode and is referred to as the reference point [59]. In this way without passing any current over the working electrode, its potential can be measured. Reference electrodes are selected based on their substantially recognized equilibrium potential and their firm stability. Consequently, the materials that can be utilized as REs are constrained. The silver and silver chloride electrodes are considered as most utilized electrodes [60]. The counter electrode provides the path for current flow through the circuit and therefore an essential part to complete the electrical circuit. It can be seen that the working of counter electrodes is different compared to the working electrode. For instance, whenever the working electrode behaves as a cathode then the counter electrode will behave as an anode and of course vice versa. Flow of current between the CE and the WE is measured and is often utilized in potentiometry as the output. Frequently employed potentiometry methods include cyclic voltammetry (CV), square wave voltammetry (SWV), differential pulse voltammetry (DPV), and electrochemical impedance spectroscopy (EIS).

3.2.3.5.2 Cyclic Voltammetry (CV):

Cyclic Voltammetry is a commonly implemented technique to get comprehensive information about the redox potential at the surface of the electrode and to understand the electrochemical

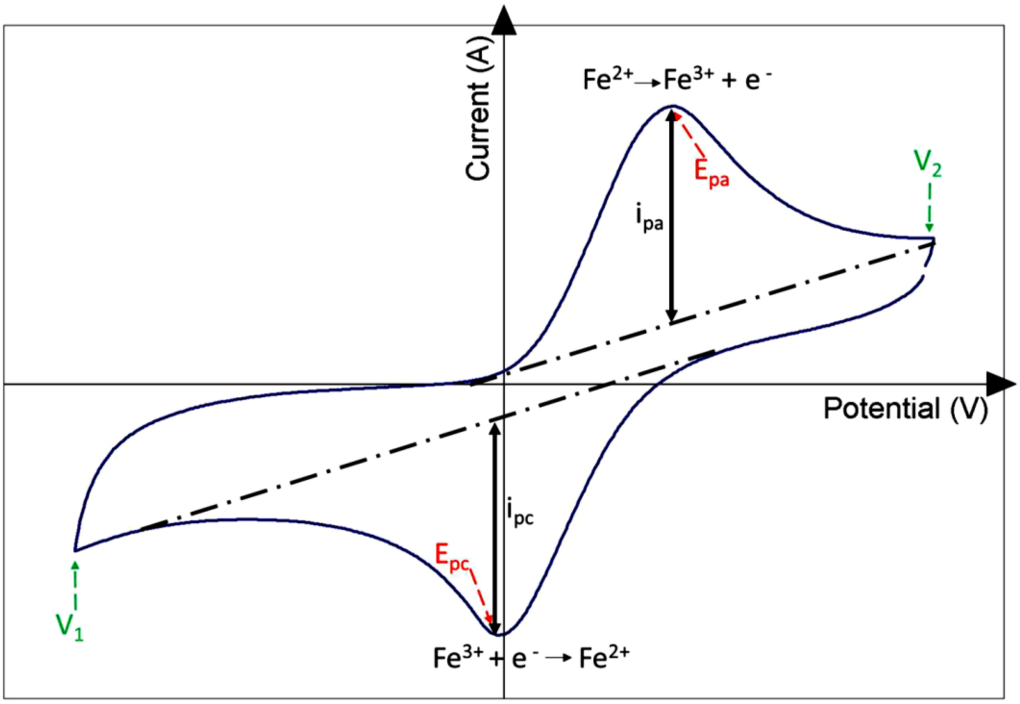

Figure 3. 14: A cyclic voltammogram showing the peak anodic potential (E_{pa}), anodic current (i_{pa}), peak cathodic potential (E_{pc}) and the cathodic current (i_{pc}).

reactions which are associated with that redox potential. In this voltammetric technique, the current flow is measured by cyclically varying the electrochemical potential at the working electrode. The potential is varied between the start and end potential (V_1 and V_2) respectively [58, 61]. The voltammetric measurements are performed at the fixed scan rate. Also, the time required to perform scanning between the start potential and end potential is fixed and is well-defined by equation 3.4. To have a precise illustration of the electrochemical reaction at the surface of the electrode, it is crucial to set the correct scan rate as this parameter is time dependent. Therefore, to achieve the appropriate electrochemical change occurring as a result of the chemical reaction taking place at the surface of the sensor, adequate time should be specified. Generally, the scan rates between 50 mV.s^{-1} and 100 mV.s^{-1} are mostly utilized [61].

$$\boldsymbol{Scan\ rate = \frac{V_2 - V_1}{t_2 - t_1}} \tag{3.4}$$

Usually, the three electrodes electrochemical cell set up is used to perform the CV measurements, this includes the working electrode (WE), reference electrode (RE), and counter electrode (CE). Typically, a current vs voltage cyclic voltammogram is generated as an output result, where the current of the working electrode is measured with respect to the counter electrode and the voltage is measured with respect to the reference electrode (**Figure 3.14**). A voltammogram usually comprises of an anodic peak also called the oxidation peak and a cathodic peak also called the reduction peak depending on the type of the sample [62]. For instance, the potassium ferricyanide and the potassium ferrocyanide ($K_3[Fe(CN)_6]/K_4[Fe(CN)_6]$) system which is also a well-known redox couple that is capable of undergoing a reversible redox reaction i.e., it can go through both the reduction and oxidation process. This in turn results in the formation of both the anodic and the cathodic peaks (equation 3.5).

$$\boldsymbol{Fe^{3+} \leftrightarrow Fe^{2+} + \bar{e}} \tag{3.5}$$

In equation 3.5 the reduction process is Fe^{3+}: ($Fe(CN)_6^{3-}+e^-\rightarrow Fe(CN)_6^{4-}$) followed by the oxidation of Fe^{2+}: ($Fe(CN)_6^{4-}\rightarrow Fe(CN)_6^{3-}+e^-$) [63].

The current starts to increase from the initial current when the potential is shifted from the initial point (V_1) to the final point (V_2). As a result of an increase in the current the ferricyanide (Fe^{2+}) is oxidized into the ferrocyanide (Fe^{3+}). Upon completion of oxidation of ferricyanide, the current starts to return towards the initial current i.e., zero. In this process, an oxidation peak is created at the anodic potential of the target analyte. On the other hand, when the applied potential is switched towards the negative direction, the ferrocyanide (Fe^{3+}) is reduced to ferricyanide (Fe^{2+}) and the current measured increasingly becomes negative. Therefore, in this case, the current flow increases in an opposite direction as compared to that observed in the oxidation process. Upon completion of the reduction of all of the ferrocyanide (Fe^{3+}), the current starts to return towards zero i.e., the initial current and a reduction peak will be created at the cathodic potential of the target analyte [58]. These peak potentials i.e., anodic potential and the cathodic potential are denoted by E_{pa} and E_{pc}**.** Whereas the subsequent peak currents are usually written as the i_{pa} and the i_{pc} (**Figure 3.14**).

Randles Sevcik equation is utilized to evaluate the numerous features of the electrochemical cell.

$$\boldsymbol{ip = (2.69 \times 10^5) n^{3/2} A C D^{1/2} \upsilon^{1/2}} \qquad \textbf{(3.6)}$$

where $\mathbf{i_p}$ represents peak current (measured in amperes), **n** presents the electron numbers transported per molecule either oxidized or reduced, and **n** is 1 in the case of redox couple ($[Fe(CN)_6]^{3-/4-}$). **A** represents the area of electrode in cm^2, **D** stands for the diffusion coefficient measured in $cm^2.s^{-1}$, **v** presents the scan rate ($V.s^{-1}$), and **C** denotes the concentration of analyte in the bulk solution, respectively [64].

For this thesis, the Autolab PGSTAT302N was used to perform the CV which was procured from Metrohm Dropsens (UK). The Pt counter electrode and the Ag/AgCl reference electrode utilized during all the experiments were obtained from IJ Cambria scientific ltd. A 5mM potassium ferricyanide and potassium ferrocyanide ($[Fe(CN)_6]^{3-/4-}$) were utilized as the electrolyte solution during all the electrochemical analysis and sensing experiments.

Nevertheless, reliant on the requirements, both scan rate and the voltage ranges of every experiment were adjusted accordingly. These specific parameters are covered in greater depth in each section.

Charge transfer diffusion coefficients of the electrode surfaces were calculated before and after the functionalization process. By this, the effect of functionalization on the electron transfer and the mass transfer of $[Fe(CN)_6]^{3-/4-}$ redox couple to the electrode surface and its effect on current is determined. Equation 3.6 was used to calculate the charge transfer diffusion coefficient. Furthermore, the amine surface coverage employed by the diazonium functionalization process and also provided by polymers with different thicknesses was calculated in chapters 4 and 5 as per the procedure reported previously in 2015 by Booth et al. [65].

In this process, the amino ferrocene which is also called the electroactive ferro-centred molecule is anchored to the amine groups present at the surface of the sensor, through the carbodiimide cross-linking process in order to estimate the amine group surface coverage as shown in the **Figure 3.15**. When the electroactive amino ferrocene groups were attached to the surface of the sensor, it increases the charge at the surface. CV was utilized to estimate the charge at the surface of the sensor. Besides, the surface coverage of amino ferrocene molecules was using equation 3.7.

$$\mathbf{\Gamma=Q/nFA} \qquad \mathbf{(3.7)}$$

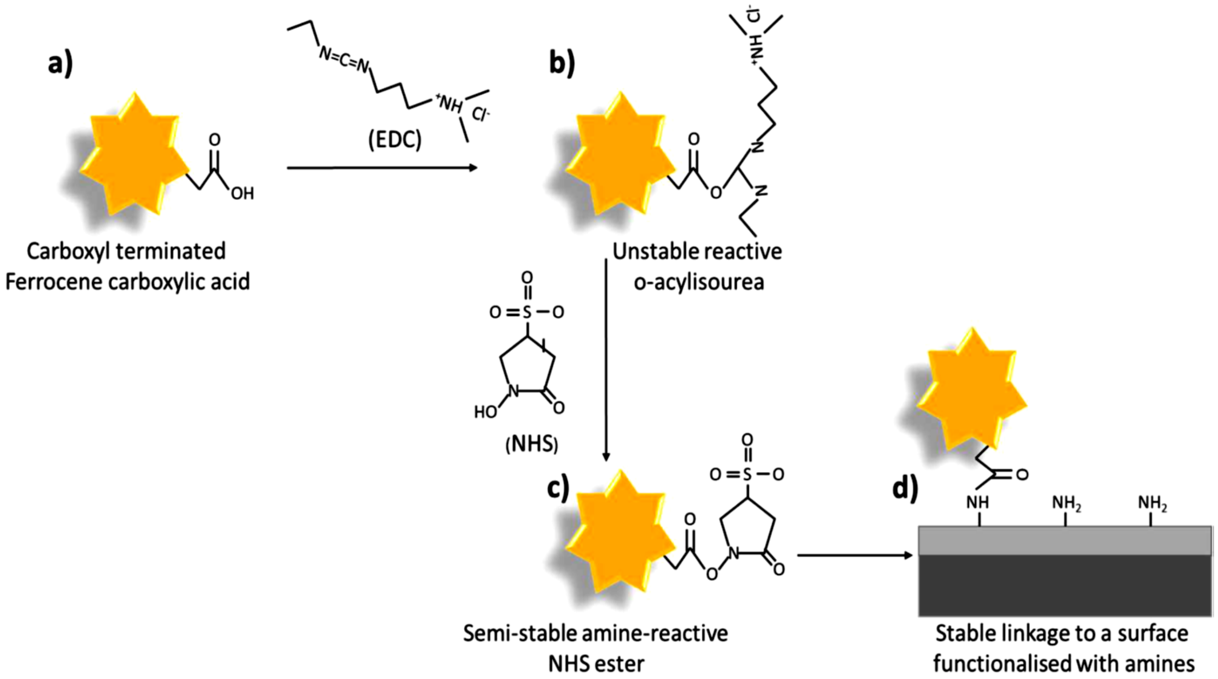

Figure 3. 15: Mechanism of immobilization of electrochemically active ferrocene carboxylic acid (FCA) to the amine functionalized surfaces via the carbodiimide cross-linking process.

Where Γ represents the surface coverage measured in mol.cm^{-2}, the flow of charge between the electrode and the electrolyte is represented by Q and is measured in coulombs, the number of transferred electrons is given by n, in this case, n = 1, F is the Faraday's constant and A represents the area of an electrode measured in cm^2 [65].

In this thesis, for the analysis of surface coverage, the ferrocene carboxyl acid (FCA) was utilized as an electroactive ferro-centered molecule, as the amine functional groups were under study.

For experiments of this thesis, FCA was attached to the amines provided by the diazonium grafting method, and the polymer DAN layers. Besides, the CV was performed between -0.3 and 0.3 V in case of diazonium grafting and -0.2 V to 0.3 V in case of pDAN functionalization method. Also, a three-electrode setup was used to perform the CV in the PBS buffer solution as an electrolyte at a very slow scan rate of 5 mV/s [66, 67]. The surface coverage of amine functional groups was calculated using the equation 3.7 under the idea that one amine molecule is attached to one ferrocene carboxylic acid molecule.

3.2.3.5.3 Square Wave Voltammetry (SWV):

Square wave voltammetry (SWV) is a potentiostatic technique that has several benefits over conventional methods such as CV. In the case of SWV, the wave generated is in the form of a series of pulses which increase with the linear baseline. Besides, the current is measured in the forward and the reverse pulse. The result obtained from SWV is the difference in the current between the forward and the reverse pulses. The current measured at each wave pulse is in a manner that it helps in reducing the measurement of the charging (background) current. Many characteristics of several pulse voltammetric procedures are merged in the SWV technique which includes the sensitivity and background suppression feature of the DPV, the normal pulse voltammetry's (NPV) diagnostic value as well as the feature of interrogating the products directly comes from the reverse NPV.

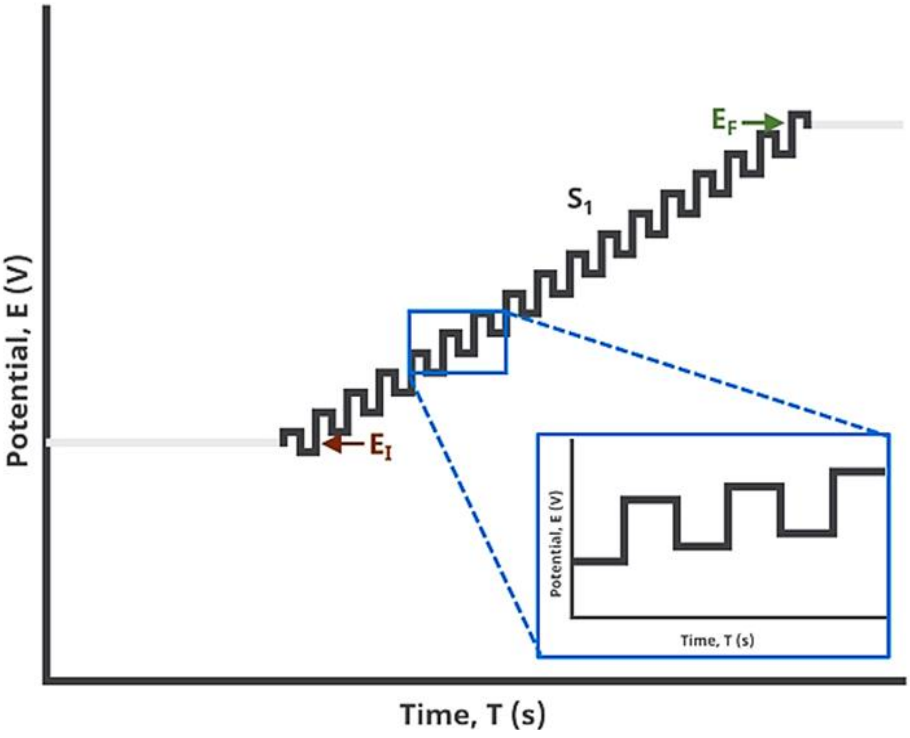

Figure 3. 16: An illustration of voltage pulses for square wave voltammetry (SWV).

In a typical SWV experiment, the working electrode's potential is increased in steps from the initial to the final potential via a series of the forward pulses and the reverse pulses. Here the square amplitude helps in the determination of the forward step whilst when the square increment is subtracted from the square amplitude, the reverse step is determined. Cyclic square wave voltammetry (CSWV) is the type of SWV in which the working electrode's potential is cycled between the upper and the lower potentials. **Figure 3.16** shows the voltage pulses in the simplest case of the SWV where segments (S_N) = 1.

Figure 3.17 presents the voltage pulses in the forward pulse as well as in the reverse pulse, alongside the baseline which is increasing linearly from the initial potential to the final potential, detecting the current at the specified time intervals.

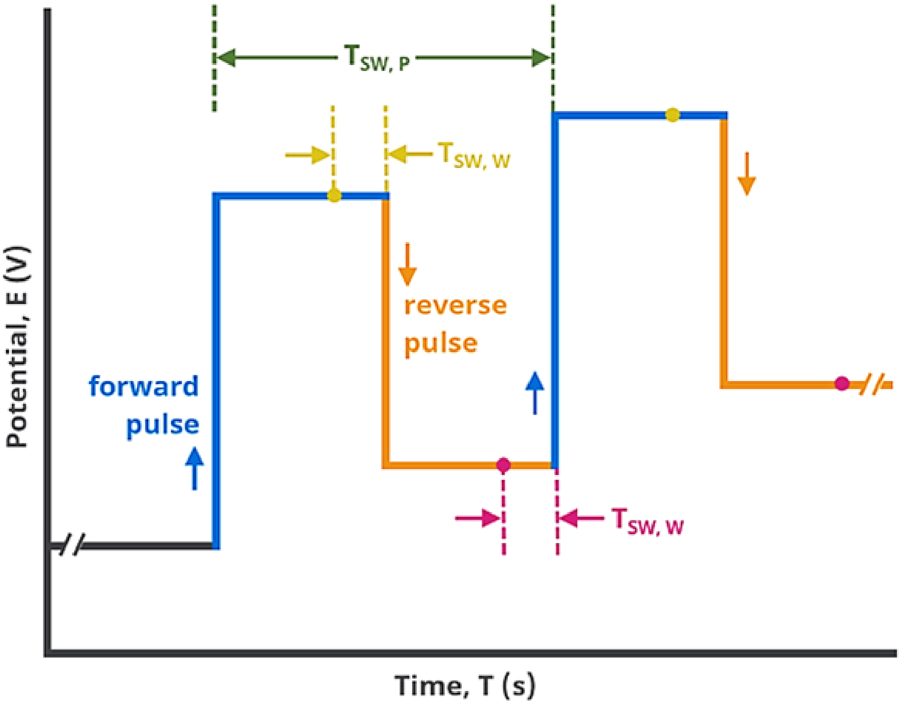

Figure 3. 17: An illustration of voltage pulses of square wave voltammetry (SWV) (forward and a reverse pulse).

The current is recorded with the simultaneous frequency within the duration of a pulse during each the forward or the reverse pulse, as specified by entering the sampling width ($T_{SW,\ W}$) parameter in the basic tab.

In **Figure 3.17** the period of the pulse $T_{SW,\ P}$ is including both the forward pulse (blue) and the reverse pulse (orange). Therefore, in this case, the current is measured in forward pulse at:

$\mathbf{1/2\ T_{SW,\ P} - T_{SW,\ W}}$

and the current measured in a reverse pulse is at:

$\mathbf{T_{SW,\ P} - T_{SW,\ W}}$

A typical square wave voltammetry (SWV) technique consists of the three electrodes electrochemical cell set up, this includes the working electrode (WE), the reference electrode (RE), and the counter electrode (CE). The current of the working electrode is measured with respect to the counter electrode and the voltage is measured with respect to the reference electrode.

SWV is utilized for high-sensitivity analysis of the samples. Higher sensitivity is achieved by utilizing the staircase potential time instead of the continuous potential ramp, which reduces the contribution of insignificant influence from the non-faradaic currents [68]. Therefore, for this reason, square wave voltammetry is utilized in various electrochemical measurement experiments. Moreover, this technique could also be observed as an improvement and development of various other conventional electroanalytical measuring techniques. For example, in the SWV method, the charging (background) currents are minimized more efficiently than in the case of CV, and therefore by using SWV the concentration of analyte at the nanomolar scale is measured. In conclusion, square wave voltammetry (SWV) offers a quick and accurate way to quantitatively and qualitatively determine analytes at very small concentrations in a solution.

3.2.3.5.4 Differential Pulse Voltammetry (DPV):

Differential pulse voltammetry (DPV) is an electrochemical technique in which the current passing through the electrode is measured as the function of time and voltage (potential). It is a type of linear sweep voltammetry which is also known as staircase voltammetry. In this technique, by increasing the amplitude pulse the potential can be varied, and the current is sampled by the system just before applying the next voltage pulse. When the base-line voltage of DPV pulses is increased, it resembles the staircase voltammetry as shown in the **Figure 3.18**.

As compared to many other electrochemical measurement methods DPV has numerous advantages. It allows the direct sample analysis at the parts per billion (ppb) level hence is known to be a very sensitive technique. Part per trillion (ppt) level analysis is also possible using DPV when it is used in the stripping mode. Besides, the differential nature and a very short pulse time also owe to the higher sensitivity of the DPV technique. Measured currents increase with the shorter pulse time, while on the other hand, the differential measurements classify the processes

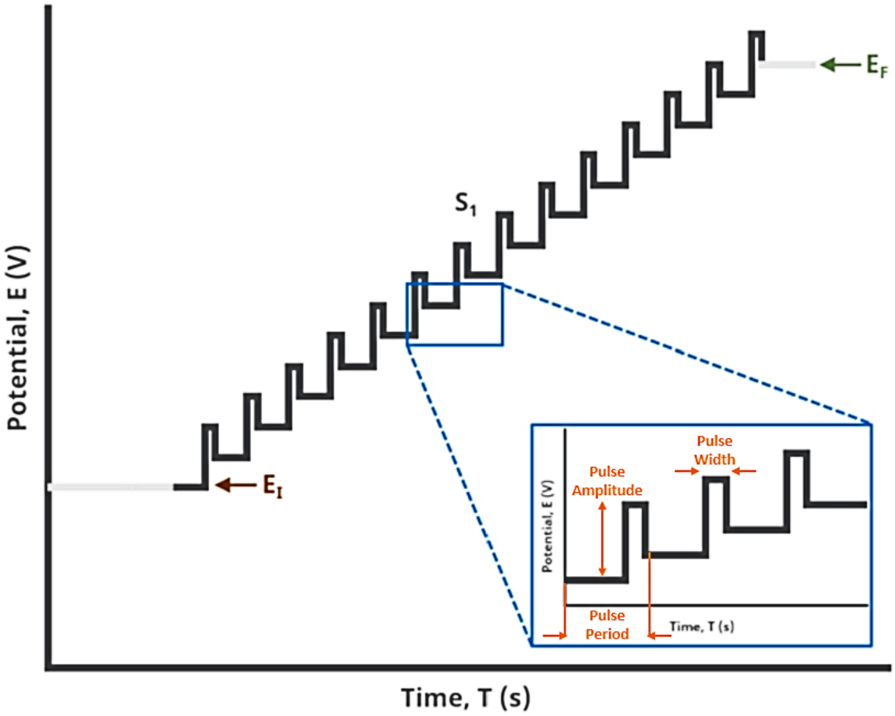

Figure 3. 18: An illustration of voltage pulses for the differential pulse voltammetry (DPV).

in the background. By doing so during the sample analysis DPV aids to reduce the background charging current. Hence it is an ideal technique due to its differential nature. In addition, during the DPV analysis, the short pulse time provides at least one ppb accuracy advantage. Therefore, differential pulse voltammetry is a valuable chemical analytical technique in real life scientific applications requiring high sensitivity.

A typical differential pulse voltammetry (DPV) technique consists of the three electrodes electrochemical cell set up, this includes the working electrode (WE), the reference electrode (RE), and the counter electrode (CE). The counter electrode aids in the transmission of voltage pulses whilst the resulting current is measured by the working electrode. In order to control the voltage pulses of the counter electrode, the reference electrode is utilized.

The range of the voltage pulses directed by the working electrode is normally between 10ms - 100ms provided with a steady rise of 10 mV to 100 mV. As the voltage returns back to the initial baseline, there is a usual idle interval of 1 to 2 seconds which in turn allows the auxiliary electrode to acquire only the Faradaic current rather than the charging current.

In this thesis, SWV and DPV measurements were performed using an Autolab PGSTAT302N, with the scanning voltage in the range of -0.2 V to 0.5 V for evaluating the electrochemical performance of blank and functionalized electrodes. Target analytes sensing was performed using DPV in chapters 4 and 5 by monitoring the change in peak current (Ip) at each concentration and a calibration curve of Ip versus the log of analyte concentration was formed. From this curve, information about the sensors, limit of detection, dynamic range, and sensitivity was determined. Whereas SWV was used in chapter 5 to analyze the change in peak current (Ip) before and after functionalization steps of the graphene-modified SPEs.

3.2.3.5.5 Electrochemical Impedance Spectroscopy (EIS):

Electrochemical impedance spectroscopy (EIS) is the dominant technique for determining how the specific processes like the addition of an analyte to the surface of the sensor create an impact on the device's electrochemical conductance, resistance, or capacitance [61]. EIS is a commonly adopted technique regarded as among the most accurate and convenient electrochemical tools for identifying the characteristics of an electrochemical system.

This technique is the combination of various steps including the electron transport and the charge transfer towards and from the electrode surface, the resistance imposed by the solution to the movement of cations and the electrons, the diffusion impedance of the electrons and cations towards and from the working electrode and finally the double layer capacitance which is the barrier that develops in the electrochemical cell between the electrolyte solution and the surface of the electrode as presented by **Figure 3.19** [69].

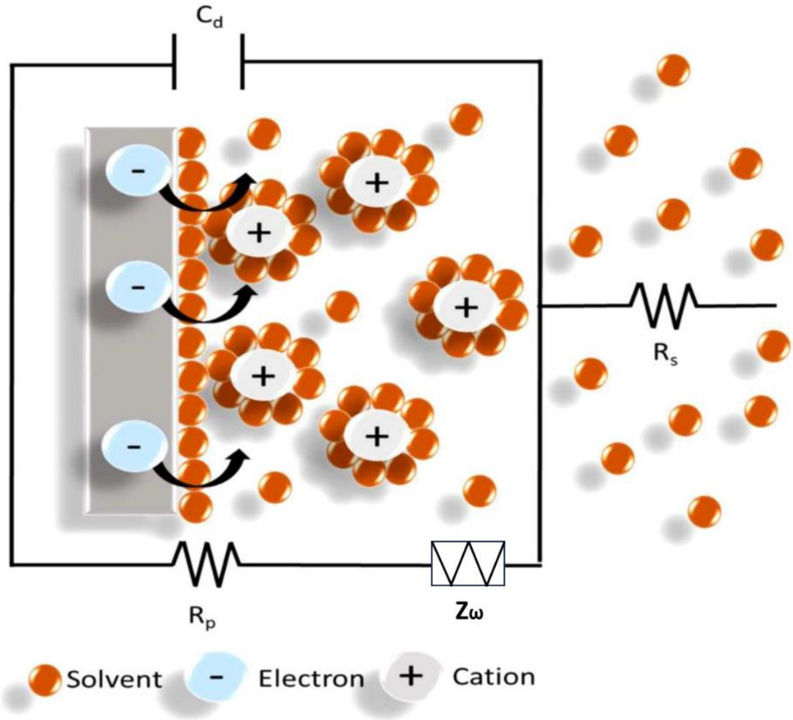

Figure 3. 19: A schematic of an interface showing the electrons at negatively charged surface and solvent is adsorbed at the surface. The corresponding Randle’s equivalent circuit for EIS analysis is also shown (Rs is the solution resistance, Rp is polarization resistance, Zω is the mass-transport (Warburg’s) impedance and Cd is the double-layer capacitance).

To explicate the electrochemical response by the working electrode, an alternating current (AC) is utilized during the EIS procedure. The impedance is estimated by implementing the sinusoidal voltage present at the low amplitude to the substrate as a function of frequency [70].

Hence, the EIS measurement is the function of time and the voltage and can be presented by the equation 3.8:

$$\boldsymbol{Z = \frac{V(t)}{i(t)}} \quad \textbf{(3.8)}$$

Typically, the Impedance |Z| is the electrochemical measurement of the flow of electrons and the ions from all the constituents of the electrochemical cell [68]. This incorporates the resistors, capacitors, and the inductors. Two profound components of impedance are the faradaic and non-faradaic impedance. Faradaic impedance has to do with overcoming the solution resistance (Rs), as well as the charge transfer resistance (R_{CT}) also known as the polarization resistance (Rp) that serves as an activation barrier. The non-faradaic impedance is the result of the double-layer capacitor (Cd) charging and the charge transfer that takes place as a result of double-layer capacitor charging. This depends on a mass-transport impedance ($Z\omega$) of oxidant and reductant at the working electrode [71]. Basically, the EIS converts an electrochemical and the biological interface to an electrical circuit that is seemingly easily understandable. Also, the different parts of the system can be measured electrochemically and understood easily.

Moreover, the EIS electrochemical circuit is presented as Randle's circuit as shown in **Figure 3.19**. Within the electrochemical system, the real and imaginary parts are analyzed in order to perform the EIS measurement. It is also normally defined as a complex number [61].

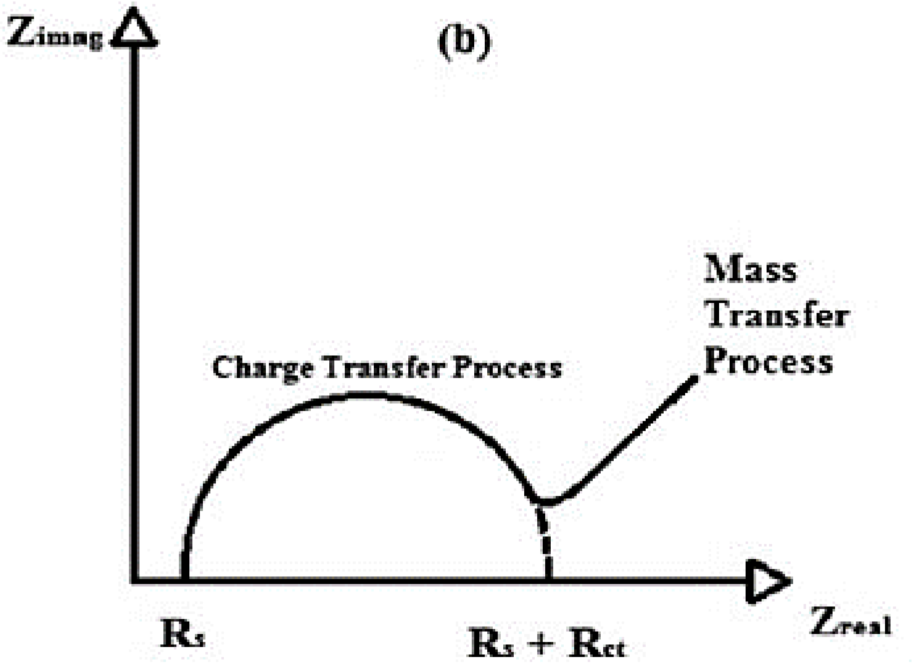

Figure 3. 20: The Nyquist plot arising from an idealized Randle's equivalent circuit.

The real component of the impedance is the ohmic resistance which is measured by the EIS process. Whereas the imaginary component of the impedance is the capacitance. The electrochemical EIS sensors are generally characterized by their Nyquist and the bode plots. The Nyquist plot is shown in **Figure 3.20**. It is plotted between the real component i.e., Z' versus the imaginary impedimetric component i.e., -Z'' at every frequency point that is measured during the EIS process. The X-axis depends on the resistance of the system at specific frequency. On the other hand, the Y-axis depends on the capacitance of the system and hence a simple RC circuit will generate a semi-circular plot.

The value of the solution resistance is determined by the initial point of the Nyquist plot whereas the total resistance comprising of the charge transfer resistance, or the polarization resistance and the solution resistance is determined by the final point of the semi-circle which is the point where that semi-circle crosses the X-axis. This shows that the charge transfer resistance is provided by the diameter of the semi-circular plot. **Figure 3.20** also displays the diffusion impedance as the mass transfer process or the Warburg impedance on the Nyquist plot. A plot with a 45° angle from the X-axis is commonly used to represent this region.

The attachment of an analyte with the bioreceptor at the surface of the sensor results in a change in the resistance of the sensor. This change in resistance is estimated by fitting an electrical circuit mostly Randle's equivalent circuit to the Nyquist plot. Randle's circuit is presented in **Figure 3.19**.

In this thesis, EIS measurements were also performed using the Autolab PGSTAT302N. All analysis was performed with frequencies ranging between 0.05 to 1000 Hz with 80 number of frequencies and an amplitude of 0.01 in a 5 mM $K_3[Fe(CN)_6]/K_4[Fe(CN)_6]$ electrolyte solution. Sensing of target analytes was performed using EIS in chapter 6 by monitoring the charge transfer resistance (R_{CT}) at each concentration and a calibration plot of change in charge transfer resistance versus the log of analyte concentration was formed. From this plot, information about the sensor's limit of detection, dynamic range, and sensitivity was determined.

All of the techniques described in this chapter were used to gain a better understanding of the effect of the chemical functionalization on the graphene, rGO as well as the overall performance of the graphene-based sensors. This chapter only gives an overview of the background and principles of the techniques used in this thesis. However, the exact methodologies of these techniques utilized for particular applications are explained in depth in the subsequent chapters.

BIBLIOGRAPHY

1. Dovbeshko, G.I., et al., *Optical properties of pyrolytic carbon films versus graphite and graphene.* Nanoscale research letters, 2015. **10**(1): p. 1-6.
2. Wu, S., et al., *Graphene-based electrochemical sensors.* small, 2013. **9**(8): p. 1160-1172.
3. Li, Z., et al., *A review of biosensing techniques for detection of trace carcinogen contamination in food products.* Analytical and bioanalytical chemistry, 2015. **407**(10): p. 2711-2726.
4. Wu, D., et al., *Two-Dimensional Nanocomposites Based on Chemically Modified Graphene.* Chemistry–A European Journal, 2011. **17**(39): p. 10804-10812.
5. Sethi, J., et al., *A label-free biosensor based on graphene and reduced graphene oxide dual-layer for electrochemical determination of beta-amyloid biomarkers.* Microchimica Acta, 2020. **187**: p. 1-10.
6. Lentz, C., et al., *Synthesis and characterization of glassy carbon nanowires.* Journal of Nanomaterials, 2011. **2011**.
7. Ossonon, B.D. and D. Bélanger, *Functionalization of graphene sheets by the diazonium chemistry during electrochemical exfoliation of graphite.* Carbon, 2017. **111**: p. 83-93.
8. Richard, W., D. Evrard, and P. Gros, *Kinetic study of redox probes on glassy carbon electrode functionalized by 4-nitrobenzene diazonium.* International Journal of Electrochemical Science, 2018. **14**(1): p. 453-469.
9. Delamar, M., et al., *Covalent modification of carbon surfaces by grafting of functionalized aryl radicals produced from electrochemical reduction of diazonium salts.* Journal of the American Chemical Society, 1992. **114**(14): p. 5883-5884.

10. Allongue, P., et al., *Covalent modification of carbon surfaces by aryl radicals generated from the electrochemical reduction of diazonium salts.* Journal of the American Chemical Society, 1997. **119**(1): p. 201-207.

11. Downard, A.J., *Electrochemically assisted covalent modification of carbon electrodes.* Electroanalysis: An International Journal Devoted to Fundamental and Practical Aspects of Electroanalysis, 2000. **12**(14): p. 1085-1096.

12. Dyke, C.A., et al., *Diazonium-based functionalization of carbon nanotubes: XPS and GC-MS analysis and mechanistic implications.* Synlett, 2004. **2004**(01): p. 155-160.

13. Li, B., et al., *Self-assembly of single-walled carbon nanotube based on diazoresin.* Synthetic metals, 2002. **132**(1): p. 5-8.

14. Abiman, P., et al., *Investigating the thermodynamic causes behind the anomalously large shifts in p K a values of benzoic acid-modified graphite and glassy carbon surfaces.* Langmuir, 2007. **23**(14): p. 7847-7852.

15. Abiman, P., G.G. Wildgoose, and R.G. Compton, *Electroanalytical Exploitation of Nitroso Phenyl Modified Carbon-Thiol Interactions: Application to the Low Voltage Determination of Thiols.* Electroanalysis: An International Journal Devoted to Fundamental and Practical Aspects of Electroanalysis, 2007. **19**(4): p. 437-444.

16. Ray, K. and R.L. McCreery, *Spatially resolved Raman spectroscopy of carbon electrode surfaces: Observations of structural and chemical heterogeneity.* Analytical Chemistry, 1997. **69**(22): p. 4680-4687.

17. Dequaire, M., C. Degrand, and B. Limoges, *Biotinylation of screen-printed carbon electrodes through the electrochemical reduction of the diazonium salt of p-aminobenzoyl biocytin.* Journal of the American Chemical Society, 1999. **121**(29): p. 6946-6947.

18. Liu, G., *Modification of aryldiazonium salts on electrodes towards designing stable and versatile sensing interfaces.* Australian Journal of Chemistry, 2011. **64**(5): p. 658-658.

19. Abiman, P., G.G. Wildgoose, and R.G. Compton, *A mechanistic investigation into the covalent chemical derivatisation of graphite and glassy carbon surfaces using aryldiazonium salts.* Journal of Physical Organic Chemistry, 2008. **21**(6): p. 433-439.

20. Koefoed, L., S.U. Pedersen, and K. Daasbjerg, *Covalent modification of glassy carbon surfaces by electrochemical grafting of aryl iodides.* Langmuir, 2017. **33**(13): p. 3217-3222.

21. Kariuki, J.K. and M.T. McDermott, *Formation of Multilayers on Glassy Carbon Electrodes via the Reduction of Diazonium Salts.* Langmuir, 2001. **17**(19): p. 5947-5951.

22. Brooksby, P.A. and A.J. Downard, *Multilayer nitroazobenzene films covalently attached to carbon. An AFM and electrochemical study.* The Journal of Physical Chemistry B, 2005. **109**(18): p. 8791-8798.

23. Ricci, A., C. Bonazzola, and E.J. Calvo, *An FT-IRRAS study of nitrophenyl mono-and multilayers electro-deposited on gold by reduction of the diazonium salt.* Physical Chemistry Chemical Physics, 2006. **8**(37): p. 4297-4299.

24. Malmos, K., et al., *Using a hydrazone-protected benzenediazonium salt to introduce a near-monolayer of benzaldehyde on glassy carbon surfaces.* Journal of the American Chemical Society, 2009. **131**(13): p. 4928-4936.

25. Combellas, C., et al., *Time-of-flight secondary ion mass spectroscopy characterization of the covalent bonding between a carbon surface and aryl groups.* Langmuir, 2005. **21**(1): p. 280-286.

26. Kariuki, J.K. and M.T. McDermott, *Nucleation and growth of functionalized aryl films on graphite electrodes.* Langmuir, 1999. **15**(19): p. 6534-6540.

27. Brooksby, P.A. and A.J. Downard, *Electrochemical and atomic force microscopy study of carbon surface modification via diazonium reduction in aqueous and acetonitrile solutions.* Langmuir, 2004. **20**(12): p. 5038-5045.

28. Safenaz, M.R. and M. Sheikha, *Synthesis and electrical properties of polyaniline composite with silver nanoparticles.* Advances in materials Physics and Chemistry, 2012. **2012**.

29. Li, J. and X. Lin, *Glucose biosensor based on immobilization of glucose oxidase in poly (o-aminophenol) film on polypyrrole-Pt nanocomposite modified glassy carbon electrode.* Biosensors and Bioelectronics, 2007. **22**(12): p. 2898-2905.

30. Pan, X., et al., *Preparation and properties of an uricase biosensor based on copolymer of o-aminophenol-aniline.* Sensors and Actuators B: Chemical, 2006. **113**(1): p. 329-334.

31. Turkmen, E., et al., *Glucose biosensor based on immobilization of glucose oxidase in electropolymerized poly (o-phenylenediamine) film on platinum nanoparticles-polyvinylferrocenium modified electrode.* Electrochimica Acta, 2014. **123**: p. 93-102.

32. Kirwan, S.M., et al., *Modifications of poly (o-phenylenediamine) permselective layer on Pt-Ir for biosensor application in neurochemical monitoring.* Sensors, 2007. **7**(4): p. 420-437.

33. Oyama, N., M. Sato, and T. Ohsaka, *Preparation of thin polymeric films on electrode surfaces by electro-polymerization of aromatic compounds with amino groups.* Synthetic Metals, 1989. **29**(1): p. 501-506.

34. Jin, C.-S., Y.-B. Shim, and S.-M. Park, *Electropolymerization and spectroelectrochemical characterization of poly (1, 5-diaminonaphthalene).* Synthetic Metals, 1995. **69**(1-3): p. 561-562.

35. Nguyen, V.-A., et al., *Electrosynthesized poly (1, 5-diaminonaphthalene)/polypyrrole nanowires bilayer as an immunosensor platform for breast cancer biomarker CA 15-3.* Current Applied Physics, 2017. **17**(11): p. 1422-1429.

36. Goyal, R.N., A.R.S. Rana, and H. Chasta, *Simultaneous monitoring of aspirin, paracetamol and caffeine in human urine at poly-1, 5-diaminonapthalene modified pyrolytic graphite sensor.* Journal of The Electrochemical Society, 2013. **160**(7): p. G3014.

37. Lesch, H.P., et al., *Avidin-biotin technology in targeted therapy.* Expert opinion on drug delivery, 2010. **7**(5): p. 551-564.

38. Jain, A. and K. Cheng, *The principles and applications of avidin-based nanoparticles in drug delivery and diagnosis.* Journal of controlled release, 2017. **245**: p. 27-40.

39. Nguyen, T.T., K.L. Sly, and J.C. Conboy, *Comparison of the energetics of avidin, streptavidin, neutrAvidin, and anti-biotin antibody binding to biotinylated lipid bilayer examined by second-harmonic generation.* Analytical chemistry, 2012. **84**(1): p. 201-208.

40. Zhao, S., D. Walker, and W. Reichert, *Cooperativity in the binding of avidin to biotin-lipid-doped Langmuir-Blodgett films.* Langmuir, 1993. **9**(11): p. 3166-3173.

41. Wang, X. and D.L. Kaplan, *Functionalization of Silk Fibroin with NeutrAvidin and Biotin.* Macromolecular Bioscience, 2011. **11**(1): p. 100-110.

42. Reimer, L., *Scanning electron microscopy: physics of image formation and microanalysis*. 2000, IOP Publishing.

43. Vernon-Parry, K., *Scanning electron microscopy: an introduction.* III-Vs Review, 2000. **13**(4): p. 40-44.

44. Goldstein, J., *Practical scanning electron microscopy: electron and ion microprobe analysis*. 2012: Springer Science & Business Media.

45. Binnig, G., C.F. Quate, and C. Gerber, *Atomic force microscope.* Physical review letters, 1986. **56**(9): p. 930.

46. Alexandre, D., C. Marianne, and C. Jean-François, *Asymmetric M-estimation and change-point analysis applied to atomic force microscopy data enhancement.* Metrologia, 2018. **55**(5): p. 637.

47. Gan, Y., *Atomic and subnanometer resolution in ambient conditions by atomic force microscopy.* Surface Science Reports, 2009. **64**(3): p. 99-121.

48. Malard, L., et al., *Raman spectroscopy in graphene.* Physics reports, 2009. **473**(5-6): p. 51-87.

49. Nanda, S.S., et al., *Raman spectrum of graphene with its versatile future perspectives.* TrAC Trends in Analytical Chemistry, 2016. **80**: p. 125-131.

50. Pandey, D.K., et al., *Overview of Raman Spectroscopy: Fundamental to Applications*, in *Modern Techniques of Spectroscopy*. 2021, Springer. p. 145-184.

51. Ferrari, A.C., *Raman spectroscopy of graphene and graphite: Disorder, electron–phonon coupling, doping and nonadiabatic effects.* Solid state communications, 2007. **143**(1-2): p. 47-57.

52. Ni, Z., et al., *Raman spectroscopy and imaging of graphene.* Nano Research, 2008. **1**(4): p. 273-291.

53. Cançado, L., et al., *Geometrical approach for the study of G' band in the Raman spectrum of monolayer graphene, bilayer graphene, and bulk graphite.* Physical Review B, 2008. **77**(24): p. 245408.

54. Liu, Y., et al., *Temperature dependence of the electrical transport properties in few-layer graphene interconnects.* Nanoscale research letters, 2013. **8**(1): p. 1-7.

55. Venezia, A.M., *X-ray photoelectron spectroscopy (XPS) for catalysts characterization.* Catalysis Today, 2003. **77**(4): p. 359-370.

56. Chastain, J. and R.C. King Jr, *Handbook of X-ray photoelectron spectroscopy.* Perkin-Elmer Corporation, 1992. **40**: p. 221.

57. Titantah, J. and D. Lamoen, *sp3/sp2 characterization of carbon materials from first-principles calculations: X-ray photoelectron versus high energy electron energy-loss spectroscopy techniques.* Carbon, 2005. **43**(6): p. 1311-1316.

58. Skoog, D.A., F.J. Holler, and S.R. Crouch, *Principles of instrumental analysis*. 2017: Cengage learning.

59. Pyun, S.-I., et al., *Electrochemistry of insertion materials for hydrogen and lithium*. 2012: Springer Science & Business Media.

60. Elgrishi, N., et al., *A practical beginner's guide to cyclic voltammetry.* Journal of chemical education, 2018. **95**(2): p. 197-206.

61. Grieshaber, D., et al., *Electrochemical biosensors-sensor principles and architectures.* Sensors, 2008. **8**(3): p. 1400-1458.

62. Gosser, D.K., *Cyclic voltammetry: simulation and analysis of reaction mechanisms*. Vol. 43. 1993: VCH New York.

63. Sirivisoot, S. and T.J. Webster, *5.523 - Carbon Nanotubes: Applications for In Situ Implant Sensors*, in *Comprehensive Biomaterials*, P. Ducheyne, Editor. 2011, Elsevier: Oxford. p. 303-315.

64. Suroviec, A. and P.J. Kulesza. *Physical and Analytical Electrochemistry, Electrocatalysis, and Photoelectrochemistry General Session*. 2016. The Electrochemical Society.

65. Booth, M.A., et al., *In-depth electrochemical investigation of surface attachment chemistry via carbodiimide coupling.* Langmuir, 2015. **31**(29): p. 8033-8041.

66. Devadoss, A., et al., Ultrathin Functional Polymer Modified Graphene for Enhanced Enzymatic Electrochemical Sensing. Biosensors, 2019. 9(1): p. 16.

67. Çevik, E., M. Şenel, and M. Fatih Abasıyanık, Construction of biosensor for determination of galactose with galactose oxidase immobilized on polymeric mediator contains ferrocene. Current Applied Physics, 2010. 10(5): p. 1313-1316.

68. Deffo, G., et al., *Differential pulse and square-wave voltammetry as sensitive methods for electroanalysis applications*, in *Reference Module in Chemistry, Molecular Sciences and Chemical Engineering*. 2023, Elsevier.

69. Ates, M., *Review study of electrochemical impedance spectroscopy and equivalent electrical circuits of conducting polymers on carbon surfaces.* Progress in Organic Coatings, 2011. **71**(1): p. 1-10.

70. Prodromidis, M.I., *Impedimetric immunosensors—A review.* Electrochimica Acta, 2010. **55**(14): p. 4227-4233.

71. Chang, B.-Y. and S.-M. Park, *Electrochemical impedance spectroscopy.* Annual Review of Analytical Chemistry, 2010. **3**: p. 207-229.

CHAPTER 4

ASSESSING SURFACE COVERAGE OF AMINOPHENYL BONDING SITES ON DIAZOTISED GLASSY CARBON ELECTRODES FOR OPTIMIZED ELECTROCHEMICAL BIOSENSOR PERFORMANCE

This chapter describes the use of electrochemical techniques to assess the surface coverage of amino-phenyl groups attached to the carbon electrode using the ferrocene carboxylic acid as a rapid and cheap assay. While the number of electrons transferred in the first step of diazotisation indicates a surface coverage of 8.02 ±0.2 × 10^{-10} (mol/cm^2); and those transferred in the second step, which is nominally the reduction from nitrophenyl to amino-phenyl, indicate an amine surface coverage of 4-5× 10^{-10} (mol/cm^2); the number of electrons transferred during attachment of the amine coupling assay compound, ferrocene carboxylic acid, indicate a much lower available amine coverage, of only 2.2× 10^{-11} (mol/cm^2). Furthermore, the available amine coverage was critically dependent upon the number of CV cycles used in the reduction, and thus the procedures used in this step influence the sensitivity of any subsequent sensor. Amine coupling of a carboxyl terminated anti-beta amyloid antibody specific to Aβ(1-42) peptide, followed the same pattern of coverage as that observed with ferrocene carboxylic acid, and at optimum amine coverage, the sensitivity of the differential pulse voltammetry sensor was in the range 0-200 ng/mL with the slope of 5.07 µA/ng.mL^{-1} and R^2=0. 98.

4.1 INTRODUCTION

There are several studies that highlight the need for rapid, sensitive techniques and emphasize that biosensor performance is highly dependent on substrate material [1,2]. Carbon-based electrochemical sensor platforms remain a high priority in the biosensor market owing to their low cost, high sensitivity, and simple surface chemistry, which gives great flexibility in designing sensors for a wide range of analytes for early disease diagnostics. Various immobilization strategies have been developed to attach biomolecules to the carbon sensor platform. Here, the selection of the functionalization process plays a key role in determining the overall sensor performance. Diazonium grafting is one of the most promising methods as it provides a simple technique to immobilize functional groups, via covalent attachment [3,4] onto a variety of substrates [5,6]. Diazotisation of carbon electrodes via the nitro group is reduced to the amino group was first reported by M. Delamer *et al*. in the early 1990s [7]. Diazonium surface modification and the chemical structure of the modification are shown in **Figure 3.1** (Chapter 3).

Later functionalization of materials via diazotisation has garnered interest, with several studies dedicated to exploring its potential in sensing applications [8–11]. Surface-immobilized groups can induce specific chemical and physicochemical properties to the surface that may be used in fields such as chemical [9,12,13] or biological sensing [14–19], molecular electronics [20–22], microbial fuel cells [11] and energy conversion applications [23,24]. Additionally, diazonium salts have been used for the attachment of metal (aluminium, gold, etc.,) nanoparticles [25–27], oxide nanoparticles [28–30], and nanotextured

anti-icing surfaces [31].

Quantifying the efficiency of surface modification is critical to achieving the best sensor performance. A wide range of tools has been reported to determine the efficiency of the diazonium grafting process and quantify the surface coverage of nitrophenyl groups produced. For example, in 1995, Y. C. Liu *et al.* used high-sensitivity surface Raman spectroscopy to obtain spectra from monolayers of nitrophenyl groups covalently bonded to glassy carbon (GC) and highly ordered pyrolytic graphite (HOPG). They demonstrated the electrochemical reduction of 4-nitrophenyl diazonium ions in acetonitrile resulting in the formation of 4-nitrophenyl radical that in turn covalently bonds to the glassy carbon surface. In their work cyclic voltammetry, X-ray photoelectron spectroscopy (XPS), and Raman spectroscopy data were used to estimate the surface coverage of 4-nitrophenyl as 6.5×10^{-10} mol/cm^2 and 1.6×10^{-10} mol/cm^2 on glassy carbon and HOPG respectively. Surface coverages from the reduction of diazonium salts for different methods and substrates are given in **Table 4.1**.

Substrate	Potential (V)	Surface Coverage (mol/cm^2) $\times 10^{-10}$	Conditions	Reference
GC		14	4 min electrolysis	
GC		6.5±0.5	10 min electrolysis	[32]
GC		18	4 min electrolysis	[33]
GC		5.6	4 min electrolysis	[34]
GC	-1.06	19±1	t=10 min &100 min	[35]
SD	-1.17	1.3	N_2 purged Glove box	[36]
EG		16.6	RT, argon atm. 20 hr	[20]
GC	-0.8	22	Argon (oxygen free)	[5]
GC	***-0.6***	***8.02 ±0.2***	***Air (atmospheric), 1 min, RT***	***This work***

Table 4. 1: 4-p-nitrophenyl surface coverage on carbon-based substrates

[GC- glassy carbon; SD - single-crystalline diamond surface; EG - epitaxial graphene]

Antibody immobilization plays a critical role in determining immunosensor performance. Antibodies are composed of hundreds of amino acids to form the characteristic Y-shape, where the carboxyl (–COOH) group is positioned at the lower end of this Y-shape structure (Fc region (**Scheme 4.1**). Through the two upper-end parts of this Y-shape that are amine-terminated (Fab region), each antibody is able to bind two antigen species. The orientation, chemical species for targeting, and dimensions of antibodies all influence the attachment of the functional groups such as $-NH_2$ and -COOH to the substrate.

Traditionally, the carboxyl group of the support surface is activated by carbodiimide and reacted with amino groups of antibodies to result in their cross-linking. This will lead to the random orientation of the antibody [37,38]. Therefore, ethyl-3-(3-(dimethylamino)-propyl) carbodiimide hydrochloride (EDC)/ N-hydroxysuccinimide (NHS) (EDC/NHS) coupling of antibody amine and carboxyl groups to surface carboxyl and amine groups [37] was selected to ensure correct orientation of antibody **(Scheme 4.1 (b)**).

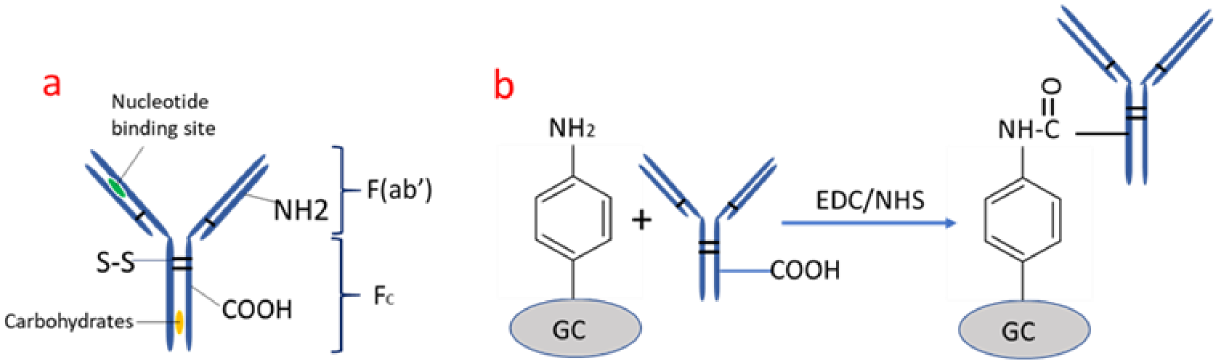

Scheme 4.1: (a) Important antibody chemical species for targeting, (b) EDC/NHS coupling of the antibody carboxyl group to surface amine group.

Alternatively, activating the carboxylic acid (Fc region) of the antibody and attaching them to the amine-terminated support surface would improve the antibody orientation [39].

Additionally, our work has already demonstrated that improving and optimizing the amine surface coverage onto the support system (carbon, graphene, etc) would improve the sensor performance. It is also achieved by improving the antibody immobilization over the sensor surface via a carbodiimide coupling reaction [17,40–42]. In addition, the utilization of carboxylic acid groups of antibodies for binding also prevents the potential loss of biological activity of antibody fragments.

Our primary motivation for this work was to establish a clear understanding of the influence of diazonium functionalization efficiency over biosensor performance. Our interest lies in developing electrochemical biomedical sensors made by the reduction of electrode-bound nitrophenol groups to amines followed by the reaction of these amine groups with sensor molecules, such as antibody receptors. A key factor in determining sensor sensitivity is the surface coverage of receptor molecules, and this, in turn, depends on the surface coverage of the intermediate aminophenyl groups. Despite extensive research on the diazotisation of carbon-based substrates, previous studies have not quantified the electrochemical conversion of 4-nitrophenyl groups to aminophenyl groups [33,34]. This research aims to combat exactly these problems; we have provided not only the optimum conditions but also a rapid and effective technique. Our focus is to report the quantification of the electrochemical conversion of 4-nitrophenyl groups to aminophenyl groups, which has never been reported. The effect of the number of CV scans is also discussed in detail. Furthermore, in order to prove this argument, we attached the antibodies on diazotised surfaces of different scan rates.

In this work, we explored this issue by quantifying the amine group coverage via measurement of electron transfer during electrochemical addition of ferrocene carboxylic acid (FCA) to aminophenyl groups on glassy carbon and highly ordered pyrolytic graphite (HOPG) electrodes. Here, we also investigated the effect of nitro to amino CV reduction scans by controlling the number of scans. The efficiency of our experimental parameter optimization was studied by developing biosensors prepared by coupling between the electrode-bound phenylamino and a carboxyl-terminated anti-beta amyloid antibody specific to Aβ (1-42) peptide, a potential marker for Alzheimer's disease. Here, Aβ (1-42) was used as a model biomarker to illustrate the successful diazotisation and validate our claim of achieving diazotisation via optimization of the experimental parameters. Aβ (1-42) is a promising biomarker for Alzheimer's disease detection, and our group has also previously worked with it and as such made an active decision to use it as the biomarker for supporting better amine coverage in this work.

4.2 MATERIALS AND METHODS

4-nitrobenzenediazonium tetrafluoroborate 97% (4-NPD), tetrabu-tylammonium tetrafluoroborate 99% (BU_4NBF_4), 1-ethyl-3-(3-(dimethylamino)-propyl) carbodiimide hydrochloride (EDC), N-hydroxysuccinimide (NHS), ferrocene carboxylic acid (FCA), potassium chloride, acetonitrile (ACN) and phosphate-buffered saline tablets (PBS; pH 7.4) were all purchased from Sigma Aldrich (St. Louis, MO, USA) and used as received. All reagents were of analytical grade, and the deionized water was used for cleaning the glassy carbon electrodes. Highly ordered pyrolytic graphite (HOPG) was purchased from MikroMasc (Wetzlar, Germany) with the following specifications: grade ZYA, mosaic spread with the value of 0.4° ± 0.1°, double-sided and with a thickness of 1 mm, and the size of 10 × 10 mm^2.

Biomarker amyloid-beta peptides Aβ ((1-42) (ab120301)) and anti-beta amyloid anti-body (ab224275), specific to Aβ (1-42) peptide Aβ, were purchased from Abcam (Cambridge, UK).

Amyloid-beta (1-42) was supplied in the lyophilized form by Abcam (Cambridge, UK). It was then dissolved in 10 mM sodium hydroxide, followed by a gentle vortex for less than 1 min to make a homogeneous solution. The peptide stock solution was then aliquoted and stored at −20

°C. Under these highly alkaline conditions, the peptide is fully dissolved and exists only as monomers [43].

4.2.1 ELECTROCHEMICAL MEASUREMENTS:

Electrochemical experiments were carried out on an Autolab electrochemical workstation at room temperature using a conventional three-electrode system: a bare or modified Glassy Carbon Electrode **(**GCE) (MF-2012, 3 mm diameter, BASi West Lafayette, USA) was used as the working electrode, with a platinum wire counter electrode and Ag/AgCl (3 M NaCl, +0.197 V vs SHE) reference electrode, and a scan rate of 50 mV/s. The GCEs were polished stepwise with aqueous alumina slurries of 0.3 and 0.05 μm particle size using micro-cloth, followed by rinsing thoroughly with isopropyl alcohol (IPA) and then with deionized water for 30 min. HOPG samples were prepared by the removal of graphite layers from its surface using the Sellotape. As a result, a fresh HOPG surface layer is exposed to be used as a working electrode, which was then rinsed with the acetone and dried with N_2.

Electrochemical grafting of the diazonium salt was performed using 0.1M BU_4NBF_4 electrolyte in acetonitrile. Typically, blank cyclic voltammetry (CV) was recorded using a freshly cleaned GCE in the electrolyte, following which, the active diazonium compound (5 mM) was added to the electrolyte, and further voltammograms were recorded for 5 cycles. Subsequent electrochemical reduction of the nitro group (NO_2) to an amino group (NH_2) was carried out in 0.1M KCl in water: ethanol (9:1) electrolyte, using reduction cyclic scanning at 50 mV/s scan rate between -1.2 V and +1 V versus Ag/AgCl.

To prepare the samples for surface characterization using SEM and AFM, HOPG was used as the working electrode. HOPG was immersed into the electrolyte solution with the help of a crocodile clip.

Functionalizing the amine groups with FCA was carried out as follows: 5 mM EDC/NHS (ratio 1:1) solution was added to 250 µM FCA solution, followed by 40 minutes of incubation at room temperature. The resultant solution was drop-cast onto the freshly prepared amine terminated GC and left for 10 min before scanning between −0.3 V and 0.3 V at 5 mV/s in fresh PBS solution, which acted as the electrolyte.

Diazonium functionalization to prepare a sensor incorporating a carboxyl terminated anti-beta amyloid antibody specific to Aβ (1-42) peptide was carried out using an EDC/NHS protocol [3,22,30]. The Aβ antibody was 'activated' in a 5 mM EDC/NHS solution for 40 minutes. This was followed by drop-casting the solution over the electrode surface and incubating for 30 min at 4 °C. The electrode was then rinsed thoroughly with deionized water and dried with N_2. After that, amyloid beta Aβ (1-42) peptides were added to the electrode surface ranging from 0 ng/mL to 200 ng/mL at 4°C, each for an incubation time of 20 minutes. Differential pulse voltammograms (DPV), obtained by sweeping the potential from -0.4 V to +0.3 V with a step potential of 5 mV, an amplitude of 25 mV, and an interval time of 0.5 seconds, were used in examining the attachment of antigens to antibody.

4.2.2 CHARACTERIZATION TECHNIQUES:

The layers that form the electrodes were characterized to determine their thickness and topography using different techniques to check the quality of the functionalization of the layers. These techniques include atomic force microscopy (AFM) and scanning electron microscopy (SEM). These were applied at the different stages of functionalization.

Atomic force microscopy (AFM) was carried out using a JPK NanoWizard II (Berlin, Germany), in intermittent contact mode with tip resonant frequency, spring constant, and nominal radius of 320 kHz, 40 N/m, and 8 nm, respectively.

Scanning electron microscopy (SEM; Ultra-High-Resolution FE-SEM S-4800, Hitachi, Tokyo, Japan) was carried out at 10 kV acceleration voltage and a 20 mA emission current. The magnification was approximately ×3k and the working distance was 10 mm.

4.3 RESULTS AND DISCUSSION

4.3.1 SURFACE FUNCTIONALIZATION OF GLASSY CARBON VIA DIAZOTIZATION:

4.3.1.1 Attachment of 4-nitrophenyl to the glassy carbon electrode (GCE) surface:

Electrochemical grafting of the diazonium salt was performed using 0.1 M BU_4NBF_4 electrolyte in acetonitrile. Typically, blank cyclic voltammetry (CV) was recorded using a freshly cleaned GCE in the electrolyte, following which, the active diazonium compound (5 mM) was added to the electrolyte, and further voltammograms were recorded for 5 cycles. **Figure 4.1** shows the cyclic voltammetry response of GCEs before and after the addition of diazonium to the electrolyte. As anticipated, no redox processes were noticed for the blank scan (black line), with the diazonium salt present a broad irreversible peak (orange curve) was observed at 0.2 V (vs Ag/AgCl). It corresponds to the first step of the reaction that involves the electron transfer from the GCE substrate to the aryl diazonium cation resulting in the formation of an aryl radical with the cleavage of dinitrogen (N_2) **(Figure 4.2(a))**. The aryl radical subsequently reacts with the

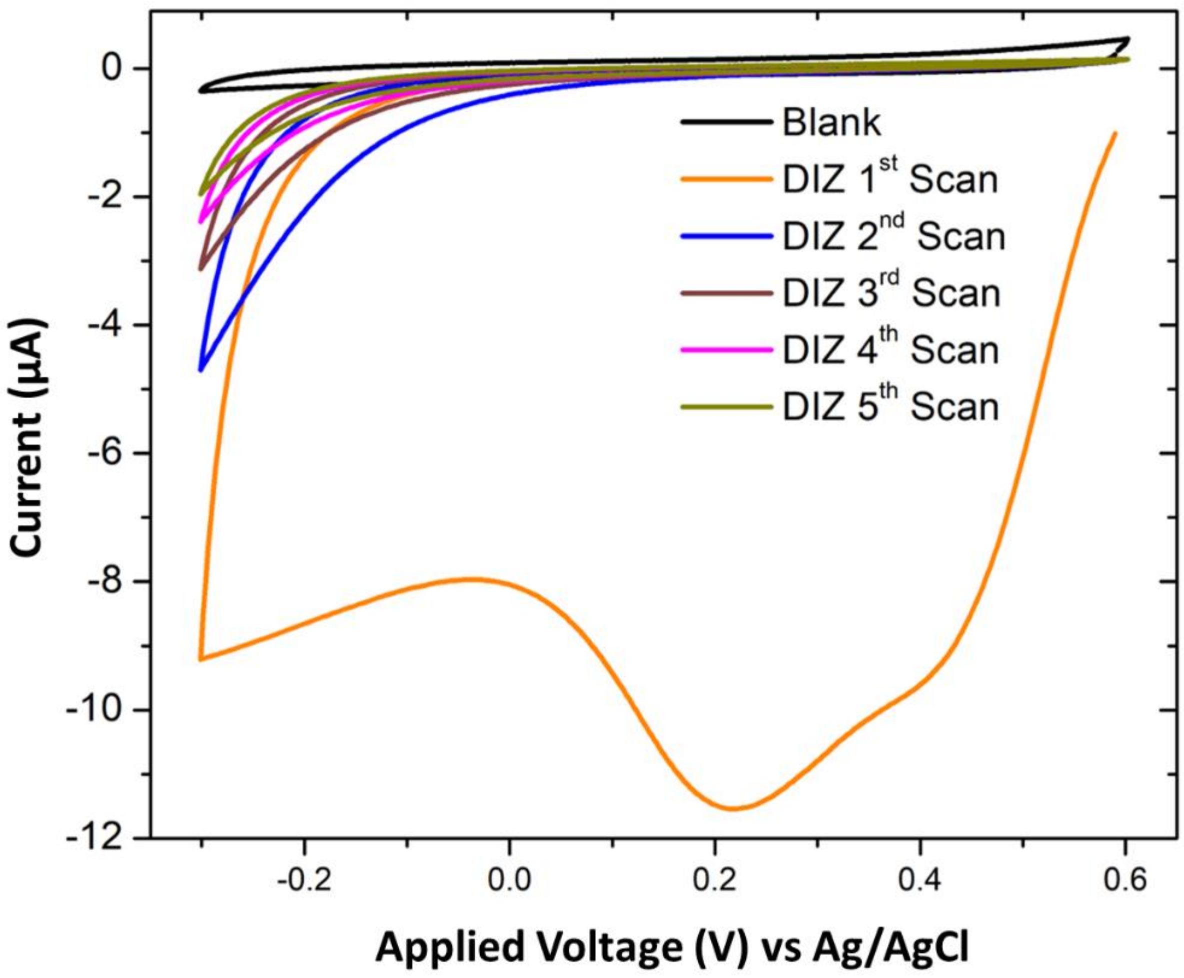

Figure 4. 1: Cyclic voltammograms (50 mV/s) of glassy carbon electrode (GCE) in Bu_4NBF_4 in acetonitrile 0.1 M before (black curve) and after the addition of diazonium (DIZ) (orange curve); after repeated voltammetry cycles (five scans, fifth scan olive green curve), there was no further reduction. The experiment was repeated four times.

GCE substrate **(Figure 4.2(b))**. The attachment of the nitro-phenyl group to the GCE electron represents the overall reduction process.

The peak at 0.2 V completely disappeared in subsequent scans, indicating no further reduction, presumably due to saturation of the available GCE surface with nitrophenyl groups (green curve). This observation is consistent with previous reports [19].

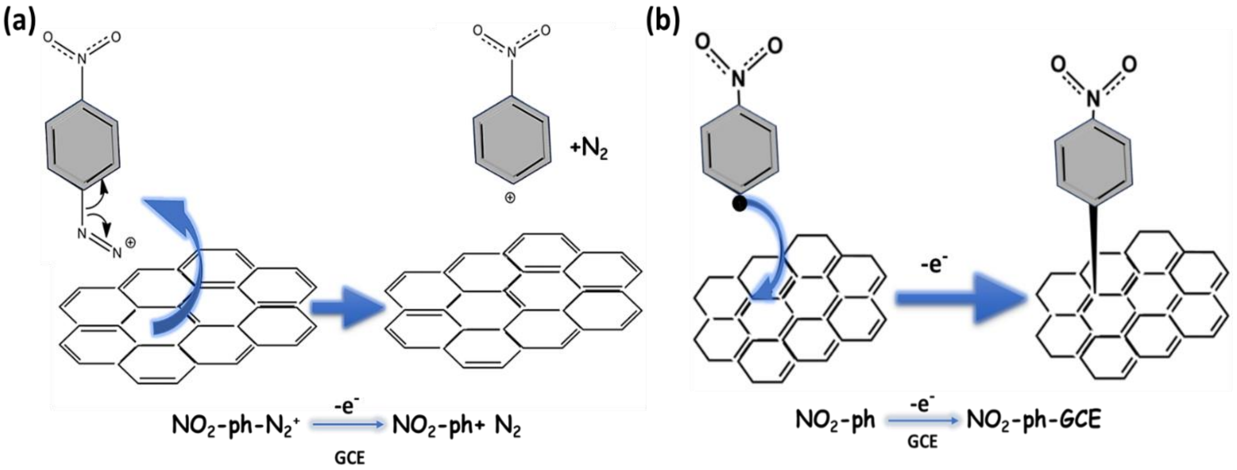

Figure 4. 2: (a) Electron transfer from a glassy carbon electrode to the diazonium cation and subsequent loss of N_2 to form an aryl radical. (b) Nitrophenyl radical and an electron from the surface glassy carbon electrode generate covalent bond with the release of an electron.

4.3.1.2 Electrochemical reduction of 4-nitrophenyl layers on glassy carbon:

Subsequent electrochemical reduction of the nitro group (NO_2) to an amino group (NH_2) was carried out in 0.1M KCl in water: ethanol (9:1) electrolyte. The nitro group (NO_2) to an amino group (NH_2) reduction occurs in the following three steps and are also presented in **Scheme 4.2** [19].

GC Surface-Ph-NO_2+$2H^+$ $\xrightarrow{+2e^-}$ GC Surface-Ph-NO+H_2O **Step 1**

GC Surface-Ph-NO+$2H^+$ $\xleftrightarrow{+2e^-}$ GC Surface-Ph-NHOH **Step 2**

GC Surface-Ph-NHOH+$2H^+$ $\xrightarrow{+2e^-}$ GC Surface-Ph-NH_2 + H_2O **Step 3**

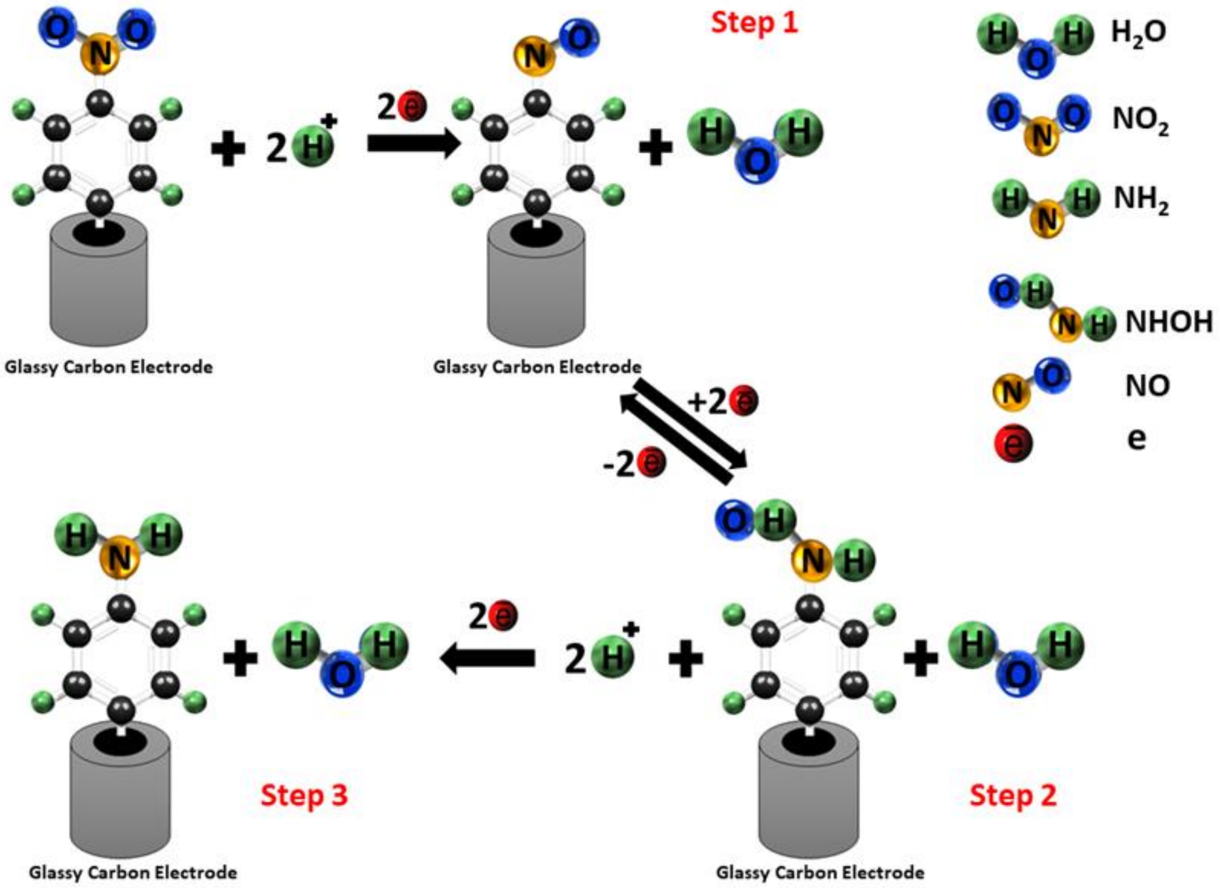

Scheme 4. 1: Electrochemical reduction pathway of nitro group (NO_2) to an amino group (NH_2) in an aqueous electrolyte [19].

Figure 4.3 shows the cyclic voltammetry response of 4-nitrophenyl modified GCEs upon subsequent reduction cycles. A strong reversible reduction peak was observed at -0.9 V at the first scan [19] corresponding to the formation of the hydroxylamine (PhNHOH). In the subsequent scans, a pair of reversible redox peaks disappeared at a half-wave potential of approximately (-0.45 V). This reversible electrochemistry is attributed to the formation of hydroxy aminophenyl on the GCE surface (step 2). The CV data indicate that the reduction of Ar-NO_2 is irreversible. It was also observed from **Figure 4.3** that three CV scans are sufficient for aminophenyl conversion, as overlap in the reduction peaks indicates that no further reduction occurs on the electrode surface after 3 scans (**Figure 4.3 inset**).

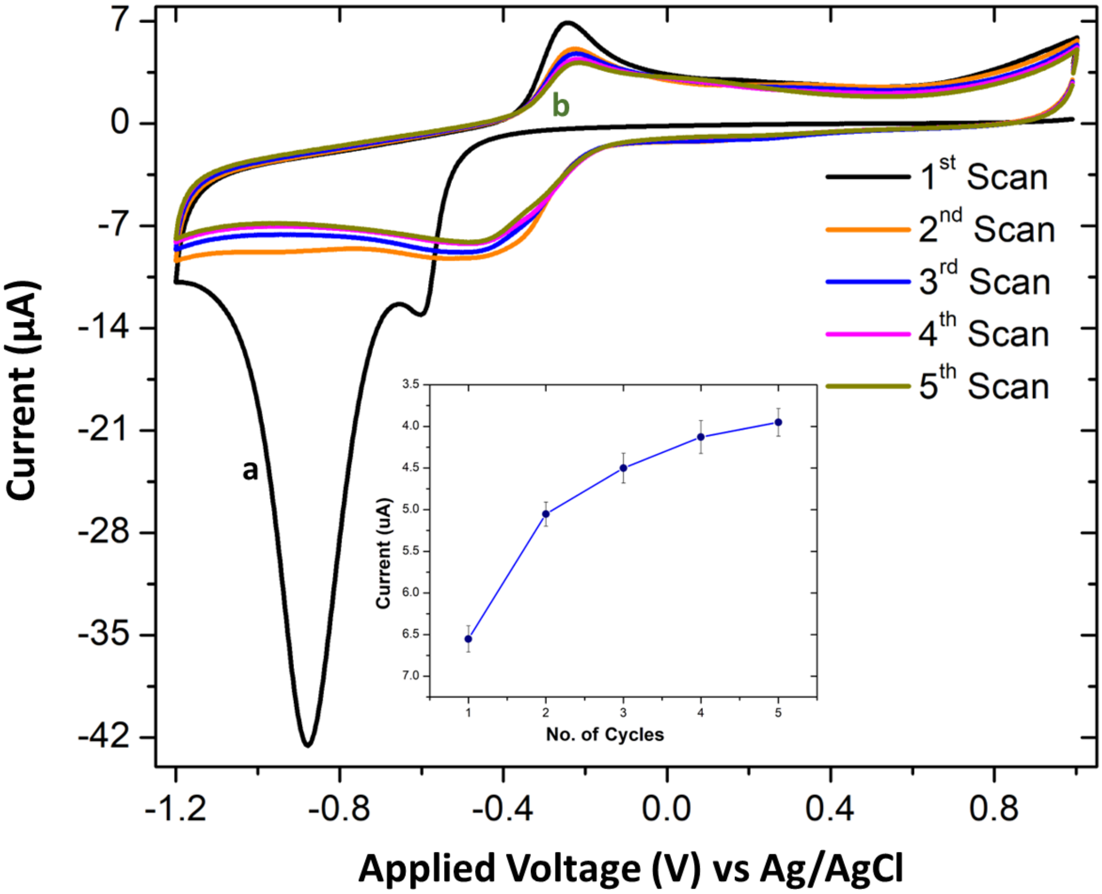

Figure 4. 3: Cyclic voltammograms (50 mV/s) of the reduction of surface-grafted 4-nitro-phenyl on GCE in 0.1 M KCl in water: ethanol (9:1) electrolyte: (a) black curve - one scan; (b) green curve- five scans. The inset figure shows the change of peak current with the number of cycles at -0.2 V. The experiment was repeated four times.

4.3.1.3 Calculation of the number of molecules on the surface:

The surface coverage of aminophenyl after the reduction step in 0.1 M KCl in water: ethanol (9:1) electrolyte was estimated using equation 4.1:

$$\Gamma = Q/nFA \qquad (4.1)$$

Where, Γ is the surface coverage of aminophenyl groups (mol/cm^2), A is the surface area of the electrode (cm^2), n represents the number of electrons involved in the reaction, F is the Faraday constant (C /mol), and Q is the total amount of charge calculated from the integration of the reduction peak recorded using cyclic voltammetry.

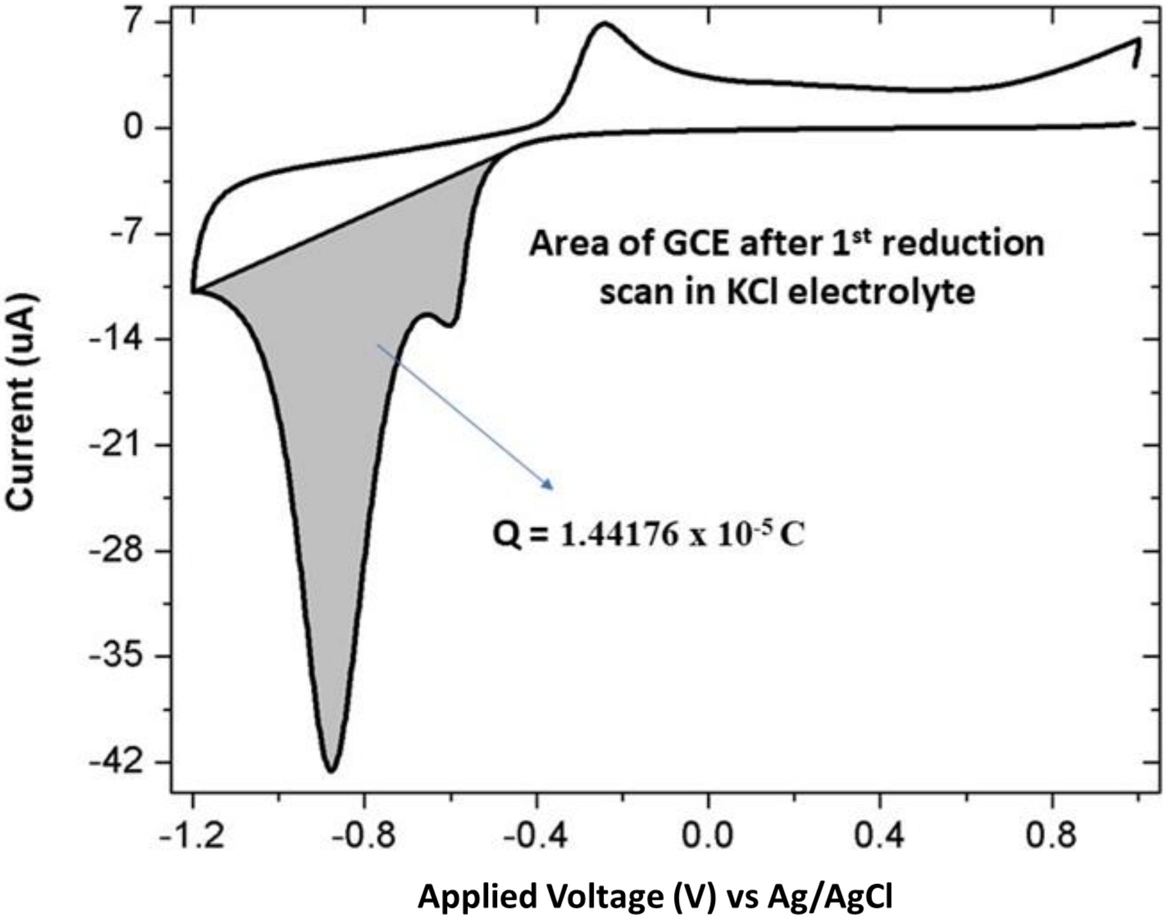

Figure 4. 4: Area under the reduction curve of surface-grafted 4-nitrophenyl on GCE in 0.1 M KCl in water: ethanol (9:1) electrolyte, with scan rate of 50 mV/s the shaded area corresponds to a charge of 1.44176 x10^{-5} C (see Table 4.2).

To calculate the surface coverage of the working electrode, the area under the reduction part of the CV curve can be integrated as indicated in **Figure 4.4**.

The total surface charge on the electrode can be extracted from CV measurements (**Figure 4.4**). When the total surface charge is divided by the charge of one electron, in Coulombs, this gives us the number of molecules attached to the surface (per unit area).

The calculation method is as follows:

Diameter of Glassy Carbon Electrode (D)= **3mm**

Total Area of Glassy Carbon Electrode (A)= $\pi r^2 = 3.14x(1.5mm)^2 =$ **$0.07065cm^2$**

The area occupied by aniline molecule is calculated as:

Area = $\pi r^2 = \pi (2.76\ A^{\circ})^2$ = $\mathbf{23.92\times 10^{-16}\ cm^2}$ [44]

Where r is the radius of the aniline molecule. This shows the minimum area that an aniline molecule will occupy, however, the actual area could be large than this due to the electrostatic repulsion between the aniline molecules. Thus, there should be a correction factor added to the above-calculated area. The tightest way to pack circles in 2D is Hexagonally Close Packed or HCP structure. The volume fraction of HCP Circles is 0.9069 [45]. It is also used as the correction factor. Hence;

The actual area occupied by one aniline molecule = $(1/0.9069) \times (23.92\times 10^{-16})$ = $\mathbf{2.64x10^{-15}}$

The number of molecules on the electrode surface, if completely covered, is then equal to:

Total area of the electrode / area of one molecule = $0.07065/ 2.64\times 10^{-15}$ = $\mathbf{2.67 \times 10^{13}}$

The method for calculating the number of nitrophenyl molecules on the surface that are reduced to aminophenyl groups uses the total charge density of the surface divided by the product of the charge of an electron and the number of electrons involved in the reaction as mentioned before. i.e.,

Number of nitrophenyl molecules reduced = Total charge / (electron charge × 1)

No. of nitrophenyl molecules reduced = $2.46766\times 10^{-6} / (1.6 \times 10^{-19}\times 1)$ = $\mathbf{1.54228 \times 10^{13}}$

(where n=1 and Charge of an electron = 1.6×10^{-19} Coulomb and total charge Q is obtained by integrating the reduction peak (red curve) obtained by CV in **Figure 4.1**)

4.3.1.4 Calculating the surface coverage:

The surface coverage at 50 mV.s^{-1} scan rate was estimated using equation 4.1:

$\mathbf{\Gamma = Q/nFA}$

Here, Charge Q is calculated from the integration of the reduction peak of CV curves in the KCl electrolyte after different scans (**Figure 4.4**).

4.3.1.4.1 Surface Coverage of aminophenyl after reduction in 0.1M KCL:

Number of electrons involved in the reaction (n) = 6

Number of Scans	Area of Electrode (cm^2)	Area Under the Curve Q × 10^{-6} (C)	Number of Molecules × 10^{-12}	Surface Coverage of aminophenyl × 10^{-10} (mol/cm^2)
1	0.071	14.5	15.1	**3.53**
2	0.071	5.34	5.55	**1.30**
3	0.071	5.36	5.56	**1.32**
4	0.071	4.87	5.06	**1.19**
5	0.071	4.56	4.73	**1.11**

Table 4. 2: Surface coverage of aminophenyl groups, estimated using an electrochemical method.

4.3.2 QUANTIFICATION OF SURFACE AMINE GROUPS:

The surface coverage of amines on modified electrodes was quantified by functionalizing the amine groups with FCA, using a standard N-(3-dimethylaminopropyl)-N’-ethyl carbodiimide EDC/NHS coupling reaction (**Scheme 4.3**), as follows.

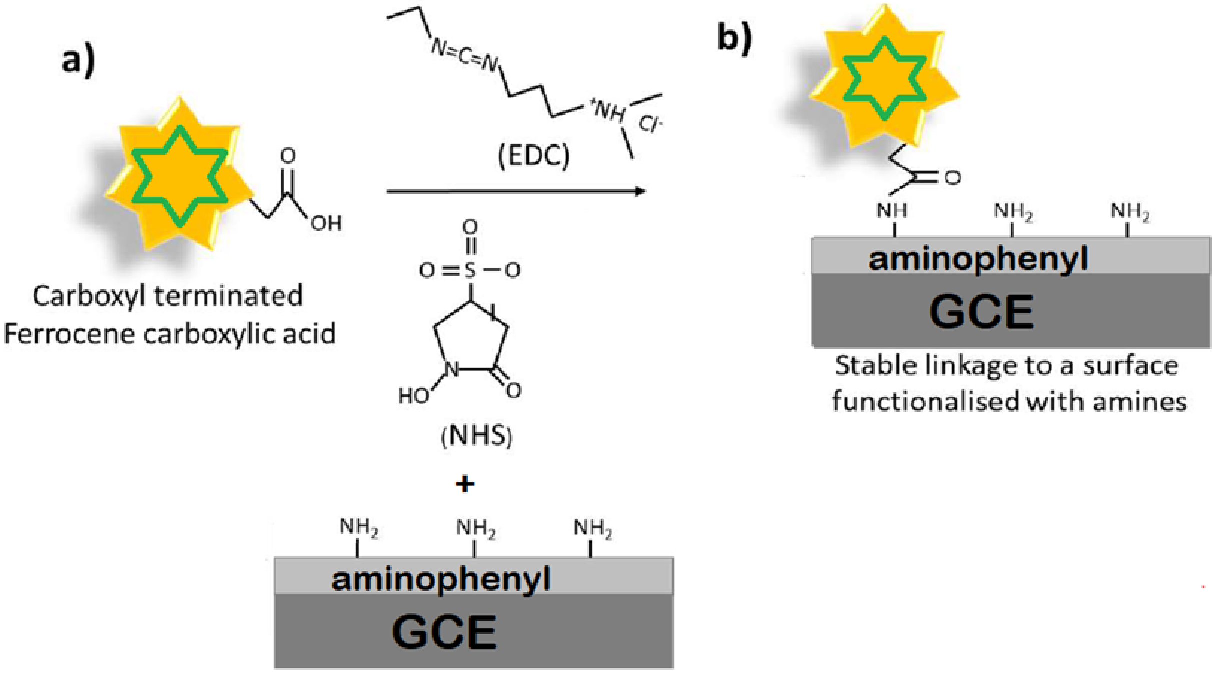

Scheme 4. 2: Immobilisation mechanism of electrochemically active FCA on to an amine modified GCE through carbodiimide linking.

Figure 4.5 shows the CV measurements performed in order to confirm the attachment of FCA to surface-bound amino phenyl groups.

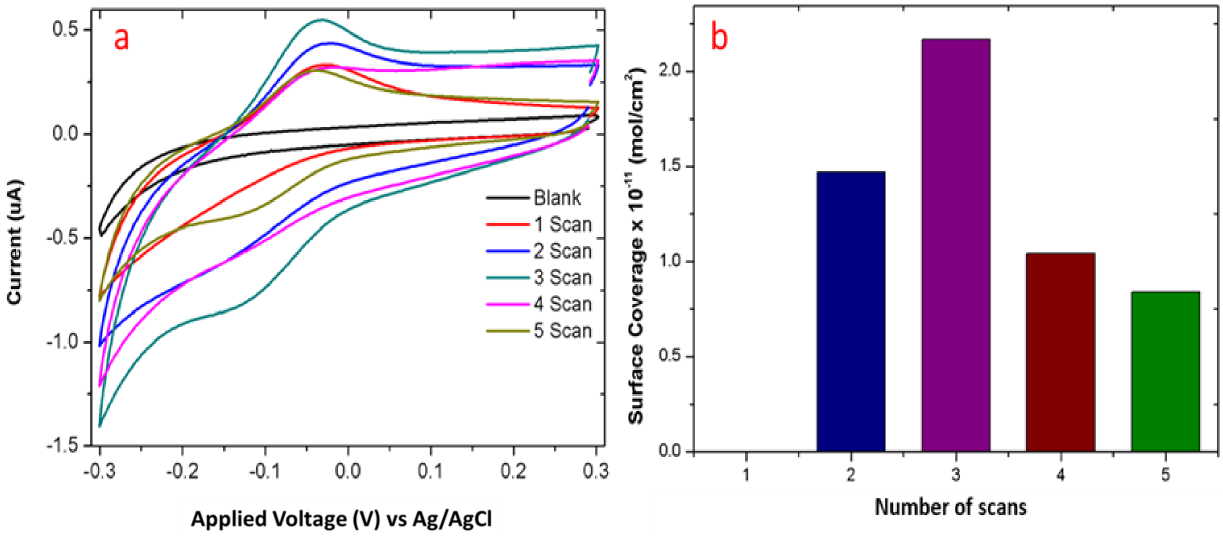

Figure 4. 5: (a) Cyclic voltammograms (5 mV/s) of FCA-functionalization of amine functionalized GCEs prepared using a different number of reduction scans (scans 1-5), in PBS electrolyte. (b) The bar chart shows the degree of FCA functionalization which is a maximum for the amine functionalized GCE prepared using three scans.

4.3.2.1 Surface Coverage estimation after FCA attachment:

Here, the charge Q is calculated from the integration of the reduction peak of CV curves after FCA functionalization after different scans (**Figure 4.6**).

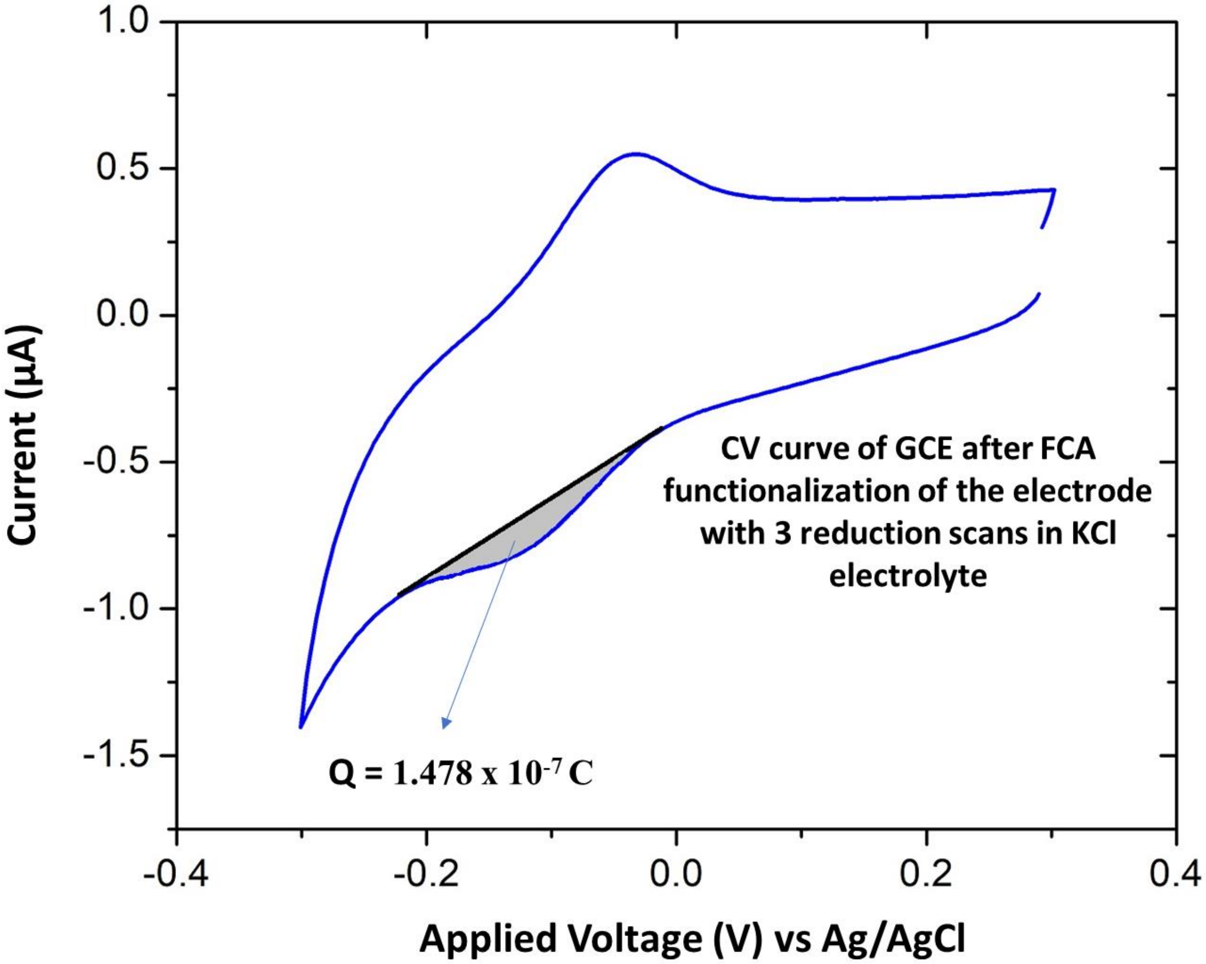

Figure 4. 6: Area under the reduction curve of FCA functionalized GCE after 3 scans of nitrophenyl to aminophenyl in 0.1 M KCl in water: ethanol (9:1) electrolyte, reference electrode (Ag/AgCl), with scan rate of 5 mV s^{-1} the shaded area corresponds to a charge of 1.478 $x10^{-7}$ C (see Table 4.3).

Number of electrons involved in the reaction (n) = 1

Number of Scans	Area of Electrode (cm^2)	Area Under the Curve Q × 10^{-8} (C)	Number of Molecules × 10^{12}	Surface Coverage × 10^{-12} (mol/cm^2)
1	0.071	0	0	**0**
2	0.071	10.1	0.63	**14.7**
3	0.071	14.8	0.93	**21.7**
4	0.071	7.12	0.45	**10.4**
5	0.071	5.75	0.36	**8.4**

Table 4. 3 Surface coverage of aminophenyl groups, estimated using an electrochemical method.

As anticipated, our electrochemical measurements show no FCA attachment to measurements conducted on the first control of blank GCE due to the lack of amine surface groups on pristine GCE (first control).

It was expected to observe strong FCA binding to the GCE-$PhNO_2$ (reduction scan-1) as the current literature reports that the large irreversible reduction peak in the first scan, towards the negative potential, is due to the reduction of p-nitrophenyl to p-aminophenyl. However, in striking contrast, the scan where GCE-$PhNO_2$ (reduction scan-1) underwent only a single reduction cycle in KCl, showed no redox peaks upon FCA functionalization. However, FCA binding was observed for the electrodes under consecutive scans (reduction scan 2-5 in KCl). The surface coverage of FCA at reduction scan-2 was found to be 14.7 $pmol/cm^2$ (**Table 4.3**). This may be due to the fact that a single reduction of GCE-$PhNO_2$ was not sufficient to generate amine surface moieties, instead produces only an intermediate GCE-PhNHOH moiety, which further needs additional scans to generate amine groups [46].

It is also found that the surface coverage of FCA varies strongly depending on the number of reduction scans (as shown in **Figure 4.5**). It is found that the maximum degree of surface coverage is achieved for the sample prepared at reduction scan-3 (21.7 pmol/cm^2), whereas any further increase in scan reduces the FCA coverage.

4.3.3 ELECTROCHEMICAL SENSING VIA ANALYSIS OF THE ELECTRODES:

In order to confirm this behavior in a practical sensor, we have used diazonium functionalization to prepare a sensor incorporating a carboxyl terminated anti-beta amyloid antibody specific to Aβ (1-42) peptide, a potential marker for Alzheimer's disease. In this case, the sensor response is a reduction in current in differential pulsed voltammetry (DPV) as the bound peptide acts as a barrier to electron transfer at the electrode surface.

Figure 4.7 shows the percentage current reduction (%I_R) plotted against the log of analyte concentrations. The sensing results indicate that electrode made from an amino substrate prepared using reduction scan-3 shows significantly higher sensitivity (slope: 5.07 and R^2=0. 98) than those prepared using scans-5 (slope: 2.85 and R^2= 0.65). The regression equation has a logarithmic linear relation with Aβ (1-42) concentration (0 ng/mL to 200 ng/mL) with $R^2 = 0.98$ as the correlation coefficient.

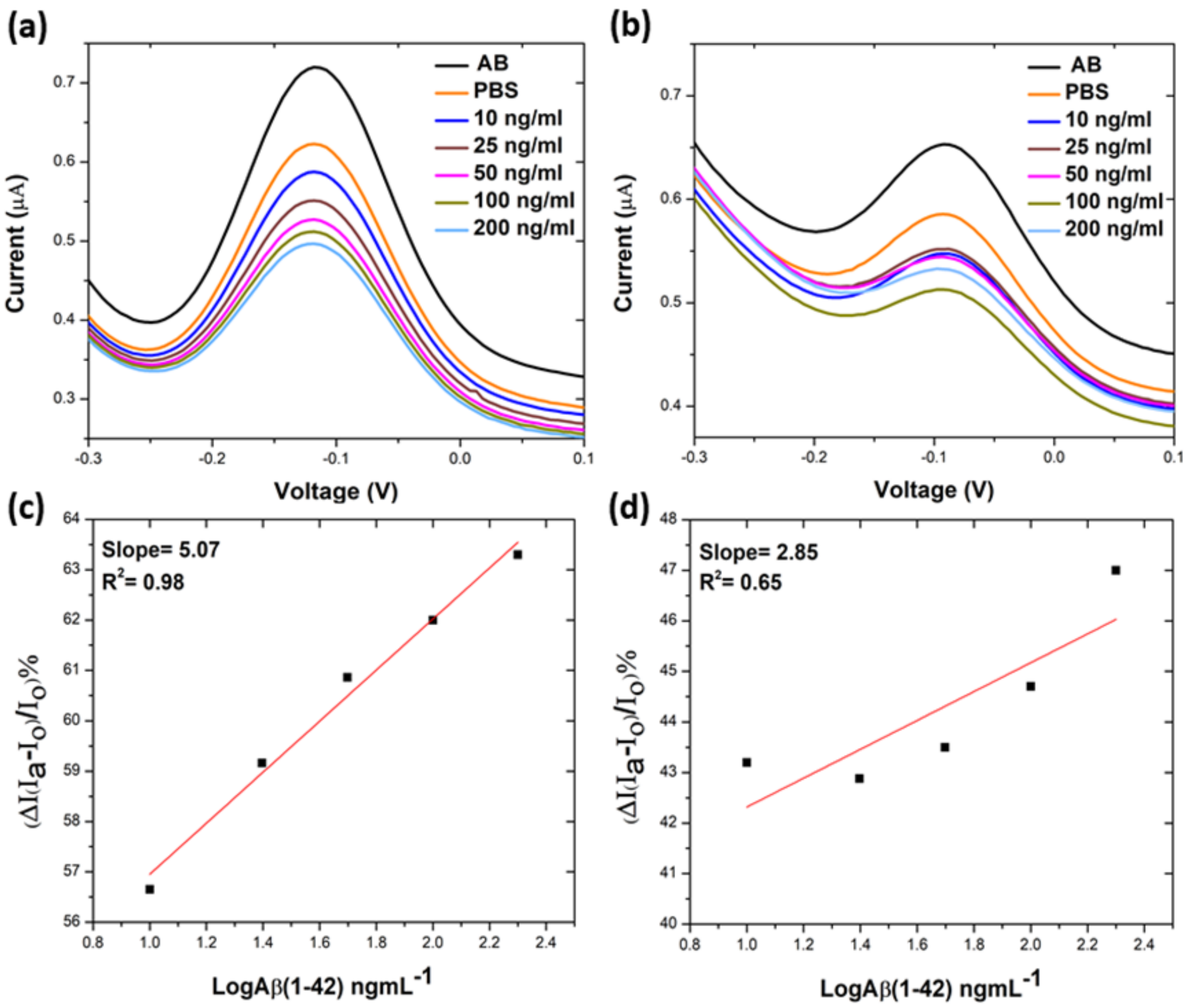

Figure 4. 7: Differential pulse voltammetry (DPV) results for Aβ (1-42) peptide sensors made from amino functionalized substrates using different numbers of reduction scans. (a-b) 3 and 5scans; (c-d) corresponding calibration curves of %I_R [$\Delta I(I_a-I_o)/I_o)\%$] (percentage current reduction) against log Aβ(1-42) concentrations.

It is worth mentioning that the control electrodes (GCE, reduction scan-0, and reduction scan-2) (**Figure 4.8**) showed weak to no significant change in signal upon exposure to the peptide. This confirms that the experimental conditions of diazotisation greatly influence the sensor performance and the nitrophenyl to aminophenyl conversion occurs at the reduction scan-2, instead of reduction scan-1.

The pattern of results obtained from these reduction cycles with antibodies match those conducted with FCA attachment, and utilizing FCA is a novel, fast and cheap way of gauging

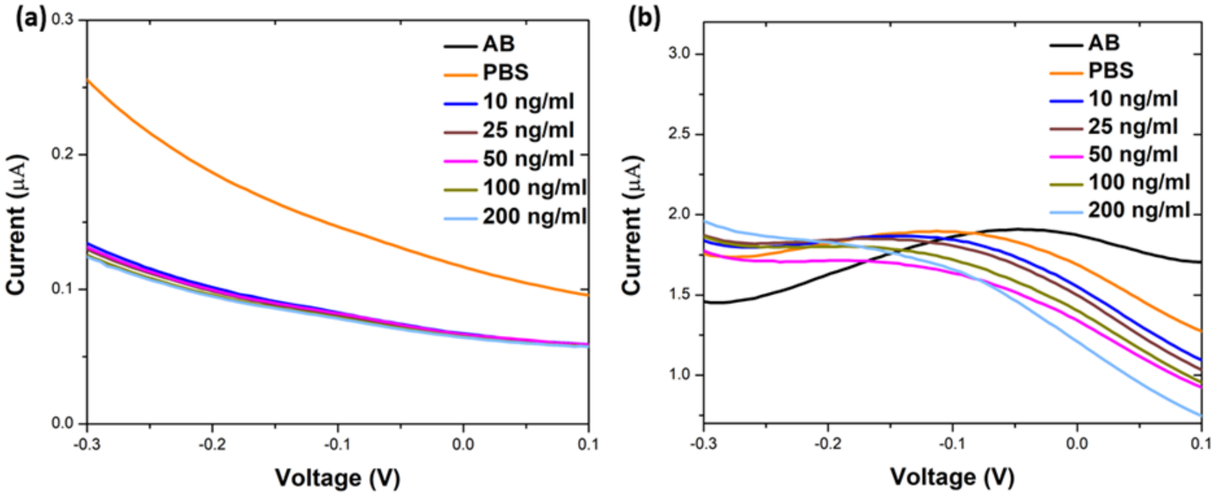

Figure 4. 8: Control Differential pulse voltammetry (DPV) results for Aβ (1-42) peptide sensors made from amino functionalized substrates using different numbers of reduction scans. (a-b) 0 and 2 scans respectively.

the potential sensitivity of a sensor platform made by any particular process, without the need for complete manufacture of the sensor itself.

4.3.4 CHARACTERIZATION OF SURFACE MORPHOLOGY ELECTRODE:

The effect on the surface morphology of surface diazotization was investigated using AFM on the HOPG electrode. 40×40 µm AFM scans were conducted in intermittent contact mode. The data was levelled using a linear background and a high pass filter was used to remove large-scale undulations in the HOPG. The roughness and morphology of functionalized substrate are shown in **Figure 4.9**.

The surface roughness appears similar between samples after 1, 3, and 5 scans, with graphite step edges still visible after 5 cycles. The Root Mean Square (RMS) roughness was generally higher on the blank samples (~5 nm) when compared with the functionalized samples (1-2 nm).

However, no clear difference is observed in roughness values between the functionalized samples, with similar topography apparent in the AFM images (**Figure 4.9 (b-d)**).

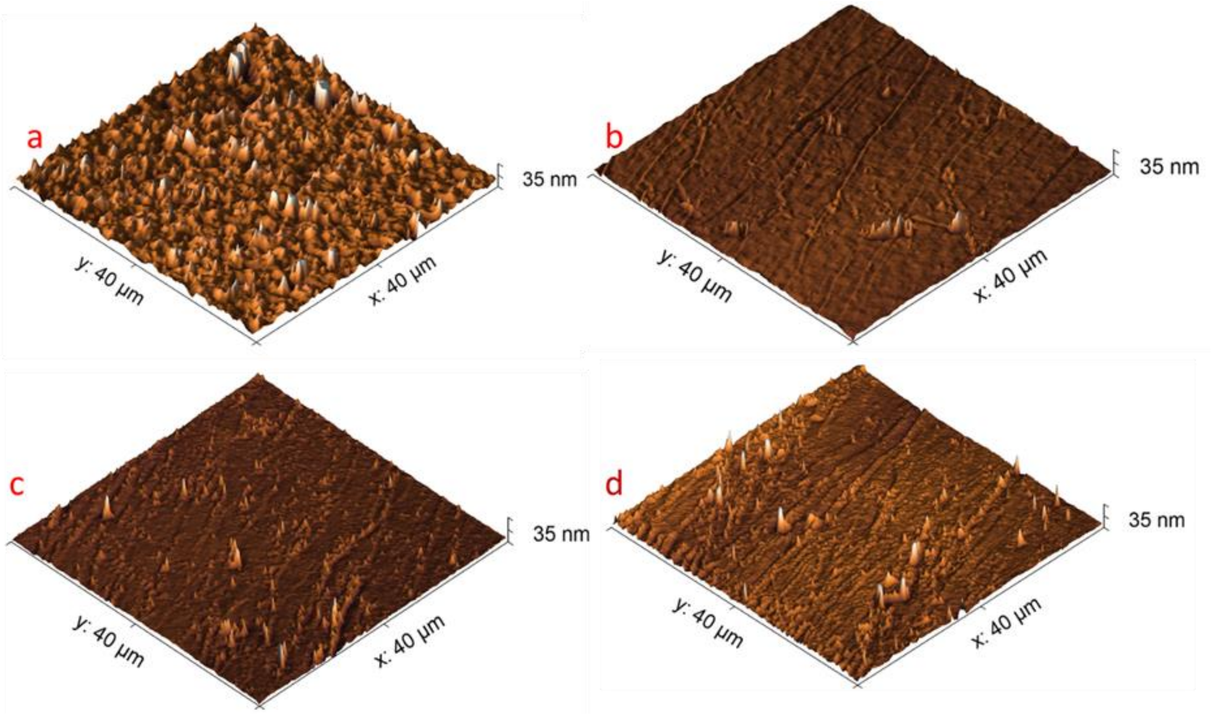

Figure 4. 9: Morphology of HOPG electrode with AFM (a) blank -before diazotisation (b) after diazotisation one scan (c) after three scans (d) after five scans.

Scanning electron microscopy (SEM) of the HOPG surface reveals a similar suppression of surface features following initial functionalization with the diazotisation method (**Figure 4.10 (a-b)**), in agreement with AFM.

However, a reduction in visible step edges in the underlying HOPG with the increasing number of cycles is also observed (**Figure 4.10 (b-d)**). This could be explained by the suppression of low-energy secondary electron contrast at step edges due to the presence of an overlayer or thin film [47].

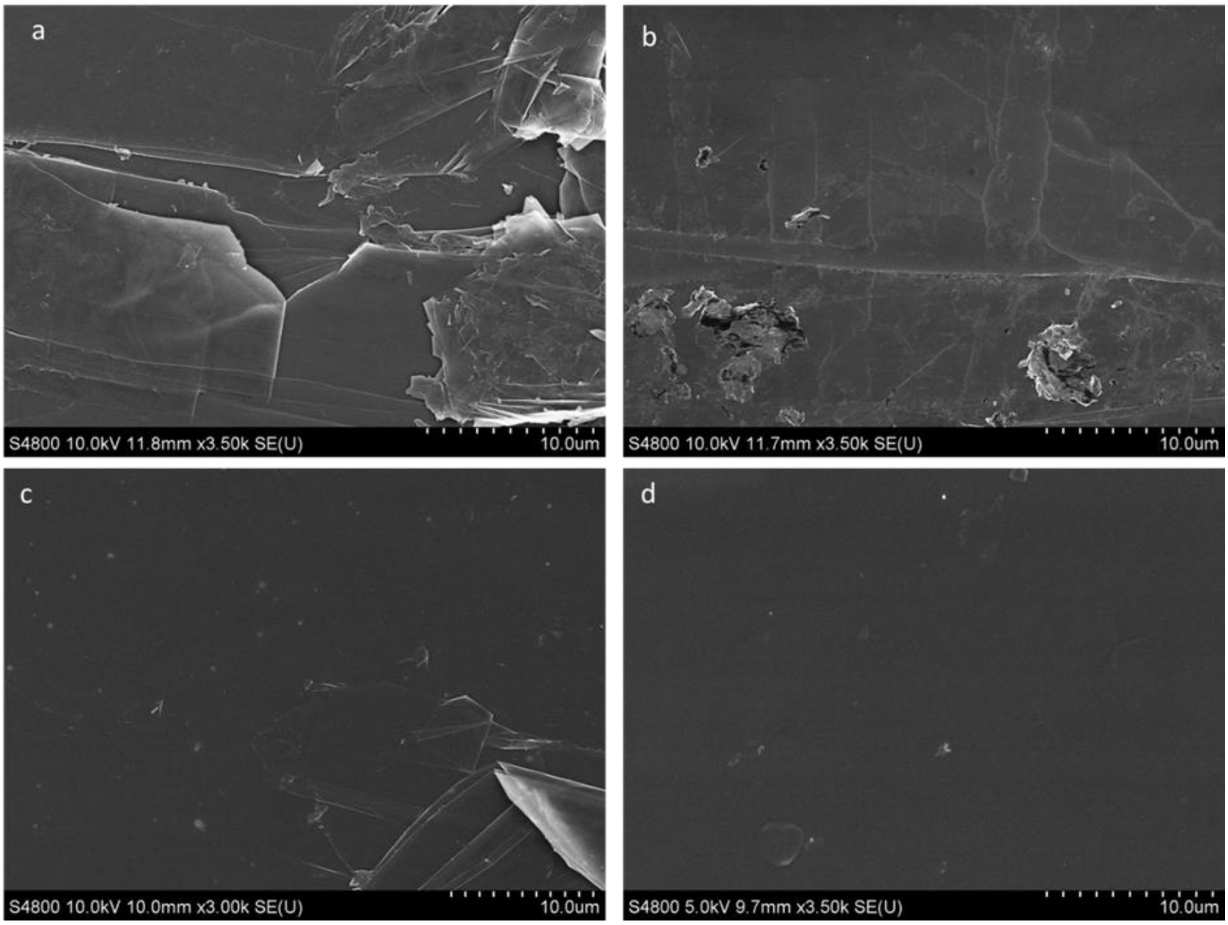

Figure 4. 10: Morphology of HOPG electrode with SEM (a) blank -before diazotisation (b) after diazotisation one scan (c) after three scan (d) after five scans

It is possible that AFM in intermittent contact mode is probing some underlying topography through the functional layer, explaining this discrepancy in observed surface morphology.

4.4 CONCLUSIONS

Despite diazotisation being a well-researched topic, there have been no previous reports concerning the quantification of surface coverage of aminophenyl groups, following the conversion of 4-nitrophenyl films (deposited via electrochemical methods), or the optimal conditions required for this reaction. Understanding the extent of conversion of the nitro moiety on different electrode surfaces provides useful information for electroanalytical chemistry researchers in their design of surfaces, and electrochemical procedures, for biosensor molecule immobilization.

Ferrocene carboxylic acid was introduced as a rapid and cheap assay to assess the surface coverage of amino-phenyl groups on electrodes. The number of electrons transferred during attachment of ferrocene carboxylic acid indicates an available amine coverage of only ca 1/40th of that which might be expected from the number of electrons used in the initial diazotisation process, i.e., $2.2\times l0^{-11}$ mol/cm^2 compared to $8.02 \pm 0.2 \times l0^{-10}$ (mol/cm^2). Furthermore, the available amine coverage was critically dependent upon the number of CV cycles used in the reduction, and thus the procedures used in this step influence the sensitivity of any subsequent sensor. The applicability of these ideas was explored in the preparation of a sensor incorporating a carboxyl terminated anti-beta amyloid antibody specific to Aβ (1-42) peptide, a potential marker for Alzheimer's disease. At optimum amine coverage, the sensitivity of the differential pulse voltammetry sensor was in the range of 0-200 ng/mL with a slope of 5.07 µA/ng. mL^{-1} and R^2=0. 98.

BIBLIOGRAPHY

---

[1] M. Asal, Ö. Özen, M. Şahinler, H.T. Baysal, İ. Polatoğlu, An overview of biomolecules, immobilization methods and support materials of biosensors, Sens. Rev. 39 (2019) 377–386. https://doi.org/10.1108/SR-04-2018-0084.

[2] M.D. Sonawane, S.B. Nimse, Surface Modification Chemistries of Materials Used in Diagnostic Platforms with Biomolecules, J. Chem. (2016). https://doi.org/10.1155/2016/9241378.

[3] M.A. Booth, K. Kannappan, A. Hosseini, A. Partridge, In-Depth Electrochemical Investigation of Surface Attachment Chemistry via Carbodiimide Coupling, Langmuir. 31 (2015) 8033–8041. https://doi.org/10.1021/acs.langmuir.5b01863.

[4] M. Revenga-Parra, A.M. Villa-Manso, M. Briones, E. Mateo-Martí, E. Martínez-Periñán, E. Lorenzo, F. Pariente, Bioelectrocatalytic platforms based on chemically modified nanodiamonds by diazonium salt chemistry, Electrochim. Acta. 357 (2020) 136876. https://doi.org/10.1016/j.electacta.2020.136876.

[5] L. Pichereau, I. López, M. Cesbron, S. Dabos-Seignon, C. Gautier, T. Breton, Controlled diazonium electrografting driven by overpotential reduction: A general strategy to prepare ultrathin layers, Chem. Commun. 55 (2019) 455–457. https://doi.org/10.1039/c8cc08331b.

[6] M. Cesbron, S. Dabos-Seignon, C. Gautier, T. Breton, Enhanced electrocatalytic activity on TEMPO mixed film grafted by diazonium reduction, Electrochim. Acta. 345 (2020) 136190. https://doi.org/10.1016/j.electacta.2020.136190.

[7] M. Delamar, R. Hitmi, J. Pinson, J. Savéant, Covalent Modification of Carbon Surfaces by Grafting of Functionalized Aryl Radicals Produced from Electrochemical Reduction of Diazonium Salts, J. Am. Chem. Soc. 114 (1992) 5883–5884.

https://doi.org/10.1021/ja00040a074.

[8] A.J. Downard, Electrochemically assisted covalent modification of carbon electrodes, Electroanalysis. 12 (2000) 1085–1096. https://doi.org/10.1002/1521-4109(200010)12:14<1085::AID-ELAN1085>3.0.CO;2-A.

[9] J. Pinson, F. Podvorica, Attachment of organic layers to conductive or semiconductive surfaces by reduction of diazonium salts, Chem. Soc. Rev. 34 (2005) 429–439. https://doi.org/10.1039/b406228k.

[10] R.L. McCreery, Advanced carbon electrode materials for molecular electrochemistry, Chem. Rev. 108 (2008) 2646–2687. https://doi.org/10.1021/cr068076m.

[11] M. Picot, L. Lapinsonnière, M. Rothballer, F. Barrière, Graphite anode surface modification with controlled reduction of specific aryl diazonium salts for improved microbial fuel cells power output, Biosens. Bioelectron. 28 (2011) 181–188. https://doi.org/10.1016/j.bios.2011.07.017.

[12] Y.R. Leroux, F. Hui, J.M. Noël, C. Roux, A.J. Downard, P. Hapiot, Design of robust binary film onto carbon surface using diazonium electrochemistry, Langmuir. 27 (2011) 11222–11228. https://doi.org/10.1021/la202250y.

[13] D. Hetemi, C. Combellas, F. Kanoufi, J. Pinson, F.I. Podvorica, Surface modification by electrochemical reduction of alkyldiazonium salts, Electrochem. Commun. 68 (2016) 5–9. https://doi.org/10.1016/j.elecom.2016.04.001.

[14] F. Zen, M.D. Angione, J.A. Behan, R.J. Cullen, T. Duff, J.M. Vasconcelos, E.M. Scanlan, P.E. Colavita, Modulation of Protein Fouling and Interfacial Properties at Carbon Surfaces via Immobilization of Glycans Using Aryldiazonium Chemistry, Sci. Rep. 6 (2016) 1–10. https://doi.org/10.1038/srep24840.

[15] O.J. Guy, G. Burwell, Z. Tehrani, A. Castaing, K.A. Walker, S.H. Doak, Graphene nano-biosensors for detection of cancer risk, Mater. Sci. Forum. 711 (2012) 246–252.

https://doi.org/10.4028/www.scientific.net/MSF.711.246.

[16] O.J. Guy, A. Castaing, Z. Tehrani, S.H. Doak, Fabrication of ultrasensitive graphene nanobiosensors, Proc. IEEE Sensors. 711 (2010) 907–912. https://doi.org/10.1109/ICSENS.2010.5690883.

[17] Z. Tehrani, G. Burwell, M.A. Mohd Azmi, A. Castaing, R. Rickman, J. Almarashi, P. Dunstan, A. Miran Beigi, S.H. Doak, O.J. Guy, Generic epitaxial graphene biosensors for ultrasensitive detection of cancer risk biomarker, 2D Mater. 1 (2014) 025004. https://doi.org/10.1088/2053-1583/1/2/025004.

[18] Z. Tehrani, D.J. Thomas, O.J. Guy, Electrochemical Biofunctionalization of Highly Oriented Pyrolytic Graphite for Immunosensor Applications, E-Journal Surf. Sci. Nanotechnol. 14 (2016) 193–197. https://doi.org/10.1380/ejssnt.2016.193.

[19] A.L. Gui, G. Liu, M. Chockalingam, G. Le Saux, E. Luais, J.B. Harper, J.J. Gooding, A Comparative Study of Electrochemical Reduction of 4-Nitrophenyl Covalently Grafted on Gold and Carbon, Electroanalysis. 22 (2010) 1824–1830. https://doi.org/10.1002/elan.201000164.

[20] A.M. Mahmoud, A.J. Bergren, N. Pekas, R.L. McCreery, Towards Integrated Molecular Electronic Devices: Characterization of Molecular Layer Integrity During Fabrication Processes, Adv. Funct. Mater. 21 (2011) 2273–2281. https://doi.org/10.1002/adfm.201002496.

[21] S.Q. Lud, M. Steenackers, R. Jordan, P. Bruno, D.M. Gruen, P. Feulner, J.A. Garrido, M. Stutzmann, Chemical grafting of biphenyl self-assembled monolayers on ultrananocrystalline diamond, J. Am. Chem. Soc. 128 (2006) 16884–16891. https://doi.org/10.1021/ja0657049.

[22] E. Bekyarova, M.E. Itkis, P. Ramesh, C. Berger, M. Sprinkle, W.A. De Heer, R.C. Haddon, Chemical modification of epitaxial graphene: Spontaneous grafting of aryl

groups, J. Am. Chem. Soc. 131 (2009) 1336–1337. https://doi.org/10.1021/ja8057327.

[23] Y.L. Zhong, A. Midya, Z. Ng, Z.K. Chen, M. Daenen, M. Nesladek, K.P. Loh, Diamond-based molecular platform for photoelectrochemistry, J. Am. Chem. Soc. 130 (2008) 17218–17219. https://doi.org/10.1021/ja805977f.

[24] J.T. Abrahamson, C. Song, J.H. Hu, J.M. Forman, S.G. Mahajan, N. Nair, W. Choi, E.J. Lee, M.S. Strano, Synthesis and energy release of nitrobenzene-functionalized single-walled carbon nanotubes, Chem. Mater. 23 (2011) 4557–4562. https://doi.org/10.1021/cm201947y.

[25] Y.A. Atmane, L. Sicard, A. Lamouri, J. Pinson, M. Sicard, C. Masson, S. Nowak, P. Decorse, J.Y. Piquemal, A. Galtayries, C. Mangeney, Functionalization of aluminum nanoparticles using a combination of aryl diazonium salt chemistry and iniferter method, J. Phys. Chem. C. 117 (2013) 26000–26006. https://doi.org/10.1021/jp406356s.

[26] V.Q. Nguyen, Y. Ai, P. Martin, J.C. Lacroix, Plasmon-Induced Nanolocalized Reduction of Diazonium Salts, ACS Omega. 2 (2017) 1947–1955. https://doi.org/10.1021/acsomega.7b00394.

[27] R. Ahmad, L. Boubekeur-Lecaque, M. Nguyen, S. Lau-Truong, A. Lamouri, P. Decorse, A. Galtayries, J. Pinson, N. Felidj, C. Mangeney, Tailoring the surface chemistry of gold nanorods through Au-C/Ag-C covalent bonds using aryl diazonium salts, J. Phys. Chem. C. 118 (2014) 19098–19105. https://doi.org/10.1021/jp504040d.

[28] N. Griffete, A. Lamouri, F. Herbst, N. Felidj, S. Ammar, C. Mangeney, Synthesis of highly soluble polymer-coated magnetic nanoparticles using a combination of diazonium salt chemistry and the iniferter method, RSC Adv. 2 (2012) 826–830. https://doi.org/10.1039/c1ra00577d.

[29] N. Griffete, F. Herbst, J. Pinson, S. Ammar, C. Mangeney, Preparation of water-soluble magnetic nanocrystals using aryl diazonium salt chemistry, J. Am. Chem. Soc. 133 (2011)

1646–1649. https://doi.org/10.1021/ja108928b.

[30] S. Maldonado, T.J. Smith, R.D. Williams, S. Morin, E. Barton, K.J. Stevenson, Surface modification of indium tin oxide via electrochemical reduction of aryldiazonium cations, Langmuir. 22 (2006) 2884–2891. https://doi.org/10.1021/la052696l.

[31] S. Gam-Derouich, J. Pinson, P. Decorse, Y. Luo, R. Herbaut, L. Royon, C. Mangeney, Diazonium salt chemistry for the design of nano-textured anti-icing surfaces, Chem. Commun. 54 (2018) 8983–8986. https://doi.org/10.1039/c8cc02601g.

[32] Y.C. Liu, R.L. McCreery, Reactions of Organic Monolayers on Carbon Surfaces Observed with Unenhanced Raman Spectroscopy, J. Am. Chem. Soc. 117 (1995) 11254–11259. https://doi.org/10.1021/ja00150a024.

[33] C. Saby, B. Ortiz, G.Y. Champagne, D. Bélanger, Electrochemical modification of glassy carbon electrode using aromatic diazonium salts. 1. Blocking effect of 4-nitrophenyl and 4-carboxyphenyl groups, Langmuir. 13 (1997) 6805–6813. https://doi.org/10.1021/la961033o.

[34] B. Ortiz, C. Saby, G.Y. Champagne, D. Bélanger, Electrochemical modification of a carbon electrode using aromatic diazonium salts. 2. Electrochemistry of 4-nitrophenyl modified glassy carbon electrodes in aqueous media, J. Electroanal. Chem. 455 (1998) 75–81. https://doi.org/10.1016/S0022-0728(98)00252-6.

[35] A.J. Downard, Potential-dependence of self-limited films formed by reduction of aryldiazonium salts at glassy carbon electrodes, Langmuir. 16 (2000) 9680–9682. https://doi.org/10.1021/la000866i.

[36] D. Shin, N. Tokuda, B. Rezek, C.E. Nebel, Periodically arranged benzene-linker molecules on boron-doped single-crystalline diamond films for DNA sensing, Electrochem. Commun. 8 (2006) 844–850. https://doi.org/10.1016/j.elecom.2006.03.014.

[37] N.G. Welch, J.A. Scoble, B.W. Muir, P.J. Pigram, Orientation and characterization of

immobilized antibodies for improved immunoassays (Review), Biointerphases. 12 (2017) 02D301. https://doi.org/10.1116/1.4978435.

[38] Y.K. Yen, C.Y. Huang, C.H. Chen, C.M. Hung, K.C. Wu, C.K. Lee, J.S. Chang, S. Lin, L.S. Huang, A novel, electrically protein-manipulated microcantilever biosensor for enhancement of capture antibody immobilization, Sensors Actuators, B Chem. 141 (2009) 498–505. https://doi.org/10.1016/j.snb.2009.06.038.

[39] N.S. Ferreira, M.G.F. Sales, Disposable immunosensor using a simple method for oriented antibody immobilization for label-free real-time detection of an oxidative stress biomarker implicated in cancer diseases, Biosens. Bioelectron. 53 (2014) 193–199. https://doi.org/10.1016/j.bios.2013.09.056.

[40] A. Devadoss, R. Forsyth, R. Bigham, H. Abbasi, M. Ali, Z. Tehrani, Y. Liu, O.J. Guy, Ultrathin Functional Polymer Modified Graphene for Enhanced Enzymatic Electrochemical Sensing, Biosensors. 9 (2019) 16. https://doi.org/10.3390/bios9010016.

[41] F. Walters, M. Munem Ali, G. Burwell, S. Rozhko, Z. Tehrani, E. Daghigh Ahmadi, J.E. Evans, H.Y. Abbasi, R. Bigham, J. John Mitchell, O. Kazakova, A. Devadoss, O.J. Guy, A facile method for the non-covalent amine functionalization of carbon-based surfaces for use in biosensor development, Nanomaterials. 10 (2020) 1–14. https://doi.org/10.3390/nano10091808.

[42] M.A. Mohd Azmi, Z. Tehrani, R.P. Lewis, K.A.D. Walker, D.R. Jones, D.R. Daniels, S.H. Doak, O.J. Guy, Highly sensitive covalently functionalised integrated silicon nanowire biosensor devices for detection of cancer risk biomarker, Biosens. Bioelectron. 52 (2014) 216–224. https://doi.org/10.1016/j.bios.2013.08.030.

[43] E. House, J. Collingwood, A. Khan, O. Korchazkina, G. Berthon, C. Exley, Aluminium, iron, zinc and copper Influence the in vitro formation of amyloid fibrils of Aβ42 in a manner which may have consequences for metal chelation therapy in Alzheimer's disease,

J. Alzheimer’s Dis. 6 (2004) 291–301. https://doi.org/10.3233/JAD-2004-6310.

[44] Drexel-University. Hexagonally-Closed-Packed (HCP) Circles. 2012; Available from: http://www.pages.drexel.edu/~bel23/HCP.html

[45] Reis, S.D.S., et al., How dense can one pack spheres of arbitrary size distribution? Europhysics Letters, 2012. 97(1): p. 18004.

[46] W. Wang, L. Ge, X. Sun, T. Hou, F. Li, Graphene-Assisted Label-Free Homogeneous Electrochemical Biosensing Strategy based on Aptamer-Switched Bidirectional DNA Polymerization, ACS Appl. Mater. Interfaces. 7 (2015) 28566–28575. https://doi.org/10.1021/acsami.5b09932.

[47] K. Shihommatsu, J. Takahashi, Y. Momiuchi, Y. Hoshi, H. Kato, Y. Homma, Formation Mechanism of Secondary Electron Contrast of Graphene Layers on a Metal Substrate, ACS Omega. 2 (2017) 7831–7836. https://doi.org/10.1021/acsomega.7b01550.

CHAPTER 5

GRAPHENE BASED ELECTROCHEMICAL IMMUNOSENSOR FOR THE ULTRA-SENSITIVE LABEL FREE DETECTION OF ALZHEIMER'S BETA AMYLOID PEPTIDES AB(1-42)

This chapter discusses the development of an immunosensor capable of high-sensitivity detection of beta-amyloid peptides using screen-printed graphene electrodes (SPGEs) modified with ultra-thin layers of polymerized 1,5-diaminonaphthalene (pDAN). Electropolymerization of 1,5-diaminonaphthalene (DAN) was used to coat the SPGEs in a continuous polymer layer with controlled thickness. The effects of polymer thickness on the electron transfer rates were also investigated. An immunosensor for selective detection of beta-amyloid peptides Aβ(1-42) was developed via biofunctionalization of the pDAN modified SPGE with the anti-beta amyloid antibody used as the peptide bioreceptor. The immunosensor has been used for specific detection of Aβ(1–42) with a linear range of 1 pgmL^{-1} to 1000 pgmL^{-1} and has shown 1.4 pgmL^{-1} and 4.25 pgmL^{-1} detection and quantification limit, respectively. The biosensor was further validated for the analysis of spiked human plasma. The immunosensor enables rapid, accurate, precise, reproducible, and highly sensitive detection of Aβ(1-42) using a low-cost SPGE platform, which opens the possibilities for diagnostic ex vivo applications and research-based real-time studies.

5.1 INTRODUCTION

Section 2.2 discussed in detail about Alzheimer's Disease (AD) as the most common cause of dementia influencing millions of people across the world. AD is a neurodegenerative disease triggered by the extracellular accumulation of amyloid β peptide (Aβ), the intracellular appearance of neurofibrillary tangles, and neuronal loss [1-3]. The existing investigation methods for AD are complicated and are usually made when the disease is already in an advanced stage. In addition, there are no treatments available to avoid this condition [4] and current therapies only slow the advancement of the disease [4]. Thus, there is an intense need for the development of easy analytical tools for the rapid detection of AD biomarkers for early-stage point-of-care diagnosis [5-7]. Aβ(1–42) peptide, is the key element of the senile plaques present in AD [8]. Other pathological characteristics of AD consist of intraneuronal inclusions of hyperphosphorylated tau protein in neurofibrillary tangles, together with downstream processes such as inflammation and oxidative stress. Additionally, a certain isoform of apolipoprotein ApoE4, is a foremost genetic risk factor for AD, because it also leads to an excess of amyloid formation in the brain [9]. All these components cause the loss of synaptic integrity, progressive neurodegeneration, and effective neural network connectivity [6, 10, 11].

Aβ(1–42) is usually expressed in cerebrospinal fluid (CSF) and plasma and it is found that the CSF levels of Aβ(1–42) are lower in AD patients than in normal controls, which reflects amyloid pathology. Gagni et al. reported the detection of low CSF Aβ(1–42) levels at preclinical disease stages that predicted future cognitive decline and neurodegeneration [12]. An Aβ(1–42) concentration of < 500 pgmL^{-1} (0.1 nM) is indicative that Aβ(1–42) is accumulating in the brain and not circulating in the CSF [12]. However, more recently Emadi et al. reported that Aβ(1-42) concentration levels in peripheral blood serum samples at the preclinical disease stage are 3.41 ± 2.17 pgmL^{-1} in aged people and 3.34 ±1.95 pgmL^{-1} in young people [13]. They stated that in female AD patients with increasing age, more amounts of Aβ(1-42) remain in the brain, and thus less appears in the patient's serum. Whereas, in male AD patients the amount of Aβ(1-42) that remains in the brain is smaller than that of Aβ(1-40). It was concluded that female AD patients would show more adverse cognitive decline than males with increasing age because the toxicity of Aβ(1-42) has been shown to be far more than Aβ(1-40) [13]. It is therefore suggested that detection of Aβ(1-42) in physiological fluids such as CSF, serum, and plasma at lower levels can be used for both screenings of AD at an early stage and for monitoring of the disease progression. However, CSF biomarkers have some limitations i.e., the CSF procedural route through Lumbar puncture is regarded as a complex and expensive technique. This is also an invasive method that may be harmful to individuals and lead to several other health-related complications. Therefore, the main focus of this thesis is on blood-based biomarkers.

In addition, the use of plasma Aβ42/Aβ40 ratios is also emerging as the surrogate biomarkers responsible for cortical Aβ deposition [14]. Increasing experimental results in the last decade indicated that a lower Aβ42/Aβ40 plasma ratio is associated with more buildup of amyloid in the brain thus resulting in greater cognitive decline as well as increased risk of developing Alzheimer's at follow up stage [15-17]. Nevertheless, some research also reports to have weak or no connection of Aβ42/Aβ40 plasma ratio with Alzheimer's disease [18, 19].

Several methods have been introduced to detect amyloid beta using different sensing platforms [20-26]. An enzyme-linked immunosorbent assay (ELISA), which is evaluated by western or dot blot analysis, is currently used for its clinical detection. Although these tests are reliable, they are labour intensive, time-consuming, and require complicated instruments to perform measurements. Also, the sensitivity of these tests is not adequate to detect the ultra-low levels of the disease biomarkers at the early stages of disease onset.

In 2013 Jeseung et al. reported a CNT film-based biosensor with a metal-semiconductor field effect transistor structure (CNT-MESFET) for the real-time detection of amyloid-β (Aβ) in human serum. Their sensor showed a LOD of 1 pgmL^{-1} within the linear range of 10^{-12}–10^{-9} gmL^{-1}. Nevertheless, the fabrication of this sensor is complex, costly, and labour-intensive [22].

Electrochemical biosensors offer a rapid, cost-effective, easy, and sensitive testing technique [11, 21, 23, 27, 28]. Furthermore, label-free electrochemical immunosensors reduce sample complexity because of the exclusion of potentially confounding molecular labels [29, 30]. They provide a promising approach for both sensitive and selective analysis due to their high compatibility and repeatability, rapidness, simple instrumentation, low power requirements, easy signal quantification, etc [31-33]. Label-free sensors on the other hand can also be integrated into lab-on-a-chip platforms and have the benefit of using small volumes for rapid and inexpensive measurements as opposed to label-based technologies which are often more costly and time-consuming [34]. Pedro and co-workers used a modified gold electrode surface for the sensitive detection of Aβ(1-42). This sensor showed good accuracy and reproducibility with the limit of detection being 5.2 pgmL^{-1}. However, the selected antibody was also able to recognize Aβ(1–40), limiting the specificity of the study [23]. Furthermore, Troung et al. presented a label-free impedimetric immunosensor using carbon disposable electrochemical printed chips modified with AuNPs, for the detection of amyloid beta. They bound protein G to the antibody for its controlled immobilization which in turn lowered the LOD to 0.57 nM [28].

It has been reported that coating polymeric films on the electrode surface may well improve the behavior and performance of electrochemically modified electrodes [35, 36]. Furthermore, such modifications may increase the reaction rate, enhance electrocatalytic properties of the substrates, reproducibility and stability of the electrodes [37]. Poly(1,5-diaminonaphthalene) (pDAN) is a conducting polymer that is attained from the polymerization of aromatic monomers comprising of two amino groups [38]. Thus, there are free amine groups present in the polymer structure that aids in binding the biomolecules to the electrode surface. The unique properties of pDAN, make it an outstanding material for electrochemical electrode modification. Several studies have used pDAN in electrochemical sensors for the detection of for example H_2O_2, cholesterol, H_2O and dopamine, and lactose [39-43]. Rehman et al. presented an electrochemical poly(1,5-DAN) nanofibers-based biosensor for water (H_2O) sensing. The linear dynamic range of the reported biosensor was from 0.05 to 20%, and the limit of detection of 0.01% was reported, which was comparable to other methods for water detection. Their sensor also showed a longer shelf life and the sensitivity retained 97% of the initial sensitivity for up to 40 days [41]. In another study, Abdelwahab et al. developed a method for the detection of dopamine (DA) with the incorporation of cibacron blue (F3GA) into poly(1,5-DAN) layer. The concentration range of the reported sensor was from 5.0–100 µM with a LOD of 0.1 ± 0.01 µM. Moreover, their sensor was also validated with the determination of DA in a human urine sample and showed a rapid response with excellent selectivity, and stability [42]. In addition, Nguyen et al. reported a biosensor for lactose detection utilizing the Platinum microelectrodes which are modified with graphene and poly (1,5-DAN) film. Their sensor successfully determine the lactose with a correlation coefficient (R_2) of 0.995, a detection limit of 1.3 µg.mL$^{-1,}$ and sensitivity was determined to be 1.33 µA/(µgmL^{-1}).

In this work, we have used a graphene-based electrode, due to its high conductivity, large surface-to-volume ratio, low cost, and low environmental impact, in the fabrication of sensors and biosensor-based devices [44, 45]. Graphene biosensors enable the advantages of high sensitivity, lower detection limits, and high throughput detection when compared to other methods such as ELISA, Polymerase Chain Reaction (PCR), and fluorescence assays. Myung-Sic et al. used oxygen-plasma-treated rGO surfaces as reactive interfaces for the electrical detection of Aβ peptides, which in turn improved the antibody immobilization on electrodes and yielded improved sensing performance due to the enhancement in surface functionality. This was confirmed by measuring the changes in the electrode's electrical characteristics, with a 3.33-fold steeper slope for electrical responses versus the analyte concentration curve of the oxygen plasma treated sample compared to the untreated [46]. More recently a graphene/rGO dual-layer SPE was reported by Sethi and co-workers for the detection of Aβ(1-42). The proposed sensor showed a detection limit of 2.398 pM with high selectivity [47].

Here, we report the development of a label-free, electrochemical immunosensor, using graphene-modified screen printed electrodes (SPGEs) for high-sensitivity detection of beta-amyloid peptides, isoform 42. The graphene surface was modified with amine functional groups using a 1,5-diaminonaphthalene (DAN) electropolymerization process with optimized amine surface coverage [48], whilst maintaining minimal thickness for better charge transfer from the electrolyte solution to the electrode surface. Polymer DAN (pDAN) modification provided a controlled amount of amines without even compromising the actual graphene properties. Subsequent attachment of the anti-beta amyloid antibody onto the sensor was performed and the influence of antibody concentrations with respect to Aβ(1-42) peptide sensing efficiency has been analyzed in detail. BSA was used as a blocking agent. The implications of this work towards developing a commercially viable, robust, and sensitive immunosensor for Alzheimer's disease by using biomarker Aβ(1-42) are presented.

5.2 MATERIALS AND METHODS

5.2.1 MATERIALS:

Graphene-modified screen printed electrodes (SPGEs) were purchased from Metrohm Ltd.; 1,5-diaminonaphthalene (DAN) (97%), 1-Ethyl-3-(3-(dimethylamino)-propyl) carbodiimide hydrochloride (EDC) (>98%), N-hydroxysuccinimide (NHS) (98%), Ferrocene carboxylic acid (FeCOOH) (97%), Potassium hexacyanoferrate(III) (>99%), Potassium hexacyanoferrate(II) trihydrate (98.5-102%) and Phosphate buffered saline (PBS) tablets were supplied by Sigma-Aldrich and used as received. Anti-beta Amyloid antibodies and beta-Amyloid Peptide (1-42) human were obtained from abcam Ltd.

5.2.2 ELECTROPOLYMERIZATION:

Graphene electrode surfaces were functionalized with ultra-thin polymer layers of 1,5-diaminonaphthalene (DAN) via an electropolymerization technique mentioned in detail in our previous work [48]. Typically, the polymer films were deposited from 10 mM DAN in 0.25 M H_2SO_4 using a standard graphene modified screen printed electrodes (SPGEs), where graphene was used as working, carbon as counter, and Ag/AgCl as the reference electrode. The electropolymerization of monomer DAN results in the deposition of ultra-thin polymer DAN (pDAN) layers on the graphene electrode surface, with the resulting pDAN layer containing NH_2 functional groups which can subsequently be used for attachment of “bioreceptor” antibodies to the graphene surface. Following pDAN deposition, the electrodes were rinsed with Deionized (DI) water and dried under nitrogen.

5.2.3 BIO-FUNCTIONALIZATION:

Bio-functionalization protocols were optimized for improved sensor performance. Typically, the anti-beta Amyloid antibody was ‘activated’ in a solution containing 5mM EDC/NHS for 40 minutes. Once activated, the antibody solution was added to the sensor surface and incubated for 30 minutes at 4^{o}C. The antibody incubation time was optimized to achieve the highest sensitivity for the proposed biosensor (**Figure 5.1**). The antibody functionalized SPGE was then rinsed thoroughly with deionized water, to wash away any non-specifically bound probe on the surface. Blocking of unbound NH_2 surfaces was performed by drop-casting 1% BSA onto the electrode surface and incubating for 30 minutes at 4^{o}C, subsequently removing any unbound BSA by rinsing with DI water and drying with N_2. In this work, 0.1 mM concentration of PBS (pH= 7.4) was used in all experiments in order to increase the Debye length (λ_D) to approximately (~7.3nm) and hence to achieve better signal amplification [49].

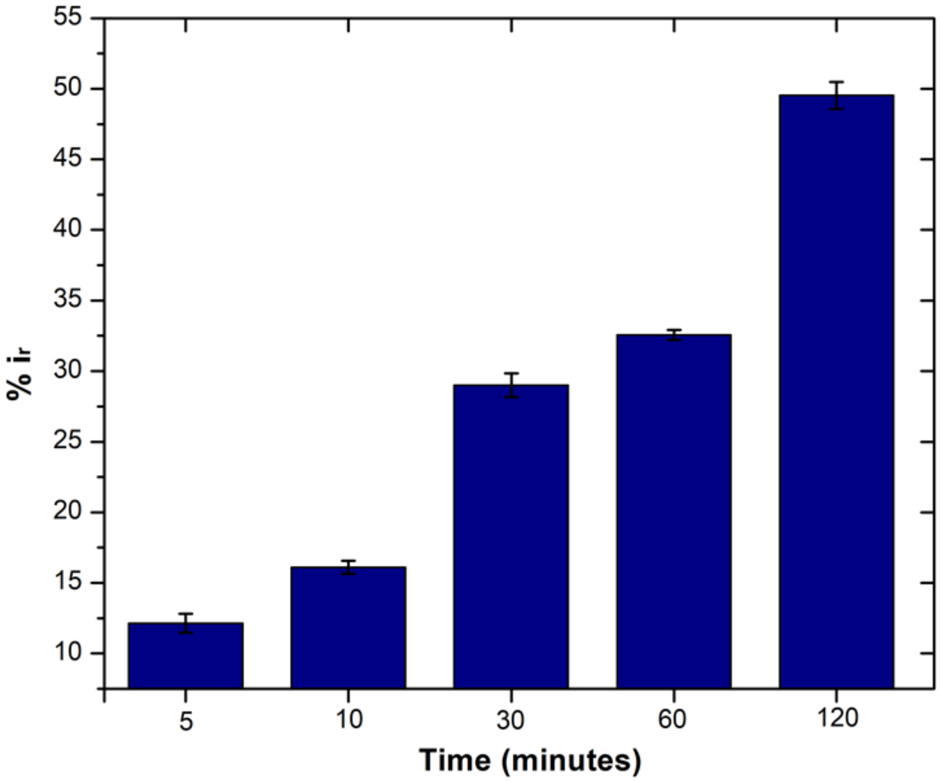

Figure 5. 1: Bar chart representing the antibody incubation time vs the percentage reduction in the peak current obtained from DPV analysis (n=3).

5.2.3.1 Debye Length:

When the voltage is applied to the electrode surface, an interfacial charge separation occurs between the electrolyte and the surface of the electrode. This separation creates two layers of charges which serve as the dielectric layer on top of the substrate surface. The distance between these two layers of charges is typically known as the Debye screening length (λ_D) [50].

The Debye length (λ_D) for an electrolyte solution is presented by the following equation [5.1]:

$$\boldsymbol{\lambda_D = \sqrt{\frac{\varepsilon_r \,.\, \varepsilon_0 \,.\, k_B \,.T}{2N_A \cdot e^2 \cdot I}}} \qquad \textbf{(5.1)}$$

where ε_r is the dielectric constant of an electrolyte; ε_o shows the permittivity of free space, k_B demonstrates the Boltzmann constant, T is the temperature (kelvins), N_A is the Avogadro constant, and e shows the electron charge, and I is the ionic strength of an electrolyte.

From equation 5.1 the Debye length (λ_D) in a physiological salt environment which is 1 X PBS is estimated to be 0.7 nm. The regular IgG antibody is approximately 5~10 nm [51]. Hence, the probe-target interaction on the biosensor surface occurs outside the Debye length (λ_D) and is not effectively measured. Greater Debye length (λ_D) leads to the effective detection of proteins. For that reason diluted buffer solutions are mostly utilized such as 0.1 X PBS ($\lambda_D = 2.4$ nm) or 0.01 X PBS ($\lambda_D = 7.4$nm) [52-54]. However, diluting the buffer solution reduces its ionic strength which causes a change in the structure of the protein leading to loss of protein activity, and the binding affinity as well. Most biological reactions occur in a physiological high-salt environment therefore a biosensor that can be used with physiological samples directly is preferred. Hence, it is important to use the buffer solution with optimum ionic strength which is close to the physiological samples as well as provides the larger Debye length(λ_D).

5.2.4 AMYLOID BETA (1-42) PRE-TREATMENT METHOD:

Aβ(1–42) was received in lyophilized form. It was first dissolved in 10 mM sodium hydroxide, followed by a gentle vortex for less than 1 minute to make a homogeneous solution. It is reported that under these highly alkaline conditions the peptide is fully dissolved and exists only as monomers [55]. The stock solution was then aliquoted and stored at -20°C until further use.

5.2.5 HUMAN BLOOD COLLECTION AND PLASMA PREPARATION:

Human Plasma samples were received from IRCCS - Istituto di Ricerche Farmacologiche "Mario Negri" Via La Masa 19, 20156 Milan – Italy. Fasting blood samples (3 mL) from AD patients were collected by the venipuncture method. The aliquot was centrifuged at 2000 rpm for 15 minutes at 4°C to separate the plasma fraction. After that plasma was transferred to a fresh tube, aliquoted, and immediately frozen at -80°C till further use. Informed consent was obtained from all human subjects. Besides all of the investigation protocols in this study have been approved by the relevant local ethics committee for clinical research (Milan, Italy).

5.2.6 CHARACTERIZATION:

The electrode layers were characterized for their thickness using Raman spectroscopy and X-ray photoelectron spectroscopy to check the quality of the electrode.

X-ray photoelectron spectroscopic (XPS) measurements were performed using a Kratos Axis Supra, with an Al Kα monochromatic X-Ray source, running at an emission current of 15 mA. Raman mapping measurements were performed using a Renishaw system, with a 532 nm excitation laser and 2 mW of power, before and after pDAN modification on the electrode surface.

Electrochemical analysis was done using an Autolab. Square wave voltammetry (SWV) and differential pulse voltammetry (DPV) were used as characterization techniques with the scanning voltage in the range of -0.2 V to 0.5 V for evaluating the electrochemical performance of blank and modified electrodes. 5 mM $K_3[Fe(CN)_6]/K_4[Fe(CN)_6]$ in 0.1 mM PBS solution (pH= 7.4) was used as an electrolyte.

5.3 RESULTS AND DISCUSSIONS

5.3.1 GRAFTING PDAN LAYERS ON SPGES:

To enable biofunctionalization, SPGE surfaces were modified with poly-1,5-diamino naphthalene (pDAN) layers using electropolymerization as described in section 5.2.2. **Figure 5.2** shows the voltammetric response of SPGEs during the electropolymerization process. In the first layer (Blue highlighted curve), the dominant peak at 0.55 V (vs Ag/AgCl) corresponds to the oxidation of monomer DAN species, which reduces subsequently with an increase in the number of scan cycles, indicating that DAN monomers are being oxidized and converted into polymers. Also, a new peak at 0.3 V originating during the second cycle is attributed to polymer layer formation, and this peak increases with an increase in the scan cycles. The polymer layer thickness was controlled by controlling the number of scan cycles. In order to achieve a greater number of surface amine groups for biofunctionalization, SPGE electrodes were modified with pDAN layers of different thicknesses [48].

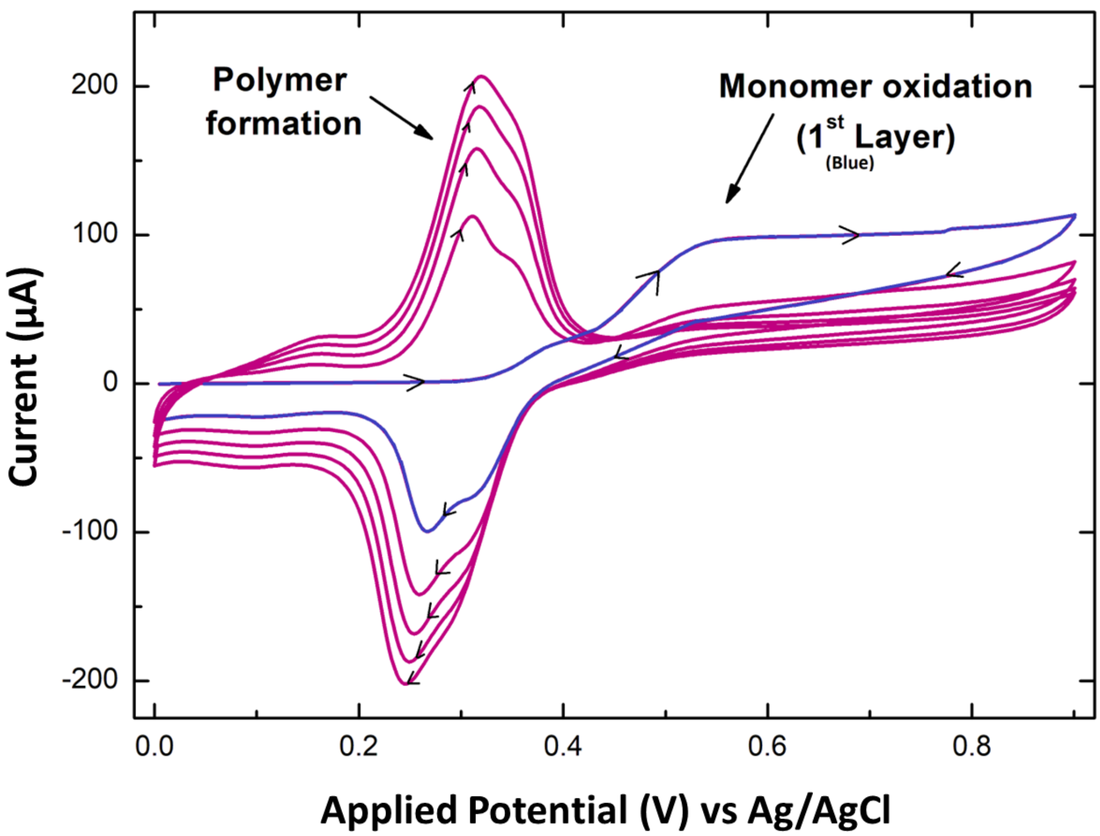

Figure 5. 2: Electropolymerization of pDAN for after 5 repeated voltammetry cycles. Cyclic voltammetry (CV) was carried out between 0 V to 0.9 V with 50 mVs^{-1} scan rate.

5.3.2 MECHANISM OF ACTION OF PDAN/GRAPHENE INTERFACES:

5.3.2.1 Electrochemical Analysis:

The electroactivity of deposited pDAN films was studied using cyclic voltammetry. **Figure 5.3** shows cyclic voltammetry curves of pDAN layers in 5mM Fe^{2+}/Fe^{3+} redox couple at the scan rates of 10-100 mVs^{-1}. The Blank SPGE (**Figure 5.3 (a)**) shows typical oxidation and reduction peaks at 0.18V and 0.05V, which are attributed to $[Fe(CN)_6]^{3-/4-}$redox reactions. Whereas polymer DAN modified SPGEs (**Figure 5.3 (b-f)**) exhibited a slight shift in the redox potentials with increasing scan rates which possibly shows the occurrence of further

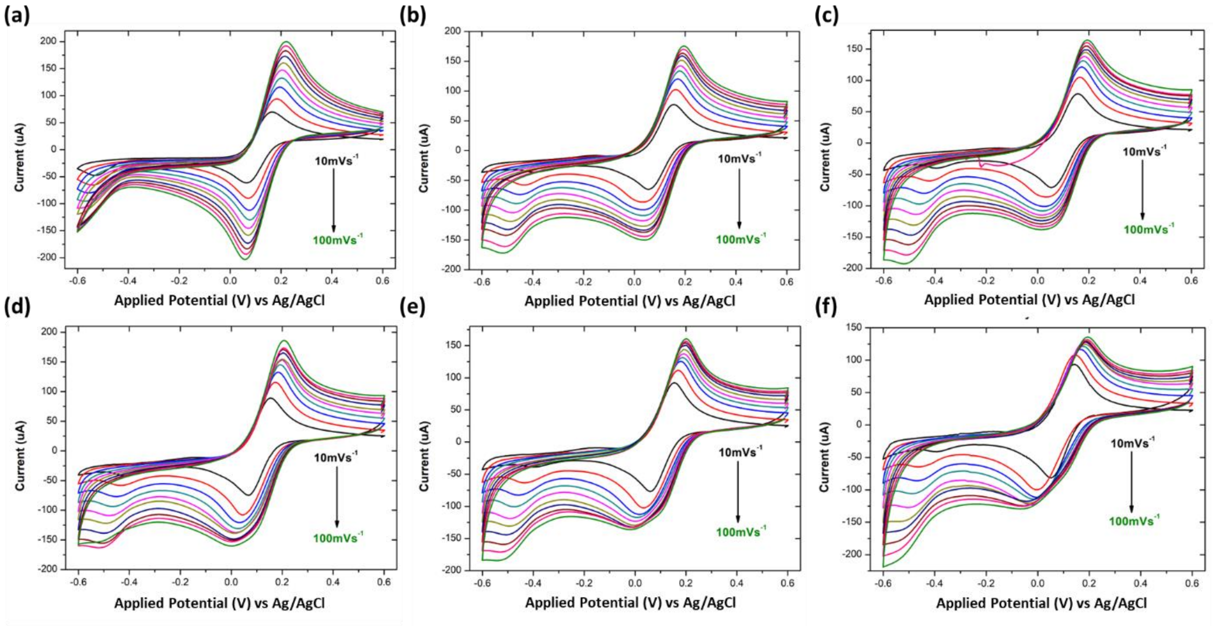

Figure 5. 3: Cyclic Voltammograms of Blank and pDAN modified SPGEs in 5mM $[Fe(CN)_6]^{3-/4-}$ redox couple at scan rates 10 mVs^{-1}, 20 mVs^{-1}, 30 mVs^{-1}, 40 mVs^{-1}, 50 mVs^{-1}, 60 mVs^{-1}, 70 mVs^{-1}, 80 mVs^{-1}, 90 mVs^{-1}, and 100mVs^{-1} and step size of -0.00244 V (a) Blank SPGE (b) 1 Cycle pDAN SPGE (c) 2 Cycles pDAN SPGE (d) 3 Cycles pDAN SPGE (e) 5 Cycles pDAN SPGE and (f) 10 Cycles pDAN SPGE.

chemical reactions [48]. A strong linear dependence of the peak current with the square root of the scan rate was observed, which attests to a diffusion-controlled process on pDAN modified electrodes. The linearity dependence is also confirmed by the regression coefficient (R^2) value (**Figure 5.4)**. The linearity indicates a typical diffusion-controlled quasi reversible process.

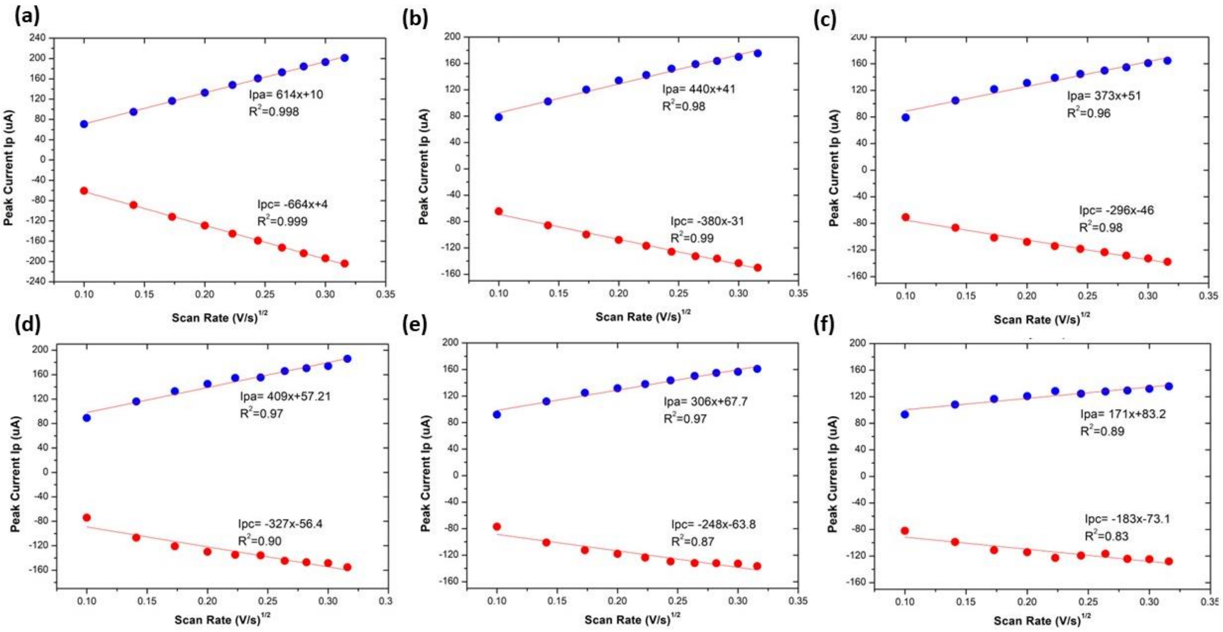

Figure 5. 4: Anodic and Cathodic Peak Current (Ip) values from CV curves of Blank and pDAN modified SPGEs (a) Blank SPGE (b)1 Cycle pDAN SPGE (c) 2 Cycles pDAN SPGE (d) 3 Cycles pDAN SPGE (e) 5 Cycles pDAN SPGE (f) 10 Cycles pDAN SPGE.

To further analyze these systems, the charge transfer diffusion coefficient, D_{CT}, was calculated using Randles-Sevcik (equation 5.2):

$$\boldsymbol{Ip = (2.69 \times 10^5) n^{3/2} A C D^{1/2}\, \upsilon^{1/2}} \qquad \textbf{(5.2)}$$

Where, $\boldsymbol{Slope = \frac{Ip}{\upsilon^{1/2}}}$

Hence, the **equation 5.2** would be:

$$\boldsymbol{D^{1/2} = \frac{Slope}{(2.69 \times 10^5) n^{3/2} A C}} \qquad \textbf{(5.3)}$$

where Ip represents the peak current, A is the area of the electrode (0.1256 cm^2), n is the number of electrons transferred (n = 1), C is the concentration of redox species (5 mM), D is the charge transfer diffusion coefficient (D_{CT}) and υ is the scan rate. The blank graphene electrode displayed a typical D_{CT} of 13.2 x 10^{-6} cm^{2}s^{-1} due to its high electron mobility. The charge transfer diffusion coefficient was highest (6.80 x 10^{-6} cm^{2}s^{-1}) during the first cycle of pDAN deposition, which was as expected as the single layer of monomer DAN (**Figure 5.5**) allows the most facile charge transfer to the graphene surface. With the increase in pDAN layer thickness to 2 cycles, D_{CT} decreases to 4.88 x 10^{-6} cm^2s^{-1} and again increases at its maximum (5.87 x 10^{-6} cm^2s^{-1}) at 3 cycles indicating that a uniform pDAN monolayer is achieved. Followed by a decrease again to 3.29 x 10^{-6} cm^2s^{-1} and 1.03 x 10^{-6} cm^2s^{-1} at 5 and 10 cycles, respectively. This shows that the electron transfer rates are affected by the thickness of the pDAN layer and thus, the pDAN layer should be optimized in terms of maximizing the number of surface NH_2 groups, whilst maintaining the highest possible electron transfer rates.

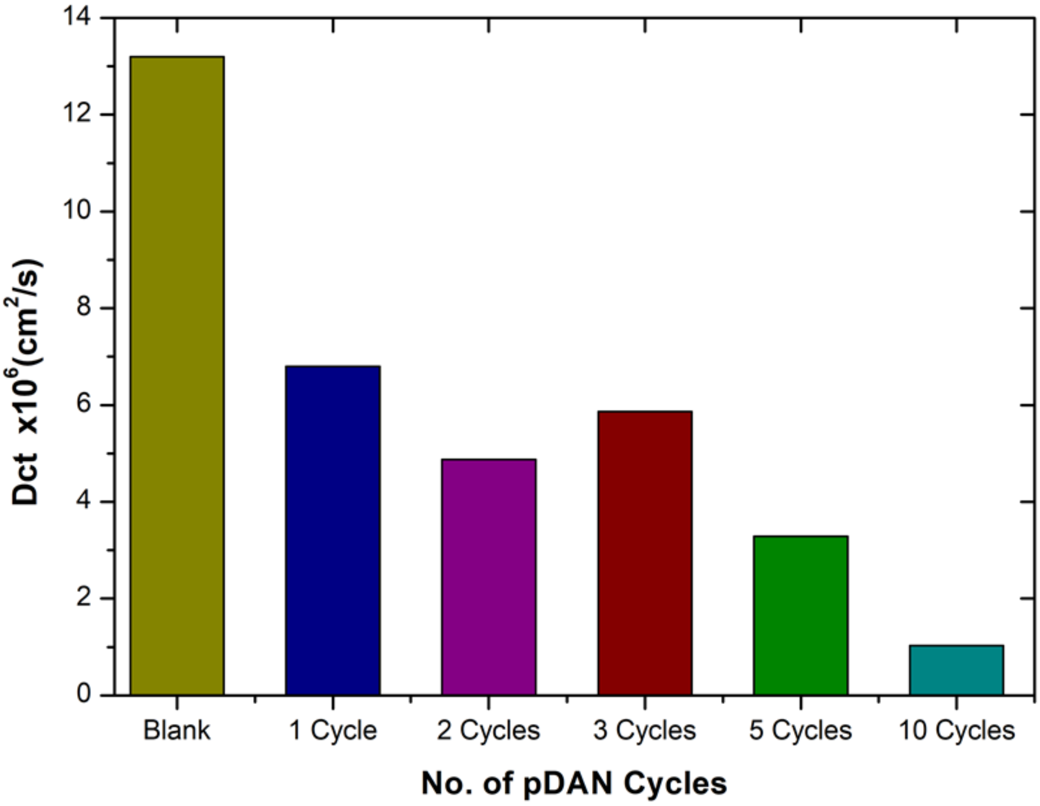

Figure 5. 5: Bar chart illustrating the change in charge transfer diffusion coefficient (D_{CT}) vs. number of pDAN scan cycles.

5.3.2.2 Quantification of Amine surface groups:

The efficiency of chemical functionalization was analyzed by estimating the number of surface amine groups upon pDAN modification via functionalizing the DAN-modified electrodes with ferrocene carboxylic acid (FCA), using a standard EDC/NHS coupling reaction. **Figure 5.6 (a)** shows the cyclic voltammogram of FCA functionalized graphene and pDAN modified SPGEs.

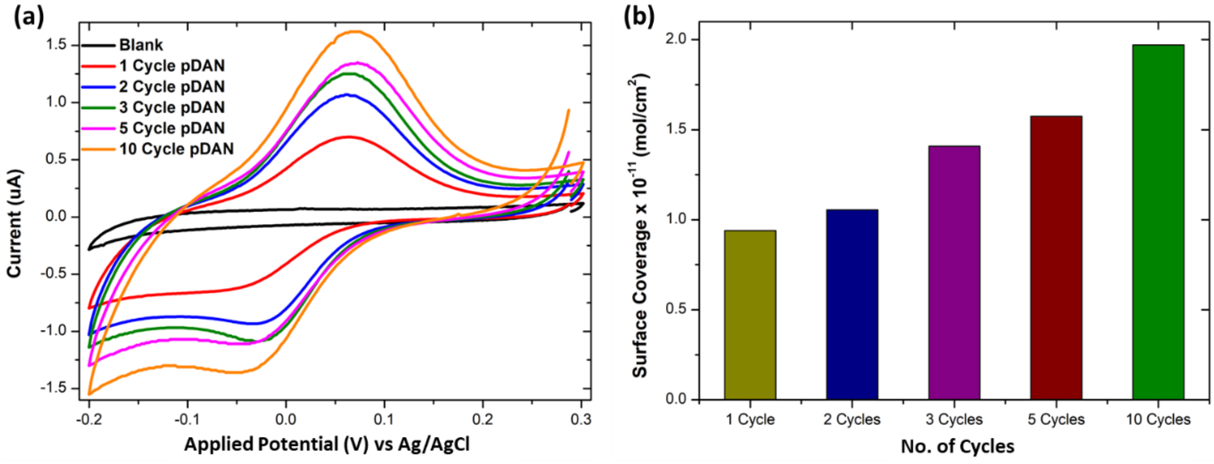

Figure 5. 6: (a) Cyclic voltammogram of ferrocene carboxylic acid functionalized SPGE and pDAN modified SPGEs at different scan cycles. PBS was used as the electrolyte and the CVs were recorded at a 5 mVs^{-1} scan rate. (b) Bar chart showing amine surface coverage vs the number of pDAN scan cycles.

The electrodes were scanned between -0.2 V and 0.3 V at a 5 mVs^{-1} scan rate. No redox peak is found for blank SPGE upon FCA functionalization due to the lack of amine functional groups present on the surface. Whereas, at 0.07 V and -0.04 V strong redox peaks are observed for FCA functionalized pDAN modified SPGEs, that correlate with the oxidation and reduction of the ferrocene moiety, respectively. The ferrocene surface coverage was estimated using equation 4.1:

$$\Gamma = Q/nFA$$

where Q is the charge obtained by integrating the anodic peak at a low scan rate (coulomb), n is the number of electrons transferred, F is the Faraday constant (96485 C Mol^{-1}) and A is the geometrical area of the electrode (0.1256 cm^2). **Figure 5.6 (b)** shows the surface coverage dependence on the number of scan cycles. As anticipated, it is found that the amine surface coverage increases with an increase in pDAN layer thickness (scan cycles), which is also attested by the increase in the capacitive current (**Table 5.1**). Although the higher pDAN layer thickness produces a large amine density on the surface, it is found that the charge transfer characteristics decreases after reaching a certain thickness (section 5.3.2.1). Thus, it is critical to find a fair balance between increased amine surface coverage as well as charge transfer characteristics. For our experiments - 3 cycles of pDAN layers (3-pDAN) were chosen to be the optimal layer thickness for further electrochemical sensor development as they showed the highest surface coverage.

No. of Cycles	Area Under the Curve (10^{-7})	Surface Coverage (10^{-11}) mol.cm^{-2}
1	1.14	**0.94**
2	1.28	**1.06**
3	1.71	**1.40**
5	1.91	**1.58**
10	2.39	**1.97**

Table 5. 1: Surface coverage values are calculated by integrating the reduction part of CV curves obtained after FeCOOH attachment on the SPGEs at different scan cycles.

5.3.2.3 Structural and Chemical Analysis:

Raman spectroscopic analysis on pristine SPGEs and pDAN-modified SPGEs is shown in **Figure 5.7 (a)**. The Raman spectrum of pristine SPGE is similar to that of the pristine graphene, showing the D, G, and 2D band positions at 1350 cm^{-1}, 1580 cm$^{-1,}$ and 2700 cm^{-1} respectively [56]. The corresponding intensity ratio of G and 2D bands of the pristine SPGEs was found to be an average of 0.46633, which confirms the presence of a few-layer graphene structure on the screen-printed electrode. After pDAN modification, the pDAN modified SPGE is found to be 0.42407. The intensity ratios between the D and G bands between the pristine and pDAN modified SPGEs were calculated to be 0.46633 and 0.42407, respectively. Taking device variation into consideration, no significant variations were found in the intensity and position of the D, G, and 2D bands upon pDAN modification, alluding that very little structural deformation is induced to the graphene upon electropolymerization.

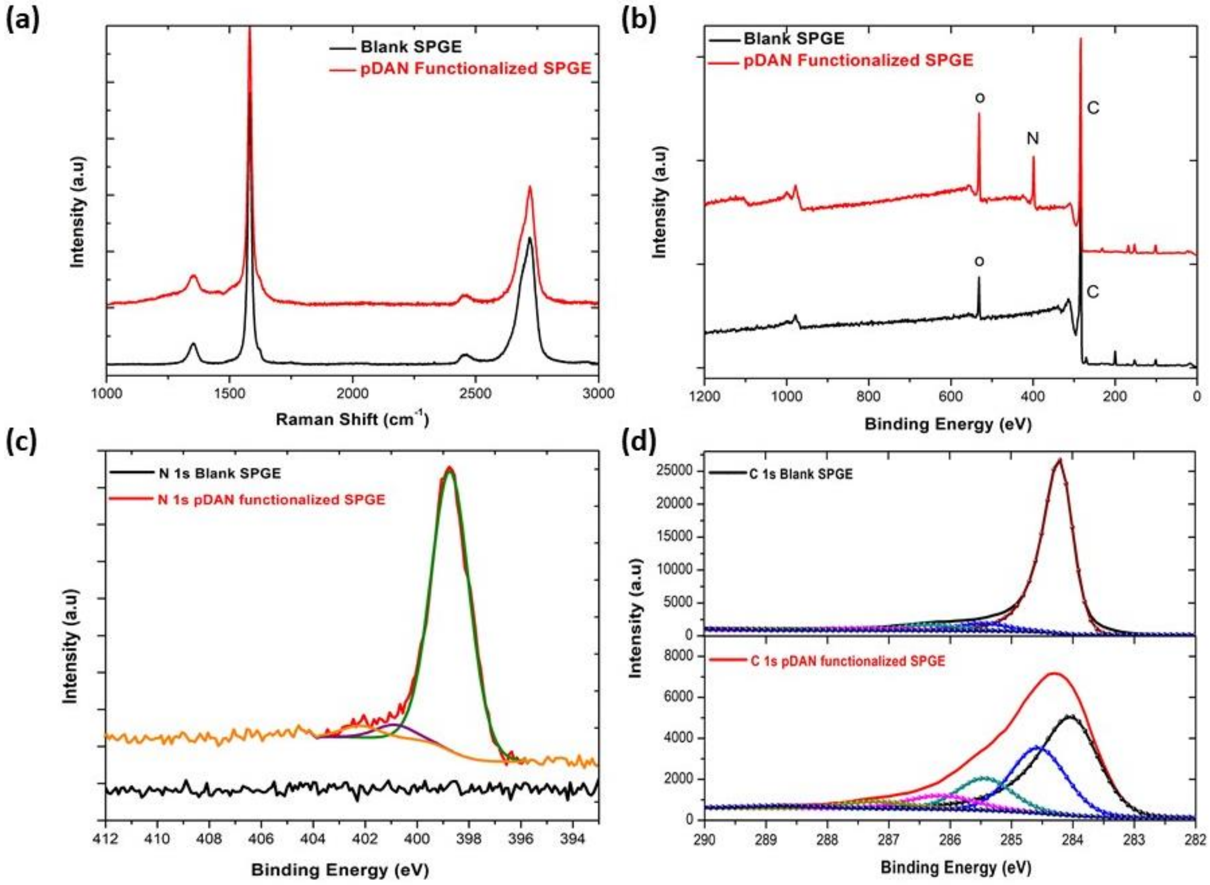

Figure 5. 7: Comparison of Blank and pDAN functionalized graphene SPE at 3 scan cycles (a) Raman Spectrum (b) XPS spectrum showing wide scan, pDAN functionalized SPGE showing (c) N 1s spectrum (d) C 1s spectrum.

X-ray photoelectron spectroscopy is a tool used to investigate the chemical environment of graphene modified with foreign dopants [48, 57]. To study the influence of electropolymerization on SPGEs, XPS measurements were carried out on blank and pDAN-modified SPGE surfaces. **Figure 5.7 (b-d)** shows XPS graphs of the wide spectrum (b), N 1s spectrum (c), and C 1s spectrum (d) of pristine graphene and pDAN modified SPGEs. The wide scan acquisition of pristine and pDAN modified SPGE shows a typical C 1s peak at ~284 eV. Unlike the pristine graphene, the pDAN modified SPGE shows a clear peak at ~400 eV in the wide spectra (**Figure 5.7 (b)**), confirming that nitrogen-based moieties were introduced after electropolymerization. The atomic concentrations of C, O, and N present were calculated from the XPS spectra and are listed in **Table 5.2, Table 5.3, and Table 5.4.** It is found that the atomic percentage of N increases drastically upon electropolymerization, and additional components appear in the C spectra (**Figure 5.7 (d)**), which can be ascribed to the carbon and nitrogen species present in DAN. To further analyze the nature of C, O, and N species, the N 1s (**Figure 5.7 (c)**), and C 1s (**Figure 5.7 (d)**) peaks were fitted with Gaussian/Lorentzian peaks to analyze the distribution of carbon and nitrogen bonding. The C 1s peak of pDAN modified graphene was deconvoluted into six carbon peaks, which are ascribed to $C_{aromatic}$ (~284.04 eV), $C_{aliphatic}$ (~284.56 eV), C-N (~285.44 eV), C-O (~286.14), C=O/C=N (~287.20 eV) and O-C=O/N-C=O (~288.76 eV). The N 1s peak of pDAN modified graphene is observed at 400.16 eV, indicating that nitrogen compounds are present upon successful electropolymerization. Furthermore, the three fitted peaks at ~400.12 eV, 402.26 eV, and ~403.59 eV corresponds to C-N, C-NH, and N-H groups respectively, confirming that the pDAN electropolymerization process generates $-NH^2$ groups on the graphene surface [58].

Atomic Concentration, %		
Sample Element	**Blank SPGE**	**pDAN Modified SPGE**
Carbon	95.11	75.81
Oxygen	04.89	14.29
Nitrogen	00.00	09.89

Table 5. 2: List of Elemental Concentrations of Blank SPGE and pDAN-Modified SPGEs.

Atomic Concentration, %		
Sample C Component	**Blank SPGE**	**pDAN Modified SPGE**
$C_{aromatic}$	82.08	47.06
$C_{aliphatic}$	03.01	27.66
C-N	04.98	14.18
C-O	03.66	06.39
C=O/C=N	04.31	03.52
O-C=O/N-C=O	01.96	01.19

Table 5. 3: List of Carbon Component Concentrations of Blank SPGE and pDAN-Modified SPGEs.

Atomic Concentration, %		
Sample N Component	**Blank SPGE**	**pDAN Modified SPGE**
C-N	00.00	91.76
C-NH	00.00	04.45
N-H	00.00	03.79

Table 5. 4: List of Nitrogen Component Concentrations of Blank SPGE and pDAN-Modified SPGEs.

The surface topography was analyzed using atomic force microscopy (AFM) analysis. **Figure 5.8** shows the AFM images of blank SPGE (a) and pDAN modified SPGEs (b–d) with different scan cycles. It is found that the electropolymerization process produces a good coverage of ultra-thin polymer layers on SPGEs. The surface roughness of the pDAN modified films increases with increasing the scan cycles, confirming the formation of thicker layers at higher scan cycles.

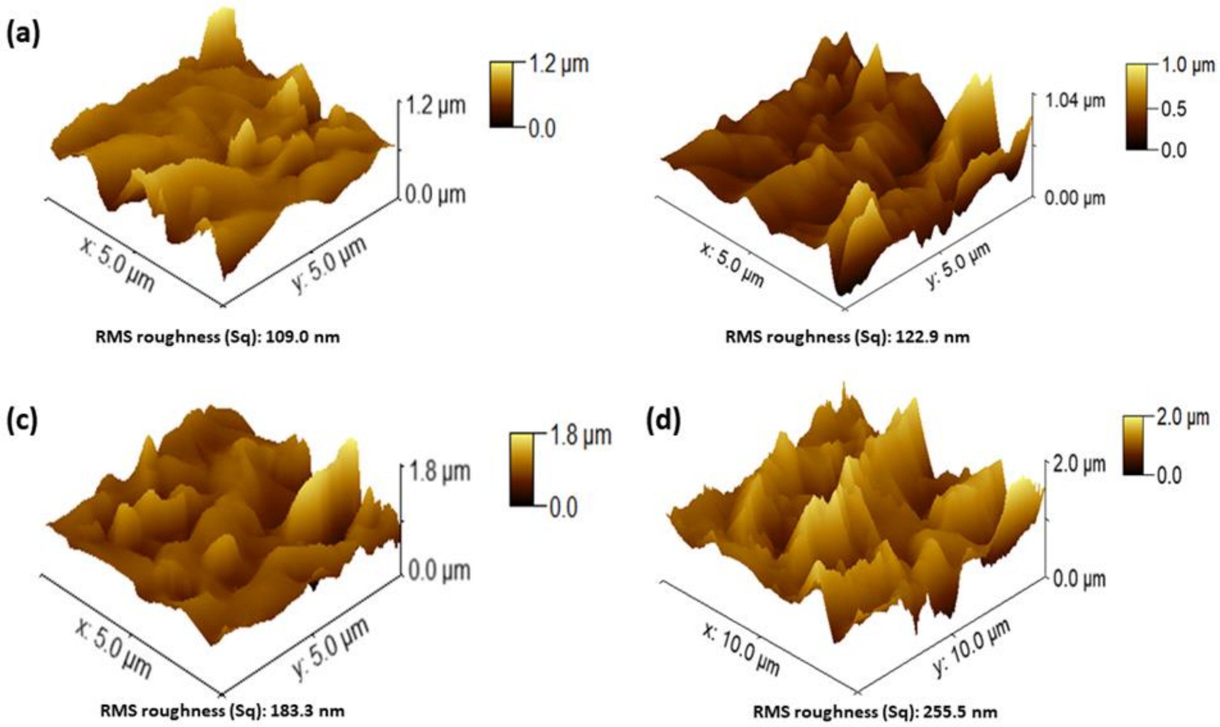

Figure 5. 8: AFM images of pDAN layers deposited on SPGE surface at different scan cycles (a) 0 cycles (Blank) (b) 3 cycles (c) 5 cycles (d) 10 cycles.

5.3.3 MECHANISM OF ANTIBODY/PDAN/GRAPHENE INTERFACES:

5.3.3.1 Electrochemical Analysis:

A carboxyl terminated anti-beta amyloid antibody specific to Aβ(1-42) peptide was immobilized onto the pDAN modified SPGE surface via carbodiimide linking using an EDC/NHS protocol [59]. **Figure 5.9 (a)** shows the schematic representation of the sensor, **Figure 5.9 (b)** shows the differential pulse voltammetric (DPV) response, and **Figure 5.9 (c)** shows the square wave voltammetric (SWV) response of SPGE at each stage of functionalization. An increase in the peak current is observed upon pDAN functionalization, which could be attributed to the increased charge transfer at the electrode/electrolyte interface due to the high conductivity of the amine (NH_2) layer [60]. Slight peak broadening is also observed which may be due to the non-

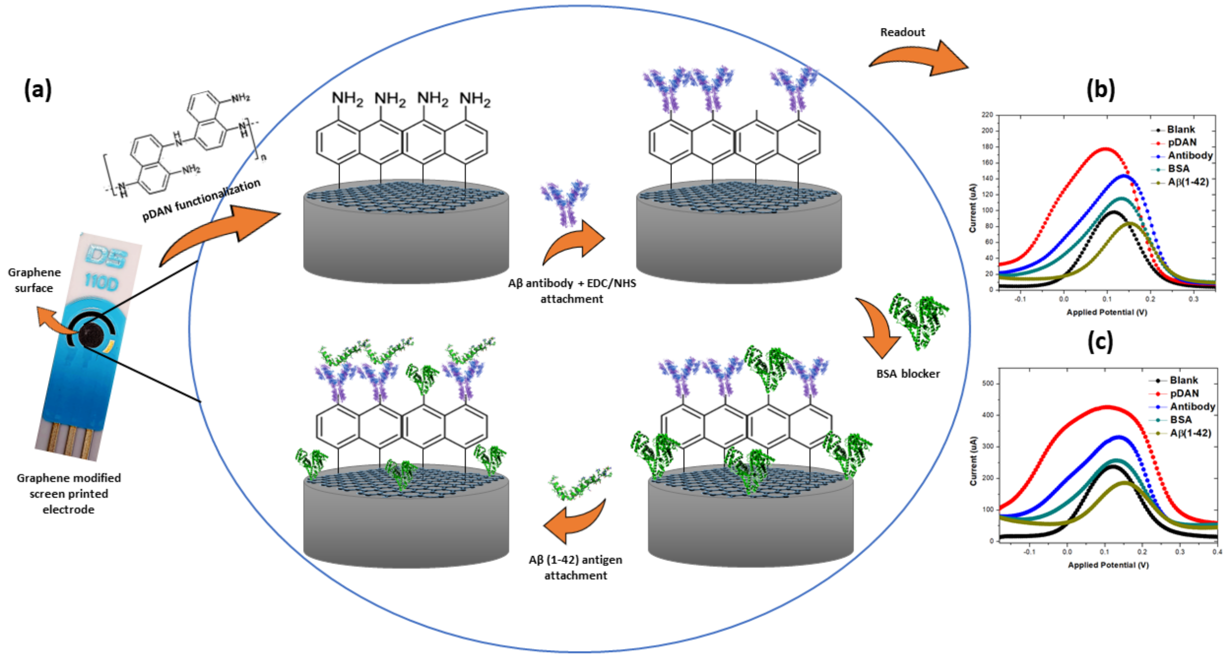

Figure 5. 9: (a) Schematic representation of electrochemical immunosensor showing change on surface after each functionalization stage (b) Differential pulse voltammetry (DPV) response (c) Square wave voltammetry (SWV) response.

uniform coating of pDAN layers. The subsequent antibody functionalization reduces the available sites for charge transfer via blocking, and thus a drastic reduction in the peak current is observed. This shows that the antibody functionalization impedes the charge transfer process at the electrode/electrolyte interface. Similarly, blocking of unbound NH_2 sites at the electrode surface using BSA further reduces the peak current, suggesting the successful biofunctionalization of pDAN modified SPGEs with antibody and BSA.

5.3.3.2 Optimizing the Antibody Concentrations:

The concentration of the biomolecules immobilized onto the electrode surface greatly influences the immunosensor performance. Thus, optimizing antibody concentration is critical to ensure the superior performance of the electrochemical immunosensor. In this work, we have investigated the influence of immobilized antibody concentrations on sensing. A controlled immobilization of anti-beta amyloid antibody onto pDAN modified SPGEs was achieved by varying the antibody concentrations (20, 40, and 60 μgmL^{-1}). The electrochemical analysis on the antibody attached SPGEs were performed using DPV and SWV, respectively. It is observed that the peak current produced via the electron transfer upon $[Fe(CN)6]^{3-/4-}$ redox process is greatly influenced by the amount of antibody immobilized onto the electrode surface. **Figure 5.10 (a)** shows the dependence of the percentage of peak current reduction with the concentration of the antibodies. It is evident that 60 μgmL^{-1} Aβ antibodies reduce the current by ~25% whereas 40 μgmL^{-1} antibodies reduce the current by ~20% and a much lower level of peak current reduction by ~14% is observed with 20 μgmL^{-1} anti-beta amyloid antibodies. This could be clearly attributed to the increased antibody surface coverage at the electrode which could increase the steric barrier for the $[Fe(CN)6]^{3-/4-}$ redox system in accessing the electrode surface - resulting in decreased peak current generation.

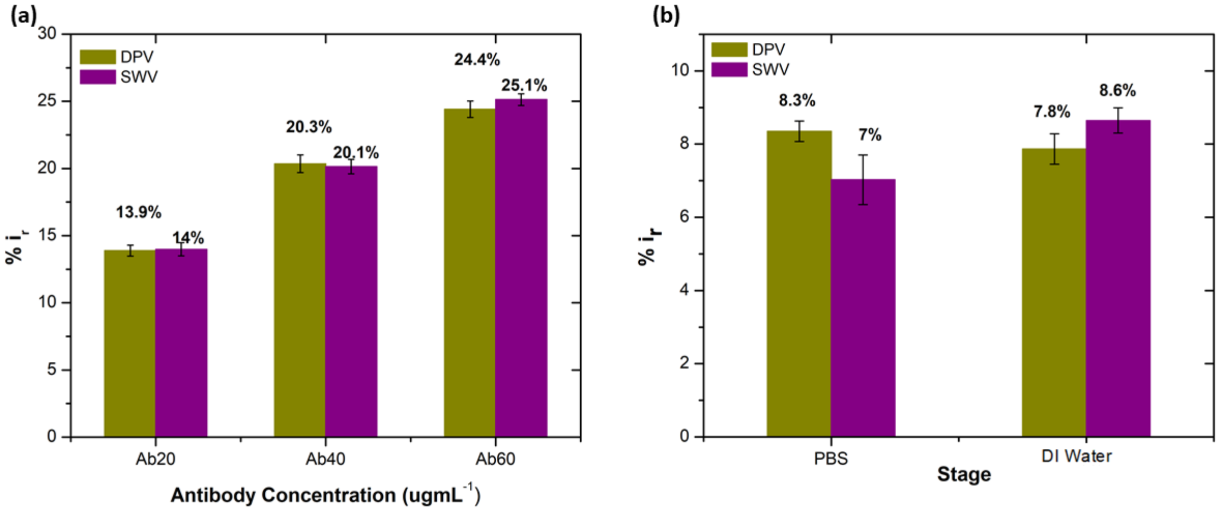

Figure 5. 10: (a) Peak current reduction in DPV and SWV measurements (%i_r) at each concentration of Aβ antibody. (b) Percentage reduction in peak current to the exposure to DI water and PBS (0.1 mM) (n=3).

5.3.3.3 Optimising the Sensor for False-Positive:

Analysis of the effect of sensor response to false-positive i.e., to PBS (pH= 7.4) and DI water was performed by considering the effect of 0.1 mM PBS (pH= 7.4) and DI water exposure on the sensors (antibody functionalized SPGEs). Exposure to PBS and DI water was repeated multiple times. **Figure 5.10 (b)** shows the percentage change in the peak current upon exposing the sensors to 0.1 mM PBS and DI water. A considerable change (~7-8%) in the peak current is observed upon exposure to 0.1 mM PBS (pH= 7.4). A similar effect is observed for DI water exposure, which could be ascribed to the high sensitivity of the graphene-based electrode surface. The relative current change corresponding to 0.1 mM PBS and beta-amyloid peptides Aβ(1-42) binding to the antibody/BSA-bound surface was estimated using equation 5.4 [61]:

$$\%\boldsymbol{i}_{\boldsymbol{rA\beta(1-42)peptide\ or\ PBS}} = \frac{i_{baseline} - i_{antibody/\ BSA/antigen\ or\ PBS}}{i_{baseline}}\ \boldsymbol{i}_{\boldsymbol{baseline}} * \mathbf{100} \qquad \mathbf{(5.4)}$$

Where, $i_{baseline}$ and $i_{antibody/BSA/antigen\ or\ PBS}$ are the mean DPV currents obtained at unmodified (blank) and antibody/BSA/Aβ(1-42) antigen or PBS modified electrodes, respectively. It is found that antibody functionalized electrodes show a significant change in the peak current with exposure to the relative peptide Aβ(1-42) compared to changes observed in exposure to 0.1 mM PBS only. Therefore, in **Figure 5.11**, the response from the electrodes exposed to 0.1 mM PBS only can be viewed as the 'baseline' signal, and the changes observed due to peptide binding are seen to be above the baseline. The repeated exposure of antibody functionalized SPGEs to 0.1 mM PBS only showed reproducible changes in current. However, the current change was minimal (1-1.5%) when compared to the change measured upon peptide binding. Thus, to moderate the effect of PBS, every sensor was exposed to 0.1 mM PBS first before performing the actual peptide sensing measurement in order to saturate the electrode surface with PBS. **Figure 5.11** also shows that the electrode surface was saturated above 1000 pgmL^{-1} concentration of peptides.

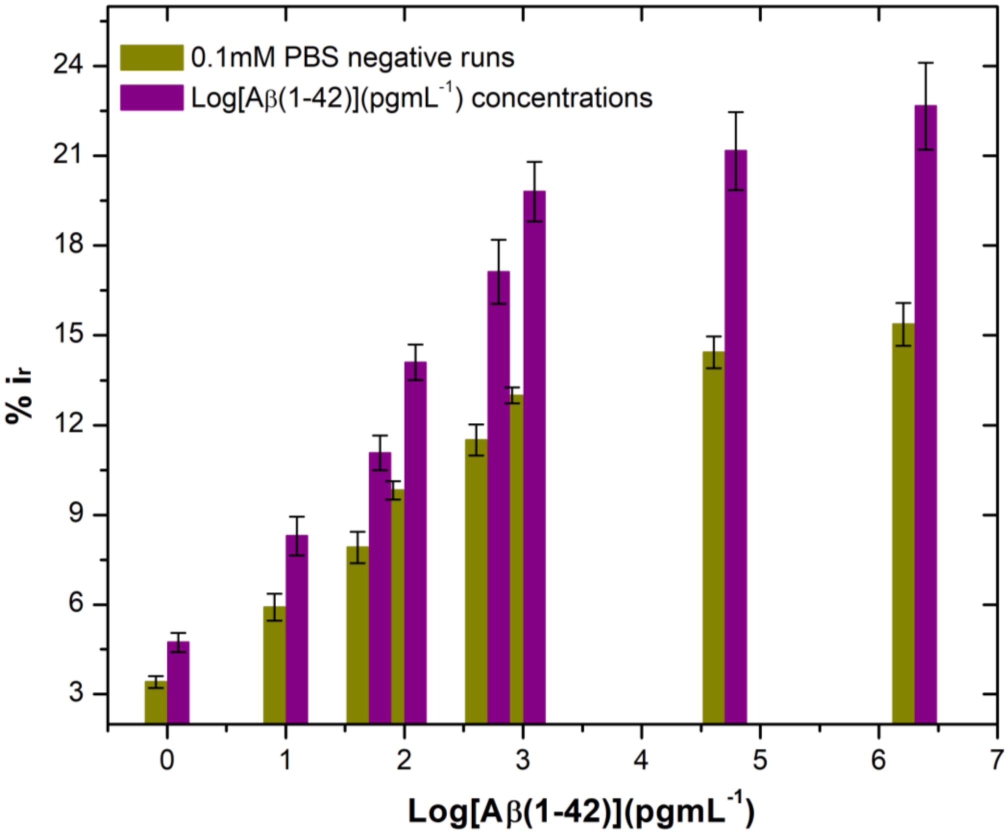

Figure 5. 11: Bar chart illustrating the peak current reduction (%i_r) with exposure to the 0.1 mM PBS only (negative runs with respect to each peptide concentration) and log of different concentrations of beta amyloid peptide.

5.3.4 EVALUATING THE ELECTROCHEMICAL IMMUNOSENSOR PERFORMANCE:

5.3.4.1 Sensitivity Analysis:

The electrochemical immunosensor performance was evaluated by exposing the antibody functionalized electrodes to different concentrations of beta-amyloid peptides Aβ(1-42) ranging from 1 pgmL^{-1} to 2 µgmL^{-1} at 4^{o}C, each for incubation times of 20 minutes. This was expected to result in the successful binding of the beta-amyloid peptides Aβ(1-42) to the anti-beta amyloid antibodies, which would in turn affect the [Fe(CN)6]$^{3-/4-}$ electron transfer. It is found that the peak current decreased significantly with an increase in the peptide concentration from 1 pgmL^{-1} to 2 µgmL^{-1}. This is because increasing the concentration leads to a high accumulation of proteins on the electrode that in turn blocks the [Fe(CN)6]$^{3-/4-}$ redox system from accessing the electrode surface. Saturation of the electrode surface is observed at >1000 pgmL^{-1} peptide concentrations with 20 µgmL^{-1} antibody electrode**. Figure 5.12** shows the sensor performance and calibration curve of peak current variation vs log of the concentration of the beta-amyloid peptides for SPGEs modified with antibody Aβ(1-42) concentrations of 20, 40, and 60 µgmL^{-1}, respectively. The calibration curve shows a linear relationship between the peak current and Log [peptide concentration]. Our electrochemical sensor showed a wide linear response between 1 pgmL^{-1} to 1000 pgmL^{-1} (**Figure 5.12 (d-f)**).

The limit of detection (LOD) and limit of quantitation (LOQ) for the precise detection of amyloid β peptide (1-42) were calculated within the linear range of 1 pgmL^{-1} to 1000 pgmL^{-1}, utilizing the standard deviation of the intercepts and the average of slopes of the straight lines from the analytical curves, using following equations [23, 47, 62, 63]:

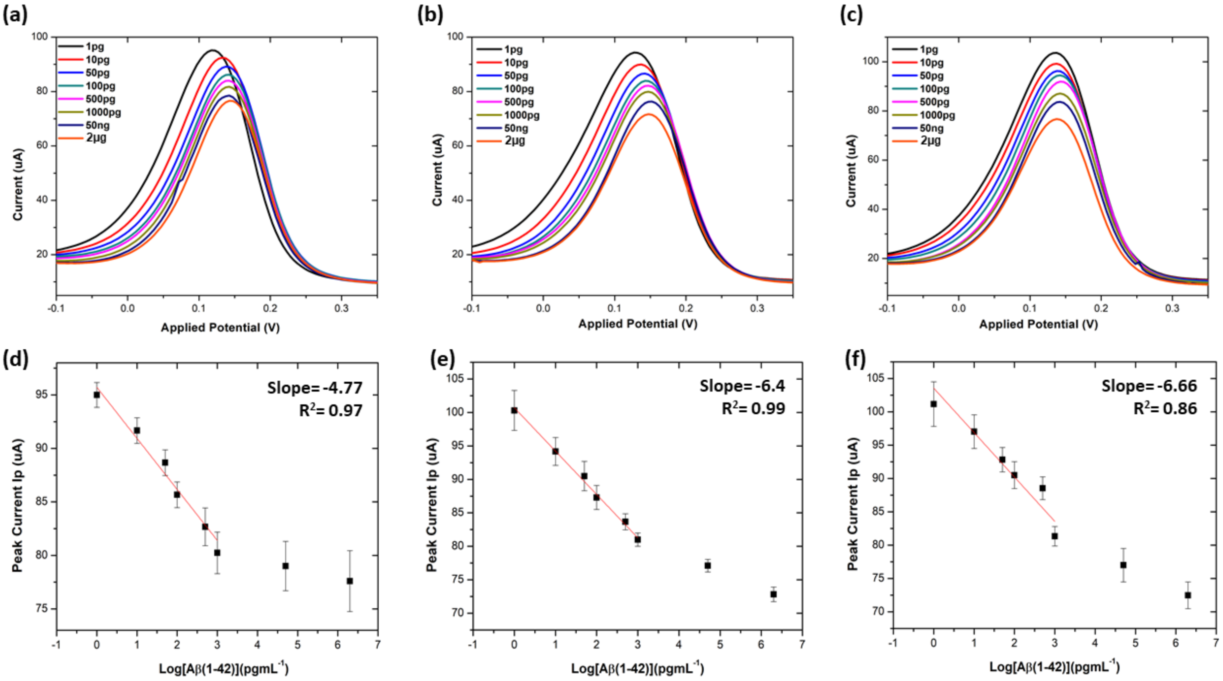

Figure 5. 12: Differential pulse voltammetry (DPV) results at 20 µgmL^{-1}, 40 µgmL^{-1} and 60µgmL^{-1} concentration of Aβ antibodies: (a-c) DPV plots of 20 µgmL^{-1}, 40 µgmL^{-1} and 60µgmL^{-1} antibodies at each stage of sensing (d-f) Corresponding calibration curves of Ip as against Log Aβ(1-42) concentrations. All data points are mean value of three independent electrodes. The error bars (calculated as standard deviation) provide a measure of repeatability of the system (n=3).

LOD = 3.3*(SD of lowest concentration/SLOPE) (5.5)

LOQ = 10*(SD of lowest concentration/SLOPE) (5.6)

Where SD is the standard deviation of the predicted peak current values, and SLOPE is the slope of the calibration line. The limit of detection (LOD) is defined as the lowest possible concentration of analyte that can be reliably separated from the background noise. Besides, the limit of quantification (LOQ) is the analyte's smallest concentration that can be quantified by the method in some reliable way.

Table 5.5 shows the list of LOD and LOQ obtained for the electrodes functionalized with different concentrations of antibodies. Sensors functionalized with 20 µgmL^{-1} antibody show the lowest LOD, 1.4 pgmL$^{-1,}$ and 4.25 pgmL^{-1} LOQ. It is observed that the LOD increased with an increase in the concentration of the surface-bound antibodies, indicating the significance of achieving an optimal antibody loading onto the sensor surface.

Aβ antibody Concentrations (μgmL^{-1})	Limit of Detection (LOD)	Limit of Quantification (LOQ)
20	**1.4**	**4.25**
40	**2.6**	**7.9**
60	**2.8**	**8.7**

Table 5. 5: List of LOD and LOQ obtained for the electrodes functionalized with different concentrations of antibody.

Our sensor shows higher sensitivity over the other existing label-free biosensors (**Table 5.6**).

Electrode Materials	Receptor System	Detection techniques	LOD (pgmL^{-1})	Ref.
Au	anti-Aβ(1–42)/AuNPs/MPA/Au electrode	EIS, SWV	5.2	[23]
SiO_2	anti-Aβ(1–16)/Glutaraldehyde/PVP-CHO/3-aminopropyl triethoxysilane	Electrical Impedance	-	[64]
Graphene/rGO SPE	anti Aβ(1–42) antibody (H31L21)/Pyr-NHS/graphene-rGO SPE	DPV	10.8*	[47]
Si/SiO_2	(range of antibodies**)/ poly(DMA-co-NAS-co-MAPS)/silicon microarrays	Fluorescence	73	[12]
Carbon ink electrode of DEP chip	monoclonal Aβ antibody/protein G/MHDA SAM/AuNPs/ carbon DEP chip	EIS	2573.02 *	[28]
ICE-Au	anti-Aβ antibody (MOAB-2)/EDC-NHS/MHA SAM/ICE	EIS	70, 100	[65]
Graphene SPE	***anti Aβ(1–42) antibody/pDAN/graphene SPE***	***DPV***	***1.4***	***This work***

Table 5. 6: An overview of recently reported label-free biosensors for Aβ(1–42) detection.

5.3.4.2 Specificity and Stability Analysis:

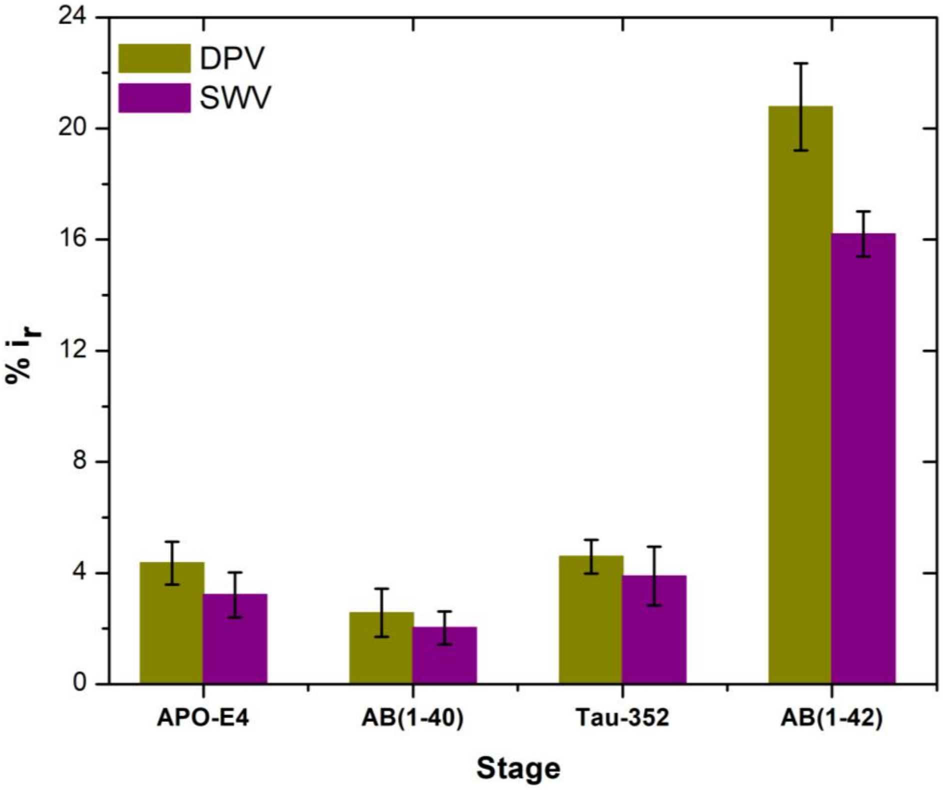

Figure 5. 13: Peak current reduction %i_r obtained from DPV and SWV plots for non-specific testing using APO-E4, Aβ(1-40), Tau-352 and Aβ(1-42) (n=3).

To test the selectivity and specificity of our sensors for Aβ(1-42) detection, the antibody immobilized sensors were incubated with 1000 pgmL^{-1} concentrations of APO-E4, Aβ(1-40), Tau-352, and Aβ(1-42) proteins, respectively. **Figure 5.13** shows the percentage change in the peak current (DPV measurements) upon binding with APO-E4, Aβ(1-40), Tau-352, and Aβ(1-42). A very small change (2-4.5%) in peak current is observed for APO-E4, Aβ(1-40), and Tau-352 proteins compared to Aβ(1-42) protein (16 -21% change). The small changes in exposure to non-specific proteins may be because of graphene’s sensitivity towards PBS (as discussed in section 5.3.3.3) and some non-specific adsorption of the peptides onto the sensors. In contrast, a very strong change is observed after the addition of Aβ(1-42) peptides due to the formulation of the antibody-antigen complex. This data confirms the selectivity of the fabricated sensor to the Aβ(1-42) peptides.

The stability of the immunosensor was also examined by storing the antibody-modified SPGEs in a refrigerator at 4 °C for 1 week. The current response of the prepared immunosensor decreased by 22% after eight days, thus representing acceptable stability. However, the glucose sensors, i.e., the continuous glucose monitoring (CGM) devices that are commercially available in the market are shown to be used for 7 days with the requirement of multiple calibrations per day [66]. Therefore, more work is needed to improve the stability of our reported graphene-based biosensors.

5.3.4.3 Spiked Plasma Analysis:

Blood-based detection of Alzheimer's biomarkers is emerging as a promising alternative to traditional strategies [67]. In this study, human plasma was first diluted with PBS in the ratio of 1:10 and later spiked with known concentrations of beta-amyloid peptide Aβ(1-42) including 1, 10, 100, and 1000 pgmL^{-1} respectively. The percentage reduction in peak current (%i$_r$) vs log of

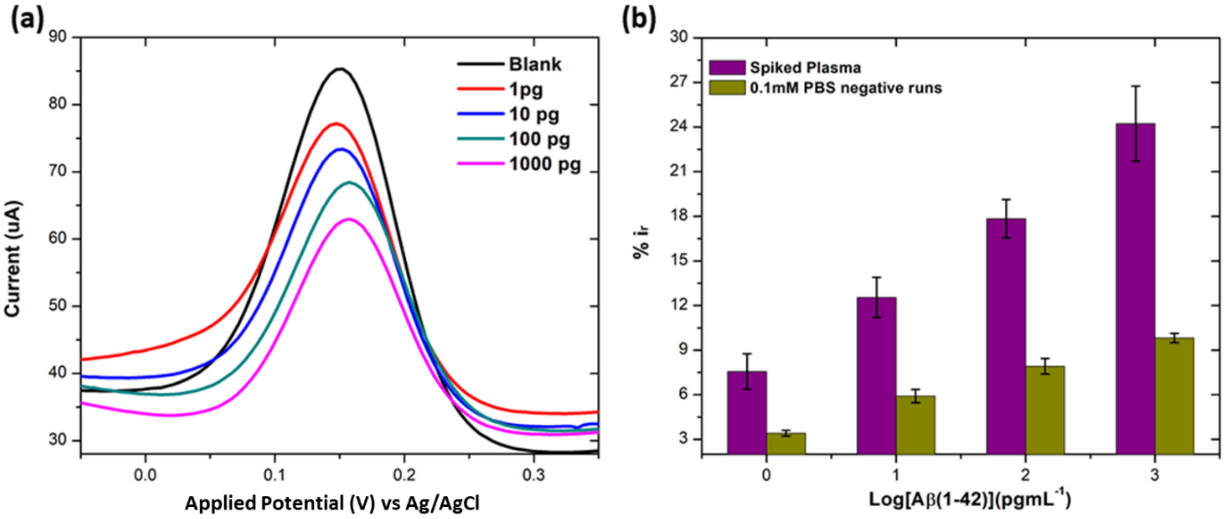

Figure 5. 14: (a) DPV response from spiked concentrations of Aβ(1–42) (at 1, 10, 100 and 1000 pgmL^{-1}) in human plasma. (b) Bar chart illustrating comparison of peak current reduction (%i$_r$) with exposure to the different concentrations of Aβ(1-42) spiked in human plasma and 0.1 mM PBS (negative runs with respect to each peptide concentration) (n=3).

peptide concentrations (pgmL^{-1}) is shown in **Figure 5.14.** The peak current reduction (%i_r) with exposure to the 0.1 mM PBS was also replotted here to show a comparison with the human plasma results. As discussed in section 5.3.3.3, the reduction in the peak current with PBS-only exposure is attributed to the high sensitivity of the graphene-based electrode surface. A significant reduction of DPV signal (up to 27%) in spiked samples was observed as compared to the PBS-only samples (up to 9.8%). These results validate the applicability of the proposed method in clinical sample analysis.

5.4 CONCLUSIONS

In Summary, a simple and rapid label-free electrochemical biosensor, based on a modified graphene screen printed electrode, has been developed for highly sensitive and selective detection of Aβ(1–42). Under the optimized conditions, our proposed immunosensor exhibited excellent analytical performance for Aβ(1–42) with a wide linear range and low detection limit. Antibodies targeted against Aβ(1–42) were immobilized onto the amine surface using EDC/NHS chemistry to obtain preferential antibody orientation attachment. Furthermore, three different concentrations of anti-beta Amyloid antibody were used in order to understand the effects that each concentration had on Aβ(1–42) detection sensitivity. The sensor showed negligible response to the non-specific interactions with Tau-352, Aβ(1-40), and APO-E4 proteins. It also showed excellent sensing performance for spiked human plasma samples. Our proposed immunosensor modification method can certainly be used for the detection of other proteins, with optimization of detection platforms enabling tuning of the sensitivity range. With all these characteristics, the main limitation of our biosensor is its sensitivity toward water and PBS-only samples. Therefore, for future work, we are aiming to develop a biosensor with negligible sensitivity toward these fluids.

BIBLIOGRAPHY

1. Blennow, K., M.J. de Leon, and H. Zetterberg, *Alzheimer's disease.* The Lancet, 2006. **368**(9533): p. 387-403.
2. Cummings, J.L. and G. Cole, *Alzheimer disease.* Jama, 2002. **287**(18): p. 2335-2338.
3. Cummings, J.L., *Biomarkers in Alzheimer's disease drug development.* Alzheimer's & Dementia, 2011. **7**(3): p. e13-e44.
4. Association, A.s., *2019 Alzheimer's disease facts and figures.* Alzheimer's & Dementia, 2019. **15**(3): p. 321-387.
5. Kang, D.-Y., et al., *Ultra-sensitive immunosensor for β-amyloid (1–42) using scanning tunneling microscopy-based electrical detection.* Biosensors and Bioelectronics, 2009. **24**(5): p. 1431-1436.
6. Hampel, H., et al., *Biological markers of amyloid β-related mechanisms in Alzheimer's disease.* Experimental neurology, 2010. **223**(2): p. 334-346.
7. Craig-Schapiro, R., A.M. Fagan, and D.M. Holtzman, *Biomarkers of Alzheimer's disease.* Neurobiology of disease, 2009. **35**(2): p. 128-140.
8. Hardy, J. and D.J. Selkoe, *The amyloid hypothesis of Alzheimer's disease: progress and problems on the road to therapeutics.* science, 2002. **297**(5580): p. 353-356.
9. Polvikoski, T., et al., *Apolipoprotein E, dementia, and cortical deposition of β-amyloid protein.* New England Journal of Medicine, 1995. **333**(19): p. 1242-1248.
10. Cummings, J.L., *Biomarkers in Alzheimer's disease drug development*. 2011, Elsevier.
11. Zetterberg, H., K. Blennow, and E. Hanse, *Amyloid β and APP as biomarkers for Alzheimer's disease.* Experimental gerontology, 2010. **45**(1): p. 23-29.

12. Gagni, P., et al., *Development of a high-sensitivity immunoassay for amyloid-beta 1–42 using a silicon microarray platform.* Biosensors and Bioelectronics, 2013. **47**: p. 490-495.

13. Emadi, S., et al., *Serum concentration of β amyloid peptide and the activity of angiotensin converting enzyme in Alzheimer's disease patients: Search for a potential biomarker.* Int. J. Res. Med. Sci, 2016. **4**: p. 421-427.

14. Fandos, N., et al., *Plasma amyloid β 42/40 ratios as biomarkers for amyloid β cerebral deposition in cognitively normal individuals.* Alzheimers Dement (Amst), 2017. **8**: p. 179-187.

15. Chouraki, V., et al., *Plasma amyloid-β and risk of Alzheimer's disease in the Framingham Heart Study.* Alzheimer's & Dementia, 2015. **11**(3): p. 249-257. e1.

16. Fandos, N., et al., *Plasma amyloid β 42/40 ratios as biomarkers for amyloid β cerebral deposition in cognitively normal individuals.* Alzheimer's & Dementia: Diagnosis, Assessment & Disease Monitoring, 2017. **8**: p. 179-187.

17. Doecke, J.D., et al., *Total Aβ₄₂/Aβ₄₀ ratio in plasma predicts amyloid-PET status, independent of clinical AD diagnosis.* Neurology, 2020. **94**(15): p. e1580-e1591.

18. Lopez, O., et al., *Plasma amyloid levels and the risk of AD in normal subjects in the Cardiovascular Health Study.* Neurology, 2008. **70**(19): p. 1664-1671.

19. Hansson, O., et al., *Evaluation of plasma Aβ40 and Aβ42 as predictors of conversion to Alzheimer's disease in patients with mild cognitive impairment.* Neurobiology of aging, 2010. **31**(3): p. 357-367.

20. Vestergaard, M.d., et al., *A Rapid Label-Free Electrochemical Detection and Kinetic Study of Alzheimer's Amyloid Beta Aggregation.* Journal of the American Chemical Society, 2005. **127**(34): p. 11892-11893.

21. Rushworth, J.V., et al., *A label-free electrical impedimetric biosensor for the specific detection of Alzheimer's amyloid-beta oligomers.* Biosensors and Bioelectronics, 2014. **56**: p. 83-90.

22. Oh, J., et al., *A carbon nanotube metal semiconductor field effect transistor-based biosensor for detection of amyloid-beta in human serum.* Biosensors and Bioelectronics, 2013. **50**: p. 345-350.

23. Carneiro, P., et al., *Alzheimer's disease: Development of a sensitive label-free electrochemical immunosensor for detection of amyloid beta peptide.* Sensors and Actuators B: Chemical, 2017. **239**: p. 157-165.

24. Oh, E.S., et al., *Comparison of conventional ELISA with electrochemiluminescence technology for detection of amyloid-β in plasma.* Journal of Alzheimer's disease: JAD, 2010. **21**(3): p. 769.

25. Bruggink, K.A., et al., *Amyloid-β oligomer detection by ELISA in cerebrospinal fluid and brain tissue.* Analytical biochemistry, 2013. **433**(2): p. 112-120.

26. Englund, H., et al., *Sensitive ELISA detection of amyloid-β protofibrils in biological samples.* Journal of neurochemistry, 2007. **103**(1): p. 334-345.

27. Liu, L., et al., *Competitive electrochemical immunoassay for detection of β-amyloid (1–42) and total β-amyloid peptides using p-aminophenol redox cycling.* Biosensors and bioelectronics, 2014. **51**: p. 208-212.

28. Lien, T.T.N., et al., *Modified screen printed electrode for development of a highly sensitive label-free impedimetric immunosensor to detect amyloid beta peptides.* Analytica Chimica Acta, 2015. **892**: p. 69-76.

29. Mousavi, M.Z., et al., *Label-free detection of rare cell in human blood using gold nano slit surface plasmon resonance.* Biosensors, 2015. **5**(1): p. 98-117.

30. de Castro, A.C.H., et al., *Label-free electrochemical immunosensor for detection of oncomarker CA125 in serum.* Microchemical Journal, 2020. **155**: p. 104746.

31. Fang, Y.-S., et al., *Electrochemical immunoassay for procalcitonin antigen detection based on signal amplification strategy of multiple nanocomposites.* Biosensors and Bioelectronics, 2014. **51**: p. 310-316.

32. Zhang, X., et al., *A label-free electrochemical immunosensor based on a new polymer containing aldehyde and ferrocene groups.* Talanta, 2017. **164**: p. 483-489.

33. Zeng, Y., et al., *A sensitive label-free electrochemical immunosensor for detection of cytokeratin 19 fragment antigen 21-1 based on 3D graphene with gold nanopaticle modified electrode.* Talanta, 2018. **178**: p. 122-128.

34. Uygun, Z.O., L. Yeniay, and F.G.r.n. Sağın, *CRISPR-dCas9 powered impedimetric biosensor for label-free detection of circulating tumor DNAs.* Analytica Chimica Acta, 2020. **1121**: p. 35-41.

35. Pournaghi-Azar, M. and R. Ojani, *Preparation of polypyrrole-coated platinum modified electrode in chloroform in the presence of various supporting electrolytes and its use for the catalytic oxidation of hydroquinone in aqueous and chloroform solutions.* Talanta, 1995. **42**(4): p. 657-662.

36. Ojani, R., J.B. Raoof, and S.R.H. Zavvarmahalleh, *Preparation of Ni/poly(1,5-diaminonaphthalene)-modified carbon paste electrode; application in electrocatalytic oxidation of formaldehyde for fuel cells.* Journal of Solid State Electrochemistry, 2009. **13**(10): p. 1605-1611.

37. Hassan, K., et al., *Electrochemical and analytical applications for NADH detection at glassy carbon electrode modified with nickel nanoparticles dispersed on poly 1, 5-diaminonaphthalene.* Journal of Solid State Electrochemistry, 2015. **19**(4): p. 1063-1072.

38. Jackowska, K., M. Skompska, and E. Przyłuska, *Electro-oxidation of 1, 5 and 1, 8 diaminonaphthalene: an RDE study.* Journal of Electroanalytical Chemistry, 1996. **418**(1-2): p. 35-39.

39. Vidal, J., E. Garcıa, and J. Castillo, *In situ preparation of overoxidized PPy/oPPD bilayer biosensors for the determination of glucose and cholesterol in serum.* Sensors and Actuators B: Chemical, 1999. **57**(1-3): p. 219-226.

40. Vidal, J.C., et al., *Comparison of biosensors based on entrapment of cholesterol oxidase and cholesterol esterase in electropolymerized films of polypyrrole and diaminonaphthalene derivatives for amperometric determination of cholesterol.* Analytical and bioanalytical chemistry, 2003. **377**(2): p. 273-280.

41. Rahman, M.A., et al., *Water sensor for a nonaqueous solvent with poly (1, 5-diaminonapthalene) nanofibers.* Analytical chemistry, 2008. **80**(14): p. 5307-5311.

42. Abdelwahab, A.A., H.-M. Lee, and Y.-B. Shim, *Selective determination of dopamine with a cibacron blue/poly-1, 5-diaminonaphthalene composite film.* Analytica chimica acta, 2009. **650**(2): p. 247-253.

43. Nguyen, B.H., et al., *Development of label-free electrochemical lactose biosensor based on graphene/poly (1, 5-diaminonaphthalene) film.* Current Applied Physics, 2016. **16**(2): p. 135-140.

44. Geim, A.K. and K.S. Novoselov, *The rise of graphene*, in *Nanoscience and Technology: A Collection of Reviews from Nature Journals*. 2010, World Scientific. p. 11-19.

45. Tehrani, Z., et al., *Generic epitaxial graphene biosensors for ultrasensitive detection of cancer risk biomarker.* 2D Materials, 2014. **1**(2): p. 025004.

46. Chae, M.-S., et al., *Enhancing surface functionality of reduced graphene oxide biosensors by oxygen plasma treatment for Alzheimer's disease diagnosis.* Biosensors and Bioelectronics, 2017. **92**: p. 610-617.

47. Sethi, J., et al., *A label-free biosensor based on graphene and reduced graphene oxide dual-layer for electrochemical determination of beta-amyloid biomarkers.* Microchimica Acta, 2020. **187**: p. 1-10.

48. Devadoss, A., et al., *Ultrathin Functional Polymer Modified Graphene for Enhanced Enzymatic Electrochemical Sensing.* Biosensors, 2019. **9**(1).

49. Wu, G., et al. *The effect of ionic strength on the sensing performance of liquid-gated biosensors*. in *2017 IEEE 17th International Conference on Nanotechnology (IEEE-NANO)*. 2017. IEEE.

50. Debye, P., *Dieletric Properties of Pure Liquids.* Chemical Reviews, 1936. **19**(3): p. 171-182.

51. Lin, S.-P., et al., *A reversible surface functionalized nanowire transistor to study protein–protein interactions.* Nano Today, 2009. **4**(3): p. 235-243.

52. Chen, K.-I., B.-R. Li, and Y.-T. Chen, *Silicon nanowire field-effect transistor-based biosensors for biomedical diagnosis and cellular recording investigation.* Nano today, 2011. **6**(2): p. 131-154.

53. Zheng, G., et al., *Multiplexed electrical detection of cancer markers with nanowire sensor arrays.* Nature biotechnology, 2005. **23**(10): p. 1294-1301.

54. Stern, E., et al., *Label-free biomarker detection from whole blood.* Nature nanotechnology, 2010. **5**(2): p. 138-142.

55. House, E., et al., *Aluminium, iron, zinc and copper influence the in vitro formation of amyloid fibrils of Abeta42 in a manner which may have consequences for metal chelation therapy in Alzheimer's disease.* J Alzheimers Dis, 2004. **6**(3): p. 291-301.

56. Barros, E.B., et al., *Raman spectroscopy of graphitic foams.* Physical Review B, 2005. **71**(16): p. 165422.

57. Tehrani, Z., et al., *Printable and Flexible Graphene pH sensors utilising Thin Film Melanin for Physiological Applications.* 2D Materials, 2020.

58. Eby, D.M., et al., *Probing the molecular structure of antimicrobial peptide-mediated silica condensation using X-ray photoelectron spectroscopy.* Journal of Materials Chemistry, 2012. **22**(19): p. 9875-9883.

59. Booth, M.A., et al., *In-Depth Electrochemical Investigation of Surface Attachment Chemistry via Carbodiimide Coupling.* Langmuir, 2015. **31**(29): p. 8033-8041.

60. Wang, W., et al., *Graphene-assisted label-free homogeneous electrochemical biosensing strategy based on aptamer-switched bidirectional DNA polymerization.* ACS applied materials & interfaces, 2015. **7**(51): p. 28566-28575.

61. Islam, F., et al., *An electrochemical method for sensitive and rapid detection of FAM134B protein in colon cancer samples.* Scientific Reports, 2017. **7**(1): p. 133.

62. Lorenzetti, A.S., et al., *Electrochemically reduced graphene oxide-based screen-printed electrodes for total tetracycline determination by adsorptive transfer stripping differential pulse voltammetry.* Sensors, 2020. **20**(1): p. 76.

63. Palla, G., et al., *Immunosensor incorporating half-antibody fragment for electrochemical monitoring of amyloid-β fibrils in artificial blood plasma.* Bioelectrochemistry, 2021. **137**: p. 107643.

64. Yoo, Y.K., et al., *A highly sensitive plasma-based amyloid-β detection system through medium-changing and noise cancellation system for early diagnosis of the Alzheimer's disease.* Scientific reports, 2017. **7**(1): p. 1-10.

65. Le, H.T.N., et al., *Sensitive electrochemical detection of amyloid beta peptide in human serum using an interdigitated chain-shaped electrode.* Biosensors and Bioelectronics, 2019. **144**: p. 111694.

66. Pullano, S.A., et al., *Glucose biosensors in clinical practice: principles, limits and perspectives of currently used devices.* Theranostics, 2022. **12**(2): p. 493-511.

67. Kim, H., et al., *A nanoplasmonic biosensor for ultrasensitive detection of Alzheimer's disease biomarker using a chaotropic agent.* ACS sensors, 2019. **4**(3): p. 595-602.

CHAPTER 6

AN ELECTROCHEMICAL IMPEDIMETRIC BIOSENSOR BASED ON NEUTRAVIDIN- BIOTIN INTERACTION FOR FEMTOMOLAR RANGE DETECTION OF AD BIOMARKERS IN HUMAN PLASMA USING FLEXIBLE SCREEN-PRINTED GRAPHENE ELECTRODES

This chapter demonstrates a highly sensitive immunosensor for the detection of three biomarkers Aβ(1-40), Aβ(1-42), and Tau-352, which are potential candidates for AD. Neutravidin-biotin technology has been applied on reduced graphene oxide (rGO) based flexible screen-printed electrodes and used to demonstrate the highly specific detection of a panel of AD biomarkers. The surface characteristics of electrodes have been examined via Raman and X-ray photoelectron spectroscopy (XPS) and the performance of functionalized electrodes have been assessed using the electrochemical impedance spectroscopy (EIS) technique. The approach provided a wide logarithmically linear range of detection from 10 fg/mL –10 ng/mL, with a low detection limit in both diluted human plasma as well as phosphate-buffered saline (PBS) solutions. Moreover, the fabricated biosensors also showed stability for up to 6 weeks. The flexible rGO-based biosensor platform presented in this work has great potential for the early diagnosis of AD in clinical use.

6.1 INTRODUCTION

Alzheimer’s disease (AD) is discussed in detail in section 2.2. The major components of senile plaques that are generated due to AD are aggregates of an amyloid β peptide (Aβ) such as oligomers and fibrils [1, 2]. Aβ comprises 39−43 amino acid residues, where Aβ(1-40) and Aβ(1-42) are the major subtypes [3]. Aβ and tau protein play a vital role in the early diagnosis of AD and are considered as core candidate biomarkers for AD [4, 5]. These proteins are also related to the initial progression of AD [6]. Recently it has been reported by Park et al. that neurodegeneration in AD patients has a high correlation with the ratio of the concentration of tau protein in plasma to that of amyloid β [7]. Chen et al. reported that Aβ(1-42) and total-tau (t-Tau) levels in plasma might predict amnestic mild cognitive impairment (MCI) [8]. Rather than the detection of a single protein, combined analysis of biomarkers such as Aβ and tau protein is becoming important in diagnostics [9]. Therefore, the requirement for multiplex detection platforms for these biomarkers is also becoming increasingly important.

One of the most familiar analytical techniques used to quantify the concentration of AD biomarkers is enzyme-linked immunosorbent assays (ELISA) [10, 11]. Nevertheless, this technique does not sufficiently satisfy the sensitivity or limit of detection (LOD) of biomarkers present in a few picograms in biofluids, particularly in serum or plasma. To overcome the limitations of conventional methods, several studies have been conducted for the analysis of AD biomarkers using optical [12], electrical [13, 14], electrochemical [15-17], and impedimetric [18-20] methods. Amongst these methods, electrochemical biosensors are the most attractive in terms of cost and sensitivity and, hence, widely preferred. The potential applications of electrochemical biosensors in clinical diagnosis for sensing and quantification of proteins is one of the most ubiquitous research areas [21, 22]. This is ascribed to various advantages such as portability[20], high sensitivity [23], the possibility of label-free sensing[16, 17], simplicity of apparatus, and easy handling [16]. In this work, we have evaluated electrochemical biosensors based on electrochemical impedance spectroscopy (EIS) as a tool for the development of a diagnostic method for the detection of AD markers. EIS detection has aided the simplification of detection and development of measurement sensitivity [24-26]. In the EIS method, the impedance is measured by applying a small sinusoidal applied potential difference, at a particular frequency, to the electrode-electrolyte interface. The impedance of the electrode-electrolyte interface changes upon immobilization of the target analyte onto the electrode probe surface. Therefore, the concentration of the target analyte can be detected in relation to the impedance variations [27].

The immobilization of receptors on the sensor surface is another critical step, which directly influences the sensing performance of the biosensor. Immobilization is often attained through specific linker chemistry [28, 29]. In 2019, a paper-based graphene impedimetric biosensor was developed for the detection of human interferon-gamma (IFN-γ), a biomarker for tuberculosis, utilizing electropolymerized aniline (PANI). The PANI layer was used for linking the antibody on the graphene surface via EDC/NHS coupling chemistry and for signal amplification. The biosensor showed a limit of detection (LOD) of 3.4 pg/mL [30].

Conjugation of linkers with nanomaterials such as graphene and reduced graphene oxide (rGO) has been shown to remarkably enhance biosensor performance [31, 32]. rGO provides a highly sensitive material for sensing due to its high electrical conductivity and a large number of electroactive sites and therefore is widely preferred for biosensors [33]. Combining both graphene and rGO further enhances their properties by increasing the conductivity and providing a large number of available active sites for bioreceptor attachment. Due to the presence of some functional groups (i.e., -COOH and -OH) the rGO surface can be chemically modified to attach the antibodies on its surface [34]. This can be achieved by both covalent and non-covalent methods. Recently, Sethi and co-workers reported highly sensitive detection of Aβ(1-42) using a graphene/rGO dual-layer SPE. Their sensor showed a detection limit of 2.398 pM with high selectivity [32].

Neutravidin Protein is a deglycosylated form of native avidin with four biotin binding sites and is cheaper than streptavidin. It has reduced mass compared to avidin (60 kDa) however retains its high biotin-binding affinity. Azzouzi et al. reported a neutravidin biosensor for multiplex detection of microRNAs via electrochemically encoded responsive nano labels. In their work neutravidin was directly immobilized onto the glassy carbon electrode surface via the drop cast technique [35]. Macwan and coworkers reported a study on the direct interactions amongst 2D graphene and avidin stating that avidin is highly stabilized on the graphene surface and also preserves its molecular structure and biotin-binding sites. They demonstrated a graphene–polypyrrole–avidin nanocomposite-based biosensing platform showing selective adsorption of avidin molecules on the surface of graphene [36]. More recently, Wang et al. developed a GFET biosensor consisting of single-layer graphene for detecting biotin molecules with high sensitivity and specificity. The graphene surface was modified with 1-Pyrenebutanoic Acid Succinimidyl Ester (PBASE) before avidin attachment. The biosensor showed a LOD of 90 fg/mL [37].

In this work, we report the development of a novel impedimetric immunosensor using flexible printed graphene screen printed electrodes (SPEs) for ultra-sensitive detection of multiple biomarkers of AD pathogenesis in two different physiological solutions (i.e., PBS and diluted human plasma). The immunosensor comprises of covalent attachment of neutravidin protein to the rGO surface via amide bonds using carbodiimide crosslinking chemistry. To the best of our knowledge, this is the first report on the direct immobilization of neutravidin protein onto a rGO surface. Antibody immobilization with accurate orientation represents a great step forward in attaining ideal immunosensor performance via high signal amplification and lowering the limit of detection [38]. Therefore, we used biotinylated antibodies for the specific attachment of antibodies to the neutravidin-modified sensor surface. The biosensor showed highly sensitive and selective detection of Aβ(1-40), Aβ(1-42), and Tau-352 with one of the lowest reported LODs; in the femtomolar range. Our biosensor platform is expected to present a universal electrochemical biosensing strategy for multiplexed detection of protein biomarkers and their associated clinical diagnosis.

6.2 MATERIALS AND METHODS

6.2.1 MATERIALS:

Graphene Oxide (GO) solution (4mg/ mL) (DRP-GPHOXSOL-AQU) was purchased from Metrohm ltd. 1-Ethyl-3-(3-(dimethylamino)-propyl) carbodiimide hydrochloride (EDC) (>98%), N-hydroxysuccinimide (NHS) (98%), Ferrocene carboxylic acid (FeCOOH) (97%), Potassium hexacyanoferrate(III) (>99%), Potassium hexacyanoferrate(II) trihydrate (98.5-102%), Potassium chloride (KCl), Bovine serum albumin (BSA) and Phosphate buffered saline (PBS) tablets were supplied by Sigma-Aldrich and used as received. Neutravidin protein was purchased from ThermoFisher Scientific. Recombinant human Tau-352, biotin anti-tau 210-230 antibody, human β-Amyloid peptide (1-40), biotin anti-β-Amyloid (1-40) antibody, human β-Amyloid peptide (1-42), and biotin anti-β-Amyloid (1-42) antibody were purchased from Biolegend UK.

6.2.2 CHARACTERIZATION:

Electrochemical impedance spectroscopy (EIS) was used as a characterization technique for evaluating the electrochemical performance of blank and modified electrodes. Electrochemical impedance spectroscopy (EIS), differential pulse voltammetry (DPV), and cyclic voltammetry (CV) measurements were performed at room temperature using AutoLab and controlled by Nova 2.1.2 software.

The surface of the electrode was characterized using Raman spectroscopy and X-ray photoelectron spectroscopy (XPS) to check its quality.

6.2.3 ELECTROCHEMICAL MEASUREMENTS:

The electrochemical measurements (EIS, CV, and DPV) were performed with an electrolyte solution of 5 mM $K_3[Fe(CN)_6]/K_4[Fe(CN)_6]$. EIS was performed with frequencies ranging from 0.05 to 1000 Hz with 80 number of frequencies. CV was acquired at a scan rate of 50 mV/s from −0.3 V to 0.6 V without applying any pre-conditioning potential or accumulation time. DPV was recorded from −0.2 V to +0.5 V, with a step potential of 5 mV and an interval time of 0.5 seconds.

6.2.4 BIOSENSOR FABRICATION:

Figure 6.1 shows the schematic representation of the reported biosensor. Firstly, the flexible graphene-modified SPEs were coated with the GO layer followed by rGO reduction using the protocol mentioned elsewhere [33]. In short, 0.15 mg/mL GO aqueous solution was prepared in deionized (DI) water. The solution was then carefully drop cast onto the graphene electrode surface and dried for 2 hours at room temperature to promote the strong bond formation of GO on the graphene SPE, followed by 3 times washing with DI water. After that, the GO layer was electrochemically reduced in 10 mM $K_3[Fe(CN)_6]$ containing 1 M KCl solution via one CV cycle. A scan rate of 100 mV/s was applied, and the potential was varied between 0.5 V and -1.5 V [33]. After that 5 mM EDC/NHS solution was drop cast onto rGO coated SPEs and incubated for 40 minutes to activate the carboxylic groups. Once activated, the prepared 1 mg/

mL neutravidin solution was drop cast onto the electrode and covalently immobilized on the electrode surface by a coupling reaction between the amine groups of neutravidin and the EDC/NHS activated rGO moieties. Then the electrodes were left in the refrigerator for 16 hours at 4˚C. Subsequently, the electrodes were washed with 1 × PBS (pH 7.4) to remove the loosely bound neutravidin molecules. In the next step, 15 µL of 20 µg/mL of biotin anti-β-Amyloid (1-40) (Aβ(1-40)) antibody was added to the electrode surface and incubated for 16 hours in the refrigerator at 4˚C. Biotin anti-β-Amyloid (1-42) (Aβ(1-42)) antibody and biotin anti-tau antibody were also used in a similar concentration and incubated for the same time. Biotinylated antibodies were attached to the electrode surface via the avidin-biotin bio-recognition system.

Following antibody attachment, again the electrodes were washed with 1 × PBS to remove any loosely bound biotinylated antibodies. Subsequently, 1% BSA was drop cast onto the electrode surface and incubated for 30 minutes at 4˚C. to prevent any non-specific binding of the target protein. Thus, the Graphene/rGO/EDC-NHS/Neutravidin/Biotin-antibody/BSA bioelectrode

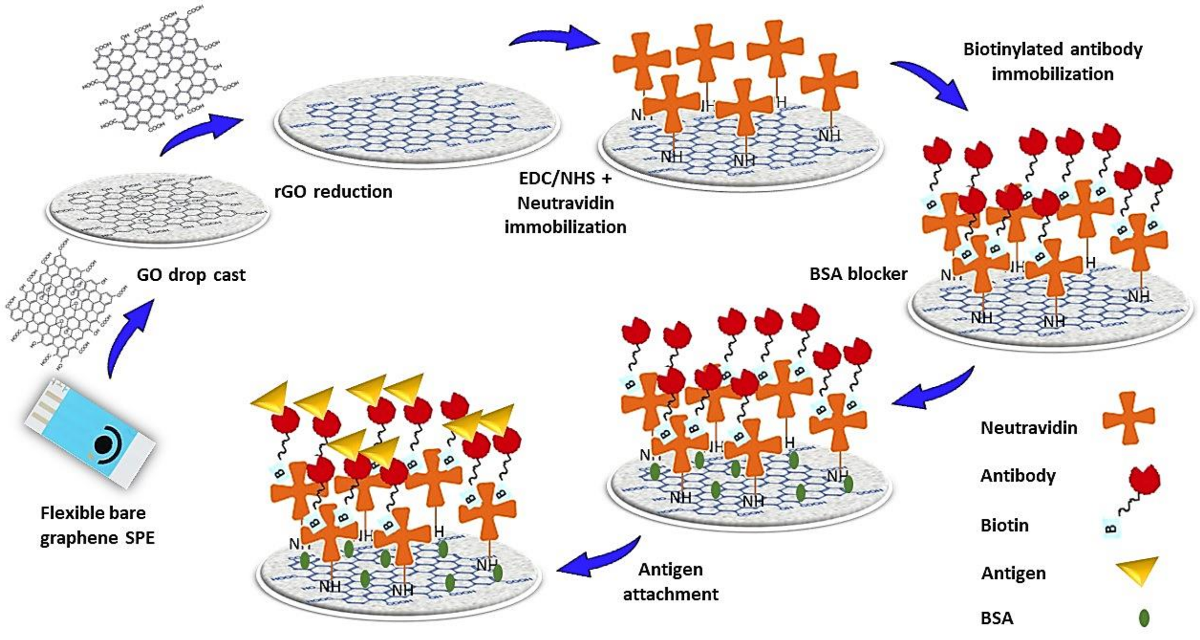

Figure 6. 1: Schematic representation of electrochemical immunosensor showing changes on the surface of flexible printed graphene electrode after each functionalization stage.

was fabricated. All the incubation steps were optimized in order to achieve the highest sensitivity for the proposed biosensor.

6.2.5 INTERACTION OF BIOMARKERS WITH THE SENSOR:

Aβ(1-40), Aβ(1-42), and Tau-352 proteins were spiked into both the PBS (pH 7.4) and diluted human plasma solution at various concentrations. 15 µL of each protein solution was drop cast onto the electrode surface and incubated at 4˚C for 30 minutes. This process was followed by rinsing the sensor with 1 x PBS (pH 7.4) to remove any unbound proteins. The measurement time for each sensor is approximately 6 minutes.

6.2.6 PLASMA SAMPLE ANALYSIS:

Our impedimetric biosensor was validated with both human and mouse plasma samples. Human Plasma samples were received from Istituto di Ricerche Farmacologiche "Mario Negri" IRCCS. Fasting blood samples (3 mL) from AD patients were collected by the venipuncture method. The blood aliquot was centrifuged at 2000 rpm for 15 minutes at 4°C to separate the plasma fraction. Subsequently, plasma was transferred to a fresh tube, aliquoted, and immediately frozen at -80°C until further use. Mice plasma samples were collected in a similar way starting from around 0.5 mL of whole blood. Informed consent was obtained from all human subjects. Besides all of the investigation protocols in this study have been approved by the relevant local ethics committee for clinical research (Milan, Italy).

6.3 RESULTS AND DISCUSSION

6.3.1 SURFACE MORPHOLOGY:

The surface morphology of bare graphene and rGO-coated graphene working electrodes was imaged using scanning electron microscopy (SEM) analysis. (**Figure 6.2**). The SEM images illustrate that graphene modification to rGO did not have any considerable effect on the electrode surface which confirms that no structural damage has been done. This contrasts with the intense modification procedures which are used for graphene sensors that could damage its chemical structure [39]. Consequently, the unique electrical properties of the graphene remain unchanged, and a high redox current has been observed for rGO-graphene dual layers.

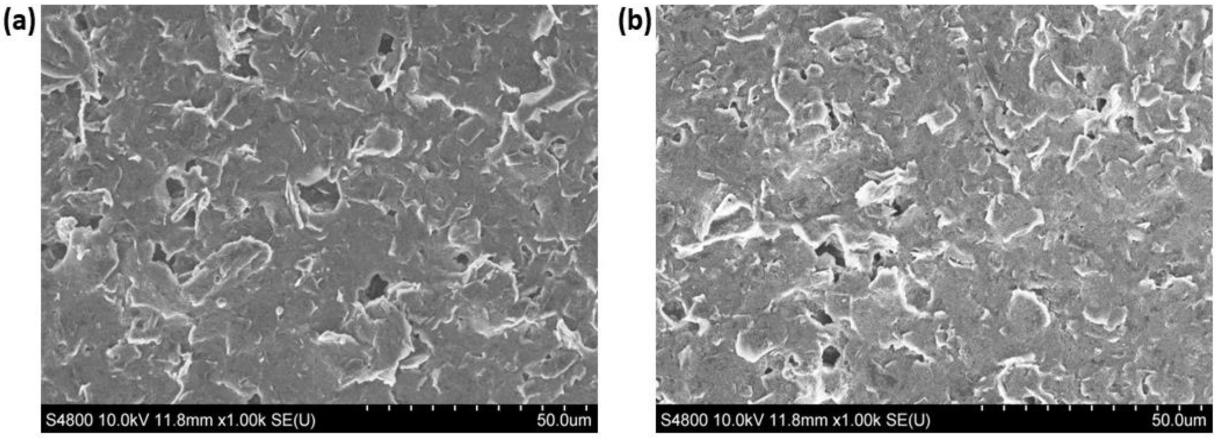

Figure 6. 2: SEM images of (a) graphene and (b) rGO-graphene dual layer

6.3.2 STRUCTURAL AND CHEMICAL ANALYSIS:

A comparison of Raman spectra obtained from unmodified graphene and rGO-coated graphene electrodes is shown in **Figure 6.3 (a)**. The Raman spectrum of bare graphene electrodes showed the D, G, and 2D band positions at 1350 cm^{-1}, 1580 cm$^{-1,}$ and 2700 cm^{-1} respectively similar to that of pristine graphene [40]. The intensity ratio between the D and G bands (I_D/I_G) was found to be 0.08 (black). After rGO modification on the graphene electrode, the I_D/I_G increased to 0.71 (red). Moreover, the significant increase in the I_D/I_G indicates the decrease in sp^2 carbon atoms revealing that the GO layer on the surface of the graphene electrode was successfully reduced to rGO [41].

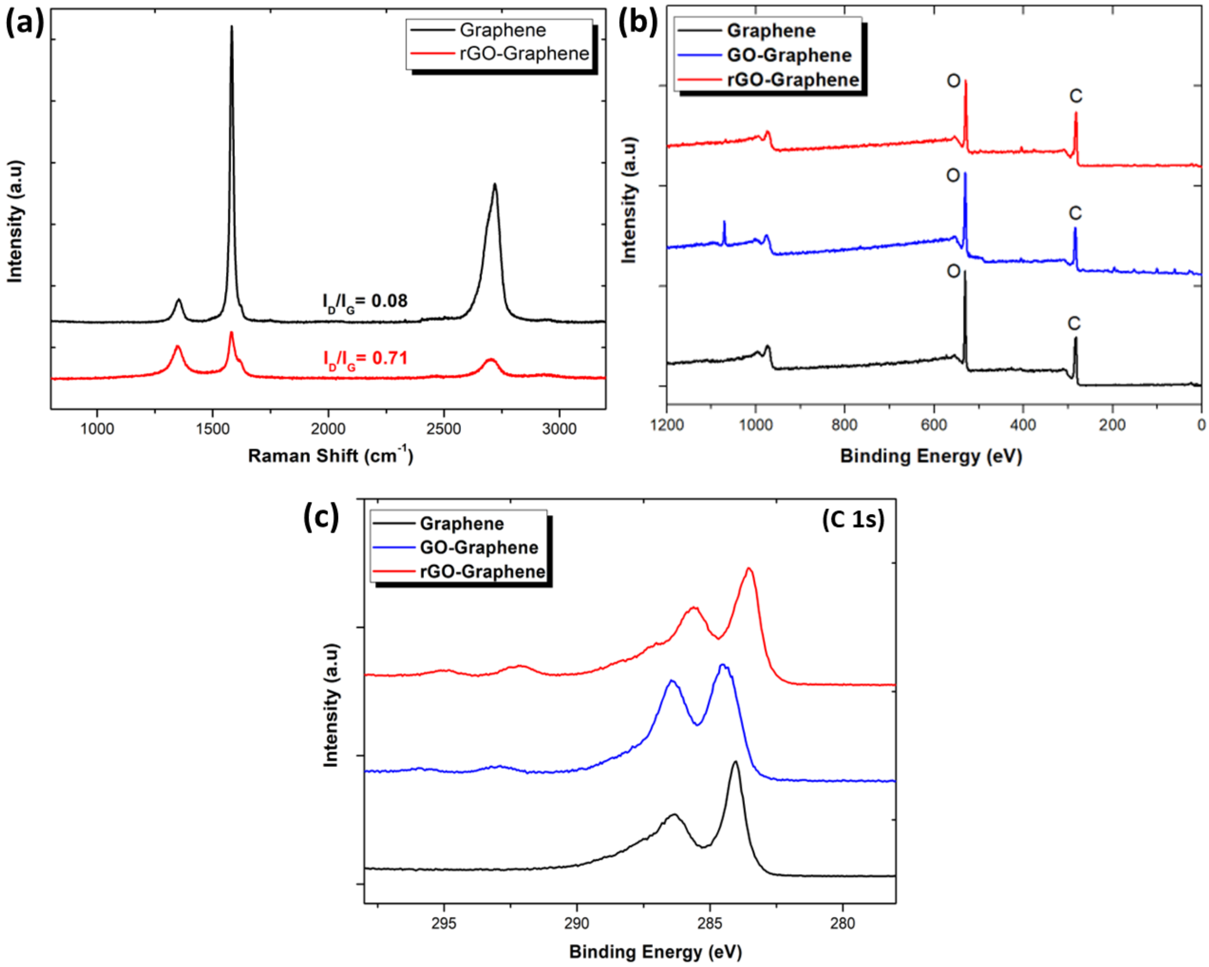

Figure 6. 3: Comparison of Blank and rGO modified SPE (a) Raman Spectrum (b) Wide XPS Spectrum (c) C 1s spectrum.

Additionally, I_D/I_G increases when the oxygen-containing functionalities on the GO surface are partly removed with electrochemical reduction. This is because the I_D/I_G ratio is the function of the average distance between the defective sites [33]. A drastic decrease in the 2D band was also observed, which indicates that the number of sp^3 carbon sites on the electrode surface are increased [42]. In addition, using a Kratos Axis Supra XPS, graphene and rGO coated SPEs were also characterized with XPS before and after functionalization with GO and rGO using a monochromatic Al Kα source with a pass energy of 20 eV. **Figure 6.3 (b)** shows the wide XPS spectrum. Peaks associated with C-C sp^2, C-C $sp^{3,}$ and C-O can be seen at 284 eV, 284.8 eV, and 286.2 eV, respectively [43]. The additional C-C sp^3 and C-O peaks are due to the presence of other organic compounds found in the graphene ink, such as resin and mixed solvents. After the addition of GO, the peak denoting C-O at 286.3 eV increased due to the additional presence of oxygen in GO [44]. After reducing the GO, the C-O peak decreases. This confirms the successful reduction of the GO to rGO. Additional peaks can be seen at 293 eV and 296 eV, which are attributed to potassium-based contaminants found in the commercial GO solution.

6.3.3 REACTION MECHANISM OF RGO/NVD/BIOTIN-ANTIBODY INTERFACES: `

6.3.3.1 Electrochemical Analysis:

Amine-terminated neutravidin protein was immobilized on the rGO coated electrode surface via carbodiimide coupling, where EDC/NHS was used for activating rGO moieties. 20 µg/mL of biotinylated antibodies (Aβ(1-40), Aβ(1-42), and Tau 210-230) were then added onto the neutravidin surface. Each neutravidin protein has four biotin-binding sites per molecule that bind biotin with high affinity and selectivity. The interaction of avidin (Neutravidin) and biotin is the strongest noncovalent attachment found so far [38]. EIS measurements were taken after each

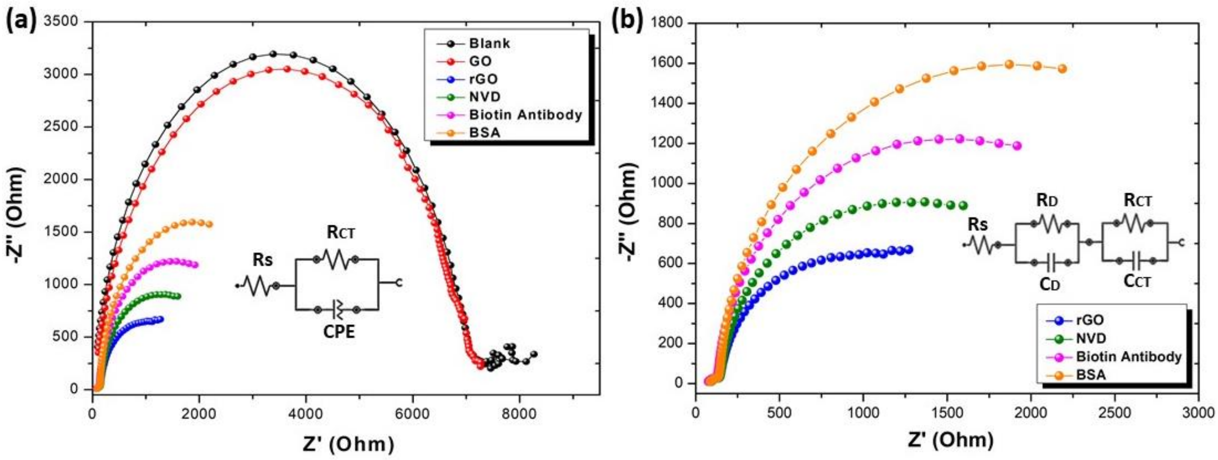

Figure 6. 4: Nyquist plots (−Z″ vs Z′) of graphene electrodes (a) blank (black) and after each modification step. Inset: Equivalent circuit for unmodified and GO modified electrode (b) rGO/NVD/ antibody/BSA electrode. Inset: Equivalent circuit for rGO/NVD/ antibody/BSA/Antigen electrode.

functionalization step. **Figure 6.4** shows the Nyquist plots of impedance spectra for the modified and un-modified graphene SPEs in the presence of the redox probe. The experimentally obtained data was closely fitted to simulated data obtained by two different Randle's equivalent circuits, depending on the extent of surface modification (**Figure 6.4 inset**).

The Randle's equivalent circuit (**Figure 6.4 (a), inset**) was successfully applied to fit the initial modification of the bare graphene SPE and after GO incubation. After rGO conversion, the system became highly conductive, and a drastic decrease in R_{CT} was observed. Therefore, another equivalent circuit was proposed in all the experiments as presented in **Figure 6.4 (b), inset**, which shows two circuits connected in series with each other. The equivalent circuit model with two circuits depicts the presence of two interfaces created in the process. The first interface is created between rGO and the electrolyte and another interface is created between the rGO defect sites and the electrolyte solution. Where Rs is the solution resistance, R_{CT} is the charge transfer resistance between the graphene/rGO dual layer and the electrolyte, R_D is the resistance to charge transfer at the graphene/rGO defect sites/electrolyte interface and C_{CT} and C_D are the capacitance corresponding to each resistor. Here, we used the changes in the charge transfer resistance (R_{CT}) to detect the immobilization of the antigen on the electrode surface.

The bare graphene electrode showed 7.25 kΩ of charge transfer resistance (R_{CT}). A slight decrease in the R_{CT} (7.19 kΩ) was observed upon the addition of GO solution on to the bare graphene electrode. This could be attributed to the fact that the coated graphene has more insulating behavior due to the quality of graphene ink used for the device fabrication and the GO solution has increased the charge transfer between the redox probe and the electrode because of its semiconducting properties. When GO was electrochemically reduced to rGO, a drastic decrease in R_{CT} (1.27 kΩ) was observed. This is attributed to the excellent conductive properties of rGO and indicated the successful modification of the graphene electrode. The subsequent neutravidin functionalization reduces the available sites on rGO for the charge transfer and results in again a slight increase in the R_{CT} to 1.77 kΩ. Immobilization of biotinylated antibodies decreases the current and increases the resistance to 2.38 kΩ. This shows that antibody functionalization impedes the charge transfer process at the electrode/ electrolyte interface. Similarly, blocking any non-specific sites at the electrode surface using BSA further increases the R_{CT} to 3.08 kΩ, suggesting the successful formation of Graphene/rGO/EDC-NHS/Neutravidin/Biotin-antibody/BSA bioelectrode.

6.3.4 OPTIMIZING SENSOR PARAMETERS:

Optimizing different sensor parameters is crucial for achieving the best performance of the sensor and also affects the device sensitivity as well as the detection limit. Here, we have optimized the following sensor parameters:

6.3.4.1 Neutravidin immobilization time:

DPV was carried out in order to optimize the immobilization time for neutravidin on the electrode surface. Neutravidin immobilization is limited to the availability of the activated functional group at the rGO surface and therefore it is important to optimize the incubation time. NVD solution was incubated for five different times i.e., 3, 6, 16, 20, and 24 hours. Results showed that the maximum value of peak current was obtained at 16 hours (ΔI = 42.5 µA) after which it starts decreasing to 27 µA and 22.3 µA at 20 and 24 hours. This is due to the saturation of the neutravidin layer over the rGO surface and excess protein reducing the charge transfer rate (**Figure 6.5 (a)**). Therefore, the optimum drop cast time was set at 16 hours.

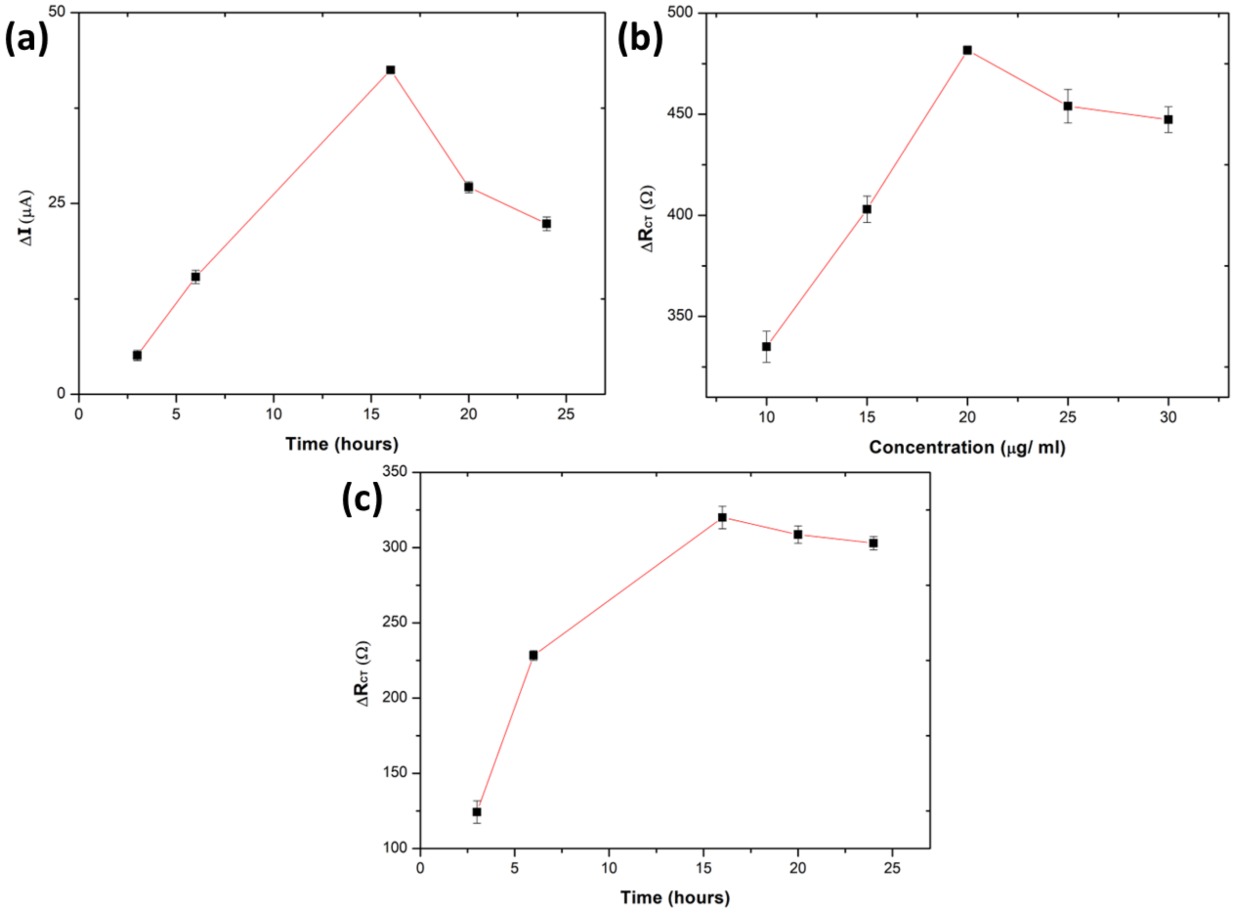

Figure 6. 5: Optimization parameters (a) Neutravidin immobilization time (b) Biotin antibody concentration (c) Biotin antibody incubation time.

6.3.4.2 Antibody concentration:

The immunosensor performance is also greatly influenced by the total amount of biomolecules immobilized onto the sensor surface. Consequently, optimizing antibody concentration is essential to achieve superior performance of the electrochemical immunosensor. As the biotin-avidin attachment system works similarly in the case of all biotinylated antibodies, we choose a biotinylated anti-tau antibody for optimizing the antibody concentration. Biotin antibody was immobilized onto neutravidin-modified electrodes at various concentrations i.e., 10, 15, 20, 25, and 30 µg/mL. The electrochemical analysis was performed using EIS. **Figure 6.5 (b)** shows that the change in resistance of charge transfer ΔR_{CT} first increases from 335**Ω** to 403**Ω** with the increase in antibody concentration to 15 µg/mL until it reaches the maximum at 20 µg/mL (481.6 **Ω**) after that slightly decreased again to 454 **Ω** and 447 **Ω** at 25 and 30 µg/mL respectively. The reason for the decrease at 25 µg/mL and above, may be the amount of tau antibody on the surface of the electrode tending to saturate after reaching the optimum concentration and this hinders the charge transfer from the electrolyte to the electrode surface. Further increase in the concentration of antibodies did not show any noticeable change suggesting that there is no need to increase the concentration. Thus, it was demonstrated that a 20 µg/mL concentration of biotinylated antibodies was the optimum choice.

6.3.4.3 Antibody immobilization time:

Antibody incubation time is another factor affecting the performance of our immunosensor. Therefore, we optimized the incubation time (3, 6, 16, 20, and 24 hours) for 20 µg/mL of biotin anti-tau antibody attachment. The change in charge transfer resistance ΔR_{CT} was found to be increased with the increase of incubation time from 124.3 **Ω** to 228.3 **Ω** at 3 and 6 hours (**Figure 6.5 (c)**). Maximum ΔR_{CT} was observed at 16 hours incubation time to be 320 **Ω**. Further, longer immobilization time somewhat decreased the ΔR_{CT} to 308 Ω and 303 Ω respectively. Therefore 16 hours was selected as the optimal incubation time for antibodies.

6.3.5 ANALYTICAL PERFORMANCE OF IMPEDIMETRIC IMMUNOSENSOR:

6.3.5.1 Specific detection of target proteins in PBS:

Prior to AD detection in a biofluid, the fabricated Graphene/rGO/EDC-NHS/Neutravidin/Biotin-antibody/BSA devices were analyzed to determine their capabilities for specific protein detection in a PBS buffer solution. Aβ(1-40), Aβ(1-42), and Tau-352 are known as the hallmarks of AD and are composed of 40, 42, and 352 amino acids, respectively. EIS was used to evaluate the sensitivity of the biosensor against a wide range of Aβ and tau-352 concentrations (10 fg/mL to 10 ng/mL). The semicircle of the Nyquist plot of impedance spectra represents the charge transfer resistance (Rct) of the system which is very sensitive to small changes that occur at the interface of electrode and electrolyte. Data acquired from Nyquist plots were closely fitted to simulated data obtained by Randle's equivalent circuit shown in **Figure 6.4 (b) inset**. **Figure 6.6 (a, b, and c)** shows the Nyquist plots obtained for Aβ(1-40), Aβ(1-42), and Tau-352 biomarkers and the corresponding calibration plots for the log of concentrations (in pg/mL) versus ΔR_{CT} are shown in **Figure 6.6 (d, e, and f)**. The results of the EIS studies showed that the increase in the concentration of Aβ(1-40) from 10 fg/mL to 10 ng/mL increases the Rct values which indicates the blocking of the electrode surface resulting in electron transfer hindrance. From **Figure 6.6 (d)** ΔR_{CT} values were measured as 0.073 kΩ, 0.12 kΩ, 0.17 kΩ, 0.213 kΩ, 0.26 kΩ, 0.303 kΩ, 0.36 kΩ and 0.453 kΩ with Aβ(1-40) concentrations of 10 fg/mL, 100 pg/mL, 1 pg/mL, 10 pg/mL, 100 pg/mL, 500 pg/mL, 1 ng/mL and 10 ng/mL respectively. ΔR_{CT} implies the change in the charge transfer resistance, which is formulated as:

$$\Delta R_{CT} = R_{CT,\ before\ incubation} - R_{CT,\ after\ incubation} \qquad (6.1)$$

A linear relationship was obtained between the log of Aβ(1-40) concentration and ΔR_{CT} from 10 fg/mL to 500 pg/mL concentration. A regression equation of the response was formulated as ΔR_{CT} = 0.05 log C + 0.168, with a correlation coefficient (R_2) of 0.99, where C is the Aβ(1-40) concentration. From this result, LOD was determined to be 1 pg/mL. LOD was calculated using equation 5.5 (Chapter 5).

Similarly increasing Aβ(1-42) concentration also increased the Rct values. From **Figure 6.6 (e)** ΔR_{CT} values for Aβ(1-42) were measured as 0.026 kΩ, 0.076 kΩ, 0.11 kΩ, 0.14 kΩ, 0.177 kΩ, 0.213 kΩ, 0.24 kΩ and 0.276 kΩ with concentrations of 10 fg/mL, 100 pg/mL, 1 pg/mL, 10 pg/mL, 100 pg/mL, 500 pg/mL, 1 ng/mL and 10 ng/mL respectively. A linear relationship was obtained between the log of Aβ(1-42) concentration and ΔR_{CT} from 10 fg/mL to 10 ng/mL

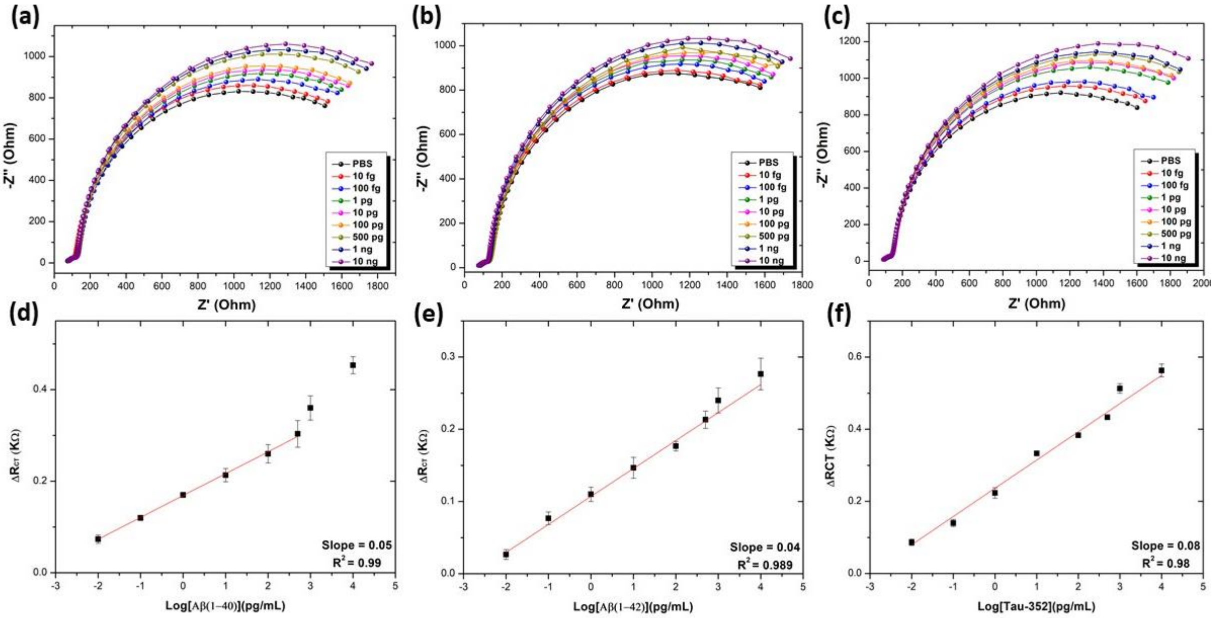

Figure 6. 6: Electrochemical impedimetric performances of the biosensor with different target concentrations in PBS; (a,b,c) Nyquist plots obtained as a function of different concentrations of Aβ(1-40), Aβ(1-42) and Tau-352; (d,e,f) Corresponding calibration plots Aβ(1-40), Aβ(1-42) and Tau-352 (n=3). The error bar provides the measure of reproducibility of the system.

concentration with the LOD of 0.95 pg/mL, which represents the clinically relevant range to diagnose AD. A regression equation of the response was formulated as ΔR_{CT} = 0.04 log C + 0.107, with a correlation coefficient (R_2) of 0.989, where C is the concentration of Aβ(1-42). Likewise, Tau-352 also showed an increase in ΔR_{CT} with increasing concentrations. From **Figure 6.6 (f)** ΔR_{CT} values for Tau-352 were measured as 0.087 kΩ, 0.14 kΩ, 0.223 kΩ, 0.34 kΩ, 0.383 kΩ, 0.434 kΩ, 0.514 kΩ and 0.563 kΩ with concentrations of 10 fg/mL, 100 pg/mL, 1 pg/mL, 10 pg/mL, 100 pg/mL, 500 pg/mL, 1 ng/mL and 10 ng/mL respectively. A linear relationship was observed between the log of Tau-352 concentration and ΔR_{CT} from 10 fg/mL to 10 ng/mL, and LOD was determined to be 0.63 pg/mL, which is again the clinically relevant range to diagnose AD. A regression equation of the response was formulated as ΔR_{CT} = 0.08 log C + 0.236, with a correlation coefficient (R_2) of 0.98, where C shows the Tau-352 concentration.

6.3.5.2 Specific detection of target proteins in human plasma:

The detection of Aβ(1-40), Aβ(1-42), and Tau-352 was validated in human plasma to investigate the clinical applicability of our flexible printed graphene electrodes. Human plasma was diluted in 10 mM PBS buffer (pH 7.4) at the ratio of 1:100. Different concentrations of Aβ(1-40), Aβ(1-42), and Tau-352 ranging from 10 fg/mL to 10 ng/mL were spiked into the diluted human plasma. The responses to Aβ and Tau-352 proteins revealed almost the same proclivity of changes in R_{CT} as that obtained in PBS buffer-based detections. **Figure 6.7 (a, b, and c)** shows the Nyquist plots obtained for Aβ(1-40), Aβ(1-42), and Tau-352 and the corresponding calibration plots for the log of concentrations (in pg/mL) versus ΔR_{CT} are shown in **Figure 6.7 (d, e, and f)**. As the concentration of Aβ(1-40) increased from 10 fg/mL to 10 ng/mL, ΔR_{CT} was measured to be 0.198 kΩ, 0.30 kΩ, 0.422 kΩ, 0.48 kΩ, 0.568 kΩ, 0.632 kΩ, 0.712 kΩ and 0.782 kΩ (**Figure 6.7 (d)**). A linear relationship was obtained between the log of Aβ(1-40) concentration and ΔR_{CT} from 10 fg/mL to 10 ng/mL concentration with the LOD of 1.59 pg/mL. A regression equation of the response was obtained as $\Delta R_{CT} = 0.095 \log C + 0.393$, with a correlation coefficient (R_2) of 0.99. In addition, with the increase in Aβ(1-42) concentration from 10 fg/mL to 10 ng/mL, the values of ΔR_{CT} were 0.13 kΩ, 0.226 kΩ, 0.368 kΩ, 0.446 kΩ, 0.52 kΩ, 0.574 kΩ, 0.602 kΩ, and 0.648 kΩ. Besides, there is no significant difference in the sensitivity in PBS. The linear dependence of ΔR_{CT} on the logarithmic concentrations of Aβ(1-42) was also determined ($R_2 = 0.97$) within the clinically relevant range of 10 fg/mL to 10 ng/mL with LOD of 1.4 pg/mL.

In Figure 6.7 (e), the regression equation is $\Delta R_{CT} = 0.08 \log C + 0.359$. In the case of Tau-352, as the concentration increased from 10 fg/mL to 10 ng/mL, the ΔR_{CT} values were obtained as 0.0.15 kΩ, 0.234 kΩ, 0.294 kΩ, 0.39 kΩ, 0.462 kΩ, 0.53 kΩ, 0.596 kΩ and 0.672 kΩ (**Figure 6.7 (f)**). A linear relationship also exists within a clinically relevant range (from 10 fg/mL to 10 ng/mL), and there were no significant differences in the sensitivity compared with that of PBS. The regression equation is $\Delta R_{CT} = 0.09 \log C + 0.312$ and $R_2 = 0.991$. The LOD of Tau-352

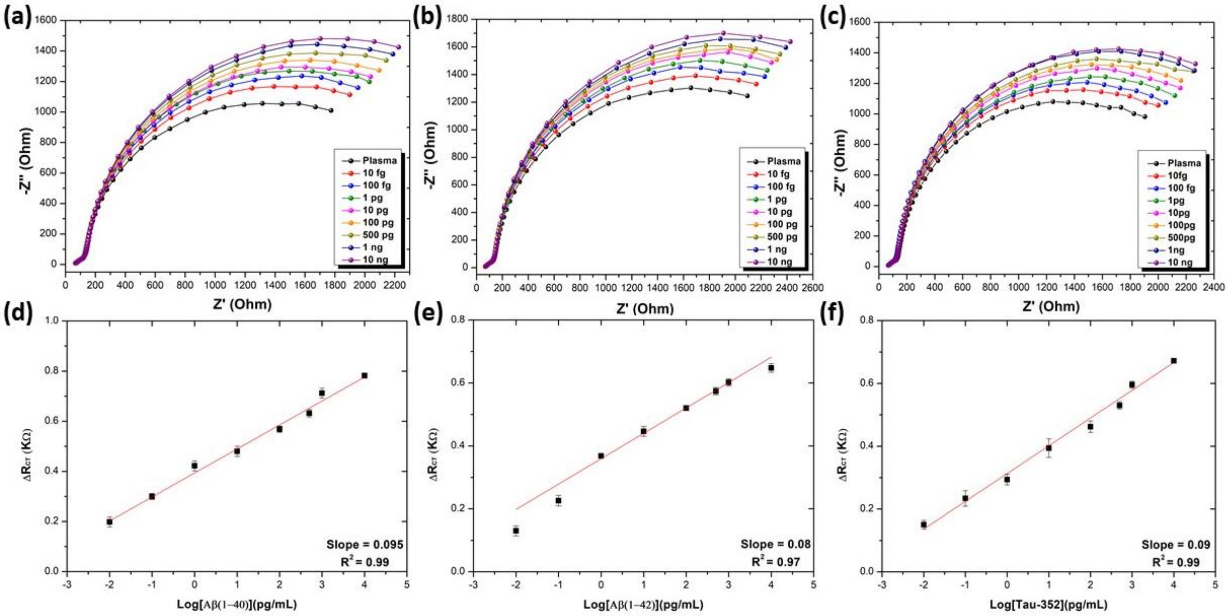

Figure 6. 7: Electrochemical impedimetric performances of the biosensor with different target concentrations in diluted human plasma; (a,b,c) Nyquist plots obtained as a function of different concentrations of Aβ(1-40), Aβ(1-42) and Tau-352; (d,e,f) Corresponding calibration plots Aβ(1-40), Aβ(1-42) and Tau-352 (n=5). The error bar provides the measure of reproducibility of the system.

spiked in human plasma was estimated as 1.1 pg/mL. These results showed that our proposed impedimetric biosensor can be applied to clinical samples with significantly good sensitivity in PBS, as well as in biofluids such as human plasma. This represents a major step forward in using SPE electrochemical sensors to detect AD markers in the blood.

6.3.5.3 Optimizing the sensor for false-positive:

Analysis of the effect of sensor response to false-positive was carried out by considering the effect of 1 x PBS (pH 7.4) and diluted human plasma (1:100) exposure on the biotin antibody functionalized sensor devices. **Figure 6.8** shows the comparison of the change in charge transfer resistance (ΔR_{CT}) of the sensors upon exposure to blank PBS and diluted human plasma with the tau-352 spiked PBS and plasma samples. Exposure to both solutions was repeated multiple times. It is clear from the figure that there was minimal change in ΔR_{CT} upon exposure to both PBS and plasma i.e., for PBS change in R_{CT} was measured as 0.0125 kΩ to 0.0225 kΩ, 0.05 kΩ, 0.06 kΩ, 0.0725 kΩ, 0.095 kΩ and 0.115 kΩ (**Figure 6.8 (a)**). Whereas for diluted human plasma ΔR_{CT} was measured to be 0.0425 kΩ, 0.085 kΩ, 0.1125 kΩ, 0.1525 kΩ, 0.185 kΩ, 0.2175 kΩ, 0.2575

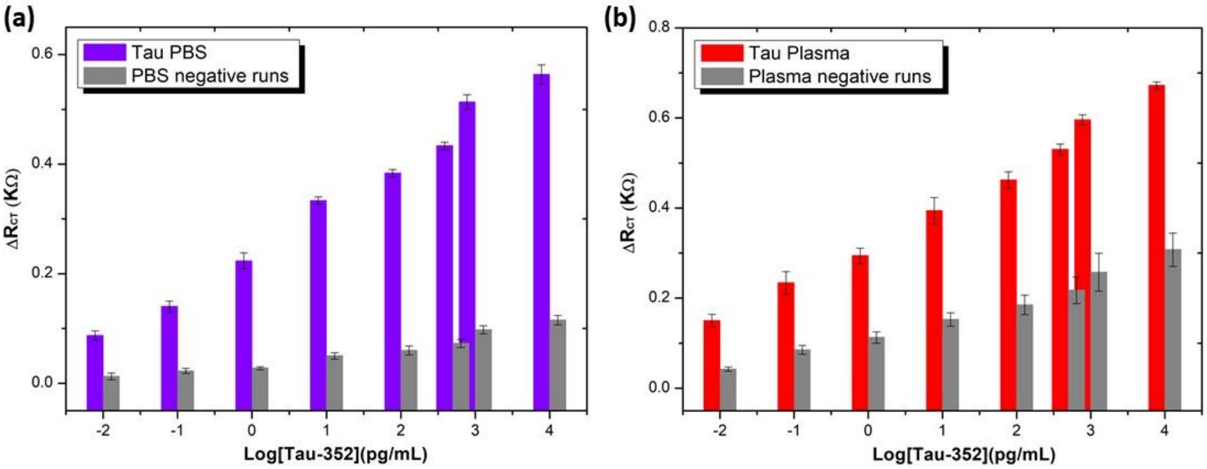

Figure 6. 8: Bar chart illustrating the change in charge transfer resistance (ΔR_{CT}) with exposure to (a) PBS only (b) diluted human plasma (negative runs with respect to each peptide concentration) and log of different concentrations of Tau-352 (n=3).

kΩ, and 0.3075 kΩ respectively (**Figure 6.8 (b)**). On the other hand, a significant change in R_{CT} was observed in the devices with exposure to the spiked target protein-containing samples compared to the changes observed in exposure to PBS only and diluted plasma samples (**Figure 6.8**). The repeated exposure of antibody-functionalized SPEs to biofluids showed reproducible changes in resistance. The small changes observed may be due to the adsorption of impurities on the sensor surface. However, these change was negligible when compared to the changes measured upon protein binding.

6.3.5.4 Mouse plasma sample analysis:

In this set of experiments, plasma samples obtained from aged non-transgenic (NTG) and 9 and 15-month-old AD transgenic (3TG) mice were analyzed without any pre-treatment. Tau is only developed in transgenic mice when they are 15 months old or later, likely because Tau pathology

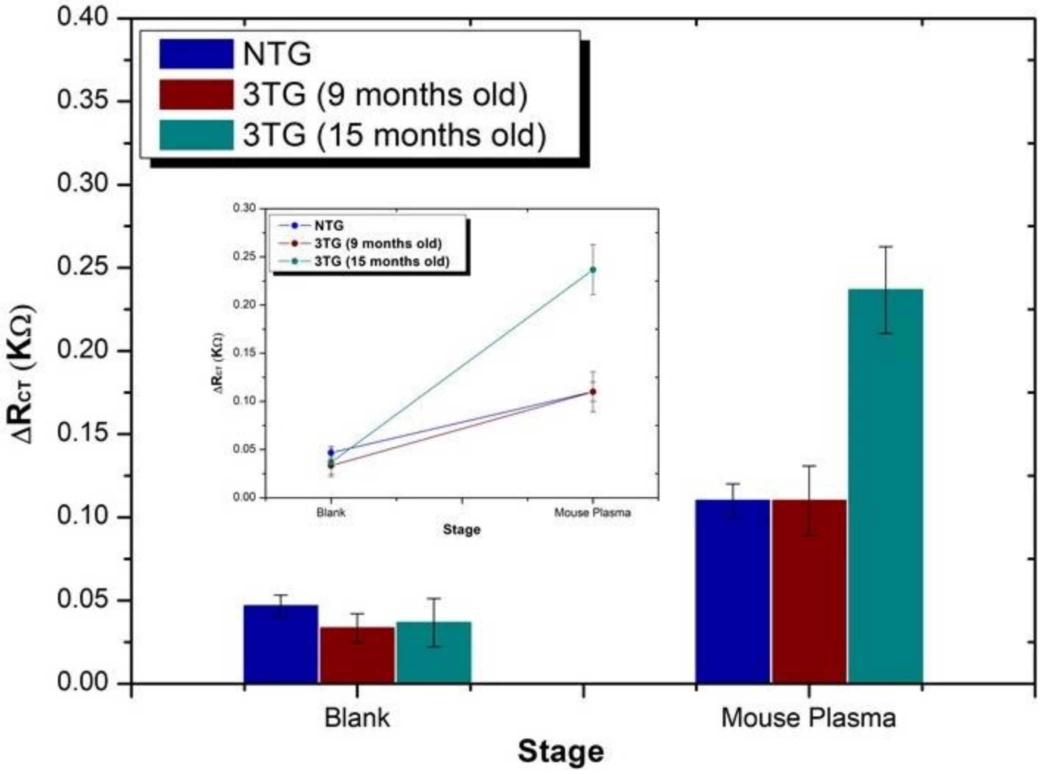

Figure 6. 9: Bar chart illustrating the responses obtained from EIS measurements from mouse plasma samples of non-transgenic (NTG), 9 months and 15 months old AD transgenic (3TG) mice respectively (n=3).

is detectable in these animals later than amyloidosis, and Tau released at the plasma level increases with aging [45]. Therefore, we decided to validate these mice samples with our biotin anti-tau 210-230 antibody modified devices. The EIS measurements were performed before and after the incubation of mouse plasma samples (**Figure 6.9**). Results indicated that 15 months old 3TG mice plasma samples showed a drastic increase in the ΔR_{CT} i.e., from 0.037 to 0.236 kΩ, suggesting the presence of tau protein in the plasma of 15 months 3TG mice. Whereas NTG and 9 months old 3TG samples did not show any perceptible change in ΔR_{CT} i.e., 0.046 to 0.11 kΩ for NTG and 0.033 to 0.11 kΩ as compared to 15 months old 3TG mice samples. The small change could be due to the adsorption of impurities from non-treated plasma samples on the sensor surface. These findings clearly indicate that our biosensors are capable of highly selective detection from blood plasma samples and suggest that they are viable in blood-based AD diagnostics.

6.3.5.5 Specificity analysis:

The specificity and selectivity of our biosensors towards Aβ(1-40), Aβ(1-42), and Tau-352 were also evaluated using EIS measurements. The biosensors were incubated with 20 ug/mL of biotinylated Aβ and tau antibodies. Subsequently, the respective devices were immobilized with 1 ng/mL of interfering agents and target proteins under similar experimental conditions. Furthermore, in order to analyze the specific detection of the target analyte from a solution containing a high concentration of non-specific proteins, a complex specificity test was also performed. For that purpose, we incubated the devices with a mixture of specific and non-specific proteins i.e., the mixture solution. **Figure 6.10 (a, b, c)** demonstrates the change in charge transfer resistance ΔR_{CT} of devices upon binding with different protein solutions. There was no significant response from non-specific analytes and this behavior was observed in all the devices

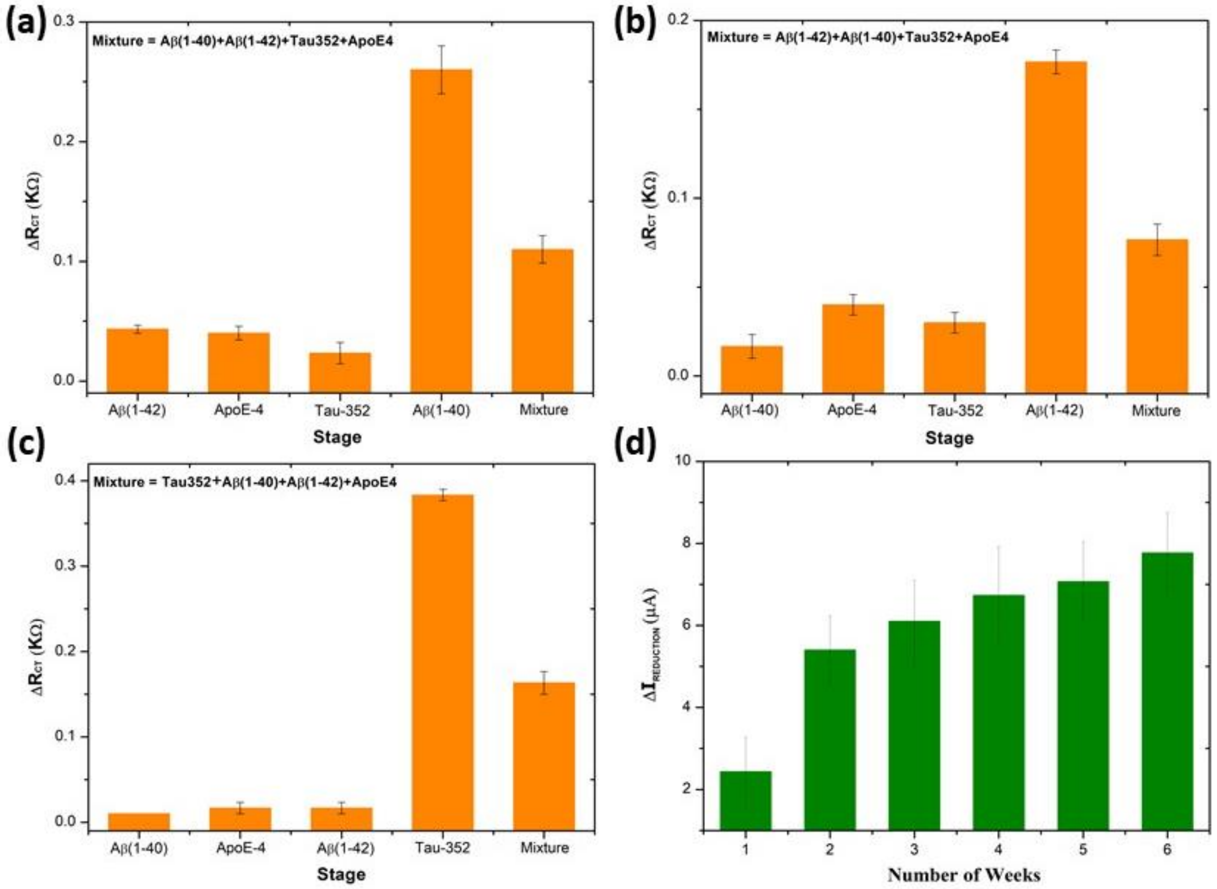

Figure 6. 10: (a, b and c) Changes in R_{CT} obtained from EIS analysis for specificity study of (a) Aβ(1-40), (b) Aβ(1-42), (c) Tau-352 using 1ng/mL concentration of interfering agents (n=3). (d) Changes in peak current reduction obtained from CV measurements for stability study of biotin anti tau 210-230 antibody modified devices (n=3).

as shown in **Figure 6.10 (a, b, c)**. The small changes may be due to the adsorption of these analytes on the electrode surface. In contrast, significant changes in ΔR_{CT} were observed only in the devices when their specific target proteins were immobilized. However, a slightly lower response was obtained from the sensors when the mixture solution containing the specific and non-specific target analytes was immobilized on them. As **Figure 6.10 (a, b, c)** clearly shows that the response from the non-specific analytes is negligible therefore, the response obtained from the mixture solution is considered to be obtained from the specific target proteins. These results confirm that our impedimetric biosensors are highly specific as well as being capable of performing multiplexed detection of AD biomarkers.

6.3.5.6 Stability studies:

The stability of our impedimetric immunosensor was also evaluated using CV measurements. The analysis was done on five different devices modified with biotin anti-tau 210-230 antibody and the prepared sensors were stored at 4 °C for periods up to 6 weeks. **Figure 6.10 (d)** shows that after one week, the CV current $\Delta I_{REDUCTION}$ was reduced to 2.43 µA and after 6 weeks the mean current was reduced up to 7.76 µA. The results suggest that our proposed immunosensor had acceptable stability over this period and potentially over longer periods.

6.4 CONCLUSION

In this study, a highly specific and ultra-sensitive graphene-modified flexible screen-printed electrode capable of detecting multiple biomarkers of AD pathogenesis has been developed. Using the neutravidin-biotin biorecognition system, biotinylated antibodies were immobilized in a specific orientation, and the number of binding sites for antibodies was also enhanced, which lead to an increase in the sensitivity and detection limit of the biosensor. The functionalized electrodes were employed for the detection of three important and recognized biomarkers of AD: Aβ(1-40), Aβ(1-42), and Tau-352 in PBS as well as in diluted human plasma solutions. In PBS, LOD of 1 pg/mL was achieved for Aβ(1-40), 0.95 pg/mL was achieved for Aβ(1-42), and 0.63 pg/mL was achieved for Tau-352 respectively. The successful validation of sensors using spiked human plasma samples achieved LODs of 1.59 pg/mL for Aβ(1-40), 1.4 pg/mL for Aβ(1-42), and 1.1 pg/mL for Tau-352 respectively, which are much lower than the LODs reported elsewhere for of detection of the same biomarkers in human plasma samples. The results suggest that the flexible printed graphene electrode platform developed in this work can be successfully applied in clinical practice as several studies have recently demonstrated that combined factors

(Aβ(1-40), Aβ(1-42), and Tau-352) derived from multiplexed detection can be used to provide a more accurate method for early diagnosis of AD compared to the detection of individual biomarkers.

BIBLIOGRAPHY

1. Calderon-Garcidueñas, A.L. and C. Duyckaerts, *Chapter 23 - Alzheimer disease*, in *Handbook of Clinical Neurology*, G.G. Kovacs and I. Alafuzoff, Editors. 2018, Elsevier. p. 325-337.
2. DeTure, M.A. and D.W. Dickson, *The neuropathological diagnosis of Alzheimer's disease.* Molecular Neurodegeneration, 2019. **14**(1): p. 32.
3. Lee, S.J.C., et al., *Towards an understanding of amyloid-β oligomers: characterization, toxicity mechanisms, and inhibitors.* Chemical Society Reviews, 2017. **46**(2): p. 310-323.
4. Lee, J.C., et al., *Diagnosis of Alzheimer's disease utilizing amyloid and tau as fluid biomarkers.* Experimental & Molecular Medicine, 2019. **51**(5): p. 1-10.
5. Parnetti, L., et al., *CSF and blood biomarkers for Parkinson's disease.* The Lancet Neurology, 2019. **18**(6): p. 573-586.
6. Nisbet, R.M., et al., *Tau aggregation and its interplay with amyloid-β.* Acta Neuropathologica, 2015. **129**(2): p. 207-220.
7. Park, J.-C., et al., *Plasma tau/amyloid-β1–42 ratio predicts brain tau deposition and neurodegeneration in Alzheimer's disease.* Brain, 2019. **142**(3): p. 771-786.
8. Chen, T.-B., et al., *Plasma Aβ42 and Total Tau Predict Cognitive Decline in Amnestic Mild Cognitive Impairment.* Scientific Reports, 2019. **9**(1): p. 13984.
9. Janelidze, S., et al., *Cerebrospinal fluid p-tau217 performs better than p-tau181 as a biomarker of Alzheimer's disease.* Nature Communications, 2020. **11**(1): p. 1683.
10. Verwey, N.A., et al., *Quantification of amyloid-beta 40 in cerebrospinal fluid.* Journal of Immunological Methods, 2009. **348**(1): p. 57-66.

11. Gagni, P., et al., *Development of a high-sensitivity immunoassay for amyloid-beta 1–42 using a silicon microarray platform.* Biosensors and Bioelectronics, 2013. **47**: p. 490-495.

12. Carrico, Z.M., G. Le, and R. Malinow, *A fluorescence assay for detecting amyloid-β using the cytomegalovirus enhancer/promoter.* J. Biol. Methods, 2017. **4**.

13. Oh, J., et al., *A carbon nanotube metal semiconductor field effect transistor-based biosensor for detection of amyloid-beta in human serum.* Biosensors and Bioelectronics, 2013. **50**: p. 345-350.

14. Park, D., et al., *Multiplexed femtomolar detection of Alzheimer's disease biomarkers in biofluids using a reduced graphene oxide field-effect transistor.* Biosensors and Bioelectronics, 2020. **167**: p. 112505.

15. Hassan, Q. and K. Kerman, *Electrochemical approaches for the detection of amyloid-β tau, and α-synuclein.* Current Opinion in Electrochemistry, 2019. **14**: p. 89-95.

16. Dai, Y., A. Molazemhosseini, and C.C. Liu, *In Vitro Quantified Determination of β-Amyloid 42 Peptides, a Biomarker of Neuro-Degenerative Disorders, in PBS and Human Serum Using a Simple, Cost-Effective Thin Gold Film Biosensor.* Biosensors, 2017. **7**(3): p. 29.

17. Abbasi, H.Y., et al., *Graphene based electrochemical immunosensor for the ultra-sensitive label free detection of Alzheimer's beta amyloid peptides Aβ (1–42).* Nanoscale Advances, 2021. **3**(8): p. 2295-2304.

18. Ngoc Le, H.T., et al., *Sensitive electrochemical detection of amyloid beta peptide in human serum using an interdigitated chain-shaped electrode.* Biosensors and Bioelectronics, 2019. **144**.

19. Ngoc Le, H.T., et al., *Sensitive electrochemical detection of amyloid beta peptide in human serum using an interdigitated chain-shaped electrode.* Biosensors and Bioelectronics, 2019. **144**: p. 111694.

20. Lien, T.T., et al., *Modified screen printed electrode for development of a highly sensitive label-free impedimetric immunosensor to detect amyloid beta peptides.* Analytica Chimica Acta, 2015. **892**: p. 69-76.

21. Mascini, M., I. Palchetti, and S. Tombelli, *Aptamers smart molecules for biosensing clinical samples.* CHIMICA OGGI-CHEMISTRY TODAY, 2011. **29**(2): p. 16-18.

22. Zhou, J., M.R. Battig, and Y. Wang, *Aptamer-based molecular recognition for biosensor development.* Analytical and Bioanalytical Chemistry, 2010. **398**(6): p. 2471-2480.

23. Yoo, Y.K., et al., *A highly sensitive plasma-based amyloid-β detection system through medium-changing and noise cancellation system for early diagnosis of the Alzheimer's disease.* Scientific reports, 2017. **7**(1): p. 1-10.

24. Wang, Y., et al., *Unlabeled Hairpin-DNA Probe for the Detection of Single-Nucleotide Mismatches by Electrochemical Impedance Spectroscopy.* Analytical Chemistry, 2008. **80**(6): p. 2255-2260.

25. Huang, J., et al., *An electrochemical impedimetric immunosensor for label-free detection of Campylobacter jejuni in diarrhea patients' stool based on O-carboxymethylchitosan surface modified Fe3O4 nanoparticles.* Biosensors and Bioelectronics, 2010. **25**(5): p. 1204-1211.

26. Kafka, J., et al., *A label-free DNA sensor based on impedance spectroscopy.* Electrochimica Acta, 2008. **53**(25): p. 7467-7474.

27. Daniels, J.S. and N. Pourmand, *Label-free impedance biosensors: Opportunities and challenges.* Electroanalysis: An International Journal Devoted to Fundamental and Practical Aspects of Electroanalysis, 2007. **19**(12): p. 1239-1257.

28. Georgakilas, V., et al., *Functionalization of Graphene: Covalent and Non-Covalent Approaches, Derivatives and Applications.* Chemical Reviews, 2012. **112**(11): p. 6156-6214.

29. Su, H., S. Li, and K. Kerman, *Novel thiolated-PEG linker molecule for biosensor development on gold surfaces.* Biosensors and Bioelectronics, 2019. **141**: p. 111477.

30. Ruecha, N., et al., *Label-free paper-based electrochemical impedance immunosensor for human interferon gamma detection.* Sensors and Actuators B: Chemical, 2019. **279**: p. 298-304.

31. Yang, W., et al., *Carbon nanomaterials in biosensors: should you use nanotubes or graphene?* Angewandte Chemie International Edition, 2010. **49**(12): p. 2114-2138.

32. Sethi, J., et al., *A label-free biosensor based on graphene and reduced graphene oxide dual-layer for electrochemical determination of beta-amyloid biomarkers.* Microchimica Acta, 2020. **187**(5): p. 1-10.

33. Li, B., et al., *Graphene electrode modified with electrochemically reduced graphene oxide for label-free DNA detection.* Biosensors and Bioelectronics, 2015. **72**: p. 313-319.

34. Wu, D., et al., *Two-Dimensional Nanocomposites Based on Chemically Modified Graphene.* Chemistry–A European Journal, 2011. **17**(39): p. 10804-10812.

35. Azzouzi, S., et al., *Generic Neutravidin Biosensor for Simultaneous Multiplex Detection of MicroRNAs via Electrochemically Encoded Responsive Nanolabels.* ACS Sensors, 2019. **4**(2): p. 326-334.

36. Macwan, I., et al., *Interactions between avidin and graphene for development of a biosensing platform.* Biosensors and Bioelectronics, 2017. **89**: p. 326-333.

37. Wang, S., et al., *Graphene field-effect transistor biosensor for detection of biotin with ultrahigh sensitivity and specificity*. Biosensors and Bioelectronics, 2020. **165**: p. 112363.

38. Gao, S., J.M. Guisán, and J. Rocha-Martin, *Oriented immobilization of antibodies onto sensing platforms - A critical review.* Analytica Chimica Acta, 2022. **1189**: p. 338907.

39. Teixeira, S., et al., *Epitaxial graphene immunosensor for human chorionic gonadotropin.* Sensors and Actuators B: Chemical, 2014. **190**: p. 723-729.

40. Barros, E., et al., *Raman spectroscopy of graphitic foams.* Physical Review B, 2005. **71**(16): p. 165422.

41. Ni, Z., et al., *Raman spectroscopy and imaging of graphene.* Nano Research, 2008. **1**(4): p. 273-291.

42. Kim, H.J., et al., *Unoxidized graphene/alumina nanocomposite: Fracture-and wear-resistance effects of graphene on alumina matrix.* Scientific Reports, 2014. **4**.

43. Chastain, J. and R.C. King Jr, *Handbook of X-ray photoelectron spectroscopy.* Perkin-Elmer Corporation, 1992. **40**: p. 221.

44. Al-Gaashani, R., et al., *XPS and structural studies of high quality graphene oxide and reduced graphene oxide prepared by different chemical oxidation methods.* Ceramics International, 2019. **45**(11): p. 14439-14448.

45. Biella, G., et al., *Sirtuin 2 inhibition improves cognitive performance and acts on amyloid-β protein precursor processing in two Alzheimer's disease mouse models.* Journal of Alzheimer's Disease, 2016. **53**(3): p. 1193-1207.

CHAPTER 7

CONCLUSION AND FUTURE WORK

7.1 CONCLUSION

This thesis has presented the multiple types of proof-of-concept biosensors for dementia application. These biosensor devices represent newly proposed methods for monitoring and diagnosing Alzheimer's disease. The reported immunosensors can be utilized for the rapid screening of patients. In addition to that, the electrochemical sensing techniques used in this thesis are easily adaptable and hence can be miniaturized to develop portable and nonexpensive devices. These devices have the capability of performing the rapid measurements on solutions with biomolecules even at very low concentrations. Hence, point-of-care monitoring and diagnostics can be performed using these devices.

In this thesis, an easy and reliable method for accessing the surface coverage of amino-phenyl groups attached to the carbon electrode surface using ferrocene carboxylic acid (FCA), which to the best of our knowledge has not been reported before. Also presented in this thesis are two different functionalization techniques for graphene-based substrates, that have been successfully reported for the detection of potential AD biomarkers. As currently there are no treatments available to avoid AD, hence the development of these point-of-care biosensors intends to provide easy analytical tools for the rapid detection of biomarkers related to AD for early-stage diagnosis.

This chapter summarized the biosensors developed throughout the duration of this PhD. Further recommendations and possibilities for biosensor development are also provided in this chapter.

7.1.1 LITERATURE REVIEW:

This chapter has highlighted the current diagnostic and therapeutic techniques for AD along with the incidence rate of AD, its risks, and symptoms. A comprehensive analysis of the pathophysiology and different stages of AD is provided as well. Various biomarkers for AD found in CSF and blood plasma are also highlighted. Also provided is the criteria for selecting the optimum biomarkers for biosensing, which include, the molecular weight, the ionic charge, and the sensitivity and specificity of the biomarkers. The most important criteria is to check the clinical concentration levels of the biomarker in both AD and normal control patients.

Moreover, a detailed review of biosensor technology particularly electrochemical biosensors is also presented in this chapter. Various techniques that were employed for the fabrication of biosensor devices are briefly highlighted. Besides, the role of graphene for the advancement of biosensor technology is highlighted. A key point about the graphene's remarkable electronic behavior is that it leads to exceptional carrier transport properties in comparison to other semiconductors. Surface functionalization plays a very important role in the development of any biosensor device. Therefore, graphene functionalization chemistry including covalent and non-covalent techniques is also discussed in this chapter. In addition, the biofunctionalization methodology adapted for biosensor research is also discussed in detail. Lastly, a detailed review of the state-of-the-art graphene-based electrochemical biosensors reported till now is presented.

7.1.2 MATERIALS AND METHODS:

Various techniques that are employed for the fabrication and characterization of biosensor devices were highlighted in this chapter. Understanding the stages involved in the biosensor development process is crucial for the specific detection of target molecules and for the repeatability of the work. The techniques described in this chapter were all used in order to gain a better understanding of the effect of the functionalization on the graphene, rGO, and subsequently the graphene sensor performance.

7.1.3 ASSESSING SURFACE COVERAGE OF AMINOPHENYL BONDING SITES ON DIAZOTISED GLASSY CARBON ELECTRODES FOR OPTIMIZED ELECTROCHEMICAL BIOSENSOR PERFORMANCE:

Several studies highlight the need for rapid and sensitive techniques for improving biosensor performance while emphasizing the fact that it is highly dependent on the material of the substrate. Electrochemical biosensors utilizing carbon-based electrodes are widely developed for the detection of a range of different diseases. Besides, various immobilization strategies have also been developed to immobilize the biomolecules to the carbon sensor platform. Here, the functionalization process selected for the biosensor plays a vital role in determining its overall performance. One of the most promising approaches to achieving functionalization is diazonium grafting. This method attaches the amine groups to a variety of substrates via covalent attachment. A common route to biofunctionalization for sensing is via reaction of surface amine groups, with a bioreceptor molecule i.e., antibodies, etc. Attaching the antibodies to the amine-terminated surface in the correct orientation is also crucial for improving the performance of the immunosensor. For that purpose, EDC/NHS coupling chemistry was utilized to activate the carboxylic groups of antibodies. The sensitivity of the biosensor highly depends on the surface coverage of antibodies, which in turn depends on the surface coverage of the amine precursor. In this work electrochemical techniques were used to assess the surface coverage of amino-phenyl groups attached to the carbon electrode, using the ferrocene carboxylic acid as a rapid and low-cost assay. Moreover, The effect on surface morphology before and after the diazotisation process was investigated using AFM and SEM on the HOPG electrode.

In the diazotisation of carbon electrodes, the nitro group is reduced to an amino group. Even though there has been extensive research on the diazotisation of carbon-based substrates, the previous studies have not quantified the electrochemical conversion of 4-nitrophenyl groups to aminophenyl groups. Hence, the main focus of this work was to report the quantification of the electrochemical conversion of 4-nitrophenyl groups to aminophenyl groups, which has never been reported.

Electrochemical grafting of the diazonium salt is discussed in detail in section 4.2.1. Typically, blank CV was recorded using a freshly cleaned GCE, following which, the active diazonium compound was added to the electrolyte, and further voltammograms were recorded for 5 cycles (**Figure 4.1**). CV of GCEs before and after the addition of diazonium to the electrolyte showed no redox processes for the blank scan. However, with the diazonium salt present, a broad irreversible peak was observed at 0.2 V, which corresponds to electron transfer associated with the cleavage of dinitrogen from the diazonium salt. This peak completely disappeared in subsequent scans, indicating no further reduction, presumably due to saturation of the available GCE surface with nitrophenyl groups.

Subsequent electrochemical reduction of NO_2 to NH_2 was carried out in KCl electrolyte, using CV, which occurred in three steps (**Scheme 4. 2**). CV curves of 4-nitrophenyl modified GCEs upon reduction cycles are shown in **Figure 4.3**. A strong irreversible reduction peak was observed at -0.9 V at the first scan corresponding to the formation of the hydroxylamine (PhNHOH). Later scans showed that the reversible redox peaks disappeared at a half-wave potential of -0.45 V. Which is attributed to the formation of the hydroxy aminophenyl on the GCE surface. Three CV scans were considered sufficient for aminophenyl conversion, as overlap in the reduction peaks indicated no further reduction on the electrodes after 3 scans. Equation 4.1 was used to estimate the surface coverage of aminophenyl after the reduction step.

After that amine groups were functionalized with FCA by adding 5 mM EDC/NHS solution to 250 µM FCA solution, followed by 40 minutes of incubation at RT (**Scheme 4.3**). The solution was immobilized on the amine-terminated GC electrode and left for 10 min before scanning in fresh PBS solution. CV was performed to confirm the attachment of FCA to aminophenyl groups. Due to the lack of amine groups on pristine GCE, no attachment of FCA was observed (**Figure 4.5**). The scan where GCE-$PhNO_2$ (reduction scan-1) underwent only a single reduction cycle in KCl, showed no redox peaks upon FCA functionalization. However, FCA binding was observed for the electrodes under consecutive scans. The surface coverage of FCA at different reduction scans is shown in Table 4. 3. It was observed that the surface coverage of FCA strongly depends on the number of reduction scans. The highest surface coverage was achieved for the sample prepared at reduction scan-3. Any further increase in scan reduces the FCA coverage.

In addition to that, a working sensor was also prepared utilizing the anti-beta amyloid antibody specific to Aβ (1-42) peptide. DPV was used for examining the attachment of antigens to antibodies (**Figure 4.7**). The results indicated that electrode made from a substrate prepared using reduction scan-3 shows more sensitivity (slope: 5.07 and R_2=0. 98) than those prepared using scans-5 (slope: 2.85 and R_2= 0.65). The regression equation has a logarithmic linear relation with Aβ (1-42) concentration (0 ng/mL to 200 ng/mL) with $R^2 = 0.98$ as the correlation coefficient. The control electrodes showed weak to no significant change in signal upon exposure to the peptide (**Figure 4. 8**). This confirms that the experimental conditions of diazotisation greatly influence the sensor performance. Besides, the pattern of results obtained from these reduction cycles with antibodies matched those conducted with FCA attachment.

7.1.4 GRAPHENE-BASED ELECTROCHEMICAL IMMUNOSENSOR FOR THE ULTRA-SENSITIVE LABEL-FREE DETECTION OF ALZHEIMER'S BETA-AMYLOID PEPTIDES AB(1-42):

AD is a neurological disorder that progresses slowly in the brain and is the cause of 60-70% of all dementia. Early diagnostics of AD is crucial as there is no certain treatment after it has progressed in the late stage. The existing investigation methods of AD are complicated and are usually made when the disease is already in an advanced stage. Thus, there is an intense need for the development of easy analytical tools for the rapid detection of AD biomarkers for early-stage point-of-care diagnosis. Aβ(1–42) peptide, is the key element of the senile plaques present in AD, thus making it a potential biomarker for AD diagnostics.

Electrochemical immunosensors provide a promising approach for both sensitive and selective analysis due to their high compatibility and repeatability, rapidness, simple instrumentation, low power requirements, easy signal quantification, etc. Label-free sensors can also be integrated into lab-on-a-chip platforms and have the benefit of using small volumes for rapid and inexpensive measurements as opposed to label-based technologies which are often more costly and time-consuming.

Here, a label-free proof-of-concept immunosensor was developed using the graphene-modified SPEs (SPGEs) for highly sensitive and specific detection of AD biomarker beta-amyloid peptides, isoform 42 (**Figure 5.9**). Graphene biosensors provide high sensitivity, lower detection limits, and high throughput detection when compared to conventional methods such as ELISA, PCR, and fluorescence assays. Polymer DAN (pDAN) was used to functionalize the graphene surface to provide a controlled amount of amines without even compromising the actual graphene properties. The polymer layer thickness was assessed by AFM. Moreover, XPS and Raman spectroscopy were used to characterize the graphene electrodes before and after pDAN functionalization.

The effects of polymer thickness on the electron transfer rates were also investigated and the polymer layer thickness was controlled by controlling the number of CV scan cycles to achieve a higher amount of surface amine groups. For that purpose, SPGE electrodes were modified with pDAN layers of different thicknesses (**Figure 5.2**). 3 cycles of pDAN were chosen as the optimized layer thickness for achieving more amine groups whilst maintaining the charge transfer characteristics for better sensor performance (Section 5.3.2).

Antibodies targeted against Aβ(1–42) were immobilized onto the amine surface using EDC/NHS chemistry to obtain preferential antibody orientation attachment. Furthermore, three different concentrations of anti-beta Amyloid antibodies were used to understand the effects that each concentration had on Aβ(1–42) detection sensitivity (**Figure 5.10**). Besides, the sensors were also optimized for the false positive response using DI water and PBS solutions. In addition, the response of the sensor towards the 0.1 mM PBS and beta-amyloid peptides Aβ(1-42) proteins upon binding to the antibody functionalized surface were also estimated using equation 5. The immunosensor was used for specific detection of Aβ(1–42) with a linear range of 1 pgmL^{-1} to 1000 pgmL^{-1} and has shown 1.4 pgmL^{-1} and 4.25 pgmL^{-1} detection and quantification limit, respectively (**Figure 5.12**). The sensor showed negligible response to the non-specific interactions with Tau-352, Aβ(1-40), and APO-E4 proteins (**Figure 5.13**). It also showed excellent sensing performance for spiked human plasma samples (**Figure 5.14**). Our proposed immunosensor modification method can certainly be used for the detection of other proteins, with optimization of detection platforms enabling tuning of the sensitivity range.

7.1.5 AN ELECTROCHEMICAL IMPEDIMETRIC BIOSENSOR BASED ON NEUTRAVIDIN- BIOTIN INTERACTION FOR FEMTOMOLAR RANGE DETECTION OF AD BIOMARKERS IN HUMAN PLASMA USING FLEXIBLE SCREEN-PRINTED GRAPHENE ELECTRODES:

Electrochemical biosensors based on electrochemical impedance spectroscopy (EIS) were reported in this work. In the EIS method, the impedance is measured by applying a small sinusoidal applied potential difference at a particular frequency to the electrode-electrolyte interface. The impedance of the electrode-electrolyte interface changes upon immobilization of the target analyte on the probe. Therefore, the concentration of the target analyte can be detected with impedance variations. In addition, the graphene/rGO dual platform for used for the development of the sensor devices. Combining both graphene and rGO further enhances their properties by increasing the conductivity and providing a large number of available active sites for bioreceptor attachment. This proof-of-concept biosensor utilizes the neutravidin protein which is covalently attached to the rGO surface by forming amide bonds using the carbodiimide crosslinking chemistry. As antibody immobilization with accurate orientation fosters a great step forward in attaining ideal immunosensor performance via high signal amplification and lowering its limit of detection, hence, biotinylated antibodies were used for the specific attachment of antibodies over the neutravidin-modified sensors. The biosensor showed highly sensitive and selective detection of three AD biomarkers Aβ(1-40), Aβ(1-42), and, Tau-352 with one of the lowest reported LODs in the femtomolar range.

Flexible graphene-modified screen-printed electrodes used in this work were designed and manufactured at the Centre for NanoHealth (CNH) at Swansea University. Subsequently, the devices were coated with 0.15 mg/ mL GO aqueous solution followed by electrochemical reduction to rGO using CV. The surface morphology of bare graphene and rGO-coated graphene working electrodes was observed by SEM (**Figure 6.2**), which showed there was no damage done to the electrode with rGO modification. In addition, the electrodes were also analyzed with XPS and Raman before and after rGO modification (**Figure 6.3**). After modification to rGO, 5mM EDC/NHS solution was drop casted on the electrodes to activate the carboxylic groups. Once activated, the prepared neutravidin solution was covalently immobilized on the electrode surface. In the next step all three types of biotinylated antibodies i.e., Aβ(1-40)), (Aβ(1-42), and anti-tau were immobilized via the avidin-biotin bio-recognition system, one by one on the electrodes with similar concentrations and incubation time. BSA was used as the blocking agent. EIS measurements were done after each functionalization step (**Figure 6.4**). Neutravidin immobilization time and antibody concentration and incubation time were also optimized (**Figure 6.5**) and the best results were chosen as the optimal parameters for analyzing the analytical performance of the immunosensor. Specific detection of target proteins was done in both PBS solution and human blood plasma samples. and Tau-352 in human plasma to investigate the clinical applicability of our flexible printed graphene electrodes. Plasma was diluted at the ratio of 1:100 prior to use. EIS was used to evaluate the sensitivity of the biosensor against wide concentrations of Aβ(1-40), Aβ(1-42), and Tau-352 ranging from 10 fg/mL to 10 ng/mL were spiked into the PBS and diluted human plasma samples (**Figure 6.6 and 6.7**). The semicircle of the Nyquist plot of impedance spectra presents the Rct of the system and the data acquired from Nyquist plots was well fitted by simulated data obtained by Randle's equivalent circuit (**Figure 6.4 (b) inset**). In PBS, LOD of 1 pg/mL was achieved for Aβ(1-40), 0.95 pg/mL was achieved for Aβ(1-42) and 0.63 pg/mL was achieved for Tau-352 respectively. Whereas, in human plasma, the LODs of 1.59 pg/mL for Aβ(1-40), 1.4 pg/mL for Aβ(1-42), and 1.1 pg/mL for Tau-352 were achieved, which are much lower than reported elsewhere in the case of detection in human plasma samples. In addition, the sensors were also optimized for false positives both in PBS and plasma samples. The repeated exposure of SPEs to biofluids showed reproducible changes in Rct. However, the change was negligible when compared to the changes measured upon protein binding (**Figure 6.8**).

As Tau pathology is considered to develop in the transgenic mice after when they are 15 months old, therefore, plasma samples from aged non-transgenic (NTG), 9 and 15-months-old AD transgenic (3TG) mice were validated with biotin anti-tau 210-230 antibody modified devices (**Figure 6.9**). Results indicated that 15 months old 3TG mice plasma sample showed a drastic increase in the ΔR_{CT} suggesting the presence of tau protein in the plasma of 15 months 3TG mice. Whereas NTG and 9 months old 3TG samples did not show any perceptible change in ΔR_{CT}. Moreover, the sensor exhibited a negligible response to the non-specific interactions and also showed stability for up to 6 weeks (**Figure 6.10**). The reported biosensor platform is expected to present a universal electrochemical biosensing strategy for multiplexed detection of protein biomarkers and their associated clinical diagnostics.

7.2 FUTURE WORK

In recent years, designing a suitable and reliable biosensor for Alzheimer's has attracted great interest with astonishing growth. In this thesis, multiple proof-of-concept biosensor platforms for detecting the biomarkers related to AD were successfully developed and tested. However, the sensor devices also showed sensitivity toward biofluids for instance PBS and blood plasma. Firstly, in order to fabricate the biosensors with more reliable results further optimization of each functionalization chemistry can be executed. This could be achieved by adjusting the concentration of linking molecules e.g., DAN, Neutravidin protein, EDC/NHS, etc. In addition, further optimization of antibody immobilization can be implemented. For that purpose, the bioreceptor concentration along with its immobilization time and temperature all have the potential to be further optimized. Additionally, the pH of the solution used for the reaction can also be optimized.

Incorporating metal nanoparticles into the sensing processes can further improve the sensor process. The addition of nanoparticles such as gold nanoparticles on the surface of graphene sensors results in an increase in surface area which in turn increase the bioreceptor attachment and hence amplify the biosensor's sensitivity by orders of magnitude. In addition, for manufacturing the SPE devices the quality of the ink used for the working electrode also plays a vital role in biosensor performance. Hence, using better quality graphene ink should also be aimed for the next stage of development. The blocking step can also be optimized by exploring more blockers from literature with smaller molecular sizes to decrease the debye length. This will result in improving the LOD of the sensor. Optimizing the blocker will also help to analyze the actual patient blood samples, which is a crucial requirement for POC diagnostics. This thesis reported the detection of analytes from spiked blood plasma samples but using the biosensors developed in this thesis, patients' pure blood samples still need to be tested.

Optimizing all such parameters will lead to the promising potential of these biosensors to be transformed into hand-held diagnostic tools for AD diagnostics. Furthermore, this biosensor technology has the capability of becoming the tool for multiplexed analysis that is capable of differentiating amongst the Alzheimer's and other brain-related diseases i.e., MCI. This can be achieved by developing the biosensor containing multiple working electrodes which can be individually and selectively functionalized to be specific for multiple AD-related biomarkers. For instance, a single graphene-based electrochemical biosensor device can be functionalized with different bioreceptors i.e. Aβ(1-40), Aβ(1-42), and Tau-352. Detecting these three biomarkers from patients' blood will indicate whether the person has or is likely to have the AD in future. Multiplexed biosensors can further be integrated with the micro-fluidics technology in order to develop a 'lab on a chip' point-of-care device, which is another exciting area for sensor development.

APPENDICES

SUBMITTED/ PUBLISHED ARTICLES:

1. **Abbasi, H. Y.**, Tehrani, Z., Devadoss, A., Ali, M. M., Moradi-Bachiller, S., Albani, D., & Guy, O. J. (2021). Graphene based electrochemical immunosensor for the ultra-sensitive label free detection of Alzheimer's beta amyloid peptides Aβ (1–42). Nanoscale Advances, 3(8), 2295-2304.
2. Tehrani, Z., **Abbasi, H. Y.**, Devadoss, A., Evans, J. E., & Guy, O. J. (2021). Assessing Surface Coverage of Aminophenyl Bonding Sites on Diazotised Glassy Carbon Electrodes for Optimised Electrochemical Biosensor Performance. Nanomaterials, 11(2), 416.
3. Legge, E. J., Ali, M. M., **Abbasi, H. Y.**, Reed, B. P., Brennan, B., Matjačić, L., ... & Pollard, A. J. (2021). Understanding the bonding mechanisms of organic molecules deposited on graphene for biosensing applications. *The Journal of Chemical Physics*, *155*(17), 174703.
4. Walters, F., Ali, M.M., Burwell, G., Rozhko, S., Tehrani, Z., Daghigh Ahmadi, E., Evans, J.E., **Abbasi, H.Y.**, Bigham, R., Mitchell, J.J. and Kazakova, O., 2020. A facile method for the non-covalent amine functionalization of carbon-based surfaces for use in biosensor development. *Nanomaterials*, *10*(9), p.1808**.**
5. Devadoss, A., Forsyth, R., Bigham, R., **Abbasi, H.Y.**, Ali, M., Tehrani, Z., ... & Guy, O. J. (2019). Ultrathin functional polymer modified graphene for enhanced enzymatic electrochemical sensing. Biosensors, 9(1), 16.

PLANNED PUBLICATIONS:

1. **Abbasi, H. Y.**, Tehrani, Z., Ali, M. M., Devadoss, A., Moradi-Bachiller, S., Albani, D., & Guy, O. J. An Electrochemical Impedimetric Biosensor Based On Neutravidin- Biotin Interaction For Femtomolar Range Detection Of AD Biomarkers In Human Plasma Using Flexible Screen-Printed Graphene Electrodes.

CONFERENCES AND NETWORK EVENTS:

1. European Horizon-2020 Marie Skłodowska Curie project "Blood Biomarker-based Diagnostic Tools for Early-Stage Alzheimer's Disease, NE3 Residential Workshop, 19th – 21st March 2018, Rome, Italy.
2. BBDiag China-Europe Alzheimer's disease symposium- Biomarkers and early diagnosis, 20th – 25th May 2018, Beijing China.
3. BioMedEng18 Conference, 6-7 September 2018, Imperial College London, UK.
4. BBDiag Mid Term Review Meeting, 9th -11th October 2018, Madrid, Spain.
5. ISSC-22 Interdisciplinary Surface Science Conference, 15th -18th April 2019, Village Hotel, Swansea UK.
6. BBDiag Summer School 17th -19th June 2019, Rostock, Germany.